

Nonlinear Self-Interference Cancellers
for In-Band Full-Duplex Radios
(帯域内全二重無線のための
非線形自己干渉キャンセラ)

January, 2021

Doctor of Philosophy (Engineering)

Kazuki Komatsu

小松 和暉

Toyohashi University of Technology

Date of Submission: Jan. 7th, 2021

Department of Electrical and Electronic Information Engineering	Student ID Number	D143229	Supervisors	Hideyuki Uehara Takashi Ohira Shuichi Ichikawa
Applicant's name	Kazuki Komatsu			

Abstract (Doctor)

Title of Thesis	Nonlinear Self-Interference Cancellers for In-Band Full-Duplex Radios
-----------------	-----------------------------------------------------------------------

Approx. 800 words

As the demand for wireless communications is increasing unabated, the achievement of efficient frequency utilization is an ongoing challenge. In-band full-duplex (IBFD) technology, which simultaneously transmits and receives on the same frequency band and can theoretically achieve twice the spectral utilization efficiency of conventional half-duplex systems, is an emerging technique in recent wireless communications. However, self-interference (SI) interferes significantly with the desired signal propagated from another terminal and disturbs the system capacity, as the distance between the transmission and reception antennas is extremely close compared to the distance between the terminal and another terminal. Unfortunately, orthogonal frequency division multiplexed (OFDM) modulation, which is commonly used in numerous systems at present, causes a high peak-to-average power ratio and the nonlinearities of the terminals have a significant impact on the signals. Furthermore, SI is distorted by other transceiver non-idealities, such as imbalances of the I/Q mixers and the phase noise of the local oscillators. Thus, the IBFD literature includes reports of nonlinear SI cancellers that have been developed to achieve improved cancellation performance. However, nonlinear cancellers exhibit certain problems, such as high computational complexity, the requirement of large training data, and vulnerability to the nonlinearity of low-noise amplifiers (LNAs). Moreover, no theoretical studies have been conducted on the performance of IBFD radios with nonlinear cancellers. This thesis presents studies on nonlinear cancellers with regard to the above problems.

Chapter 1 provides a general introduction to and summary of this thesis. It contains the background of the studies in this thesis and details of time-domain parallel Hammerstein cancellers, which are among the most well-studied SI cancellers.

In Chapter 2, a frequency-domain Hammerstein canceller is proposed, which achieves low computational complexity while taking into account the nonlinearity of I/Q mixers and power amplifiers (PAs). In the training period of the proposed canceller, discontinuities are produced in the OFDM symbols without destroying the cyclic prefix structure, and the parameter estimator can estimate the discontinuities of the SI signal with high accuracy in the frequency domain. In the cancellation period, the time-domain SI signal is regenerated with the estimated frequency response by the overlap-save method. The performance of the proposed scheme is assessed by equivalent baseband signal simulations of an IBFD transceiver. As a result, the proposed scheme achieves as high SI cancellation as time-domain parallel Hammerstein cancellers with a low computational cost. Furthermore, the results demonstrate that the convergence performance of the proposed scheme is faster than that of the time-domain scheme.

In Chapter 3, a basis function selection technique is presented to reduce the computational cost further and to improve the convergence performance of the frequency-domain Hammerstein canceller, which is presented in Chapter 2. The power spectral density (PSD) of the nonlinear SI

signal is theoretically analyzed in detail and a nonlinear SI PSD estimation method is developed. The proposed selection technique determines the basis functions that are necessary for cancellation and relaxes the computational cost of the frequency-domain Hammerstein canceller based on the estimated PSD of the SI of each basis function. Thereafter, the simulation results are presented, demonstrating that the proposed technique can achieve similar cancellation performance to the original frequency-domain Hammerstein canceller and a time-domain parallel Hammerstein canceller. It is also shown that the proposed technique improves the computational cost and convergence performance of the original frequency-domain Hammerstein canceller.

In Chapter 4, an iterative nonlinear SI canceller is proposed to consider the nonlinearities of not only the PA and I/Q mixers, but also the LNA. The estimation process of the proposed scheme consists of three stages: the channel response estimation, I/Q imbalance estimation, and PA and LNA nonlinearity estimation. The channel response is estimated in the time domain, whereas the I/Q imbalance and nonlinearities are estimated in the frequency domain by using features of OFDM modulation for a more straightforward estimation and superior accuracy. In the cancellation process of the proposed scheme, the received signal is compensated for with the estimated parameters of the LNA and receiver I/Q imbalance prior to cancellation, because the desired signal is received with a high-power SI and is distorted by the radio frequency impairments of the receiver. The simulation results reveal that the proposed technique can achieve higher cancellation performance than the Hammerstein canceller when the LNA is saturated by SI. Moreover, the performance of the proposed canceller converges much faster than that of the time-domain parallel Hammerstein canceller.

In Chapters 2 to 4, the development of cancellers that can achieve higher cancellation performance and a lower computational cost is presented, but a more detailed discussion of nonlinear cancellers is required to improve the performance of IBFD radios further. For a more in-depth discussion, Chapter 5 presents a theoretical analysis technique that takes into account the PA and LNA nonlinearities for IBFD radios with parallel Hammerstein SI cancellers. The envelope of an OFDM signal with a sufficiently large number of subcarriers can be assumed to follow a complex Gaussian distribution according to the central limit theorem. Thus, the nonlinear characteristics of the system can be expanded by a generalized Fourier series using orthonormal Laguerre polynomials. Subsequently, the canceller performance and system symbol error rate (SER) are analyzed using the obtained Fourier coefficients. The analytical results are compared with the simulation results, demonstrating strong correlation in various situations, from extremely nonlinear cases to good linear cases. Furthermore, the results demonstrate that the SER of the IBFD system is reduced by moderately nonlinearizing rather than linearizing the amplifier.

Chapter 6 concludes this thesis and provides a discussion on future works.

Contents

List of Figures	v
List of Tables	x
Acknowledgements	xi
1 General Introduction	1
1.1 In-Band Full-Duplex Radios	1
1.2 Overview of SI Cancellation	3
1.2.1 Analog-domain cancellation	3
1.2.2 Digital-domain cancellation	4
1.3 RF Non-Ideality in IBFD	6
1.3.1 Notations	7
1.3.2 RF non-ideality of I/Q mixers and oscillators	7
1.3.3 Amplifier AM–AM and AM–PM nonlinearity	12
1.4 Time-Domain Parallel Hammerstein Canceller	15
1.5 Summary of Dissertation	18
References	21
2 Frequency-Domain Hammerstein Canceller	27
2.1 Introduction	27
2.2 Self-Interference Signal Model	29
2.2.1 IQ mixer	29

2.2.2	Power amplifier	30
2.2.3	Self-interference coupling channel	31
2.2.4	Received self-interference signal	31
2.3	Proposed Frequency-Domain Canceller Based on Parallel Hammerstein Model	32
2.3.1	Generating training symbols	32
2.3.2	Frequency-domain training	34
2.3.3	Time-domain canceling using frequency response	36
2.3.4	Computational cost and complexity	37
2.4	Performance Simulations	38
2.4.1	Cancellation performance	38
2.4.2	Computational complexity and cost	41
2.5	Conclusion	42
	References	43
3	Basis Function Selection for Frequency-Domain Hammerstein Canceller	46
3.1	Introduction	46
3.2	Self-Interference Signal Model	48
3.2.1	IQ mixer	49
3.2.2	Power amplifier	50
3.2.3	Wireless channel and RF self-interference cancellation	51
3.2.4	Received self-interference signal	52
3.2.5	Received subcarriers	52
3.3	Proposed Scheme	53
3.3.1	Premeasurement	54
3.3.2	Training	56
3.3.3	Self-interference reconstruction	63
3.4	Numerical Simulations	64
3.4.1	Simulation environment	65
3.4.2	Results and discussion	66
3.5	Conclusion	74
	Appendix 3.A Derivation of (3.52) and (3.53)	75
	References	78

4	Iterative Nonlinear SI Canceller	80
4.1	Introduction	81
4.2	Self-Interference Signal Model	83
4.2.1	Transmit signal	84
4.2.2	Imbalance of IQ mixers	84
4.2.3	Nonlinear distortions of amplifiers	85
4.2.4	SI channel and RF cancellation	86
4.3	Proposed Scheme	87
4.3.1	Definitions of operators	88
4.3.2	IQ imbalance estimation	89
4.3.3	Channel estimation	91
4.3.4	Amplifier nonlinearity estimation	92
4.3.5	Self-interference cancellation	94
4.3.6	Pseudo code and computational cost	94
4.4	Numerical Simulations	98
4.4.1	Simulation environment	98
4.4.2	Results and discussions	101
4.4.3	Limitations of the proposed canceller	107
4.4.4	Computational cost	109
4.5	Conclusion	110
	Appendix 4.A Derivations of (4.26)–(4.30)	110
	References	112
5	Theoretical Analysis of IBFD Radios	116
5.1	Introduction	116
5.1.1	IIP-based distortion analysis	117
5.1.2	Contributions	118
5.1.3	Organization and notations	119
5.2	Theoretical Background and Theorems	120
5.2.1	Generalized Fourier series expansion with orthonormal Laguerre polynomials	121
5.2.2	Theorems related to the parallel Hammerstein canceller	125
5.3	Theoretical Analysis of Nonlinear Self-Interference Canceller	128
5.3.1	Analytical model	129
5.3.2	Cancellation performance	131

5.3.3	Symbol error rate	132
5.3.4	Analysis summary	133
5.4	Examples and Verification	135
5.4.1	Cancellation performance	136
5.4.2	Symbol error rate	139
5.4.3	How can a nonlinear amplifier performance be better than the linearized amplifier?	141
5.5	Conclusion	141
Appendix 5.A	Proof of Theorem 2	142
Appendix 5.B	Condition of $\dot{c}_p(\tau) = \dot{h}_p(\tau)$	143
Appendix 5.C	Probability Density Function of (5.57)	145
Appendix 5.D	Analysis Examples on Saleh Model	146
References		148
6	Overall Conclusions	151
A	Weighted Least Squares with Orthonormal Polynomials and Numerical Integration for Estimation of Memoryless Nonlinearity	154
A.1	Introduction	154
A.2	Proposed Method	158
A.2.1	Example 1: Gauss–Laguerre quadrature	159
A.2.2	Example 2: Rectangular rule	160
A.2.3	Theoretical error analysis	161
A.3	Results of Numerical Experiments	163
A.4	Conclusion	166
References		168
B	List of Related Publications by the Author	170
B.1	Journal Papers and Letters	170
B.2	Conference Papers	171
B.3	Presentations in Japanese	171
B.4	Awards	173

List of Figures

1.1	Block diagram of I/Q mixers	7
1.2	Effect of I/Q imbalance on I/Q constellation	9
1.3	Effect of I/Q imbalance on frequency domain	9
1.4	Effect of phase noise	10
1.5	Block diagram of up-converter with I/Q imbalance and phase noise .	11
1.6	Block diagram of down-converter with I/Q imbalance and phase noise	12
1.7	Block diagram of time-domain parallel Hammerstein canceller	16
2.1	A model of the assumed full duplex transceiver.	29
2.2	Proposed SI canceller.	32
2.3	Swapped training OFDM symbols.	33
2.4	The SI cancellation performance at $N_{tr} = 60$	40
2.5	The convergence of each canceller at INR = 50 dB and IRR = 25 dB.	40
2.6	The convergence performance of the proposed scheme with RLS algorithm at $N_{swp} = 0 \dots 4$ and IRR = 25 dB.	41
3.1	A model of the assumed full-duplex transceiver.	48
3.2	The median SICR of the proposed scheme at $-10 \text{ dB} \leq \gamma \leq 10 \text{ dB}$ with INR = 50 dB. The RLS algorithm is used as the training algorithm. The smoothness factor of the LNA is $S_{LNA} = 3$	67

3.3	The percentage of trails where the SICR of the proposed scheme is lower than 47 dB in all trials at $-10 \text{ dB} \leq \gamma \leq 10 \text{ dB}$ with $\text{INR} = 50 \text{ dB}$. The RLS algorithm is used as the training algorithm. The smoothness factor of the LNA is $S_{\text{LNA}} = 3$	68
3.4	The computational cost of the proposed scheme at $-10 \text{ dB} \leq \gamma \leq 10 \text{ dB}$ with $\text{INR} = 50 \text{ dB}$. The RLS algorithm is used as the training algorithm. The smoothness factor of the LNA is $S_{\text{LNA}} = 3$	69
3.5	The median SICR value of each canceller with the LS algorithm at $N_{\text{tr}} = 60$. The smoothness factor of the LNA is $S_{\text{LNA}} = 3$. For the proposed scheme, $\beta = -20 \text{ dB}$ and $\gamma = 0 \text{ dB}$	70
3.6	The median SICR value of each canceller with the LS algorithm at $N_{\text{tr}} = 60$. The smoothness factor of the LNA is $S_{\text{LNA}} = 1$. For the proposed scheme, $\beta = -20 \text{ dB}$ and $\gamma = 2 \text{ dB}$	71
3.7	The convergence of each canceller with the LS algorithm at $\text{INR} = 50 \text{ dB}$. SICR values are median values of all trials at each situation. The smoothness factor of the LNA is $S_{\text{LNA}} = 3$. For the proposed scheme, $\beta = -20 \text{ dB}$ and $\gamma = 2 \text{ dB}$	72
3.8	The convergence of each canceller with RLS algorithm at $\text{INR} = 50 \text{ dB}$. SICR values are median values of all trials at each situation. The smoothness factor of the LNA is $S_{\text{LNA}} = 3$. For the proposed scheme, $\beta = -20 \text{ dB}$ and $\gamma = 2 \text{ dB}$	73
3.9	The convergence of each canceller with NLMS algorithm at $\text{INR} = 50 \text{ dB}$. SICR values are median values of all trials at each situation. The smoothness factor of the LNA is $S_{\text{LNA}} = 3$. For the proposed scheme, $\beta = -20 \text{ dB}$ and $\gamma = 2 \text{ dB}$	74
3.10	The computational cost at a training stage with $\beta = -20 \text{ dB}$ and $\gamma = 2 \text{ dB}$	75
3.11	The selected percentage in all subcarriers for each basis function. In this figure, $\beta = -20 \text{ dB}$, $\gamma = 2 \text{ dB}$, and $S_{\text{LNA}} = 3$	76
3.12	The percentage of trails where the SICR of the proposed scheme is lower than 47 dB in all trials when nonlinear parameters are varied on log-normal distribution. In this simulation, the LS algorithm is used as the training algorithm. INR , β , γ , and S_{LNA} are 50 dB, -20 dB , 2 dB, and 3 respectively.	77

4.1	In-band full-duplex transceiver model with the proposed digital self-interference canceller	83
4.2	Block diagram and signal flow of the self-interference with each RF component and operator	88
4.3	Frequency region to estimate $d_{\phi,p}$	92
4.4	Performance of the proposed canceller with different numbers of iterations of Newton's method. The INR is 60 dB, and the proposed canceller estimates parameters in ten iterations. The canceller is trained with 20 OFDM symbols.	101
4.5	Performance of the proposed canceller with different numbers of iterative estimation and different orders of estimation. The INR is 60 dB, and the number of iterations of Newton's method is one. The canceller is trained with 20 OFDM symbols.	102
4.6	Performance of the proposed canceller with different numbers of subcarriers for estimation of nonlinear coefficients. The INR is 60 dB; the number of iterations of Newton's method is one; the number of iterations of the estimation process is three. The canceller is trained with 20 OFDM symbols.	103
4.7	Performance of each canceller with 100 training symbols on different amounts of RF attenuation A_{RF} and different transmission powers. The numbers in parentheses in the legend denote the values of A_{RF} . In the proposed scheme, $M_n = 1$, $L = 3$, and $K = 8$	104
4.8	Performance of each canceller with 100 training symbols and different self-interference powers. In this result, $M_n = 1$, $L = 3$, and $K = 8$	105
4.9	Convergence of each canceller at INR = 50 dB. In this result, $M_n = 1$, $L = 3$, and $K = 8$	106
4.10	Short span convergence of each canceller at INR = 50 dB. In this result, $M_n = 1$, $L = 3$, and $K = 8$	107
4.11	Performance of each canceller with 100 training symbols and different IRR values. In this result, $M_n = 1$, $L = 3$, and $K = 8$	108
5.1	The linear and nonlinear component powers of two-tone and OFDM signals in the Rapp model. The smoothness factor of the Rapp model is $s = 2$, and the saturation level is $V_{\text{sat}} = 1$. In the two-tone case, each component power is computed by simulation. In the OFDM case, each component power is theoretically calculated as [9].	118

5.2	The signal model used in Section 5.2.1. The input signal has a complex Gaussian distribution with zero mean and unit variance. The nonlinear transfer function $\alpha(x)$ has AM-AM and AM-PM nonlinearities.	121
5.3	The signal model for Section 5.2.2. The self-interference model has infinite-order nonlinear components corresponding to the orthonormal polynomials $\psi_p(x)$. In contrast, the canceller can regenerate and cancel finite-order nonlinear components corresponding to the simple powers $x x ^{p-1}$	125
5.4	Analysis model of the full-duplex transceiver.	128
5.5	The performance of nonlinear self-interference cancellers with different values of received self-interference powers. The nonlinear amplifiers $\alpha_n(x)$ and $\beta_n(x)$ were modeled using the Rapp model.	137
5.6	The performance of nonlinear self-interference cancellers with different values of smoothness factors for both terminals' PAs. The nonlinear amplifiers $\alpha_n(x)$ and $\beta_n(x)$ were modeled using the Rapp model. Arrows on the y-axis indicate the SICR ₁ value of the infinite smoothness factor (ideally predistorted amplifier).	138
5.7	The average SER of the two full-duplex terminals with different values of input back-offs for both terminals' PAs. The nonlinear amplifiers $\alpha_n(x)$ and $\beta_n(x)$ were modeled using the Rapp model.	139
5.8	The average SER of the two full-duplex terminals with different values of smoothness factors for both terminals' PAs. The nonlinear amplifiers $\alpha_n(x)$ and $\beta_n(x)$ were modeled using the Rapp model. Arrows on the y-axis indicate results for the infinite smoothness factor (ideally predistorted amplifier).	140
5.9	Domain of the two-dimensional integration in (5.89).	145
5.10	The average symbol error rate (SER) of the two full-duplex terminals with different values of input-back-offs of both terminals' PAs. The nonlinear amplifiers $\alpha_n(x)$ and $\beta_n(x)$ are modeled using the Saleh model.	147
A.1	Condition number of the Gram matrix of each method when $P = 7$. The value is averaged over 10^4 times independent Monte Carlo simulation.	164

A.2	Total reconstruction error E_{tot}^2 of each method with $P = 7$ and $\sigma_z^2 = 10^1$. The lines indicate theoretical results, and the markers indicate simulation results.	165
A.3	Total reconstruction error E_{tot}^2 of each method with $P = 13$ and $\sigma_z^2 = 10^{-1}$. The lines indicate theoretical results, and the markers indicate simulation results.	165
A.4	Total reconstruction error E_{tot}^2 of each method with $P = 7$ and $\sigma_z^2 = 10^{-4}$. The lines indicate theoretical results, and the markers indicate simulation results.	166
A.5	Total reconstruction error E_{tot}^2 of each method with $P = 13$ and $\sigma_z^2 = 10^{-7}$. The lines indicate theoretical results, and the markers indicate simulation results.	167

List of Tables

1.1	Digital cancellers and RF impairments in literature	4
2.1	Simulation Specifications	39
2.2	Computational complexity and cost per sample	42
3.1	Simulation Specifications	64
3.2	CMOPS of time-domain cancellers	71
4.1	Digital Cancellers and RF Impairments in the Literature	82
4.2	Computational Cost of Primitive Operations with n -Length Signal . .	96
4.3	Pseudo Code and Computational Cost of IQI Estimation Stage	96
4.4	Pseudo Code and Computational Cost of Channel Estimation Stage .	97
4.5	Pseudo Code and Computational Cost of Nonlinear Estimation Stage	97
4.6	OFDM Modulation Specifications	99
4.7	Simulation Specifications	100
4.8	Parameters, and Their Values, for Comparing Computational Costs .	110
5.1	Variables used in this chapter	120
5.2	OFDM Modulation Specifications	135
5.3	Simulation and Analysis Specifications	135

Acknowledgements

This dissertation presents a collection of studies that were carried out under the direction and guidance of Professor Hideyuki Uehara and Assistant Professor Yuichi Miyaji of the Department of Electrical and Electronic Information Engineering, Toyohashi University of Technology, Japan, from 2014 to 2021. Therefore, I would like to take this opportunity to thank all those who helped me and provided me with a comfortable environment in which I could accomplish this work.

My sincere gratitude and deepest appreciation should first be given to Professor Hideyuki Uehara and Assistant Professor Yuichi Miyaji for their valuable suggestions, guidance, and continuous encouragement throughout the work.

I wish to gratefully acknowledge my indebtedness to Professor Takashi Ohira, Professor Shuichi Ichikawa, and Professor Uehara Hideyuki of the Department of Electrical and Electronic Information Engineering, Toyohashi University of Technology, as well as the members of my thesis committee, for their comments and suggestions, and particularly for their careful and critical reading of this dissertation.

I am very grateful to Associate Professor Masaya Tamura of the Department of Electrical and Electronic Information Engineering, Toyohashi University of Technology, for his valuable comments and discussions on seminars of his laboratory. I also wish to thank Associate Professor Keigo Takeuchi of the Department of Electrical and Electronic Information Engineering, Toyohashi University of Technology, for his helpful suggestions and encouragement. My thanks are also extended to the Information Media Center, Toyohashi University of Technology, for providing their computer resources. I would like to thank all members

of Uehara Laboratory for a warm and interesting research environment that I have thoroughly enjoyed. Furthermore, I am grateful to Mr. Yoshiaki Murata, Mr. Toshiaki Takahashi, Mr. Shinnosuke Idogawa, Mr. Masato Kikuchi, and Ms. Shiori Hironaka, for their interesting discussions and friendly assistance during the period of this research. The seven years that I have spent with them at Toyohashi University of Technology have certainly been necessary for me to succeed in this research.

Finally, I would like to express my gratitude to my father and mother, who nourished me, encouraged me, and gave their utmost support to fulfill my educational aims and to make this study a great success.

*Department of Electrical and Electronic Information Engineering,
Toyohashi University of Technology*

Kazuki Komatsu

Chapter 1

General Introduction

1.1 In-Band Full-Duplex Radios

From the 1960s to the 1990s, researchers established the foundation of the physical layer of current wireless communications, such as the base of orthogonal frequency-division multiplexing (OFDM) in 1966 [1], its efficient modulation by fast Fourier transform in 1971 [2], and symbol detection on multiple-input and multiple-output (MIMO) systems in the late 1990s [3, 4]. In these methods, which are multiplexing techniques, a sender transmits multiplexed signals and one or more receivers receive multiplexed information from the received signals. In the fourth generation (4G) and fifth generation (5G) mobile communication systems, the maximum communication speed is 10 and 100 times higher than that of the third generation (3G) systems, respectively, which has been achieved by increasing the frequency bandwidth as well as applying technologies based on OFDM and MIMO. However, as the strong demand for wireless communications is increasing unabated, the achievement of efficient frequency utilization remains an ongoing challenge. In Japan, from 2018 to 2019, mobile traffic increased at a rate of approximately 1.2 times per year [5].

Intuitively, in contrast to multiplexing techniques, duplexing systems can be constructed very easily. For example, a terminal uses a frequency band $[f_{a1}, f_{a2}]$ and another terminal uses a different frequency band $[f_{b1}, f_{b2}]$ to avoid interference between the two terminals, where $f_{a1} < f_{a2} < f_{b1} < f_{b2}$, which is known as the frequency division duplex (FDD). Furthermore, a terminal uses a time interval

$[t_{a1}, t_{a2}]$ and another terminal uses a different time interval $[t_{b1}, t_{b2}]$, where $t_{a1} < t_{a2} < t_{b1} < t_{b2}$, which is known as the time division duplex (TDD). However, in the FDD and TDD, the two terminals need to divide the frequency or time resources in half. The FDD and TDD techniques are used in systems from the first generation (1G) to 5G, and there have been no major changes in these techniques in the history of wireless communication.

In-band full-duplex (IBFD) technology, which simultaneously transmits and receives on the same frequency band, is an emerging technique in recent wireless communications, and it is expected to improve the spectral efficiency compared to conventional duplexing systems. IBFD systems offer several advantages over conventional half-duplex systems, as follows [6]:

- improving the channel capacity up to twofold;
- reducing the latency of feedback messages such as acknowledge (ACK) and negative acknowledge (NACK) on the median access control (MAC) layer; and
- achieving secure communications where other terminals cannot demodulate information because signals from two terminals are mixed on the same frequency.

Full-duplex communication can replace the conventional half-duplex communication system, and its application to various communication systems, such as wireless local area networks (WLANs) [7,8], device-to-device relay communications [9,10], cellular networks [11,12], and self-backhauling systems [13], has been studied. In Japan, under the leadership of the Ministry of Internal Affairs and Communications, the research and development of IBFD communication will be carried out from 2019 to 2022 for further upgrading of the image transmission communication system for unmanned mobile devices and the 5G mobile communication system [14].

However, self-interference (SI) is caused by simultaneous transmission and reception on the same frequency band and limits the channel capacity. SI is the most challenging obstacle to the realization of full-duplex communications and it is important to reduce the SI to the thermal noise level. Thus, it is very difficult to achieve IBFD radios, which have attracted research attention since the early 2010s [15,16]. Advances in radio frequency (RF) circuit design and signal processing technologies have made it possible to achieve IBFD technology in the past 10 years. In general, the SI signal is gradually eliminated by introducing antenna isolation and SI cancellation in the analog RF domain and digital baseband domain [6,17].

For example, if the transmission power is 20 dBm and the thermal noise level is -90 dBm, the total performance of all SI cancellation stages needs to reach 110 dB. Furthermore, it is difficult to achieve high SI cancellation owing to the system constraints and nonlinearity of analog circuits. In the next section, an overview of SI mechanisms is presented.

1.2 Overview of SI Cancellation

1.2.1 Analog-domain cancellation

When the low-noise amplifier (LNA) and analog-to-digital converter (ADC) of the receiver are saturated owing to strong SI, the elimination of SI in the digital baseband becomes difficult. Thus, sufficient SI cancellation in the analog stage is necessary to eliminate the SI signal. For example, if the transmission power is 20 dBm and the saturated input level of the LNA is -10 dBm, the analog cancellation needs to be at least 40 dB to guarantee a 10 dB peak-to-average power ratio (PAPR). In the literature [16, 18–27], two major means of reducing the SI signal in the analog domain have been proposed.

The first method for suppressing SI is to increase the transceiver isolation between the transmitter and receiver chains. In full-duplex systems, two methods are available to accomplish this: sharing an antenna for transmission and reception [19], and separating the antennas [16]. In the antenna-sharing method, the isolation between the transmitters and receivers is only approximately 15 dB [19] because it depends on the isolation of the circulator. In antenna-separation systems, high isolation can be achieved by the orthogonalization of the polarization and direction, or by increasing the distance between the antennas [18]. However, in small terminals such as smartphones and IoT devices, the amount of isolation is reduced owing to size restrictions.

The second approach for suppressing SI is analog RF domain cancellation, which is performed to prevent saturation in the receiver LNA and ADC. The most researched analog cancellation scheme [15, 16, 19–22] is a multi-tapped delay-line RF canceller that consists of digital controllers and passive elements, such as splitters, variable attenuators, variable phase shifters, and delay lines. This delay-line canceller can remove both the linear SI signal and nonlinear components of the power amplifier (PA) output signal, because the canceller uses signals that are

Table 1.1: Digital cancellers and RF impairments in literature

	Addressed RF Impairments			
	IQI	PA NL	LNA NL	Phase Noise
Linear [16]				
Widely Linear [28]	✓			
Hammerstein [19, 22, 29–36]	✓	✓		
Auxiliary Receiver [37–39]	✓	✓		
[40]		✓	✓	
[41]				✓
[42]		✓		✓
Volterra Series [43–45]	✓	✓	✓	

obtained by the linear conversion of the PA output signal. This canceller can be configured flexibly because the number of delay lines can be increased or decreased depending on the system specifications, cost requirements, and size restrictions. Furthermore, an analog domain cancellation scheme with an auxiliary transmitter has been proposed [23–27]. This canceller can take into account the multipath fading and transmitter I/Q imbalance by including strong signal processing. However, this canceller may not be suitable for cheap terminals because it requires an additional transmitter.

1.2.2 Digital-domain cancellation

Digital SI cancellation is the final step in a series of cancellation processes. Using powerful digital signal processing techniques, digital cancellers with various features have been developed, as indicated in Table 1.1. In this field, it is common to deal with RF impairments [19, 22, 28–35, 40, 43, 44], phase noise [41, 42], and applications to MIMO systems [30, 31, 46, 47], as well as the application of blind signal processing [48, 49]. In addition to the research that is focused on digital cancellers composed only of digital signal processing, certain studies have also integrated auxiliary receivers [37–39].

The simplest digital canceller is the time-domain linear canceller, which has one finite impulse response (FIR) filter. The linear canceller can regenerate the linear component of the SI, but its performance is considerably degraded by the nonlinearity of the transceiver. In general, inexpensive terminals suffer from nonlinearity problems more often than expensive terminals. The most

problematic RF impairments are the I/Q mixer imbalance and PA nonlinearity [37]. Hammerstein cancellers [19, 22, 29–36] have been developed to deal with these impairments. This type of canceller estimates the channel responses for all nonlinear basis functions by applying a least-squares estimation. A digital canceller with an auxiliary receiver [37–39], which is used to receive the PA output signal directly, can perfectly regenerate the nonlinear SI signal caused by the transmitter nonlinearities using lightweight digital signal processing. However, the nonlinearity resulting from the receiver LNA cannot be expressed by the Hammerstein model, and the Hammerstein canceller and auxiliary receiver cannot cope with the nonlinear distortion of the LNA. In the literature [40], a canceller that addresses the nonlinearity of both the PA and LNA has been presented. This canceller estimates the radio channel and nonlinear characteristics alternately. However, the I/Q imbalance is not considered in this scheme. In other works [50–53], mitigation techniques for receiver nonlinearity have been proposed for wideband receivers. These techniques do not employ SI cancellers and cannot deal with the nonlinear distortion of the transmitter. To use these techniques for SI cancellation, it is necessary to complement them with other cancellers that can mitigate the nonlinear distortion of the transmitter. Volterra series-based cancellers [43–45] offer the potential to mitigate the PA and LNA nonlinearities as well as the I/Q imbalance. However, these cancellers require significantly higher computational power to estimate and regenerate the nonlinear SI signal than other practical cancellers. For example, the Hammerstein canceller and the canceller described in [43] need to estimate $12M = 576$ and $7M^3 + 3M^2 + 2M + 1 \approx 7.81 \times 10^5$ parameters for fifth-order nonlinearity cancellation, respectively, when the number of taps of the channel impulse response is $M = 48$. To the best of the author’s knowledge, a digital SI canceller that addresses the PA and LNA nonlinearities as well as the imbalance of I/Q mixers with a reasonable computational cost has not yet been developed. The development of such a canceller would enable the construction of inexpensive full-duplex terminals.

In systems in which the transmitter and receiver do not share a local oscillator, phase noise will be a major obstacle in addition to RF impairments. The estimation of the time-varying phase noise is generally challenging. A linear digital canceller with phase noise estimation was proposed in [41]. This canceller estimates the phase noise with the minimum mean square error (MMSE) algorithm under the presence of the desired signal. Similarly, in [42], the phase noise was estimated with the

maximum likelihood algorithm, following which the nonlinear SI was reconstructed and removed.

To achieve a higher channel capacity in IBFD communications, cancellers should have a lower number of training symbols. For example, SI cancellers with blind signal processing have been proposed for OFDM systems [48, 49]. However, these techniques require symbol synchronization between the SI and desired signal because they are applied in the frequency domain [49]. This problem is inherent in frequency-domain cancellers and limits the locations of two full-duplex terminals that communicate with one another. Hammerstein cancellers with frequency-domain cancellation exhibit the same problem and time-domain cancellation is required to avoid this issue [34].

At present, the most common communication systems are MIMO systems, and the application of digital cancellers to such systems is an important subject. Several studies [30, 31] have been conducted to upgrade single-input and single-output (SISO) Hammerstein cancellers to MIMO systems. Unlike SISO systems, MIMO systems can use additional spatial dimensions and many received signals for SI cancellation. A precoding scheme [46, 54–56] has been developed to optimize the receiver weight matrix and transmitter precoder matrix for reducing SI. In [47], it was noted that in massive MIMO systems, the SI can be reduced by a zero-forcing receiver with numerous transmitting and receiving antennas. Researches in [57, 58] have been conducted on full-duplex relay systems to mitigate SI and to maximize the spectral efficiency. In [57], a transmission power optimization technique was proposed for full-duplex multi-antenna relay systems. In [58], the conditions under which half-duplex or full-duplex modes exhibit higher spectral efficiency and an opportunistic mode selection scheme were studied. Precoding techniques of MIMO systems and power optimization techniques of relays are used in conjunction with digital SI cancellers. Thus, the development of a digital canceller with improved performance is also important for these systems.

1.3 RF Non-Ideality in IBFD

An overview of digital SI cancellers has been presented in the previous section. However, to understand nonlinear SI cancellers in detail, we need to investigate the nonlinearities and non-idealities in IBFD radios. In this section, the baseband models of the RF components of a full-duplex terminal are provided. If the reader

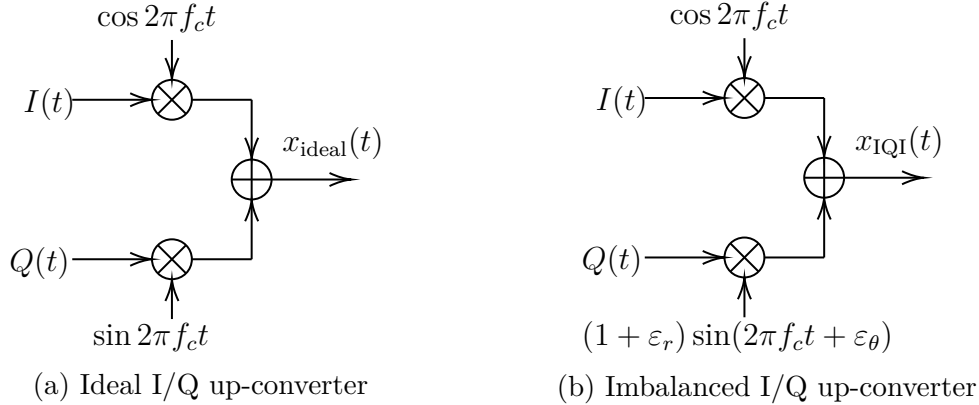


Figure 1.1: Block diagram of I/Q mixers

is familiar with the nonlinearities of RF devices, he or she can skip this section.

1.3.1 Notations

In this section, the passband signal corresponding to an equivalent baseband signal $x(t)$ is written as $\hat{x}(t)$. That is, the relation of the equivalent baseband and passband signals can be expressed as

$$\begin{aligned}\hat{x}(t) &= \text{Re} [x(t)e^{j2\pi f_c t}] \\ &= \text{Re} [x(t)] \cos(2\pi f_c t) - \text{Im} [x(t)] \sin(2\pi f_c t),\end{aligned}$$

where $\hat{x}(t)$ is a passband signal, $x(t)$ is an equivalent baseband signal of $\hat{x}(t)$, and f_c is the carrier frequency.

1.3.2 RF non-ideality of I/Q mixers and oscillators

Ideal I/Q mixer

In digital wireless communication, radio waves with high carrier frequencies ranging from several MHz to several tens of GHz are used. However, the information placed on the radio waves is a signal with a frequency that is much lower than the carrier frequency. An I/Q mixer is an RF component for placing low-frequency information on a high-frequency carrier wave. Figure 1.1 (a) presents a block diagram of an ideal I/Q mixer. In the passband domain representation, the input baseband signal $x(t) = I(t) + jQ(t)$ and output passband signal $\hat{x}_{\text{ideal}}(t)$ of the ideal I/Q mixer

exhibit the following relationship:

$$\begin{aligned}
 \hat{x}_{\text{ideal}}(t) &= I(t) \cos(2\pi f_c t) - Q(t) \sin(2\pi f_c t) \\
 &= \text{Re} \left[(I(t) + jQ(t)) e^{j2\pi f_c t} \right] \\
 &= \text{Re} \left[x(t) e^{j2\pi f_c t} \right] \\
 &= \frac{1}{2} x(t) e^{j2\pi f_c t} + \frac{1}{2} x^*(t) e^{-j2\pi f_c t},
 \end{aligned} \tag{1.1}$$

where f_c is the carrier frequency. Thus, the equivalent baseband signal of the output signal $\hat{x}_{\text{ideal}}(t)$ can be expressed as

$$x_{\text{ideal}}(t) = x(t) = I(t) + jQ(t). \tag{1.2}$$

Therefore, in the ideal I/Q mixer, the input baseband signal $x(t)$ and equivalent baseband signal of the output signal $x_{\text{ideal}}(t)$ are exactly the same.

I/Q imbalance

The equivalent baseband signals of the input and output signals do not match in real-world devices, and the in-phase and quadrature carriers are not orthogonal, or their amplitudes are misaligned. The resulting non-idealities are known as I/Q imbalances. Figure 1.1 (a) presents a block diagram of an imbalanced I/Q mixer. In the passband domain representation, the input baseband signal $x(t) = I(t) + jQ(t)$ and output passband signal $\hat{x}_{\text{IQI}}(t)$ of an I/Q mixer with imbalance exhibit the following relationship:

$$\begin{aligned}
 \hat{x}_{\text{IQI}}(t) &= I(t) \cos(2\pi f_c t) - (1 + \varepsilon_r) Q(t) \sin(2\pi f_c t + \varepsilon_\theta) \\
 &= [I(t) - (1 + \varepsilon_r) \sin \varepsilon_\theta Q(t)] \cos(2\pi f_c t) \\
 &\quad - (1 + \varepsilon_r) \cos \varepsilon_\theta Q(t) \sin(2\pi f_c t),
 \end{aligned} \tag{1.3}$$

where ε_r and ε_θ are the amplitude and phase imbalances, respectively. Therefore, the equivalent baseband signal of $\hat{x}_{\text{IQI}}(t)$ can be written as

$$\begin{aligned}
 x_{\text{IQI}}(t) &= [I(t) - (1 + \varepsilon_r) \sin \varepsilon_\theta Q(t)] + j(1 + \varepsilon_r) \cos \varepsilon_\theta Q(t) \\
 &= I(t) + j(1 + \varepsilon_r) e^{j\varepsilon_\theta} Q(t) = I(t) + j b_{\text{IQI}} Q(t),
 \end{aligned} \tag{1.4}$$

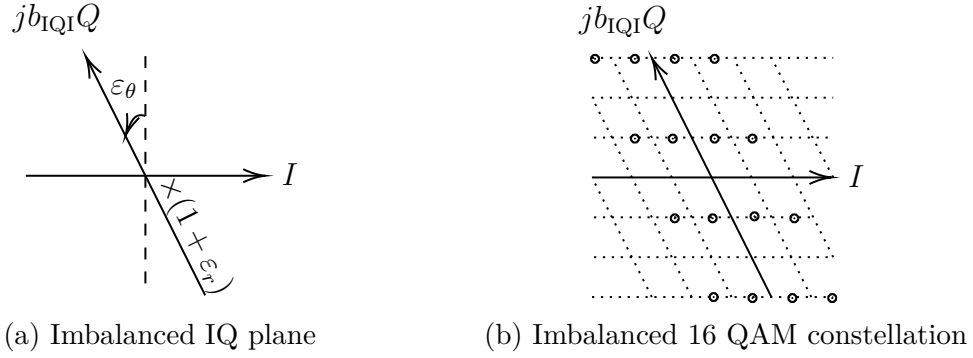


Figure 1.2: Effect of I/Q imbalance on I/Q constellation

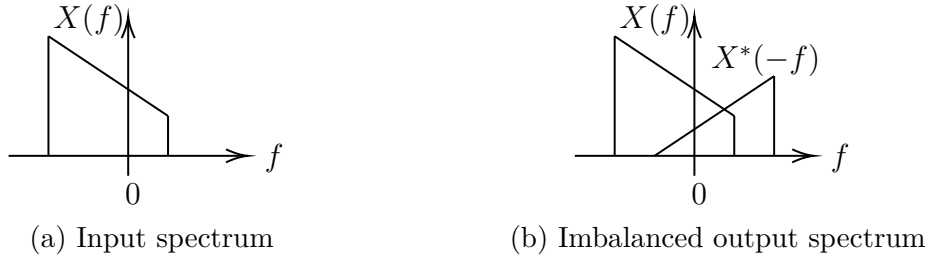


Figure 1.3: Effect of I/Q imbalance on frequency domain

where $b_{IQI} = (1 + \epsilon_r)e^{j\epsilon_\theta}$. Figure 1.2 depicts the effect of the I/Q imbalance on the I/Q constellation. The I and Q axes are no longer orthogonal and the constellation of the quadrature amplitude modulation (QAM) signal changes from a square to a parallelogram.

By assigning $I(t) = (x(t) + x^*(t))/2$ and $Q(t) = (x(t) - x^*(t))/j2$ to (1.4), the equivalent baseband signal $x_{IQI}(t)$ can be expressed as

$$\begin{aligned}
 x_{IQI}(t) &= \frac{x(t) + x^*(t)}{2} + jb_{IQI} \frac{x(t) - x^*(t)}{j2} \\
 &= \frac{1 + b_{IQI}}{2} x(t) + \frac{1 - b_{IQI}}{2} x^*(t).
 \end{aligned} \tag{1.5}$$

Furthermore, the frequency-domain representation of (1.5) can be expressed as

$$X_{IQI}(f) = \frac{1 + b_{IQI}}{2} X(f) + \frac{1 - b_{IQI}}{2} X^*(-f). \tag{1.6}$$

Figure 1.3 presents the spectra of the input and output signals from a imbalanced mixer. It shows that the output signal from a real-world mixer has the mirror-image component of the input signal $X^*(-f)$.

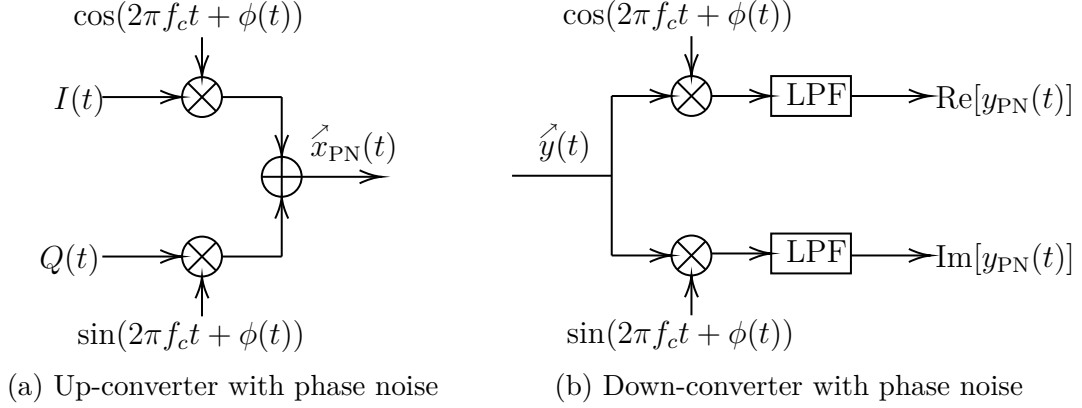


Figure 1.4: Effect of phase noise

An indicator of the I/Q imbalance is known as the image rejection ratio (IRR) [59], and it can be defined as

$$\text{IRR} = \left| \frac{1 + b_{\text{IQI}}}{1 - b_{\text{IQI}}} \right|^2. \quad (1.7)$$

Phase noise

Phase noise is a very important non-ideality that limits the performance of digital SI cancellers [60]. Figure 1.4 presents signal diagrams of an up-converter and a down-converter with phase noise. The RF up-converted signal with phase noise $\phi(t)$ can be expressed as

$$\begin{aligned} \hat{x}_{\text{PN}}(t) &= I(t) \cos(2\pi f_c t + \phi(t)) - Q(t) \sin(2\pi f_c t + \phi(t)) \\ &= \text{Re} \left[x(t) e^{j\phi(t)} e^{j2\pi f_c t} \right]. \end{aligned} \quad (1.8)$$

Thus, the equivalent baseband representation of the up-converted signal $\hat{x}_{\text{PN}}(t)$ can be written as

$$x_{\text{PN}}(t) = x(t) e^{j\phi(t)}. \quad (1.9)$$

In a receiver, the down-converted signal with phase noise $\phi(t)$ can be expressed

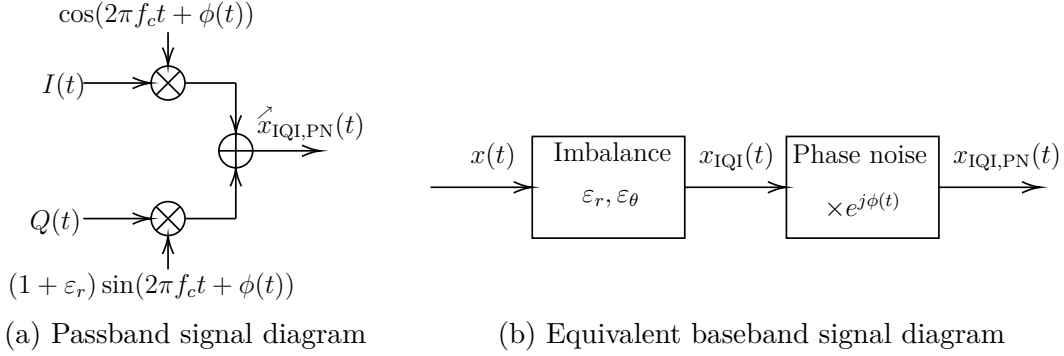


Figure 1.5: Block diagram of up-converter with I/Q imbalance and phase noise

as

$$\begin{aligned}
 y_{\text{PN}}(t) &= \text{LPF} \left[\hat{y}(t) \times 2e^{-j(2\pi f_c t + \phi(t))} \right] \\
 &= \text{LPF} \left[\left(y(t)e^{j2\pi f_c t} + y^*(t)e^{-j2\pi f_c t} \right) e^{-j(2\pi f_c t + \phi(t))} \right] \\
 &= y(t)e^{-j\phi(t)}. \tag{1.10}
 \end{aligned}$$

Comparing (1.9) and (1.10), it can be observed that the phase noise is added to the signal phase in the transmitter and subtracted in the receiver. Thus, if the local oscillator is shared by the transmitter and receiver, the phase noise that is generated by the transmitter is cancelled out by the receiver. That is, it is important for the local oscillator to be shared between the transmitter and receiver to reduce the degradation of the SI cancellation performance owing to phase noise in IBFD communications.

Composition of I/Q imbalance and phase noise

The output signal from an I/Q mixer is affected by the composited non-ideality of the I/Q imbalance and phase noise. Figure 1.5 presents signal diagrams of an up-converter with I/Q imbalance and phase noise. The up-converted signal of Fig. 1.5(a) can be expressed as

$$\begin{aligned}
 \hat{x}_{\text{IQI,PN}}(t) &= I(t) \cos(2\pi f_c t + \phi(t)) - Q(t)(1 + \varepsilon_r) \sin(2\pi f_c t + \phi(t) + \varepsilon_\theta) \\
 &= [I(t) - (1 + \varepsilon_r) \sin \varepsilon_\theta Q(t)] \cos(2\pi f_c t + \phi(t)) \\
 &\quad - (1 + \varepsilon_r) \cos \varepsilon_\theta Q(t) \sin(2\pi f_c t + \phi(t)) \\
 &= \text{Re} \left[x_{\text{IQI}}(t) e^{j\phi(t)} e^{j2\pi f_c t} \right]. \tag{1.11}
 \end{aligned}$$

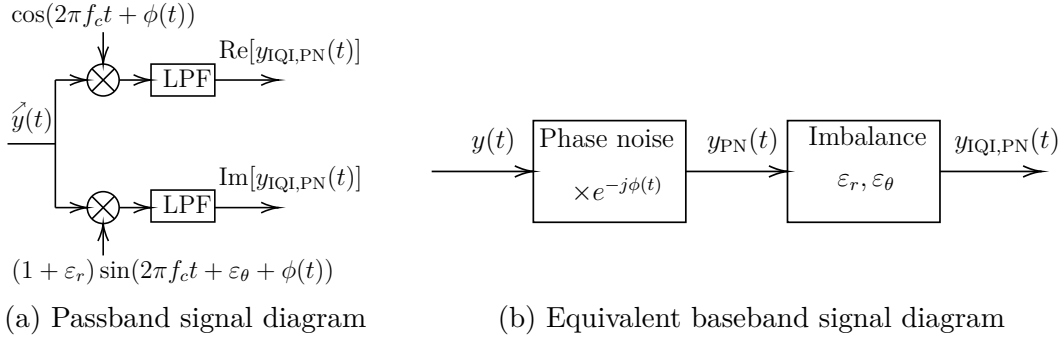


Figure 1.6: Block diagram of down-converter with I/Q imbalance and phase noise

Thus, the equivalent baseband signal of $\hat{x}_{\text{IQI,PN}}(t)$ can be written as

$$x_{\text{IQI,PN}}(t) = x_{\text{IQI}}(t)e^{j\phi(t)}, \quad (1.12)$$

and Fig. 1.5(b) presents a block diagram of the equivalent baseband signal. It can be observed from the block diagram that the effect of the imbalance is first added to the signal, and the phase noise is multiplied in the transmitter later.

Furthermore, Fig. 1.6 presents signal diagrams of a down-converter with I/Q imbalance and phase noise. The down-converted signal of Fig. 1.6(a) can be expressed as

$$\begin{aligned} y_{\text{IQI,PN}}(t) &= 2\text{LPF} \left[\hat{y}(t) \cos(2\pi f_c t + \phi(t)) \right] \\ &\quad - j2\text{LPF} \left[\hat{y}(t)(1 + \varepsilon_r) \sin(2\pi f_c t + \varepsilon_\theta + \phi(t)) \right] \\ &= \text{LPF} \left[\hat{y}(t) \left[(1 - b_{\text{IQI}})e^{j2\pi f_c t + j\phi(t)} + (1 + b_{\text{IQI}})e^{-j2\pi f_c t - j\phi(t)} \right] \right] \\ &= \frac{(1 + b_{\text{IQI}})}{2} y(t)e^{-j\phi(t)} + \frac{(1 - b_{\text{IQI}})}{2} y^*(t)e^{j\phi(t)} \\ &= \frac{1 - b_{\text{IQI}}}{2} y_{\text{PN}}(t) + \frac{1 + b_{\text{IQI}}}{2} y_{\text{PN}}^*(t). \end{aligned} \quad (1.13)$$

Figure 1.6(b) presents a block diagram of the equivalent baseband signal $y_{\text{IQI,PN}}(t)$. As opposed to the transmitter, the phase noise is multiplied to the signal first, and the imbalance effect is added later in the transmitter.

1.3.3 Amplifier AM–AM and AM–PM nonlinearity

Wireless transceivers have amplifiers for the transmission and reception of information with other distant transceivers. In general, an amplifier cannot amplify a

signal that is greater than its maximum output amplitude. In practice, a real-world amplifier has a nonlinear transfer function consisting of amplitude modulation to amplitude modulation (AM–AM) and amplitude modulation to phase modulation (AM–PM) distortion. On the equivalent baseband, the transfer function of a nonlinear amplifier can be expressed as

$$f(x) = A(|x|)e^{j\Phi(|x|)} \frac{x}{|x|}, \quad (1.14)$$

where $A(|x|)$ is the AM–AM distortion and $\Phi(|x|)$ is the AM–PM distortion. The nonlinear transfer function can be described by a power series of odd order:

$$f(x) \approx \sum_{m=0}^{\infty} a_{2m+1} x|x|^{2m}, \quad (1.15)$$

where a_p is the p -th complex coefficient of the series.

The reason that (1.15) is expressed as a series of odd order only can be explained as follows. In the passband domain, the output signal from the amplifier can be expressed as the Taylor series of the input signal (1.1):

$$\begin{aligned} a(t) &\approx \sum_{n=1}^{\infty} a'_n \hat{x}_{\text{ideal}}^n(t) \\ &= \sum_{n=1}^{\infty} \frac{a'_n}{2^n} \left(x(t)e^{j2\pi f_c t} + x^*(t)e^{-j2\pi f_c t} \right)^n \\ &= \sum_{n=1}^{\infty} \frac{a'_n}{2^n} \sum_{m=0}^n \binom{n}{m} (x(t))^{n-m} (x^*(t))^m e^{j2\pi f_c(n-2m)t}, \end{aligned} \quad (1.16)$$

where a'_n is the n -th Taylor coefficient of the amplifier passband transfer function. In general, the bandwidth of the signal $x(t)$ is sufficiently smaller than the carrier frequency f_c ; thus, the signal is only received if

$$\begin{aligned} f_c(n - 2m) &= \pm f_c \\ \Leftrightarrow n \text{ is odd, and } m &= (n \mp 1)/2 \end{aligned} \quad (1.17)$$

is satisfied. For $m_+ = (n + 1)/2$ and $m_- = (n - 1)/2$,

$$\binom{n}{m_+} = \binom{n}{m_-} \quad (1.18)$$

holds. Thus, the output from a bandpass filter with a center frequency f_c can be written as

$$\begin{aligned}
 a'(t) &= e^{j2\pi f_c t} \sum_{n=1,3,\dots}^{\infty} \frac{a'_n}{2^n} (x(t))^{\frac{n+1}{2}} (x^*(t))^{\frac{n-1}{2}} \\
 &+ e^{-j2\pi f_c t} \sum_{n=1,3,\dots}^{\infty} \frac{a'_n}{2^n} (x(t))^{\frac{n-1}{2}} (x^*(t))^{\frac{n+1}{2}}. \tag{1.19}
 \end{aligned}$$

According to (1.19), the equivalent baseband signal of the amplifier output signal can be written as

$$\begin{aligned}
 a'_{\text{base}}(t) &= \sum_{n=1,3,\dots}^{\infty} \frac{a'_n}{2^n} (x(t))^{\frac{n+1}{2}} (x^*(t))^{\frac{n-1}{2}} \\
 &= \sum_{m=0}^{\infty} \frac{a'_{2m+1}}{2^{2m+1}} x(t) |x(t)|^{2m}. \tag{1.20}
 \end{aligned}$$

Another reason that (1.15) is expressed as a series of odd order only can be explained by the Wirtinger derivative of complex analysis. In the previous explanation, the output signal in the passband system was discussed, but in this paragraph, the Wirtinger derivative and its Taylor series in the baseband domain are presented. As a complex function, the transfer function $f(x)$ is a nonregular analytic function; thus, we cannot expand $f(x)$ to a power series by Taylor expansion. However, the Taylor expansion with the Wirtinger derivative can expand a nonregular function to a power series. The Taylor series of $f(x)$ with the Wirtinger derivative can be expressed as

$$f(x) = \sum_{p=0}^{\infty} \sum_{q=0}^{\infty} \frac{f^{(p,q)}(0)}{p!q!} x^p (x^*)^q, \tag{1.21}$$

where

$$f^{(p,q)}(0) = \left(\frac{\partial^{p+q} f(x)}{\partial x^p \partial (x^*)^q} \right) \Big|_{x=0}. \tag{1.22}$$

To satisfy the identity $f(xe^{j\theta}) = f(x)e^{j\theta}$ of the AM–AM and AM–PM nonlinearity for an arbitrary phase θ , the function $f(x)$ must consist only of terms that satisfy $p - q = 1$ in (1.21). Thus, the amplifier transfer function $f(x)$ can be expressed by

a power series with an odd order only:

$$\begin{aligned} f(x) &= \sum_{q=0}^{\infty} \frac{f^{(q+1,q)}(0)}{(q+1)!q!} x^{q+1} (x^*)^q \\ &= \sum_{q=0}^{\infty} \frac{f^{(q+1,q)}(0)}{(q+1)!q!} x|x|^{2q}. \end{aligned} \quad (1.23)$$

Memoryless models are often used for modeling RF amplifiers. On the equivalent baseband, the transfer function of the ideal amplifier can be written as

$$f(x) = \begin{cases} gx, & |gx| < A_{\text{sat}} \\ A_{\text{sat}} \frac{x}{|x|}, & |gx| \geq A_{\text{sat}}, \end{cases} \quad (1.24)$$

where g is the small signal gain and A_{sat} is the maximum output amplitude. The model of (1.24) is known as the “soft limit” model¹.

Another model that is frequently used is the Rapp model [61]. The AM–AM characteristic function of the Rapp model can be written as

$$f(x) = \frac{Gx}{\left(1 + \left|\frac{Gx}{A_{\text{sat}}}\right|^{2s}\right)^{1/2s}}, \quad (1.25)$$

where G is the small signal gain, A_{sat} is the maximum output amplitude, and s is the smoothness factor of the Rapp model. A larger smoothness factor s results in stronger linearity of the Rapp model. When the smoothness factor s is infinite, the Rapp model becomes the soft limit model.

1.4 Time-Domain Parallel Hammerstein Canceller

The parallel Hammerstein canceller is one of most well-studied nonlinear cancellers in the IBFD literature. This type of canceller was initially developed to deal with amplifier nonlinearity [19, 29], but several versions have subsequently been established to deal with I/Q imbalance [28, 32, 34] and crosstalk in MIMO systems [62].

The generalized model of the time-domain parallel Hammerstein canceller can

¹ Certain papers refer to the model as “hard limit.” However, in this thesis, I call the model “soft limit.”

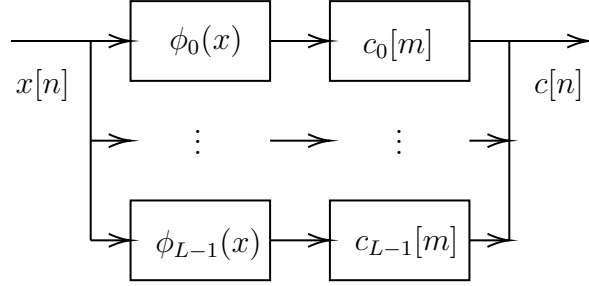


Figure 1.7: Block diagram of time-domain parallel Hammerstein canceller

be written as

$$c[n] = \sum_{l=0}^{L-1} \sum_{m=0}^{M-1} \phi_l(x[n-m])c_l[m], \quad (1.26)$$

where $c[n]$ is the regenerated SI signal, $\phi_0(x), \dots, \phi_{L-1}(x)$ are basis functions of the canceller, and $c_0[m], \dots, c_{L-1}[m]$ are the impulse responses of the basis functions.

The basis functions are determined according to which nonlinear components we wish to remove from the received signal. For example, if we wish to remove distortions from the PA up to the $(2L-1)$ -th order, we should set the basis functions as

$$\phi_l(x) = x|x|^{2l}. \quad (1.27)$$

Moreover, if we wish to remove distortions from the PA and I/Q mixer up to the P -th order, we should set the basis functions for $0 \leq p \leq P$, $0 \leq q \leq P$, and $p+q \leq P$ as

$$\phi_{\frac{2p+q(2P-q+1)}{2}}(x) = x^p (x^*)^q, \quad (1.28)$$

and $L = P(P+1)/2$.

The impulse responses of the canceller are determined by the least squares (LS) and least mean squares (LMS) algorithms. In this section, the LS learning technique for the canceller is described. Assuming that the SI is a linear combination of the basis function $\phi_l(x)$, the received SI signal can be written as

$$y[n] = \sum_{l=0}^{L-1} \sum_{m=0}^{M-1} \phi_l(x[n-m])h_l[m] + z[n], \quad (1.29)$$

where $h_p[m]$ is the impulse response of each basis function and $z[n]$ is the additive noise. Thus, the received SI $y[n]$ can be written in the vector-matrix form:

$$\mathbf{y} = \Phi \mathbf{h} + \mathbf{z}, \quad (1.30)$$

where

$$\mathbf{y} = [y[0] \ y[1] \ \cdots \ y[N-1]]^T, \quad (1.31)$$

$$\Phi = \begin{bmatrix} \phi_0(x[0]) & \cdots & \phi_0(x[1-M]) & \phi_1(x[0]) & \cdots & \phi_{L-1}(x[1-M]) \\ \phi_0(x[1]) & \cdots & \phi_0(x[2-M]) & \phi_1(x[1]) & \cdots & \phi_{L-1}(x[2-M]) \\ \vdots & \ddots & \vdots & \vdots & \ddots & \vdots \\ \phi_0(x[N-1]) & \cdots & \phi_0(x[N-M]) & \phi_1(x[N-1]) & \cdots & \phi_{L-1}(x[N-M]) \end{bmatrix}, \quad (1.32)$$

$$\mathbf{h} = [h_0[0] \ \cdots \ h_0[M-1] \ h_1[0] \ \cdots \ h_{L-1}[M-1]]^T, \quad (1.33)$$

$$\mathbf{z} = [z[0] \ z[1] \ \cdots \ z[N-1]]^T. \quad (1.34)$$

Thus, the vector of impulse responses can be estimated by the LS as follows:

$$\hat{\mathbf{h}} = (\Phi^H \Phi)^{-1} \Phi^H \mathbf{y}. \quad (1.35)$$

The computational cost is an important performance indicator of SI cancellers. In general, the computational cost of the pseudo-inverse matrix of (1.35) is very high. Furthermore, the LMS and recursive least squares (RLS) algorithms for the augmented nonlinear digital canceller [32] require computational costs of $\mathcal{O}(L^2MN)$ and $\mathcal{O}(L^4M^2N)$, respectively. However, the canceller can be trained with a low computational cost if the predetermined training sequence is used, and subsequently, the pseudo-inverse matrix of (1.35) can be computed a priori. The number of both the multiplications and additions for training the Hammerstein canceller can be expressed as LMN when applying the pseudo-inverse matrix of the LS algorithm a priori [29].

1.5 Summary of Dissertation

SI is distorted by transceiver non-idealities such as the amplifier nonlinearities, imbalances of I/Q mixers, phase noise of local oscillators, and quantization noise of ADCs. Thus, the IBFD literature includes reports of nonlinear SI cancellers that have been developed to achieve improved cancellation performance. However, compared to linear cancellers, nonlinear cancellers exhibit several problems, such as high computational complexity, the requirement of large training data, and vulnerability to LNA nonlinearity. Furthermore, no theoretical studies have been conducted on the performance of IBFD radios with nonlinear cancellers. This thesis presents studies on nonlinear cancellers with regard to the above problems.

Chapter 1 presents a general introduction to and summary of this thesis. It contains the background of the studies in this thesis.

In Chapter 2, a frequency-domain Hammerstein canceller based on the parallel Hammerstein model, which can achieve low computational complexity, is proposed. The proposed canceller estimates the frequency response of the SI channel and regenerates SI signals by means of the overlap-save method. Therefore, the computational complexity of the proposed scheme is less than that of time-domain parallel Hammerstein cancellers. The performance of the proposed scheme is assessed by equivalent baseband signal simulations of a full-duplex transceiver. The results demonstrate that the proposed scheme achieves as high SI cancellation as time-domain parallel Hammerstein cancellers with a low computational cost. Moreover, the results reveal that the convergence performance of the proposed scheme is faster than that of the time-domain scheme.

In Chapter 3, a basis function selection technique is proposed to reduce the computational cost further and to improve the convergence performance of the frequency-domain Hammerstein canceller, which is presented in Chapter 2. The PSD of the nonlinear SI signal is theoretically analyzed in detail and a nonlinear SI PSD estimation method is presented. The proposed selection technique determines the basis functions that are necessary for cancellation and relaxes the computational cost of the frequency-domain Hammerstein canceller based on the estimated SI PSD of each basis function. Thereafter, simulation results are presented, demonstrating that the proposed technique can achieve similar cancellation performance compared to the original frequency-domain Hammerstein canceller and a time-domain nonlinear canceller. Furthermore, it is shown that the proposed technique improves the computational cost and convergence performance of the original frequency-domain

Hammerstein canceller.

In Chapter 4, an iterative nonlinear SI canceller is proposed to consider the LNA nonlinearity. The estimation process of the proposed scheme consists of three stages: the channel response estimation, I/Q imbalance estimation, and PA and LNA nonlinearity estimation. For the estimation of the parameters and improvement in the accuracy, the distortions are compensated for by cancellation or inversion with the latest estimated parameters. The channel response is estimated in the time domain, whereas the I/Q imbalance and nonlinearities are estimated in the frequency domain for a more straightforward estimation and superior accuracy. In the cancellation process of the proposed scheme, the received signal is compensated for with the estimated parameters of the LNA and receiver I/Q imbalance prior to cancellation because the desired signal is received with a high-power SI and is distorted by the RF receiver impairments. The simulation results demonstrate that the proposed technique can achieve higher cancellation performance compared to the Hammerstein canceller when the LNA is saturated by the SI. Furthermore, the performance of the proposed canceller converges much faster than that of the Hammerstein canceller.

Chapter 5 presents a theoretical analysis technique for IBFD radios with parallel Hammerstein SI cancellers. The nonlinear system characteristics are expanded by a generalized Fourier series using orthonormal Laguerre polynomials. Thereafter, the canceller performance and system SER are analyzed using the obtained Fourier coefficients. The analytical results are compared with the simulation results, demonstrating strong correlation in various situations, from extremely nonlinear cases to good linear cases. Moreover, the results demonstrate that the SER of the IBFD system is reduced by moderately nonlinearizing rather than linearizing the amplifier.

Chapter 6 concludes this thesis.

In Appendix A, a novel estimation technique for the memoryless nonlinearity using weighted least squares is presented. The technique is developed using the theory of the orthonormal basis functions, which are used in Chapter 5. In the proposed method, the input signal and weight value are obtained via numerical integration formulas. Moreover, a theoretical error analysis of the proposed technique on complex Gaussian signals is provided. The simulation results reveal that the proposed method can achieve a sufficiently low reconstruction error with 10 measurement samples on the estimation of the 13th-order nonlinearity. Furthermore,

the simulation and theoretical results are consistent with one another. Although this technique is not a nonlinear canceller, it is an efficient method for estimating the nonlinearity that is required for nonlinear cancellers.

References

- [1] R. W. Chang, “Synthesis of band-limited orthogonal signals for multichannel data transmission,” *Bell Syst. Techn. J.*, vol. 45, no. 10, pp. 1775–1796, 1966.
- [2] S. Weinstein and P. Ebert, “Data transmission by frequency-division multiplexing using the discrete fourier transform,” *IEEE Trans. Commun. Techn.*, vol. 19, no. 5, pp. 628–634, 1971.
- [3] G. J. Foschini, “Layered space-time architecture for wireless communication in a fading environment when using multi-element antennas,” *Bell Labs Techn. J.*, vol. 1, no. 2, pp. 41–59, 1996.
- [4] P. W. Wolniansky, G. J. Foschini, G. D. Golden, and R. A. Valenzuela, “V-BLAST: an architecture for realizing very high data rates over the rich-scattering wireless channel,” in *Proc. 1998 URSI Int. Symp. Signals Syst. Elec. Conf.*, 1998, pp. 295–300.
- [5] Ministry of Internal Affairs and Communications of Japan, *2020 White Paper on Information and Communications in Japan*, 2020, translated from Japanese title “情報通信白書令和2年版”.
- [6] D. Kim, H. Lee, and D. Hong, “A survey of in-band full-duplex transmission: From the perspective of PHY and MAC layers,” *IEEE Commun. Surveys Tuts.*, vol. 17, no. 4, pp. 2017–2046, 2015.
- [7] A. Aijaz and P. Kulkarni, “Protocol design for enabling full-duplex operation in next-generation IEEE 802.11 WLANs,” *IEEE Syst. J.*, vol. 12, no. 4, pp. 3438–3449, Dec. 2018.
- [8] M. Kaneko, “Throughput analysis of CSMA with imperfect collision detection in full duplex-enabled WLAN,” *IEEE Wireless Commun. Lett.*, vol. 6, no. 4, pp. 490–493, Aug. 2017.

- [9] G. Liu, F. R. Yu, H. Ji, V. C. M. Leung, and X. Li, “In-band full-duplex relaying: A survey, research issues and challenges,” *IEEE Commun. Surveys Tuts.*, vol. 17, no. 2, pp. 500–524, 2015.
- [10] B. Ma, H. Shah-Mansouri, and V. W. S. Wong, “Full-duplex relaying for D2D communication in millimeter wave-based 5G networks,” *IEEE Trans. Wireless Commun.*, vol. 17, no. 7, pp. 4417–4431, July 2018.
- [11] E. Hossain and M. Hasan, “5G cellular: key enabling technologies and research challenges,” *IEEE Instrum. Meas. Mag.*, vol. 18, no. 3, pp. 11–21, June 2015.
- [12] Z. Zhang, X. Chai, K. Long, A. V. Vasilakos, and L. Hanzo, “Full duplex techniques for 5G networks: self-interference cancellation, protocol design, and relay selection,” *IEEE Commun. Mag.*, vol. 53, no. 5, pp. 128–137, May 2015.
- [13] R.-A. Pitaval, O. Tirkkonen, R. Wichman, K. Pajukoski, E. Lahetkangas, and E. Tiirola, “Full-duplex self-backhauling for small-cell 5G networks,” *IEEE Wireless Commun.*, vol. 22, no. 5, pp. 83–89, Oct. 2015.
- [14] Ministry of Internal Affairs and Communications of Japan, *Research and Development for the Expansion of Radio Wave Resources: Handbook of Research and Development Proposals*, 2020, translated from Japanese title “電波資源拡大のための研究開発 研究開発課題便覧”.
- [15] J. I. Choi, M. Jain, K. Srinivasan, P. Levis, and S. Katti, “Achieving single channel, full duplex wireless communication,” in *Proc. ACM MobiCom’10*, 2010.
- [16] M. Jain, J. I. Choi, T. Kim, D. Bharadia, S. Seth, K. Srinivasan, P. Levis, S. Katti, and P. Sinha, “Practical, real-time, full duplex wireless,” in *Proc. ACM MobiCom’11*, 2011.
- [17] K. E. Kolodziej, B. T. Perry, and J. S. Herd, “In-band full-duplex technology: Techniques and systems survey,” *IEEE Trans. Microw. Theory Techn.*, vol. 67, no. 7, pp. 3025–3041, July 2019.
- [18] E. Everett, A. Sahai, and A. Sabharwal, “Passive self-interference suppression for full-duplex infrastructure nodes,” *IEEE Trans. Wireless Commun.*, vol. 13, no. 2, pp. 680–694, Feb. 2014.
- [19] D. Bharadia, E. McMillin, and S. Katti, “Full duplex radios,” in *Proc. ACM SIGCOMM’13*, 2013.
- [20] J. Tamminen, M. Turunen, D. Korpi, T. Huusari, Y.-S. Choi, S. Talwar, and M. Valkama, “Digitally-controlled RF self-interference canceller for full-duplex radios,” in *Proc. 24th European Signal Process. Conf. (EUSIPCO)*, 2016, pp. 783–787.

- [21] J. Zhou, T.-H. Chuang, T. Dinc, and H. Krishnaswamy, “Integrated wideband self-interference cancellation in the RF domain for FDD and full-duplex wireless,” *IEEE J. Solid-State Circuits*, vol. 50, no. 12, pp. 3015–3031, Dec. 2015.
- [22] D. Korpi, Y.-S. Choi, T. Huusari, L. Anttila, S. Talwar, and M. Valkama, “Adaptive nonlinear digital self-interference cancellation for mobile inband full-duplex radio: Algorithms and RF measurements,” in *Proc. IEEE GLOBECOM*, Dec. 2015.
- [23] M. Duarte, C. Dick, and A. Sabharwal, “Experiment-driven characterization of full-duplex wireless systems,” *IEEE Trans. Wireless Commun.*, vol. 11, no. 12, pp. 4296–4307, Dec. 2012.
- [24] J.-H. Lee, J. won Choi, J.-H. Jung, S.-C. Kim, and Y.-H. Kim, “Analog cancellation for full-duplex wireless in multipath self-interference channels,” *IEICE Trans. Commun.*, vol. E98.B, no. 4, pp. 646–652, 2015.
- [25] M. Sakai, H. Lin, and K. Yamashita, “Adaptive cancellation of self-interference in full-duplex wireless with transmitter IQ imbalance,” in *Proc. IEEE GLOBECOM*, Dec. 2014, pp. 3220–3224.
- [26] ———, “Self-interference cancellation in full-duplex wireless with IQ imbalance,” *Elsevier Phy. Commun.*, vol. 18, pp. 2–14, Mar. 2016.
- [27] Y. Liu, X. Quan, W. Pan, and Y. Tang, “Digitally assisted analog interference cancellation for in-band full-duplex radios,” *IEEE Commun. Lett.*, vol. 21, no. 5, pp. 1079–1082, May 2017.
- [28] D. Korpi, L. Anttila, V. Syrjälä, and M. Valkama, “Widely linear digital self-interference cancellation in direct-conversion full-duplex transceiver,” *IEEE J. Sel. Areas Commun.*, vol. 32, no. 9, pp. 1674–1687, Sept. 2014.
- [29] L. Anttila, D. Korpi, V. Syrjälä, and M. Valkama, “Cancellation of power amplifier induced nonlinear self-interference in full-duplex transceivers,” in *Proc. 47th Asilomar Conf. Signals, Syst., Comput.*, Nov. 2013.
- [30] L. Anttila, D. Korpi, E. Antonio-Rodriguez, R. Wichman, and M. Valkama, “Modeling and efficient cancellation of nonlinear self-interference in MIMO full-duplex transceivers,” in *Proc. IEEE GC Wkshps*, Dec. 2014, pp. 777–783.
- [31] M. Heino, D. Korpi, T. Huusari, E. Antonio-Rodriguez, S. Venkatasubramanian, T. Riihonen, L. Anttila, C. Icheln, K. Haneda, R. Wichman, and M. Valkama, “Recent advances in antenna design and interference cancellation algorithms for in-band full duplex relays,” *IEEE Commun. Mag.*, vol. 53, no. 5, pp. 91–101, May 2015.

- [32] D. Korpi, T. Huusari, Y.-S. Choi, L. Anttila, S. Talwar, and M. Valkama, “Digital self-interference cancellation under nonideal RF components: Advanced algorithms and measured performance,” in *Proc. IEEE SPAWC*, June 2015, pp. 286–290.
- [33] K. Komatsu, Y. Miyaji, and H. Uehara, “Frequency-domain Hammerstein self-interference canceller for in-band full-duplex OFDM systems,” in *Proc. IEEE WCNC*, Mar. 2017.
- [34] —, “Basis function selection of frequency-domain Hammerstein self-interference canceller for in-band full-duplex wireless communications,” *IEEE Trans. Wireless Commun.*, vol. 17, no. 6, pp. 3768–3780, June 2018.
- [35] L. Tian, S. Wang, Z. Cheng, and X. Bu, “All-digital self-interference cancellation in zero-IF full-duplex transceivers,” *China Communications*, vol. 13, no. 11, pp. 27–34, Nov. 2016.
- [36] P. P. Campo, D. Korpi, L. Anttila, and M. Valkama, “Nonlinear digital cancellation in full-duplex devices using spline-based hammerstein model,” in *Proc. IEEE GC Wkshps*, Dec. 2018.
- [37] S. Li and R. D. Murch, “An investigation into baseband techniques for single-channel full-duplex wireless communication systems,” *IEEE Trans. Wireless Commun.*, vol. 13, no. 9, pp. 4794–4806, Sept. 2014.
- [38] E. Ahmed and A. M. Eltawil, “All-digital self-interference cancellation technique for full-duplex systems,” *IEEE Trans. Wireless Commun.*, vol. 14, no. 7, pp. 3519–3532, July 2015.
- [39] J. Li, H. Zhang, and M. Fan, “Digital self-interference cancellation based on independent component analysis for co-time co-frequency full-duplex communication systems,” *IEEE Access*, vol. 5, pp. 10 222–10 231, 2017.
- [40] E. Ahmed, A. M. Eltawil, and A. Sabharwal, “Self-interference cancellation with nonlinear distortion suppression for full-duplex systems,” in *Proc. 47th Asilomar Conf. Signals, Syst., Comput.*, Nov. 2013, pp. 1199–1203.
- [41] —, “Self-interference cancellation with phase noise induced ICI suppression for full-duplex systems,” in *Proc. IEEE GLOBECOM*, Dec. 2013, pp. 3384–3388.
- [42] R. Li, A. Masmoudi, and T. Le-Ngoc, “Self-interference cancellation with nonlinearity and phase-noise suppression in full-duplex systems,” *IEEE Trans. Veh. Technol.*, vol. 67, no. 3, pp. 2118–2129, Mar. 2018.

- [43] M. A. Islam and B. Smida, "A comprehensive self-interference model for single-antenna full-duplex communication systems," in *Proc. IEEE ICC*, May 2019.
- [44] D. Korpi, M. Turunen, L. Anttila, and M. Valkama, "Modeling and cancellation of self-interference in full-duplex radio transceivers: Volterra series-based approach," in *Proc. IEEE ICC Wkshps*, May 2018.
- [45] J. Liu, H. Quan, Z. Li, H. Sun, and D. Yuan, "Digital nonlinear self-interference cancellation based on LMS-Volterra algorithm," in *Proc. 3rd Int. Conf. Inf. Sci. Control Eng. (ICISCE)*, July 2016, pp. 1298–1302.
- [46] T. Riihonen, S. Werner, and R. Wichman, "Mitigation of loopback self-interference in full-duplex MIMO relays," *IEEE Trans. Signal Process.*, vol. 59, no. 12, pp. 5983–5993, Dec. 2011.
- [47] H. Q. Ngo, H. A. Suraweera, M. Matthaiou, and E. G. Larsson, "Multipair full-duplex relaying with massive arrays and linear processing," *IEEE J. Sel. Areas Commun.*, vol. 32, no. 9, pp. 1721–1737, Sept. 2014.
- [48] D. Liu, B. Zhao, F. Wu, S. Shao, X. Pu, and Y. Tang, "Semi-blind SI cancellation for in-band full-duplex wireless communications," *IEEE Commun. Lett.*, vol. 22, no. 5, pp. 1078–1081, May 2018.
- [49] X. Quan, Y. Liu, D. Chen, S. Shao, Y. Tang, and K. Kang, "Blind nonlinear self-interference cancellation for wireless full-duplex transceivers," *IEEE Access*, vol. 6, pp. 37 725–37 737, 2018.
- [50] M. Grimm, M. Allen, J. Marttila, M. Valkama, and R. Thoma, "Joint mitigation of nonlinear RF and baseband distortions in wideband direct-conversion receivers," *IEEE Trans. Microw. Theory Techn.*, vol. 62, no. 1, pp. 166–182, Jan. 2014.
- [51] M. Valkama, A. S. H. Ghadam, L. Anttila, and M. Renfors, "Advanced digital signal processing techniques for compensation of nonlinear distortion in wideband multicarrier radio receivers," *IEEE Trans. Microw. Theory Techn.*, vol. 54, no. 6, pp. 2356–2366, June 2006.
- [52] E. A. Keehr and A. Hajimiri, "Equalization of third-order intermodulation products in wideband direct conversion receivers," *IEEE J. Solid-State Circuits*, vol. 43, no. 12, pp. 2853–2867, Dec. 2008.
- [53] Q. Zou, M. Mikhemar, and A. H. Sayed, "Digital compensation of cross-modulation distortion in software-defined radios," *IEEE J. Sel. Topics Signal Process.*, vol. 3, no. 3, pp. 348–361, June 2009.

- [54] T. Riihonen, A. Balakrishnan, K. Haneda, S. Wyne, S. Werner, and R. Wichman, “Optimal eigenbeamforming for suppressing self-interference in full-duplex MIMO relays,” in *Proc. 45th Annu. CISS*, Mar. 2011.
- [55] K. Satyanarayana, M. El-Hajjar, P.-H. Kuo, A. Mourad, and L. Hanzo, “Hybrid beamforming design for full-duplex millimeter wave communication,” *IEEE Trans. Veh. Technol.*, vol. 68, no. 2, pp. 1394–1404, Feb. 2019.
- [56] K. Satyanarayana, M. El-Hajjar, A. Mourad, and L. Hanzo, “Multi-user full duplex transceiver design for mmWave systems using learning-aided channel prediction,” *IEEE Access*, vol. 7, pp. 66 068–66 083, 2019.
- [57] T. Riihonen, S. Werner, and R. Wichman, “Transmit power optimization for multiantenna decode-and-forward relays with loopback self-interference from full-duplex operation,” in *Proc. 45th Asilomar Conf. Signals, Syst., Comput.*, Nov. 2011, pp. 1408–1412.
- [58] —, “Hybrid full-duplex/half-duplex relaying with transmit power adaptation,” *IEEE Trans. Wireless Commun.*, vol. 10, no. 9, pp. 3074–3085, Sept. 2011.
- [59] M. Valkama and M. Renfors, “Digital filter design for I/Q imbalance compensation,” in *Proc. 10th European Signal Process. Conf. (EUSIPCO)*, Sept. 2000, pp. 1–4.
- [60] J. Zhou and H. Krishnaswamy, “System-level analysis of phase noise in full-duplex wireless transceivers,” *IEEE Trans. Circuits Syst. II*, vol. 65, no. 9, pp. 1189–1193, 2018.
- [61] C. Rapp, “Effects of HPA-nonlinearity on a 4-DPSK/OFDM-signal for a digital sound broadcasting system,” in *Proc. the Second European Conf. on Satellite Commun.*, Oct. 1991, pp. 179–184.
- [62] D. Korpi, L. Anttila, and M. Valkama, “Nonlinear self-interference cancellation in MIMO full-duplex transceivers under crosstalk,” *EURASIP J. Wireless Commun. Netw.*, vol. 2017, Feb. 2017.

Chapter 2

Frequency-Domain Hammerstein Canceller

Currently, several time-domain and frequency-domain SI cancellers have been proposed. Time-domain SI cancellers are based on the parallel Hammerstein (PH) model, and they have good flexibility with high computational cost. In contrast, frequency-domain SI cancellers can achieve high cancellation performance with low computational cost but they have less flexibility than time-domain PH based SI cancellers. In this chapter, the author proposes a frequency-domain SI canceller based on the PH model. The proposed canceller estimates the frequency response of the SI channel and regenerates SI signals by the overlap-save method. Therefore, the computational complexity of the proposed scheme is less than time-domain PH cancellers. The performance of the proposed scheme is assessed by equivalent baseband signal simulations of a full-duplex transceiver. As a result, the proposed scheme achieves high SI cancellation as time-domain PH cancellers with low computational cost. In addition, the results show the convergence performance of the proposed scheme is faster than the time-domain scheme.

2.1 Introduction

Digital SI cancellers are necessary to eliminate long delayed and remained SI signals since RF cancellers cannot reduce the power of the SI signal to the noise floor. Digital SI cancellation algorithms can be classified into three categories: time-domain algorithms, frequency-domain algorithms, and reference receiver based algorithms.

Time-domain digital self-interference cancellers [1–8] estimate the self-interference channel, and the self interference is canceled using the estimated channel and the known transmitted signal. In [1–6, 8], it is shown that the IQ imbalance of IQ mixers and power-amplifier (PA) nonlinear distortion are serious problems for digital cancellation, and, consequently, nonlinear self-interference cancellers are proposed. A similar idea to nonlinear self-interference cancellers has been studied in the field of acoustic echo cancellation [9, 10]. Time-domain nonlinear cancellers assume the self-interference channel including the transceiver path to be a parallel Hammerstein model, and they have high cancellation characteristics with high computational cost. For example, the least mean squares (LMS) and the recursive least squares (RLS) algorithms for the augmented nonlinear digital canceller [6] need computational costs of $\mathcal{O}(P^2N)$ and $\mathcal{O}(P^4N^2)$, respectively, where P is the highest nonlinearity order of the canceller, and N is the number of the taps of each branched finite impulse response (FIR) filter. Furthermore, they overestimate nonlinear characteristics even when the power of the self-interference is lower than the noise power because the highest nonlinearity order P is determined so that self-interference can be removed, in the worst case, during the design stage.

Conventional frequency-domain digital self-interference cancellers [11–15] estimate the frequency response of the self-interference channel in the frequency domain, and they offer lower computational cost than time-domain cancellers by using fast Fourier transform (FFT). However, they have less flexibility than the time-domain cancellers because they cannot be used with well-known adaptive algorithms such as LMS and RLS, and in [12] the nonlinear coefficients of the PA are estimated by time-domain signal processing. Also, conventional frequency-domain cancellers have several difficulties.

- The performance of the frequency-domain cancellation is degraded when the symbol timing of the desired signal and the self-interference signal are not synchronized [14].
- To avoid the degradation by the symbol timing offset, we have to apply self-interference cancellation on the time domain even though the parameter estimation process is performed on the frequency domain, as in [15].
- When pure OFDM symbols are used for the parameter estimation, the frequency response can be estimated only at the frequency where the subcarriers exist. It may cause degradation of time-domain cancellation performance, which can be found in results of [15] because we have to estimate

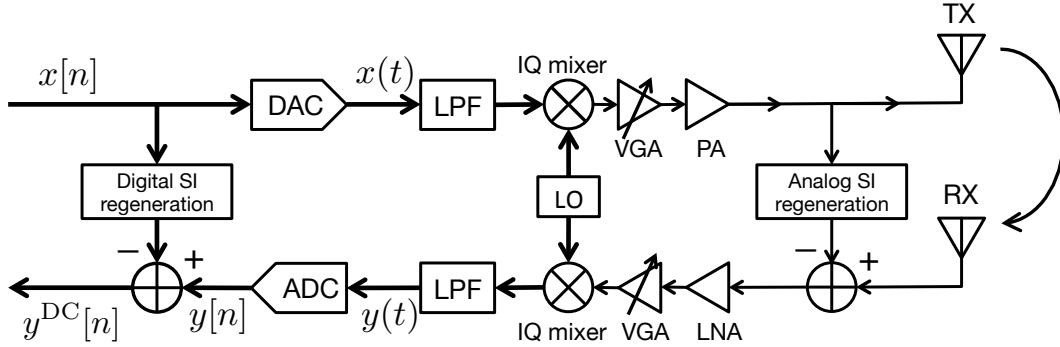


Figure 2.1: A model of the assumed full duplex transceiver.

the effect of discontinuities between symbols which yield the sidelobe of the spectra.

In this chapter, the author describes a frequency-domain SI cancellation algorithm based on the parallel Hammerstein model. In a training period, it transmits appropriate symbols and estimates frequency responses of the SI channel in frequency-domain. Then, the SI-canceled signal is computed by the overlap-save method. The proposed scheme achieves high SI cancellation with low computational cost and good flexibility like time-domain cancellers.

2.2 Self-Interference Signal Model

The structure of a transceiver subject to this study is presented in Fig. 2.1. In this section, we derive the SI signal model on the transceiver. The transceiver consists of a transmitter and a receiver which have RF components such as IQ mixers, filters, and amplifiers. The modulation method of the transceiver is orthogonalized frequency division multiplexing (OFDM). The isolation between a transmit antenna and a receive antenna is achieved by a passive antenna isolation, and a simple RF SI canceller which cancels only LOS SI signal is used. For simplicity, desired signals are not received, and both RF filters and variable gain amplifiers (VGA) of the transceiver have ideal characteristics.

2.2.1 IQ mixer

The transmission baseband signal $x[n]$ is converted to an analog baseband signal by digital to analog converter (DAC), and it is up-converted by an IQ mixer. On an

ideal IQ mixer, equivalent baseband signal of the output signal from the IQ mixer is equal to the input signal of the IQ mixer. But in fact, that is not satisfied because an actual IQ mixer has imbalances between I- and Q-phase carrier signals. Thus, the output signal of the transmitter IQ mixer can be expressed as

$$x_{\text{IQ}}(t) = g_1^{\text{TX}}(\tau) * x(t) + g_2^{\text{TX}}(\tau) * x^*(t), \quad (2.1)$$

where $g_1^{\text{TX}}(\tau)$ and $g_2^{\text{TX}}(\tau)$ are I- and Q-phase impulse responses of the transmitter IQ mixer [16], and the binary operator $f * g$ denotes a convolution of f and g . An indicator of the imbalance is called image rejection rate (IRR), and it is defined as

$$\text{IRR}^{\text{TX}}(f) = \frac{|G_1^{\text{TX}}(f)|^2}{|G_2^{\text{TX}}(f)|^2}, \quad (2.2)$$

where $G_1^{\text{TX}}(f)$ and $G_2^{\text{TX}}(f)$ are frequency responses of $g_1^{\text{TX}}(t)$ and $g_2^{\text{TX}}(t)$, respectively.

On the assumption that $G_1^{\text{TX}}(f)$ and $G_2^{\text{TX}}(f)$ are constant at a whole band, the output signal of the transmitter IQ mixer can be simplified to

$$x_{\text{IQ}}(t) = x(t) + b^{\text{TX}}x^*(t), \quad (2.3)$$

where b^{TX} is the coefficient of the image component. On the same assumption, the output signal of the receiver IQ mixer can be written by

$$y_{\text{IQ}}(t) = y_{\text{VGA}}(t) + b^{\text{RX}}y_{\text{VGA}}^*(t), \quad (2.4)$$

where b^{RX} is the coefficient of the image component, and $\text{IRR}^{\text{RX}} = |b^{\text{RX}}|^{-2}$ is an IRR of the receiver IQ mixer, and $y_{\text{VGA}}(t)$ is the output signal of the receiver VGA.

2.2.2 Power amplifier

The output signal of the transmitter IQ mixer $x_{\text{IQ}}(t)$ is amplified by the power amplifier (PA) before transmitting from the antenna. Practical characteristics of a PA can be assumed to be linear at low output power, but the distorted output signal cannot be ignored for SI cancellers at high output power. The output signal

at the PA is expressed as

$$\begin{aligned} x_{\text{PA}}(t) &= f_{\text{PA}}(\tau) * (a_1 x_{\text{IQ}}(t) + x_{\text{IMD}}(t)), \\ x_{\text{IMD}}(t) &= a_3 \psi_3(x_{\text{IQ}}(t)) + a_5 \psi_5(x_{\text{IQ}}(t)) + \dots, \\ \psi_p(x) &= x |x|^{p-1}, \end{aligned} \quad (2.5)$$

where $f_{\text{PA}}(\tau)$ is an impulse response of the PA, and $x_{\text{IMD}}(t)$ is an intermodulation distortion signal, and a_p is a gain of a distorted signal ψ_p .

2.2.3 Self-interference coupling channel

The received SI signal at the receive antenna can be written by

$$y_{\text{ANT}}(t) = h(\tau) * x_{\text{PA}}(t) + z_{\text{th}}(t), \quad (2.6)$$

where $h(\tau)$ is an impulse response of the SI channel and $z_{\text{th}}(t)$ is the thermal noise. The SI channel is strongly coupling, and a LOS wave is stronger than multi-path waves because the receive antenna is placed near the transmit antenna. Thus, the characteristic of the SI channel is modeled to Rician fading channel, and its parameter is $K = 25 \text{ dB} - 40 \text{ dB}$ when the distance between the transmit antenna and the receive antenna is less than 0.5 m [17]. The isolation between the transmit antenna and the receive antenna can be higher by using directional antennas and absorbers [18].

2.2.4 Received self-interference signal

Taking RF impairments into account, the quantized received signal is written as

$$y(t) = \sum_{p=1,3,\dots}^{\infty} \left\{ h_p(\tau) * \psi_p(x(t)) + h'_p(\tau) * \psi_p^*(x(t)) \right\} + z(t), \quad (2.7)$$

where $h_p(\tau)$ and $h'_p(\tau)$ are impulse responses of the SI channel, and $z(t)$ contains other distortions and total noise at the receiver. The received SI signal at frequency-domain is expressed as

$$Y(f) = \sum_{p=1,3,\dots}^{\infty} \left\{ H_p(f) \Psi_p(f) + H'_p(f) \Psi'_p(f) \right\} + Z(f), \quad (2.8)$$

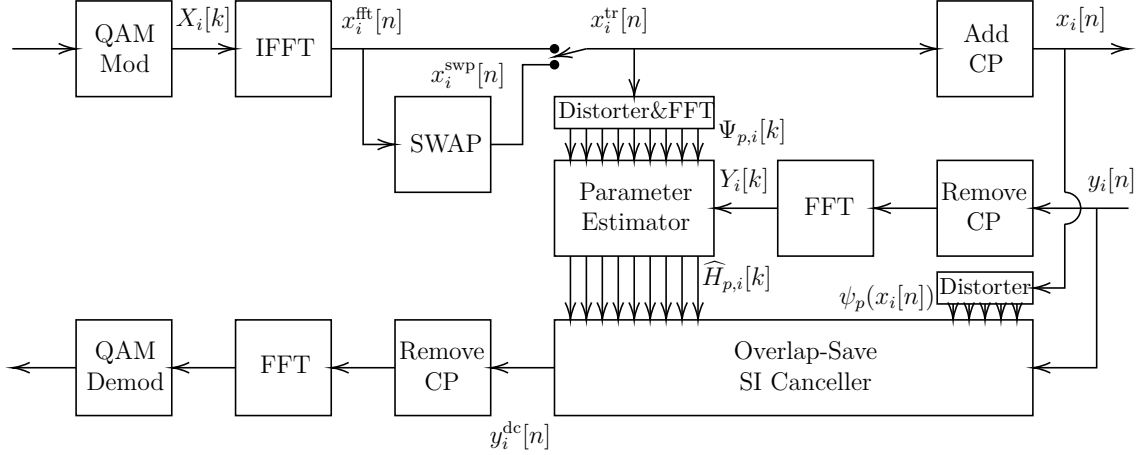


Figure 2.2: Proposed SI canceller.

where $\Psi_p(f)$ is a frequency-domain symbol of the p -th distorted transmitted signal, and $\Psi'_p(f)$ is an image signal of $\Psi_p(f)$. In addition, $H_p(f)$ and $H'_p(f)$ are frequency responses of $\Psi_p(f)$ and $\Psi'_p(f)$, respectively. Also, $Z(f)$ is the frequency-domain representation of $z(t)$. Thus, the received frequency-domain signal $Y(f)$ can be described as a linear combination of $\Psi_p(f)$ and $\Psi'_p(f)$.

2.3 Proposed Frequency-Domain Cancellor Based on Parallel Hammerstein Model

In this section, the author describes the proposed frequency-domain SI canceller based on the parallel Hammerstein model as shown in Fig. 2.2. The frequency responses $H_{p,i}[k]$ and $H'_{p,i}[k]$ are estimated in the training period of the proposed scheme. In the canceling period, the received SI signal is regenerated by the overlap-save method with estimated $H_{p,i}[k]$ and $H'_{p,i}[k]$.

2.3.1 Generating training symbols

In the training period of the proposed scheme, the i -th transmitted OFDM symbol, $x_i[n]$, is manipulated from a pure OFDM symbol $x_i^{fft}[n]$ to utilize effects of the cyclic prefix (CP) as shown in Fig. 2.3. The swapping manipulation is necessary to achieve high SI cancellation, because there are no discontinuities in an OFDM symbol, and they appear between symbols. Additionally, $H_{p,i}[k]$, which is the frequency response of $\psi_p(x_i[n])$, can be estimated with high accuracy by the CP.

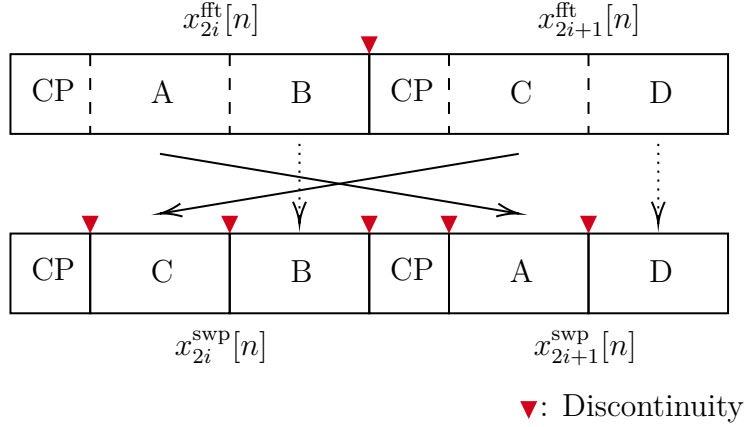


Figure 2.3: Swapped training OFDM symbols.

The first step of generating training symbols is to modulate training bits to $X_i[k]$ by QAM and to convert them to a time-domain symbol $x_i^{\text{fft}}[n]$, such that

$$x_i^{\text{fft}}[n] = \text{IFFT}\{X_i[k]\}[n] = \frac{1}{\sqrt{K}} \sum_{\substack{k=-N_{\text{sc}}/2 \\ k \neq 0}}^{N_{\text{sc}}/2} X_i[k] e^{j2\pi k \Delta f n T_s}, \quad (2.9)$$

where the operator $\text{IFFT}\{\cdot\}$ is the inverse fast Fourier transform (FFT) operator, and Δf and T_s are the frequency interval and sampling interval of the OFDM modulation, and N_{SC} is the number of subcarriers.

In the second step, the first half of x_{2i}^{fft} is swapped to the first half of x_{2i+1}^{fft} , such that

$$x_i^{\text{swp}}[n] = \begin{cases} x_{i+1}^{\text{fft}}[n] & (\{n < N_{\text{fft}}/2\} \wedge \{i \text{ is even}\}) \\ x_{i-1}^{\text{fft}}[n] & (\{n < N_{\text{fft}}/2\} \wedge \{i \text{ is odd}\}) \\ x_i^{\text{fft}}[n] & (n \geq N_{\text{fft}}/2) \end{cases} \quad (2.10)$$

where N_{fft} is the FFT size of OFDM. By this manipulation, discontinuities are produced in OFDM symbols without destructing the CP structure, and the parameter estimator of the proposed method can estimate discontinuities of the SI signal with high accuracy. Furthermore, the number of swapped OFDM training symbols can be less than pure OFDM training symbols because side lobes increased by discontinuities become the minority in all power of the SI signal.

In the final step of generating training symbols, the swapped OFDM symbols for $i = 0 \dots N_{\text{swp}} - 1$ are used as transmission symbols $x_i^{\text{tr}}[n]$, and pure OFDM symbol

is used as transmission signals after transmitting the swapped symbols as written by

$$x_i^{\text{tr}}[n] = \begin{cases} x_i^{\text{swp}}[n] & (i < N_{\text{swp}}), \\ x_i^{\text{fft}}[n] & (i \geq N_{\text{swp}}). \end{cases} \quad (2.11)$$

Then, the transmission symbols $x_i^{\text{tr}}[n]$ and N_{cp} -sized CP are jointed as (2.12) and transmitted.

$$x_i[n] = \begin{cases} x_i^{\text{tr}}[n - N_{\text{cp}} + N_{\text{fft}}] & (n < N_{\text{cp}}) \\ x_i^{\text{tr}}[n - N_{\text{cp}}] & (n \geq N_{\text{cp}}) \end{cases} \quad (2.12)$$

2.3.2 Frequency-domain training

On the proposed method, the frequency response of the SI channel can be estimated by well-known adaptive algorithms in frequency-domain scheme, and they estimate the frequency response of the SI channel at each discrete frequency, k , independently. Least squares (LS), recursive LS (RLS) and normalized least mean squares (NLMS) algorithms applied to the proposed scheme are shown in the following.

Least squares parameter estimation

LS algorithm is one of the most fundamental parameter estimation algorithms. At digital baseband, the received signal can be expressed as

$$\begin{aligned} Y_i[k] &= \frac{1}{\sqrt{N_{\text{SC}}}} \sum_{n=0}^{N_{\text{fft}}-1} y_i[n + N_{\text{cp}}] e^{-j2\pi k \Delta f n T_s} \\ &= H_{1,i}[k] \Psi_{1,i}[k] + H_{2,i}[k] \Psi_{2,i}[k] \cdots + H_{P,i}[k] \Psi_{P,i}[k] + Z_i[k], \end{aligned} \quad (2.13)$$

$$\Psi_{p,i}[k] = \begin{cases} \text{FFT} \{ \psi_p(x_i^{\text{tr}}[n]) \} [k] & (p \text{ is odd}) \\ \text{FFT} \{ \psi_{p-1}(x_i^{\text{tr}}[n]) \} [k] & (p \text{ is even}) \end{cases} \quad (2.14)$$

where $y_i[n]$ is the i -th received symbol and $Z_i[k]$ is the total noise at the receiver, and P is the number of basis functions.

To apply LS algorithm for estimating the frequency response, $H_{p,i}[k]$ is assumed to be static and equal to $H_p[k]$. Additionally, we introduce vector-matrix notations,

$\mathbf{Y}[k]$, $\Psi[k]$ and $\mathbf{H}[k]$, such that

$$\mathbf{Y}[k] = [Y_0[k] Y_1[k] \cdots Y_{N_{\text{tr}}-1}[k]]^T, \quad (2.15)$$

$$\Psi[k] = \begin{bmatrix} \Psi_{1,0}[k] & \Psi_{2,0}[k] & \cdots & \Psi_{P,0}[k] \\ \Psi_{1,1}[k] & \Psi_{2,1}[k] & \cdots & \Psi_{P,1}[k] \\ \vdots & \vdots & \ddots & \vdots \\ \Psi_{1,N_{\text{tr}}-1}[k] & \Psi_{2,N_{\text{tr}}-1}[k] & \cdots & \Psi_{P,N_{\text{tr}}-1}[k] \end{bmatrix}, \quad (2.16)$$

$$\mathbf{H}[k] = [H_1[k] H_2[k] \cdots H_P[k]]^T, \quad (2.17)$$

where N_{tr} is the number of training symbols. By using vector-matrix notations, $\mathbf{Y}[k]$ can be expressed as

$$\mathbf{Y}[k] = \Psi[k]\mathbf{H}[k] + \mathbf{Z}[k], \quad (2.18)$$

where $\mathbf{Z}[k]$ consists of $Z_i[k]$. Then, the LS-estimated frequency responses are expressed as

$$\begin{aligned} \widehat{\mathbf{H}}[k] &= [\widehat{H}_1[k] \widehat{H}_2[k] \cdots \widehat{H}_P[k]]^T \\ &= (\Psi^H[k] \Psi[k])^{-1} \Psi^H[k] \mathbf{Y}[k]. \end{aligned} \quad (2.19)$$

Recursive least squares parameter estimation

LS algorithm requires matrix inversion or singular value decomposition (SVD). On the other hand, recursive LS algorithm can recursively estimate parameters which minimize least square errors without matrix inversion and SVD. On the proposed scheme, RLS algorithm is expressed as

$$\Psi_i[k] = [\Psi_{1,k}[k] \Psi_{2,k}[k] \cdots \Psi_{P,k}[k]]^T, \quad (2.20)$$

$$\widehat{\mathbf{H}}_i[k] = \widehat{\mathbf{H}}_{i-1}[k] + E_i[k] \mathbf{G}_i[k], \quad (2.21)$$

$$E_i[k] = Y_i[k] - \Psi_i^T[k] \widehat{\mathbf{H}}_{i-1}[k], \quad (2.22)$$

$$\mathbf{G}_i[k] = \frac{\mathbf{P}_{i-1}[k] \Psi_i^*[k]}{\lambda + \Psi_i^T[k] \mathbf{P}_{i-1}[k] \Psi_i^*[k]}, \quad (2.23)$$

$$\mathbf{P}_i[k] = \lambda^{-1} \{ \mathbf{P}_{i-1}[k] - \mathbf{G}_i[k] \Psi_i^T[k] \mathbf{P}_{i-1}[k] \}, \quad (2.24)$$

where $\Psi_i[k]$ is the k -th input signal vector of an RLS adaptive filter at a discrete frequency, k , and $\widehat{\mathbf{H}}_i[k]$ is the k -th estimated frequency response at k , and λ is called forgetting factor. Furthermore, $\widehat{\mathbf{H}}_i[k]$ and $\mathbf{P}_i[k]$ are initialized to 0 and $\delta^{-1}\mathbf{I}$ where δ is very small positive value. The total number of multiplications of complex value for computing (2.20)–(2.24) is $4P^2 + 4P$.

Normalized least mean squares parameter estimation

NLMS parameter estimation algorithm has much lower computation cost and complexity than RLS algorithm. NLMS algorithm is expressed as

$$\widehat{\mathbf{H}}_i[k] = \widehat{\mathbf{H}}_{i-1}[k] + \frac{\mu}{Q_i[k]} E_i[k] \Psi_i^*[k], \quad (2.25)$$

$$E_i[k] = Y_i[k] - \Psi_i^T[k] \mathbf{H}_{i-1}[k], \quad (2.26)$$

$$Q_i[k] = (1 - \alpha) Q_{k-1}[k] + \alpha \Psi_i^H[k] \Psi_i[k], \quad (2.27)$$

where μ and α are positive constant values, and $\Psi_i[k]$ and $\widehat{\mathbf{H}}_i[k]$ are the same values as for RLS. The total number of multiplications of complex values for computing (2.25)–(2.27) is $2P$, and it is N times faster than the time-domain NLMS, where N is the number of taps of a time-domain FIR filter.

2.3.3 Time-domain canceling using frequency response

In this section, the author describes the overlap-save method for the proposed scheme on time-domain using $\mathbf{H}_{p,k}[f]$ without conversion to impulse responses. When a signal x is periodic, $(h * x)$ is known as a circular convolution and it can be computed efficiently with FFT algorithm by $\text{IFFT}\{\text{FFT}\{x\}\text{FFT}\{h\}\}$. In general, this algorithm is not used to regenerating SI signals because the transmitted signal is not periodic. For this reason, SI signals are regenerated by the overlap-save

method [19] expressed as

$$\psi_{p,i}^{\text{rg}}[n] = \text{IFFT}_{2N_{\text{fft}}} \left\{ \Psi_{p,i}^{\text{rg}}[k] \right\} [n - N_{\text{cp}} + N_{\text{fft}}], \quad (2.28)$$

$$\Psi_{p,i}^{\text{rg}}[k] = \begin{cases} H_{p,i} \text{FFT}_{2N_{\text{fft}}} \left\{ \psi_p(x_i^c[n]) \right\}, & (p \text{ is odd}), \\ H_{p,k} \text{FFT}_{2N_{\text{fft}}} \left\{ \psi_{p-1}^*(x_i^c[n]) \right\}, & (p \text{ is even}), \end{cases} \quad (2.29)$$

$$x_i^c[n] = \begin{cases} x_i[2N_{\text{cp}} + n], & (n < N_{\text{fft}} - N_{\text{cp}}), \\ x_i[n + N_{\text{cp}} - N_{\text{fft}}], & (n \geq N_{\text{fft}} - N_{\text{cp}}), \end{cases} \quad (2.30)$$

where $\psi_{p,i}^{\text{rg}}[n]$ is the p -th distorted i -th regenerated OFDM symbol of the SI signal, and $\text{FFT}_M \{ \cdot \}$, $\text{IFFT}_M \{ \cdot \}$ are M -sized FFT and inverse FFT, respectively. Finally, the digital SI canceled signal can be written by

$$y_i^{\text{dc}}[n] = y_i[n] - \sum_{p=1}^P \psi_{p,i}^{\text{rg}}[n]. \quad (2.31)$$

2.3.4 Computational cost and complexity

The author describes the derivation process of computational cost and complexity of the proposed scheme in the following.

In the training period of the proposed scheme, received OFDM symbols are decomposed to discrete frequency components by FFT after removing CPs. This process requires $\frac{1}{2}N_{\text{fft}} \log_2 N_{\text{fft}}$ times multiplications of two complex numbers per symbol. The transmitted symbols before adding CPs are distorted by $\psi_p(\cdot)$ and also decomposed to discrete frequency components by FFT, where $\psi_p(\cdot)$ can be computed a priori and implemented by a lookup table. The total computational cost of transforming received and transmitted symbols to frequency-domain is $\frac{1}{4}(P+2)N_{\text{fft}} \log_2 N_{\text{fft}}$ per symbol because $\text{FFT} \left\{ \psi_p^*(x) \right\}$ can be computed by frequency-inversion and conjugation of $\text{FFT} \left\{ \psi_p(x) \right\}$. In the next step of the training period, the proposed scheme estimates $H_{p,i}[k]$ from $Y_i[k]$ and $\Psi_{p,i}[k]$. NLMS algorithm and RLS algorithm require $2P$ and $4P^2 + 4P$ complex multiplications per discrete frequency per symbol, respectively. Thus, the whole computational cost of the training period is $\frac{1}{4}(P+2)N_{\text{fft}} \log_2 N_{\text{fft}} + AN_{\text{fft}}$ per symbol, where A is $2P$ (NLMS used) or $4P^2 + 4P$ (RLS used).

In the canceling period, the overlap-save method is used P times on the proposed scheme. By the same trivial technique for computing $\text{FFT} \left\{ \psi_p^*(x) \right\}$,

this process requires $\frac{3}{2}PN_{\text{fft}}(\log_2 N_{\text{fft}} + 1)$ complex-multiplications per symbol since one time overlap-save method can be computed by $2N_{\text{fft}}$ -sized FFT, IFFT, and multiplications.

2.4 Performance Simulations

In this section, we evaluate the performance of the proposed scheme by equivalent baseband signal simulations of a full-duplex transceiver as shown in Fig. 2.1. The simulation parameters are presented as Table 2.1, which are based on [3]. In this simulations, the dynamic range of the receiver ADC is about 79 dB [20]. The imbalance of IQ mixers is realized by adding an image signal, and the coefficients of nonlinearity of the PA are predetermined based on IIP. The parameters of both RLS algorithm and LMS algorithm are set to the optimal coefficients which can achieve the best steady-state cancellation performance in each canceller. This scenario ensures that the results show the true performance of each canceller. Additionally, in this simulations, the SI cancellation rate is defined as

$$\text{Cancellation} = \frac{\mathbb{E} [|y_i[n]|^2]}{\mathbb{E} [|y_i^{\text{dc}}[n]|^2]}, \quad (2.32)$$

where $\mathbb{E} [s]$ denotes the expected value of s .

2.4.1 Cancellation performance

Fig. 2.4 shows the cancellation performance of both the proposed frequency-domain parallel Hammerstein based method (FH) and time-domain parallel Hammerstein based method (PH) [4]. In addition, the parameters of both cancellers are optimized by LS algorithm, and the self-interference and noise power ratio (INR) varies from 20 dB to 80 dB, where INR is defined as

$$\text{INR} = \frac{\mathbb{E} [G_{\text{LNA}}^2 |(h(\tau) - h_{\text{RF}}(\tau)) * x_{\text{PA}}(t)|^2]}{\mathbb{E} [|n_{\text{LNA}}(t)|^2]}, \quad (2.33)$$

where $h_{\text{RF}}(\tau)$ is the impulse response of the RF SI canceller, and G_{LNA} is the gain of the receiver LNA, and $n_{\text{LNA}}(t)$ is a total noise of the output signal of the receiver LNA. In the situation of Fig. 2.4, the number of training symbols, N_{tr} , is 60 and

Table 2.1: Simulation Specifications

Parameter	Value
Oversampling rate	4
Modulation	OFDM
Constellation	16QAM
Size of FFT N_{fft}	256
Number of subcarriers	52
Cyclic prefix N_{cp}	64 samples
Sampling rate	80M samples/sec
Transmit data	Uniform-random data
SI channel after RF-SIC	Rayleigh fading
Channel order	64 samples
Transmit power	15 dBm
IRR	varied
Highest order of IMD	3
IIP3	17 dBm
PA Gain	27 dB
Noise figure of LNA	4 dB
Number of ADC bits	14 bits
Basis functions	$\{x, x^*, x x ^2, x^* x ^2, x x ^4, x^* x ^4\}$

swapped training symbols, N_{swp} , is ∞ , and both SI cancellers can be assumed to be trained completely. The cancellation performance of the proposed scheme is similar to the time-domain method, and they achieve perfect cancellation of the SI signal when INR is below 60 dB even under worse IRR. Thus, the proposed method has a comprehensive cancellation capability as same as the time-domain method. When INR is higher than 70 dB, SI cancellation is saturated because linear combinations of the basis functions of Table 2.1 cannot represent the received SI signal completely. The complete set of basis functions are discussed in [6], and in Chapter 3, the author apply them to the proposed method.

In Fig. 2.5, the convergence of both cancellers with NLMS and RLS algorithm is shown at INR = 50 dB and $N_{\text{swp}} = \infty$. The proposed scheme with RLS algorithm achieves about 49 dB SI cancellation with three or four training symbols, and the time-domain scheme achieves about 49 dB SI cancellation with 28 training symbols. Hence, convergence speed of the frequency-domain scheme with RLS algorithm is faster than the time-domain scheme because the time-domain signals are strongly colored. Generally, convergence speed of an adaptive algorithm decreases with

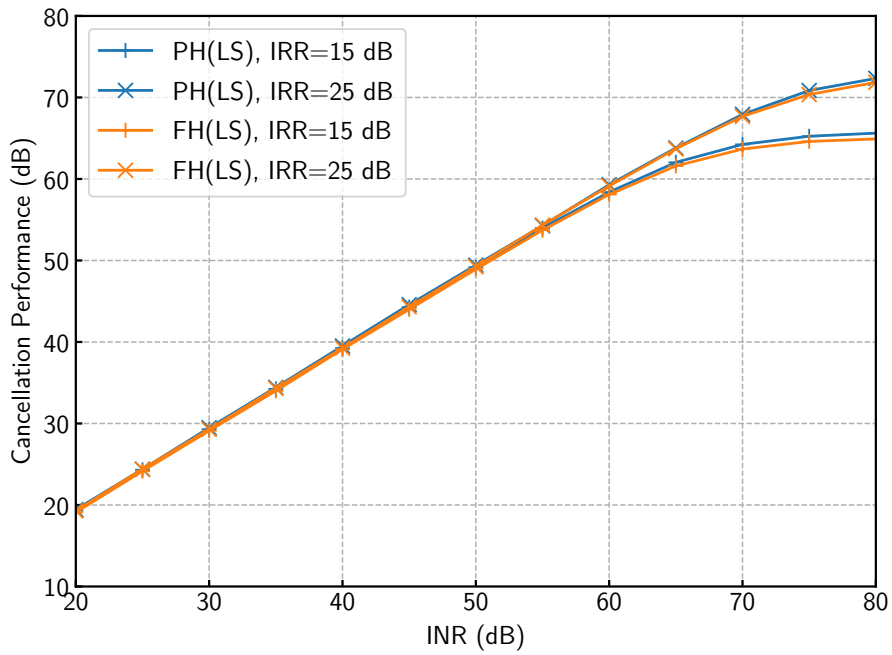


Figure 2.4: The SI cancellation performance at $N_{tr} = 60$.

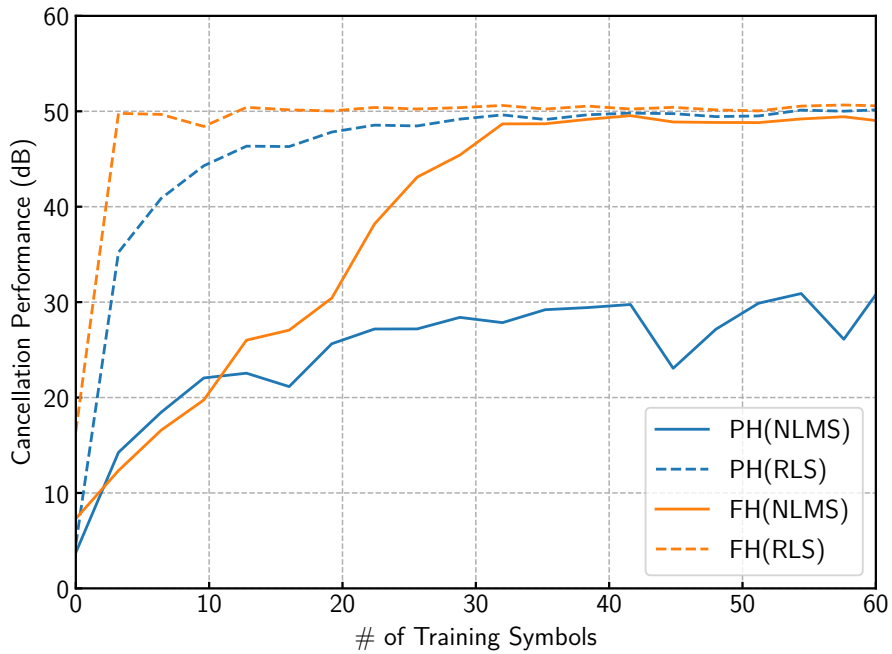


Figure 2.5: The convergence of each canceller at $INR = 50$ dB and $IRR = 25$ dB.

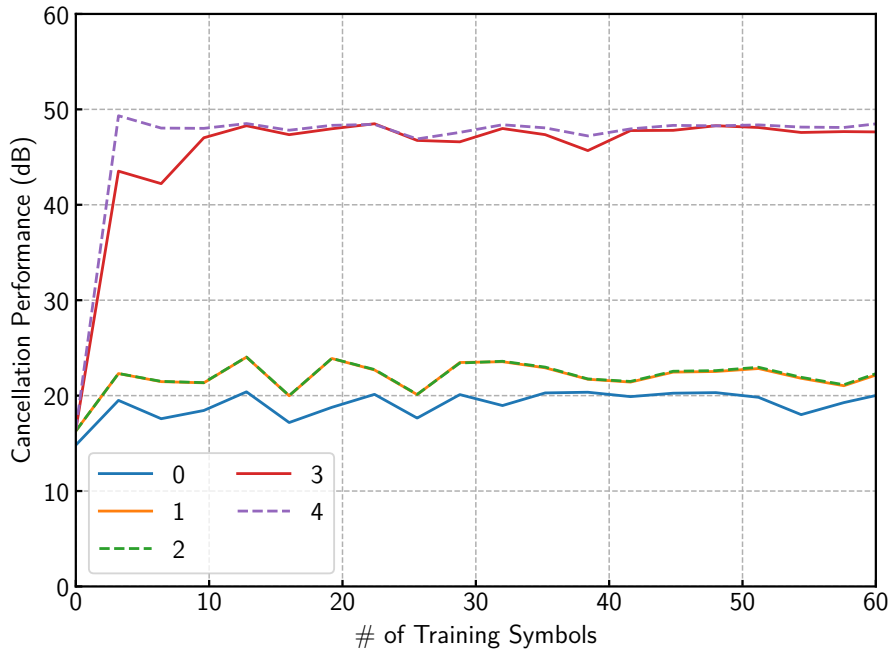


Figure 2.6: The convergence performance of the proposed scheme with RLS algorithm at $N_{\text{swp}} = 0 \dots 4$ and IRR = 25 dB.

colored input signals. On the other hand, the input signal of the RLS adaptive filter of the frequency-domain scheme has flat spectrum and weak correlation between their elements. For this reason, the time-domain scheme needs nine times more training symbols than the frequency-domain scheme. When NLMS algorithm is used, the frequency-domain scheme provides about 49 dB SI cancellation with 38 training symbols, but the time-domain scheme cannot reach 40 dB for the first 60 symbols. This is due to the same reason for the RLS case.

Fig. 2.6 shows the convergence of the frequency-domain scheme with RLS algorithm when N_{swp} is changed from 0 to 4. The proposed scheme cannot achieve 50-dB SI cancellation at $N_{\text{swp}} < 3$, and the result at $N_{\text{swp}} = 4$ is similar to the case of $N_{\text{swp}} = \infty$ shown in Fig. 2.5. Consequently, the sufficient number of N_{swp} is four to achieve high SI cancellation.

2.4.2 Computational complexity and cost

Table 2.2 shows computational complexity and cost of the time-domain parallel Hammerstein based SI canceller and the proposed frequency-domain parallel

Table 2.2: Computational complexity and cost per sample

Canceller scheme	time-domain scheme		proposed scheme	
	RLS	NLMS	RLS	NLMS
Adaptive algorithm				
Complexity of training	$\mathcal{O}(P^2N^2)$	$\mathcal{O}(PN)$	$\mathcal{O}(P^2)$	$\mathcal{O}(P)$
# of ops. of training	591×10^3	768	147	22.4
Complexity of canceling	$\mathcal{O}(PN)$		$\mathcal{O}(P)$	
# of ops. of canceling	384		64.8	

Hammerstein based SI canceller when the parameters are the same as simulation evaluations. At deriving complexity, the number of basis functions, P , and the number of taps of a time-domain FIR filter, N , are assumed to be variables, and other parameters are treated as constant. Besides, the number of operations is calculated as multiplications of two complex numbers. The proposed scheme with RLS algorithm is about 4.02×10^3 times faster than the time-domain scheme with RLS algorithm and about 5.22 times faster than the time-domain scheme with NLMS algorithm at the training period. In addition, at the canceling period, the proposed scheme is about 5.93 times faster than the time-domain scheme.

2.5 Conclusion

In this chapter, the author has described a frequency-domain digital self-interference canceller based on the parallel Hammerstein model. The proposed scheme decreases computational cost by estimating the characteristic of the SI channel on frequency-domain and using overlap-save method for regenerating SI signals. In addition, the proposed scheme has good compatibility with the time-domain parameter estimation algorithms such as least squares, recursive least squares, and normalized least mean squares algorithm. The performance of the proposed scheme is assessed by equivalent baseband signal simulations of a full-duplex transceiver. The results show that the proposed scheme achieves high SI cancellation as well as the time-domain scheme and fast convergence with low computational cost.

References

- [1] D. Bharadia, E. McMillin, and S. Katti, “Full duplex radios,” in *Proc. ACM SIGCOMM'13*, 2013.
- [2] L. Anttila, D. Korpi, V. Syrjälä, and M. Valkama, “Cancellation of power amplifier induced nonlinear self-interference in full-duplex transceivers,” in *Proc. 47th Asilomar Conf. Signals, Syst., Comput.*, Nov. 2013.
- [3] D. Korpi, L. Anttila, V. Syrjälä, and M. Valkama, “Widely linear digital self-interference cancellation in direct-conversion full-duplex transceiver,” *IEEE J. Sel. Areas Commun.*, vol. 32, no. 9, pp. 1674–1687, Sept. 2014.
- [4] M. Heino, D. Korpi, T. Huusari, E. Antonio-Rodriguez, S. Venkatasubramanian, T. Riihonen, L. Anttila, C. Icheln, K. Haneda, R. Wichman, and M. Valkama, “Recent advances in antenna design and interference cancellation algorithms for in-band full duplex relays,” *IEEE Commun. Mag.*, vol. 53, no. 5, pp. 91–101, May 2015.
- [5] D. Korpi, Y.-S. Choi, T. Huusari, L. Anttila, S. Talwar, and M. Valkama, “Adaptive nonlinear digital self-interference cancellation for mobile inband full-duplex radio: Algorithms and RF measurements,” in *Proc. IEEE GLOBECOM*, Dec. 2015.
- [6] D. Korpi, T. Huusari, Y.-S. Choi, L. Anttila, S. Talwar, and M. Valkama, “Digital self-interference cancellation under nonideal RF components: Advanced algorithms and measured performance,” in *Proc. IEEE SPAWC*, June 2015, pp. 286–290.
- [7] M. Sakai, H. Lin, and K. Yamashita, “Adaptive cancellation of self-interference in full-duplex wireless with transmitter IQ imbalance,” in *Proc. IEEE GLOBECOM*, Dec. 2014, pp. 3220–3224.

- [8] D. Korpi, S. Venkatasubramanian, T. Riihonen, L. Anttila, S. Otewa, C. Icheln, K. Haneda, S. Tretyakov, M. Valkama, and R. Wichman, “Advanced self-interference cancellation and multiantenna techniques for full-duplex radios,” in *Proc. 47th Asilomar Conf. Signals, Syst., Comput.*, Nov. 2013, pp. 3–8.
- [9] A. Nordsjo and L. Zetterberg, “Identification of certain time-varying nonlinear Wiener and Hammerstein systems,” *IEEE Trans. Signal Process.*, vol. 49, no. 3, pp. 577–592, Mar. 2001.
- [10] A. Guerin, G. Faucon, and R. L. Bouquin-Jeannes, “Nonlinear acoustic echo cancellation based on volterra filters,” *IEEE Trans. Speech Audio Process.*, vol. 11, no. 6, pp. 672–683, Nov. 2003.
- [11] M. Jain, J. I. Choi, T. Kim, D. Bharadia, S. Seth, K. Srinivasan, P. Levis, S. Katti, and P. Sinha, “Practical, real-time, full duplex wireless,” in *Proc. ACM MobiCom'11*, 2011.
- [12] R. Li, A. Masmoudi, and T. Le-Ngoc, “Self-interference cancellation with nonlinearity and phase-noise suppression in full-duplex systems,” *IEEE Trans. Veh. Technol.*, vol. 67, no. 3, pp. 2118–2129, Mar. 2018.
- [13] E. Ahmed, A. M. Eltawil, and A. Sabharwal, “Self-interference cancellation with phase noise induced ICI suppression for full-duplex systems,” in *Proc. IEEE GLOBECOM*, Dec. 2013, pp. 3384–3388.
- [14] H. Lee, J. Choi, D. Kim, and D. Hong, “Impact of time and frequency misalignments in OFDM based in-band full-duplex systems,” in *Proc. IEEE WCNC*, Mar. 2017.
- [15] M. S. Amjad and O. Gurbuz, “Linear digital cancellation with reduced computational complexity for full-duplex radios,” in *Proc. IEEE WCNC*, Mar. 2017.
- [16] M. Valkama and M. Renfors, “Digital filter design for I/Q imbalance compensation,” in *Proc. 10th European Signal Process. Conf. (EUSIPCO)*, Sept. 2000, pp. 1–4.
- [17] M. Duarte, C. Dick, and A. Sabharwal, “Experiment-driven characterization of full-duplex wireless systems,” *IEEE Trans. Wireless Commun.*, vol. 11, no. 12, pp. 4296–4307, Dec. 2012.
- [18] E. Everett, A. Sahai, and A. Sabharwal, “Passive self-interference suppression for full-duplex infrastructure nodes,” *IEEE Trans. Wireless Commun.*, vol. 13, no. 2, pp. 680–694, Feb. 2014.

- [19] W. H. Press, S. A. Teukolsky, W. T. Vetterling, and B. P. Flannery, *Numerical Recipes 3rd Edition: The Art of Scientific Computing*, 3rd ed. New York, USA: Cambridge University Press, 2007.
- [20] D. Korpi, T. Riihonen, V. Syrjälä, L. Anttila, M. Valkama, and R. Wichman, “Full-duplex transceiver system calculations: Analysis of ADC and linearity challenges,” *IEEE Trans. Wireless Commun.*, vol. 13, no. 7, pp. 3821–3836, July 2014.

Chapter 3

Basis Function Selection for Frequency-Domain Hammerstein Canceller

This chapter presents a basis function selection technique of a frequency-domain Hammerstein digital self-interference canceller for in-band full-duplex communications. The power spectral density (PSD) of the nonlinear self-interference signal is theoretically analyzed in detail, and a nonlinear self-interference PSD estimation method is developed. The proposed selection technique decides on the basis functions necessary for cancellation and relaxes the computational cost of the frequency-domain Hammerstein canceller based on the estimated PSD of the self-interference of each basis function. Furthermore, the convergence performance of the canceller is improved by the proposed selection technique. Simulation results are then presented, showing that the proposed technique can achieve similar cancellation performance compared with the original frequency-domain Hammerstein canceller and a time-domain nonlinear canceller. Additionally, it is shown that the proposed technique improves the computational cost and the convergence performance of the original frequency-domain Hammerstein canceller.

3.1 Introduction

Time-domain digital self-interference cancellers which only use a single transmitter-receiver pair are not suitable to implement on an actual transceiver because they

can only achieve high self-interference cancellation at a very high computational cost. In contrast, the author has proposed a novel frequency-domain Hammerstein canceller which decreases computational cost by estimating the characteristic of the SI channel on the frequency domain and using the overlap-save method for regenerating SI signals in Chapter 2. To the best of the author's knowledge, the frequency-domain Hammerstein self-interference canceller is the first digital self-interference canceller which estimates non-idealities of the IQ mixers and the PA in the frequency-domain with LMS, RLS, and LS algorithms. However, as with the time-domain Hammerstein canceller, the basis functions used for cancellation are determined in advance, but some of them may be unnecessary when their power is lower than the noise. In addition, the necessary basis functions for some subcarriers may not be needed on another subcarrier. Increasing the number of basis functions leads to an increase in computational cost and convergence time of training, so it is better to reduce the number of basis functions.

- In this chapter, the author introduce a basis function selection technique for a frequency-domain Hammerstein self-interference canceller. The proposed selection technique decides basis functions necessary for cancellation and relaxes the computational cost of the frequency-domain Hammerstein canceller based on the power spectral density of the self interference of each basis function.
- In the proposed technique, only the nonlinear characteristics of the transmitter, which can be regarded as static, are learned in advance. To prevent degradation of cancellation performance due to variations in nonlinear characteristics, they are used for the selection of basis functions and not for training self-interference channels.
- Since the proposed technique can be used together with a multi-tap RF canceller, the proposed technique can be applied for much of the full-duplex hardware studied so far.
- Detailed equivalent baseband simulations are performed for verifying the proposed technique, and their results show that the computational cost of the frequency-domain Hammerstein canceller decreases as the power of the self interference decreases. In addition, a canceller with least-square training achieves faster convergence characteristics by the proposed selection technique.

Unfortunately, due to specific symbols to train the canceller, the frequency-

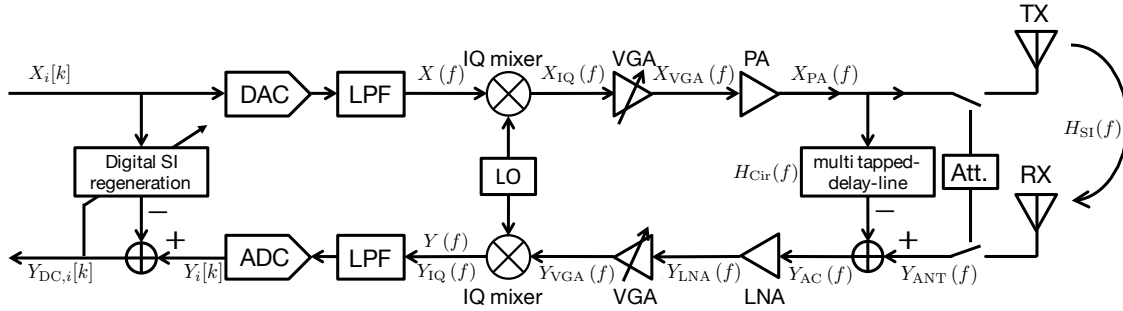


Figure 3.1: A model of the assumed full-duplex transceiver.

domain Hammerstein canceller will not be able to track channel variations simultaneously with data transmission. This problem is still not solved in this chapter. However, when the symbol timing of the desired signal and the self-interference signal are synchronized, the problem does not arise because specific training symbols are unnecessary. Although this problem is very important, the author treats it as a future work.

The rest of this chapter is organized as follows. In Section 3.2, a detailed model of the self interference which includes nonlinearities of the IQ mixers and the power amplifier is provided. The proposed selection technique with the frequency-domain Hammerstein self-interference canceller is presented in Section 3.3. In Section 3.4, the performance of the proposed technique under different scenarios is analyzed with equivalent baseband signal simulations. Finally, this chapter is concluded in Section 3.5.

3.2 Self-Interference Signal Model

Fig. 3.1 shows the full-duplex direct-conversion transceiver model discussed in this chapter. The transceiver consists of a transmitter and a receiver which have IQ mixers, RF filters, and amplifiers. For simplicity, the desired signal is not considered, and both RF low-pass filters and variable gain amplifiers (VGA) have ideal characteristics. In addition, in the derivation of the mathematical model, the nonlinear behaviors of the LNA is ignored for simplicity, but they are taken into account on simulations. The nonlinear self-interference signal model has been derived on the time domain in much literature such as [1–3]. However, the author describes the detailed frequency-domain representation of the self interference in

this section because we use it to describe the proposed scheme in the next section.

The transceiver transmits an orthogonal frequency division multiplexing (OFDM) signal which has N_{sc} subcarriers and N_{cp} -length cyclic prefix (CP). The digital-domain discrete-frequency transmit signal is expressed as $X_i[k]$ where i and k are the symbol index and the subcarrier index, respectively. The transmit signal $X_i[k]$ is transformed to time-domain signal $x[n]$ by the OFDM modulator and converted to an analog baseband signal $x(t)$ by an analog to digital converter (ADC) and a low pass filter (LPF). The analog baseband signal $x(t)$ can be expressed as

$$x(t) = \sum_{\substack{k=-N_{sc}/2 \\ k \neq 0}}^{N_{sc}/2} X_i[k] e^{j2\pi k \Delta f t} \quad (t \in \mathbf{T}_i^S \cup \mathbf{T}_i^{cp}), \quad (3.1)$$

where \mathbf{T}_i^S is the i -th symbol duration without CP, and \mathbf{T}_i^{cp} is the i -th CP duration, and Δf is the frequency interval of each subcarrier. Then we get the frequency-domain representation of the analog baseband transmit signal $X(f) = \mathcal{F}\{x(t)\}$, where $\mathcal{F}\{\cdot\}$ is the operator of the Fourier transform.

3.2.1 IQ mixer

The analog baseband transmit signal $X(f)$ is upconverted to an RF transmit signal by the IQ mixer of the transmitter. On an ideal IQ mixer, the output equivalent baseband signal of the transmitter IQ mixer $X_{IQ}(f)$ is equal to the baseband transmit signal $X(f)$. Actually, $X_{IQ}(f)$ has a mirror-image component of $X(f)$ because an actual IQ mixer has imbalances between the I- and Q-phase carrier signals. The output equivalent baseband signal of the transmitter IQ mixer $X_{IQ}(f)$ can be expressed as

$$X_{IQ}(f) = X(f) + b^{TX} X^*(-f) \quad (3.2)$$

where b^{TX} is the frequency-independent imbalance coefficient of the transmitter IQ mixer, and $(\cdot)^*$ denotes the complex-conjugate operation. An indicator of the IQ imbalance is called image rejection ratio (IRR) [4], and can be defined as

$$\text{IRR}^{TX} = |b^{TX}|^{-2}. \quad (3.3)$$

Furthermore, the received self-interference signal $Y(f)$ can be expressed as

$$Y(f) = Y_{\text{IQ}}(f) = Y_{\text{VGA}}(f) + b^{\text{RX}} Y_{\text{VGA}}^*(-f), \quad (3.4)$$

where b^{RX} is the frequency-independent imbalance coefficient of the receiver IQ mixer, and $Y_{\text{VGA}}^*(f)$ is the equivalent baseband signal of the receiver VGA output signal. As with the transmitter IRR, the receiver IRR is defined as

$$\text{IRR}^{\text{RX}} = |b^{\text{RX}}|^{-2}. \quad (3.5)$$

3.2.2 Power amplifier

The output signal of the transmitter IQ mixer $X_{\text{IQ}}(f)$ is amplified by the VGA and the PA of the transmitter because the power of $X_{\text{IQ}}(f)$ is very low for communication with a faraway terminal. Unfortunately, nonlinear distortion of the transmit signal, which is called intermodulation distortion, will occur by nonlinearities of the PA under high transmission power. On time domain, the output signal of the PA is expressed as

$$\begin{aligned} x_{\text{PA}}(t) &= h_{\text{PA}}(\tau) * \left(\sum_{p=1,3,5,\dots}^{\infty} a_p x_{\text{IQ}}(t) |x_{\text{IQ}}(t)|^{p-1} \right) \\ &= h_{\text{PA}}(\tau) * \left(\sum_{p=1,3,5,\dots}^{\infty} \sum_{q=0}^p a_p c_{q,p-q} x^q(t) (x^*(t))^{p-q} \right), \end{aligned} \quad (3.6)$$

$$\begin{aligned} c_{p,q} &= \begin{cases} 0 & ((p < 0) \vee (q < 0)), \\ (b^{\text{TX}})^q & ((p, q) \in \{(1, 0), (0, 1)\}), \\ c'_{p,q} & (\text{otherwise}), \end{cases} \\ c'_{p,q} &= c_{p-1,q-1} \left(1 + |b^{\text{TX}}|^2 \right) + c_{p-2,q} (b^{\text{TX}})^* + c_{p,q-2} b^{\text{TX}} \end{aligned} \quad (3.7)$$

where $h_{\text{PA}}(\tau)$, a_p , and $x_{\text{IQ}}(t)$ are the impulse response of the PA, the gain of the p -th nonlinear distortion, and the time-domain representation of $X_{\text{IQ}}(f)$, respectively. For simplicity, we define the following equations,

$$\Psi_{p,q}(f) = \mathcal{F} \{ \psi_{p,q}(t) \} = \mathcal{F} \{ x^p(t) (x^*(t))^q \}, \quad (3.8)$$

$$\sum_{p,q}^{\mathcal{P}}(\cdot)_{p,q} = \sum_{p=1,3,5,\dots}^{\mathcal{P}} \sum_{q=0}^p(\cdot)_{q,p-q}, \quad (3.9)$$

where $\mathcal{P} \in \mathbb{N}$. Thus, the frequency-domain representation of the PA output signal $X_{\text{PA}}(f)$ can be expressed as

$$X_{\text{PA}}(f) = H_{\text{PA}}(f) \sum_{p,q}^{\infty} a_{p+q} c_{p,q} \Psi_{p,q}(f), \quad (3.10)$$

where $H_{\text{PA}}(f)$ is the frequency-domain representation of $h_{\text{PA}}(\tau)$.

3.2.3 Wireless channel and RF self-interference cancellation

The signal $X_{\text{PA}}(f)$ is radiated from the transmitter antenna, and is received by the receiver antenna of the same terminal as a strong self interference. The received self-interference signal $Y_{\text{ANT}}(f)$ can be expressed as

$$Y_{\text{ANT}}(f) = H_{\text{SI}}(f)X_{\text{PA}}(f) + N_{\text{th}}(f), \quad (3.11)$$

where $H_{\text{SI}}(f)$ is the frequency-response of the self-interference channel, $N_{\text{th}}(f)$ denotes thermal noise. The self-interference channel can be modeled to be a Rician fading channel because the receiver antenna is located close to the transmitter antenna. In [5], it is reported that the Rician factor of the self-interference channel is $20 \text{ dB} < K < 40 \text{ dB}$ when the distance between the transmitter antenna and the receiver antenna is 0.5 meters.

The delay-line RF self-interference canceller is composed of several passive elements such as variable attenuators, phase shifters, and delay lines. Therefore, its characteristic can be modeled as a frequency response $H_{\text{Cir}}(f)$. The signal after the RF self-interference cancellation can be expressed as

$$Y_{\text{AC}}(f) = \{H_{\text{SI}}(f) - H_{\text{Cir}}(f)\} X_{\text{PA}}(f) + N_{\text{th}}(f), \quad (3.12)$$

where the characteristic of $H_{\text{SI}}(f) - H_{\text{Cir}}(f)$ is a strongly frequency-selective channel, because the RF self-interference canceller removes the direct wave and short delay waves of the self-interference signal.

3.2.4 Received self-interference signal

The input signal of the receiver IQ mixer can be expressed as

$$Y_{\text{VGA}}(f) = g_{\text{VGA}}^{\text{RX}} g_{\text{LNA}}^{\text{RX}} (H_{\text{SI}}(f) - H_{\text{Cir}}(f)) X_{\text{PA}}(f) + g_{\text{VGA}}^{\text{RX}} g_{\text{LNA}}^{\text{RX}} N_{\text{th}}(f) + N_{\text{LNA}}(f), \quad (3.13)$$

where $g_{\text{VGA}}^{\text{RX}}$, $g_{\text{LNA}}^{\text{RX}}$, and $N_{\text{LNA}}(f)$ are the gain of the receiver VGA, the gain of the LNA, and the noise generated by the LNA, respectively. Then the receiver IQ mixer downconverts the signal $Y_{\text{VGA}}(f)$ to an analog baseband signal, and the mirror-image signal of $Y_{\text{VGA}}(f)$ occurs as shown in (3.4). Therefore, the received analog baseband self-interference signal $Y(f)$ can be expressed as

$$Y(f) = H(f) \sum_{p,q}^{\infty} a_{p+q} c_{p,q} \Psi_{p,q}(f) + b^{\text{RX}} H^*(-f) \sum_{p,q}^{\infty} a_{p+q}^* c_{p,q}^* \Psi_{p,q}^*(-f) + N(f), \quad (3.14)$$

$$H(f) = g_{\text{VGA}}^{\text{RX}} g_{\text{LNA}}^{\text{RX}} \{H_{\text{SI}}(f) - H_{\text{Cir}}(f)\} H_{\text{PA}}(f), \quad (3.15)$$

$$N(f) = \{g_{\text{VGA}}^{\text{RX}} g_{\text{LNA}}^{\text{RX}} N_{\text{th}}(f) + N_{\text{LNA}}(f)\} + b^{\text{RX}} \{g_{\text{VGA}}^{\text{RX}} g_{\text{LNA}}^{\text{RX}} N_{\text{th}}(-f) + N_{\text{LNA}}(-f)\}^*. \quad (3.16)$$

In addition, by the relation $\Psi_{p,q}(f) = \Psi_{q,p}^*(-f)$, we can rewrite (3.14) as

$$Y(f) = \sum_{p,q}^{\infty} H_{p,q}(f) \Psi_{p,q}(f) + N(f), \quad (3.17)$$

$$H_{p,q}(f) = a_{p+q} c_{p,q} H(f) + a_{p+q}^* b^{\text{RX}} c_{q,p}^* H^*(-f). \quad (3.18)$$

From (3.17), we get an important fact that the received self-interference signal $Y(f)$ is a linear combination of $\Psi_{p,q}(f)$ at each frequency.

3.2.5 Received subcarriers

In the proposed scheme, we use discrete-frequency domain signals which can be generated by CP removal and discrete Fourier transform (DFT). Thus, it is important to check what kind of signal will occur in the discrete-frequency domain.

The nonlinear distortion signal $\psi_{p,q}(t)$ can be expressed as

$$\begin{aligned} \psi_{p,q}(t) = & \sum_{\substack{k_1=-N_{sc}/2 \\ k_1 \neq 0}}^{N_{sc}/2} \sum_{\substack{k_2=-N_{sc}/2 \\ k_2 \neq 0}}^{N_{sc}/2} \cdots \sum_{\substack{k_{p+q}=-N_{sc}/2 \\ k_{p+q} \neq 0}}^{N_{sc}/2} \left\{ \left(\prod_{j=1}^p X_i[k_j] \right) \left(\prod_{j=p+1}^{p+q} X_i^*[k_j] \right) \times \right. \\ & \left. \times \exp \left(j2\pi \Delta f t \left\{ \sum_{j=1}^p k_j - \sum_{j=p+1}^{p+q} k_j \right\} \right) \right\}, \end{aligned} \quad (3.19)$$

and we can simplify it as follows:

$$\psi_{p,q}(t) = \sum_{k=-(p+q)N_{sc}/2}^{(p+q)N_{sc}} \Psi_{p,q,i}[k] e^{j2\pi k \Delta f t} \quad (3.20)$$

where $\Psi_{p,q,i}[k]$ denotes a frequency-domain representation of the nonlinear distortion signal $\psi_{p,q}(t)$. Under an assumption that the self-interference channel and the RF canceller do not generate delay signals beyond CPs, the received analog baseband signal $y(t)$ can be expressed as

$$y(t) = \sum_{k=-\infty}^{\infty} Y_i[k] e^{j2\pi k \Delta f t} \quad (t \in \mathbf{T}_i^S), \quad (3.21)$$

$$Y_i[k] = \sum_{p,q} H_{p,q}[k] \Psi_{p,q,i}[k] + N_i[k], \quad (3.22)$$

$$H_{p,q}[k] = H_{p,q}(k\Delta f) \quad (3.23)$$

where $N_i[k]$ is a narrow-band noise for the k -th subcarrier. In (3.21) and (3.22), it is notable that we can get $Y_i[k]$ by applying the DFT to the received digital baseband signal after removing the CP, and $Y_i[k]$ is a linear combination of $\Psi_{p,q,i}[k]$ at each frequency as with (3.17). Additionally, we can estimate $\mathbb{E} \left[|H_{p,q}[k] \Psi_{p,q,i}[k]|^2 \right]$ by (3.22), and the next section shows how to estimate $\mathbb{E} \left[|H_{p,q}[k] \Psi_{p,q,i}[k]|^2 \right]$.

3.3 Proposed Scheme

This section describes the proposed scheme based on a frequency-domain Hammerstein self-interference canceller [6]. The proposed scheme consists of three stages: premeasurement of power ratio, training of the canceller, and cancellation.

On the premeasurement stage, we estimate the gain of the (p, q) -th nonlinear component to the linear component (GNL) as follows:

$$G_{p,q}^{N/L} = \left| \frac{a_{p+q}c_{p,q}}{a_1} \right|, \quad (3.24)$$

At the beginning of the training stage, the power of $H_{p,q}[k]\Psi_{p,q,i}[k]$ is estimated based on $G_{p,q}^{N/L}[k]$, and we determine whether the (p, q) -th basis function is necessary or not. The computational cost can be reduced by the proposed basis function selection scheme because the number of the basis functions used for training is reduced.

3.3.1 Premeasurement

Since the parameters a_{p+q} and $c_{p,q}$ depend on the RF circuits of the transceiver only, they can be assumed to be very static. Thus, we can measure the GNL by a massive computational resource at the time of design or when the terminal is inactive. In addition, we can use a coaxial cable and an attenuator instead of antennas and the RF cancellation circuit because the GNL does not depend on the frequency response of the self-interference channel and the RF cancellation circuits. Therefore, in this chapter, we use a coaxial cable and an attenuator for loopback measurements. When the test OFDM signal x^{LB} is used to measure the GNL, the received loopback signal can be expressed as

$$Y_i^{\text{LB}}[k] = \sum_{p,q}^{\infty} H_{p,q}^{\text{LB}}[k]\Psi_{p,q,i}^{\text{LB}}[k] + N_i[k], \quad (3.25)$$

$$H_{p,q}^{\text{LB}}[k] = a_{p+q}c_{p,q}H^{\text{LB}}[k] + a_{p+q}^*b^{\text{RX}}c_{q,p}^* \left(H^{\text{LB}}[-k] \right)^* \quad (3.26)$$

where $\Psi_{p,q,i}^{\text{LB}}[k]$ is the frequency-domain representation of the (p, q) -th distorted input signal, and $H_{p,q}^{\text{LB}}[k]$ denotes the loopback frequency response of the transceiver, and $H^{\text{LB}}[k]$ is the frequency response of the coaxial cable and the attenuator, and $N_i[k]$ is the noise signal of the k -th subcarrier. To measure the GNL, we estimate the loopback frequency-response $H_{p,q}^{\text{LB}}[k]$ of the transceiver. At each subcarrier, we solve the least squares problem as follows:

$$\hat{H}_{p,q}^{\text{LB}}[k] = \arg \min_{H_{p,q}^{\text{LB}}[k]} \left| Y_i^{\text{LB}}[k] - \sum_{p,q}^P H_{p,q}^{\text{LB}}[k]\Psi_{p,q,i}^{\text{LB}}[k] \right|^2 \quad (3.27)$$

for $k \in \{-N_{\text{sc}}/2, \dots, -1, 1, \dots, N_{\text{sc}}/2\}$,

where P is the maximum order to estimate distortions. It can be solved by linear least squares algorithm as follows:

$$\begin{aligned}\hat{\mathbf{H}}^{\text{LB}}[k] &= \left[\hat{H}_{p,q}^{\text{LB}}[k] \mid (p, q) \leftarrow \mathcal{I}^P \right]^T \\ &= \left\{ \left(\boldsymbol{\Psi}^{\text{LB}}[k] \right)^H \boldsymbol{\Psi}^{\text{LB}}[k] \right\}^{-1} \left(\boldsymbol{\Psi}^{\text{LB}}[k] \right)^H \mathbf{Y}^{\text{LB}}[k],\end{aligned}\quad (3.28)$$

$$\mathbf{Y}^{\text{LB}}[k] = \left[Y_0^{\text{LB}}[k], Y_1^{\text{LB}}[k], \dots, Y_{N_{\text{LB}}-1}^{\text{LB}}[k] \right]^T, \quad (3.29)$$

$$\boldsymbol{\Psi}^{\text{LB}}[k] = \left[\boldsymbol{\Psi}_0^{\text{LB}}[k], \boldsymbol{\Psi}_1^{\text{LB}}[k], \dots, \boldsymbol{\Psi}_{N_{\text{LB}}-1}^{\text{LB}}[k] \right]^T, \quad (3.30)$$

$$\boldsymbol{\Psi}_i^{\text{LB}}[k] = \left[\Psi_{p,q,i}^{\text{LB}}[k] \mid (p, q) \leftarrow \mathcal{I}^P \right]^T, \quad (3.31)$$

$$\mathcal{I}_p = [(p, 0), (p-1, 1), \dots, (0, p)], \quad (3.32)$$

$$\mathcal{I}^P = [\mathcal{I}_1, \mathcal{I}_2, \dots, \mathcal{I}_P] \quad (3.33)$$

where $[(\cdot)_{p,q} \mid (p, q) \leftarrow \Lambda] = [(\cdot)_{\Lambda[0]}, (\cdot)_{\Lambda[1]}, \dots]$, and N_{LB} is the number of OFDM symbols for the premeasurement.

In (3.18), it is notable that $H_{0,1}[k]$ is a linear combination of $H[k]$ and $H^*[-k]$. In addition, we can estimate the channel response $H[k]$ by $H_{1,0}[k] \approx a_1 c_{1,0} H[k]$ because $|c_{1,0}| \gg |b^{\text{RX}} c_{0,1}|$ when $|b^{\text{TX}}| \ll 1$ and $|b^{\text{RX}}| \ll 1$. Thus, we can rewrite $H_{0,1}^{\text{LB}}[k]$ as follows:

$$H_{0,1}^{\text{LB}}[k] \approx b^{\text{TX}} H_{1,0}^{\text{LB}}[k] + b^{\text{RX}} \left(H_{1,0}^{\text{LB}}[-k] \right)^*. \quad (3.34)$$

b^{TX} and b^{RX} can be estimated by following least squares algorithm:

$$\underbrace{\begin{bmatrix} \hat{H}_{0,1}^{\text{LB}}[1] \\ \hat{H}_{0,1}^{\text{LB}}[2] \\ \vdots \\ \hat{H}_{0,1}^{\text{LB}}[N_{\text{sc}}/2] \end{bmatrix}}_{\mathbf{H}_{0,1}} \approx \underbrace{\begin{bmatrix} \hat{H}_{1,0}^{\text{LB}}[1] & \left(\hat{H}_{1,0}^{\text{LB}}[-1] \right)^* \\ \hat{H}_{1,0}^{\text{LB}}[2] & \left(\hat{H}_{1,0}^{\text{LB}}[-2] \right)^* \\ \vdots & \vdots \\ \hat{H}_{1,0}^{\text{LB}}[N_{\text{sc}}/2] & \left(\hat{H}_{1,0}^{\text{LB}}[-N_{\text{sc}}/2] \right)^* \end{bmatrix}}_{\mathcal{H}} \begin{bmatrix} b^{\text{TX}} \\ b^{\text{RX}} \end{bmatrix}, \quad (3.35)$$

$$\begin{bmatrix} \hat{b}^{\text{TX}} \\ \hat{b}^{\text{RX}} \end{bmatrix} = \left(\mathcal{H}^H \mathcal{H} \right)^{-1} \mathcal{H}^H \mathbf{H}_{0,1}. \quad (3.36)$$

The receiver IQ imbalance interferes with estimation of the GNL because the GNL is a parameter of the transmitter. Thus, it is necessary to relax the receiver IQ

imbalance, and is achieved by the following operation:

$$\hat{H}_{p,q}^{\text{IQF}}[k] = \frac{\hat{H}_{p,q}^{\text{LB}}[k] - \hat{b}^{\text{RX}} \left(\hat{H}_{q,p}^{\text{LB}}[-k] \right)^*}{1 - |\hat{b}^{\text{RX}}|^2}. \quad (3.37)$$

When $\hat{H}_{p,q}^{\text{LB}}[k]$ and \hat{b}^{RX} are sufficiently close to the true values, (3.37) can be approximated as follows:

$$\begin{aligned} \hat{H}_{p,q}^{\text{IQF}}[k] &\approx \frac{H_{p,q}^{\text{LB}}[k] - b^{\text{RX}} \left(H_{q,p}^{\text{LB}}[-k] \right)^*}{1 - |b^{\text{RX}}|^2} \\ &= \frac{a_{p+q} c_{p,q} H^{\text{LB}}[k] - a_{p+q} |b^{\text{RX}}|^2 c_{p,q} H^{\text{LB}}[k]}{1 - |b^{\text{RX}}|^2} \\ &= a_{p+q} c_{p,q} H^{\text{LB}}[k]. \end{aligned} \quad (3.38)$$

Thus, we can estimate the GNL as follows:

$$\hat{G}_{p,q}^{\text{N/L}} = \sqrt{\frac{1}{N_{\text{sc}}} \sum_{\substack{k=-N_{\text{sc}}/2 \\ k \neq 0}}^{N_{\text{sc}}/2} \frac{|\hat{H}_{p,q}^{\text{IQF}}[k]|^2}{|\hat{H}_{1,0}^{\text{IQF}}[k]|^2}}. \quad (3.39)$$

When $\hat{H}_{p,q}^{\text{LB}}[k]$ and \hat{b}^{RX} sufficiently are close to the true values, the estimated GNL can be approximated to the true value of the GNL as follows:

$$\begin{aligned} \hat{G}_{p,q}^{\text{N/L}} &\approx \sqrt{\frac{1}{N_{\text{sc}}} \sum_{\substack{k=-N_{\text{sc}}/2 \\ k \neq 0}}^{N_{\text{sc}}/2} \frac{|a_{p+q} c_{p,q} H^{\text{LB}}[k]|^2}{|a_1 H^{\text{LB}}[k]|^2}} \\ &= \sqrt{\frac{1}{N_{\text{sc}}} \sum_{\substack{k=-N_{\text{sc}}/2 \\ k \neq 0}}^{N_{\text{sc}}/2} \left(G_{p,q}^{\text{N/L}} \right)^2} = G_{p,q}^{\text{N/L}}. \end{aligned} \quad (3.40)$$

3.3.2 Training

On the training stage, the swapped OFDM modulation, which is introduced in [6], is needed to estimate $H_{p,q}[k]$ out of the band when the symbol timing of the desired signal and the self-interference signal are not synchronized. When the symbol synchronization is achieved, we can use pure OFDM symbols instead of swapped OFDM symbols. In the rest of this chapter, we assume unsynchronized

situations. The difference between synchronized and unsynchronized situations is whether the swapped OFDM modulation is used instead of pure OFDM modulation and the subcarriers used for the channel estimation. In particular, in synchronized situations, we use pure OFDM symbols and estimate the self-interference channel at $k \in \{-N_{\text{sc}}/2, \dots, -1, 1, \dots, N_{\text{sc}}/2\}$, and in unsynchronized situations, we use the swapped OFDM symbols and estimate the channel at $k \in \{-N_{\text{fft}}/2, \dots, -1, 1, \dots, N_{\text{fft}}/2\}$ where N_{fft} is the FFT size of the OFDM modulation. By the swapped OFDM modulation, subcarriers $X_i[k]$ is modulated to a digital baseband signal $x_i^{\text{swp}}[n]$ as follows:

$$x_i[n] = \sum_{\substack{k=-N_{\text{sc}}/2 \\ k \neq 0}}^{N_{\text{sc}}/2} X_i[k] e^{j2\pi kn/N_{\text{fft}}} \quad (n \in [0, N_{\text{fft}})), \quad (3.41)$$

$$x_{2i}^{\text{swp}} = [x_{2i+1}[0], \dots, x_{2i+1}[N_{\text{fft}}/2 - 1], \quad (3.42)$$

$$x_{2i}[N_{\text{fft}}/2], \dots, x_{2i}[N_{\text{fft}} - 1]],$$

$$x_{2i+1}^{\text{swp}} = [x_{2i}[0], \dots, x_{2i}[N_{\text{fft}}/2 - 1], \quad (3.43)$$

$$x_{2i+1}[N_{\text{fft}}/2], \dots, x_{2i+1}[N_{\text{fft}} - 1]].$$

Then the received subcarrier signal $Y_i^{\text{swp}}[k]$ can be expressed as

$$Y_i^{\text{swp}}[k] = \sum_{p,q}^{\infty} H_{p,q}[k] \Psi_{p,q,i}^{\text{swp}}[k] + N_i[k], \quad (3.44)$$

$$\Psi_{p,q,i}^{\text{swp}}[k] = \sum_{n=0}^{N_{\text{fft}}-1} (x_i^{\text{swp}}[n])^p (x_i^{\text{swp}}[n])^q e^{-j2\pi \frac{kn}{N_{\text{fft}}}}, \quad (3.45)$$

where $\Psi_{p,q,i}^{\text{swp}}[k]$ is the distorted swapped OFDM modulated signal, and $N_i[k]$ denotes a noise signal. Before training the canceller parameters, we determine which basis function to use for cancellation at each discrete frequency as follows:

$$U_{p,q}[k] = \left(\gamma \mathbb{E} \left[|H_{p,q}[k] \Psi_{p,q,i}^{\text{swp}}[k]|^2 \right] > \mathbb{E} [|N_i[k]|^2] \right), \quad (3.46)$$

where $U_{p,q}[k]$ denotes whether to use the (p, q) -th basis function at the k -th subcarrier, $\mathbb{E} [|(\cdot)_i|^2]$ denotes the expected power of (\cdot) for i , and γ is called the noise margin. In (3.46), we can control the trade-off between computational

cost and accuracy of the self-interference cancellation by the noise margin γ . $\mathbb{E} \left[\left| H_{p,q}[k] \Psi_{p,q,i}^{\text{swp}}[k] \right|^2 \right]$ cannot estimate directly because we do not know the channel information $H_{p,q}[k]$. So $\mathbb{E} \left[\left| H_{p,q}[k] \Psi_{p,q,i}^{\text{swp}}[k] \right|^2 \right]$ is approximated as follows:

$$\mathbb{E} \left[\left| H_{p,q}[k] \Psi_{p,q,i}^{\text{swp}}[k] \right|^2 \right] \leq P_{p,q}^{(1)}[k] + P_{p,q}^{(2)}[k] + 2\sqrt{P_{p,q}^{(1)}[k]P_{p,q}^{(2)}[k]}, \quad (3.47)$$

$$\begin{aligned} P_{p,q}^{(1)}[k] &= \mathbb{E} \left[\left| a_{p+q} c_{p,q} H[k] \Psi_{p,q,i}^{\text{swp}}[k] \right|^2 \right] \\ &= \left(G_{p,q}^{N/L} \right)^2 R_{p,q}[k] \mathbb{E} \left[\left| a_1 H[k] \Psi_{1,0,i}^{\text{swp}}[k] \right|^2 \right], \end{aligned} \quad (3.48)$$

$$\begin{aligned} P_{p,q}^{(2)}[k] &= \mathbb{E} \left[\left| a_{p+q}^* b^{\text{RX}} c_{q,p}^* H^*[-k] \Psi_{p,q,i}^{\text{swp}}[k] \right|^2 \right] \\ &= \mathbb{E} \left[\left| a_{p+q}^* b^{\text{RX}} c_{q,p}^* H^*[-k] \left(\Psi_{q,p,i}^{\text{swp}}[-k] \right)^* \right|^2 \right] \\ &= \left| b^{\text{RX}} \right|^2 P_{q,p}^{(1)}[-k], \end{aligned} \quad (3.49)$$

$$R_{p,q}[k] = \frac{\mathbb{E} \left[\left| \Psi_{p,q,i}^{\text{swp}}[k] \right|^2 \right]}{\mathbb{E} \left[\left| \Psi_{1,0,i}^{\text{swp}}[k] \right|^2 \right]}. \quad (3.50)$$

In the derivation of (3.47), we have used the following triangle inequality:

$$|x + y|^2 \leq |x|^2 + |y|^2 + 2|x||y|. \quad (3.51)$$

Also, we can derive the following inequality:

$$\begin{aligned} \mathbb{E} \left[\left| a_1 H[k] \Psi_{1,0,i}^{\text{swp}}[k] \right|^2 \right] &\leq \mathbb{E} \left[\left| Y_{\text{VGA},i}^{\text{swp}}[k] \right|^2 \right] \\ &= \mathbb{E} \left[\left| \frac{Y_i^{\text{swp}}[k] - b^{\text{RX}} (Y_i^{\text{swp}}[-k])^*}{1 - |b^{\text{RX}}|^2} \right|^2 \right] \\ &\leq P_L[k]. \end{aligned} \quad (3.52)$$

where

$$P_L[k] = \left| 1 - |b^{\text{RX}}|^2 \right|^{-2} \left\{ \mathbb{E} \left[|Y_i^{\text{swp}}[k]|^2 \right] + |b^{\text{RX}}|^2 \mathbb{E} \left[|Y_i^{\text{swp}}[-k]|^2 \right] \right. \\ \left. + 2 |b^{\text{RX}}| \sqrt{\mathbb{E} \left[|Y_i^{\text{swp}}[k]|^2 \right] \mathbb{E} \left[|Y_i^{\text{swp}}[-k]|^2 \right]} \right\}. \quad (3.53)$$

Detailed derivation of (3.52) and (3.53) is described in Appendix 3.A. Then, we make (3.48) easier by the relation of (3.52) as follows:

$$P_{p,q}^{(1)}[k] \leq \left(G_{p,q}^{\text{N/L}} \right)^2 R_{p,q}[k] P_L[k], \quad (3.54)$$

Actually, we use (3.55) instead of $\mathbb{E} \left[|Y_i^{\text{swp}}[k]|^2 \right]$ for the basis functions selection because we do not know the true expected spectral density of the received self-interference signal. Using N_{EP} symbols for estimation received signal power spectral density, we estimate $\mathbb{E} \left[|Y_i^{\text{swp}}[k]|^2 \right]$ by

$$\mathbb{E} \left[|Y_i^{\text{swp}}[k]|^2 \right] \approx \tilde{P}_Y[k] = \frac{1}{N_{\text{EP}}} \sum_{i=0}^{N_{\text{EP}}-1} |Y_i^{\text{swp}}[k]|^2. \quad (3.55)$$

In the proposed scheme, we do not estimate and use $|b^{\text{RX}}|$ to estimate (3.49) while we can easily estimate $|b^{\text{RX}}|$ just like $G_{p,q}^{\text{N/L}}$. The reason for this decision is that (3.47) and (3.53) are very sensitive to $|b^{\text{RX}}|$ on frequency-selective self-interference channels after analog cancellation. In other word, the behavior of (3.47) and (3.53) greatly changes depending on whether or not $P_{p,q}^{(1)}[k] \approx |b^{\text{RX}}|^2 P_{q,p}^{(1)}[-k]$ and $\mathbb{E} \left[|Y_i^{\text{swp}}[k]|^2 \right] \approx |b^{\text{RX}}|^2 \mathbb{E} \left[|Y_i^{\text{swp}}[-k]|^2 \right]$ are satisfied respectively, and it may lead to deterioration of cancellation performance. To solve this problem, we introduce β as a tuning parameter instead of $|b^{\text{RX}}|$. By setting β to be greater than $|b^{\text{RX}}|$, we can avoid deterioration while computational cost increases.

To summarize the above, we can determine which basis functions to use for

self-interference channel estimation by (3.56)–(3.58),

$$\mathcal{J}[k] = \left[(p, q) \mid \gamma \tilde{P}_{p,q}[k] > \tilde{P}_N, (p, q) \leftarrow \mathcal{I}^P \right] \quad (3.56)$$

$$\begin{aligned} \tilde{P}_{p,q}[k] &= \left(G_{p,q}^{\text{N/L}} \right)^2 R_{p,q}[k] \tilde{P}_L[k] + \beta^2 \left(G_{q,p}^{\text{N/L}} \right)^2 R_{q,p}[-k] \tilde{P}_L[-k] \\ &\quad + \beta G_{p,q}^{\text{N/L}} G_{q,p}^{\text{N/L}} \sqrt{R_{p,q}[k] R_{q,p}[-k] \tilde{P}_L[k] \tilde{P}_L[-k]}, \end{aligned} \quad (3.57)$$

$$\tilde{P}_L[k] = \frac{\tilde{P}_Y[k] + \beta^2 \tilde{P}_Y[-k] + 2\beta \sqrt{\tilde{P}_Y[k] \tilde{P}_Y[-k]}}{|1 - \beta^2|^2}. \quad (3.58)$$

where $\mathcal{J}[k]$ indicates the set of selected basis functions for each subcarrier, and \tilde{P}_N is the estimated expected power of the additive white Gaussian noise $N_i[k]$.

Then, we estimate the self-interference channel $H_{p,q}[k]$ independently at each subcarrier to reconstruct the self interference. Since it can be expected that the power of the basis function not included in $\mathcal{J}[k]$ is smaller than the noise, the received training signal can be represented by a linear combination of the basis function constituting $\mathcal{J}[k]$ as

$$Y_i^{\text{swp}}[k] = \sum_{(p,q) \in \mathcal{J}[k]} H_{p,q}[k] \Psi_{p,q,i}^{\text{swp}}[k] + N'[k], \quad (3.59)$$

where $N'[k]$ is the sum of the received noise and the nonlinear components determined to be unnecessary for self-interference channel estimation.

Thus, the transmit symbol vector and the channel vector can be defined as (3.60) and (3.61), respectively.

$$\boldsymbol{\Psi}_i^{\text{swp}}[k] = \left[\Psi_{p,q,i}^{\text{swp}}[k] \mid (p, q) \leftarrow \mathcal{J}[k] \right]^T, \quad (3.60)$$

$$\mathbf{H}[k] = \left[H_{p,q}[k] \mid (p, q) \leftarrow \mathcal{J}[k] \right]^T. \quad (3.61)$$

The channel response $\mathbf{H}[k]$ can be estimated by well-known estimation algorithms such as least squares (LS) algorithms, recursive least squares (RLS) algorithms, and normalized least mean squares (NLMS) algorithms.

Least squares algorithm

To apply the LS algorithm to estimate $\mathbf{H}[k]$, we introduce the received symbol vector and the transmit symbol matrix as (3.62) and (3.63), respectively.

$$\begin{aligned}\mathbf{Y}^{\text{swp}}[k] &= \left[Y_0^{\text{swp}}[k] \ Y_1^{\text{swp}}[k] \ \cdots \ Y_{N_{\text{tr}}-1}^{\text{swp}}[k] \right]^T \\ &= \mathbf{\Psi}^{\text{swp}}[k] \mathbf{H}[k] + \mathbf{N}[k]\end{aligned}\quad (3.62)$$

$$\mathbf{\Psi}^{\text{swp}}[k] = \left[\mathbf{\Psi}_0^{\text{swp}}[k] \ \mathbf{\Psi}_1^{\text{swp}}[k] \ \cdots \ \mathbf{\Psi}_{N_{\text{tr}}-1}^{\text{swp}}[k] \right]^T \quad (3.63)$$

$$\mathbf{N}[k] = \left[N'_0[k] \ N'_1[k] \ \cdots \ N'_{N_{\text{tr}}-1}[k] \right]^T \quad (3.64)$$

Now, we get the least squares estimated channel $\widehat{H}_{p,q}[k]$ of (3.62) as

$$\begin{aligned}\widehat{\mathbf{H}}[k] &= \left[\widehat{H}_{p,q}[k] \mid (p, q) \leftarrow \mathcal{J}[k] \right]^T \\ &= \left\{ (\mathbf{\Psi}^{\text{swp}}[k])^H \ \mathbf{\Psi}^{\text{swp}}[k] \right\}^{-1} (\mathbf{\Psi}^{\text{swp}}[k])^H \ \mathbf{Y}^{\text{swp}}[k].\end{aligned}\quad (3.65)$$

Recursive least squares algorithm

Since the least squares method requires matrix inversion or singular value decomposition (SVD), it may be too complicated to actually implement. On the other hand, the RLS algorithm can recursively estimate the self-interference channel which minimizes least square errors without matrix inversion and SVD. On the proposed scheme, the RLS algorithm is expressed as

$$\widehat{\mathbf{H}}_i[k] = \widehat{\mathbf{H}}_{i-1}[k] + E_i[k] \mathbf{G}_i[k], \quad (3.66)$$

$$E_i[k] = Y_i[k] - (\mathbf{\Psi}_i^{\text{swp}}[k])^T \widehat{\mathbf{H}}_{i-1}[k], \quad (3.67)$$

$$\mathbf{G}_i[k] = \frac{\mathbf{P}_{i-1}[k] (\mathbf{\Psi}_i^{\text{swp}}[k])^*}{\lambda + (\mathbf{\Psi}_i^{\text{swp}}[k])^T \mathbf{P}_{i-1}[k] (\mathbf{\Psi}_i^{\text{swp}}[k])^*}, \quad (3.68)$$

$$\mathbf{P}_i[k] = \lambda^{-1} \left\{ \mathbf{P}_{i-1}[k] - \mathbf{G}_i[k] (\mathbf{\Psi}_i^{\text{swp}}[k])^T \mathbf{P}_{i-1}[k] \right\}, \quad (3.69)$$

where $\widehat{\mathbf{H}}_i[k]$ is the k -th estimated frequency response on the i -th iteration, and λ is called forgetting factor. At the beginning of RLS algorithm, $\widehat{\mathbf{H}}_i[k]$ and $\mathbf{P}_i[k]$ are initialized to 0 and $\delta^{-1} \mathbf{I}$ where δ is very small positive value. The total number of multiplications of complex value for computing (3.66)–(3.69) on each discrete frequency is $4|\mathcal{J}[k]|^2 + 4|\mathcal{J}[k]|$, where $|\mathcal{J}[k]|$ is the number of elements constituting

$\mathcal{J}[k]$.

Normalized least mean squares algorithm

The NLMS algorithm, which has a much lower computational cost, is often used when the computational cost of the RLS algorithm produces problems such as processing speed. In the proposed scheme, the NLMS algorithm is expressed as

$$\widehat{\mathbf{H}}_i[k] = \widehat{\mathbf{H}}_{i-1}[k] + \frac{\mu}{Q_i[k]} E_i[k] (\boldsymbol{\Psi}_i^{\text{swp}}[k])^*, \quad (3.70)$$

$$Q_i[k] = (\boldsymbol{\Psi}_i^{\text{swp}}[k])^H (\boldsymbol{\Psi}_i^{\text{swp}}[k]), \quad (3.71)$$

$$E_i[k] = Y_i[k] - (\boldsymbol{\Psi}_i^{\text{swp}}[k])^T \widehat{\mathbf{H}}_{i-1}[k], \quad (3.72)$$

where μ is positive constant values. The total number of multiplications of complex values for computing (3.70)–(3.72) is $2|\mathcal{J}[k]|$, and it is at least N times faster than the time-domain NLMS algorithm, where N is the number of taps of a time-domain FIR filter.

Computational cost of the training stage

At the beginning of the training stage, the set of the basis functions $\mathcal{J}[k]$ is determined on each discrete frequency by (3.55)–(3.58). In (3.55)–(3.58), the most complicated computation is the square root, which must be computed twice at each discrete frequency. Since it is only necessary once at the beginning of the training stage, the computational cost of (3.55)–(3.58) is sufficiently smaller than channel estimation which processes for each symbol.

In the channel estimation process of the proposed scheme, received OFDM symbols are decomposed to discrete-frequency components by FFT to get (3.59), and it requires $\frac{1}{2}N_{\text{fft}} \log_2 N_{\text{fft}}$ times multiplications of two complex numbers per symbol. In this chapter, we assume $(x[n])^p(x^*[n])^q$ can be computed a priori and implemented by a lookup table. Then, the transmitted symbols are distorted by $(x[n])^p(x^*[n])^q$ and also decomposed to discrete-frequency components by FFT. The total computational cost of transforming symbols to the frequency domain is $\frac{1}{4}(|\mathcal{I}^P| + 2)N_{\text{fft}} \log_2 N_{\text{fft}}$ per symbol because FFT $\{(x[n])^q(x^*[n])^p\}$ can be computed by frequency-inversion and conjugation of FFT $\{(x[n])^p(x^*[n])^q\}$. Next, the self-interference channel $H_{p,q}[k]$ is estimated by estimation algorithms based on $\mathcal{J}[k]$. The NLMS algorithm and the RLS algorithm require $2|\mathcal{J}[k]|$ and $4|\mathcal{J}[k]|^2 + 4|\mathcal{J}[k]|$

complex multiplications per discrete frequency per symbol, respectively. Thus, the whole computational cost of the channel estimation process is

$$\frac{\frac{1}{4} \left(|\mathcal{I}^P| + 2 \right) N_{\text{fft}} \log_2 N_{\text{fft}} + \sum_{k=-N_{\text{fft}}/2}^{N_{\text{fft}}/2} A[k]}{N_{\text{fft}} + N_{\text{cp}}} \text{ per sample,}$$

where $A[k]$ is $2 |\mathcal{J}[k]|$ (for NLMS case) or $4 |\mathcal{J}[k]|^2 + 4 |\mathcal{J}[k]|$ (for RLS case).

3.3.3 Self-interference reconstruction

After the training period, we reconstruct the received self interference from the transmit signal and channel information. We apply cancellation on the time domain because performance of the frequency-domain cancellation is degraded by the symbol timing offset. To reduce the computational cost of the time-domain reconstruction, the overlap-save algorithm [7] is used to reconstruct the received self interference, like [6]. By the overlap-save algorithm, the received self interference can be reconstructed as

$$y_{\text{rg}}[mN_{\text{OLS}} + l] = \text{IFFT} \{Y'_m\} [N_{\text{cp}} + l], \quad (3.73)$$

where

$$Y'_m[k] = \sum_{(p,q) \in \mathcal{J}[k]} \widehat{H}_{p,q}[k] \Psi'_{p,q,m}[k], \quad (3.74)$$

$$\Psi'_{p,q,m}[k] = \text{FFT} \left\{ \psi_{p,q}[mN_{\text{OLS}} - N_{\text{cp}}], \dots, \right. \quad (3.75)$$

$$\left. \psi_{p,q}[(m+1)N_{\text{OLS}} - 1] \right\} [k],$$

$$\psi_{p,q}[n] = (x[n])^p (x^*[n])^q, \quad (3.76)$$

and $N_{\text{OLS}} = N_{\text{fft}} - N_{\text{cp}}$, $l \in [0, N_{\text{OLS}})$, and $x[n]$ is the transmit baseband signal. In addition, $\text{FFT} \{ \cdot \}$ and $\text{IFFT} \{ \cdot \}$ are fast fourier transform operations with an N_{fft} -size signal. Then, we can get the digital self-interference canceled signal $y_{\text{DC}}[n]$ by subtracting the reconstructed signal $y_{\text{rg}}[n]$ from received signal $y[n]$.

$$y_{\text{DC}}[n] = y[n] - y_{\text{rg}}[n] \quad (3.77)$$

Table 3.1: Simulation Specifications

Parameter	Value
Oversampling rate	4
Modulation	OFDM
Constellation	16QAM
Size of FFT N_{fft}	256
# of subcarriers	52
Cyclic prefix N_{cp}	64 samples
Sampling rate	80M samples/sec
Transmit data	Uniform-random data
SI channel after RF-SIC	Rayleigh fading
SI channel length	64 taps
Transmit power	23 dBm
IRR	25 dB
PA IIP3	21.8 dBm based on [8]
PA Gain	28.5 dB based on [8]
PA smoothness factor, S_{PA}	1
LNA IIP3	-3 dBm based on [9]
LNA smoothness factor, S_{LNA}	1, 3
Noise figure of receiver	4 dB
# of ADC bits	14 bits
Highest order of basis function P	3
# of symbols for (3.55), N_{EP}	2
λ of the RLS	1
δ of the RLS	3×10^{-3} for time-domain 3×10^{-7} for freq.-domain
μ of the NLMS	0.2 for time-domain 0.8 for freq.-domain
# of taps for time-domain scheme	64
Trials	101

3.4 Numerical Simulations

In this section, the author provides numerical simulation results to verify the proposed scheme. To show the effectiveness of the proposed scheme, we compare the performance of the proposed scheme with a conventional scheme.

3.4.1 Simulation environment

To verify the proposed scheme, equivalent baseband simulations of the full-duplex transceiver shown in Fig. 3.1 is performed. The baseband signal simulator is implemented with the D programming language, where each non-ideality is modeled with realistic behaviors. In this simulation, we set parameters to the values in Table 3.1, which are based on [1]. Since the dynamic range of the receiver ADC is about 79 dB under these simulation parameters [10], the largest barrier to self-interference cancellation is nonlinear distortions of IQ mixers and the PA. The PA nonlinearities are realized by the Rapp model [11, 12], which is often used to simulate class AB solid state power amplifiers. The output baseband signal of the Rapp modeled PA is described as

$$y = G_{\text{PA}} \Gamma(|x|) \frac{x}{|x|}, \quad (3.78)$$

$$\Gamma(|x|) = |x| \left(1 + \left(\frac{|x|}{V_{\text{sat}}} \right)^{2S_{\text{PA}}} \right)^{-\frac{1}{2S_{\text{PA}}}}, \quad (3.79)$$

where x and y are the input and output signals of the PA, respectively. The Rapp model is characterized by the smoothness factor S_{PA} , the saturation voltage V_{sat} , and the gain G_{PA} . In this chapter, we uses $S_{\text{PA}} = 1$ because we assume there are no linearization techniques of the PA on the transceiver, and the other parameters are set according to the IIP3 and the gain in Table 3.1. In addition, we simulates the nonlinearities of the LNA by the Rapp model with smoothness factor $S_{\text{LNA}} \in \{1, 3\}$ and IIP = -3dBm. The case of $S = 1$ assume stronger nonlinearities than the case of $S_{\text{LNA}} = 3$.

The simulation model of IQ mixers has IQ imbalance achieved by adding an image signal, and its coefficients are predetermined based on the value of IRR. The parameters of both the RLS algorithm and the NLMS algorithm are set to the optimal coefficient which can achieve the best steady-state cancellation performance in each canceller. This condition ensures that the simulation results show the true performance of each canceller. Following the standard convention in literature, the self-interference cancellation ratio (SICR) is defined as

$$\text{SICR} = \frac{\mathbb{E} [|y[n]|^2]}{\mathbb{E} [|y_{\text{DC}}[n]|^2]}. \quad (3.80)$$

Additionally, we define the self interference to noise power ratio (INR) as

$$\text{INR} = \frac{\mathbb{E} [|y[n] - z[n]|^2]}{\mathbb{E} [|z[n]|^2]}, \quad (3.81)$$

where $z[n]$ is the received total noise on the digital baseband. Each simulation result shows the median value of 100 trials. In addition, the author calculates the complex multiplication operations per sample (CMOPS), which indicates the number of complex multiplications to process one sample, as the computational cost. For example, the CMOPS of the time-domain Hammerstein canceller optimized by the RLS algorithm with 64-taps FIR filters and six basis functions such as $\{x, x^*, (x)^3, x|x|^2, x^*|x|^2, (x^*)^3\}$ is

$$\begin{aligned} \text{CMOPS}_{\text{PH-RLS}} &= 4 \times (6 \times 64)^2 + 4 \times (6 \times 64) \\ &\approx 5.91 \times 10^5 \end{aligned} \quad (3.82)$$

because they update 6×64 coefficients by the RLS algorithm on each sample. In the same way, the CMOPS of the time-domain Hammerstein canceller optimized by the NLMS algorithm is

$$\text{CMOPS}_{\text{PH-NLMS}} = 2 \times (6 \times 64) = 768. \quad (3.83)$$

3.4.2 Results and discussion

Fig. 3.2 shows the median cancellation performance of all trials with different β and γ under IRR of 25 dB and INR of 50 dB. In addition, Fig. 3.3 shows the ratio of all trials to the trial where the proposed scheme achieves a SICR of less than 47 dB on the same situation as Fig. 3.2. In this scenario, we use the RLS algorithm as a estimation algorithm, and Fig. 3.4 shows the CMOPS of the proposed scheme at the training stage. In addition, the number of the training symbols N_{swp} is 60 to train the canceller completely. Looking at (3.56)–(3.58), it is easy to see that increasing the noise margin γ increases the number of elements of $\mathcal{J}[k]$. It involves higher cancellation performance and higher computational cost, which can be confirmed from Fig. 3.2 and Fig. 3.3. Additionally, it is shown that cancellation performance is increased if the image margin β is increased. The reason is that the estimated power of the (p, q) -th basis function is increased with image margin β , and then the

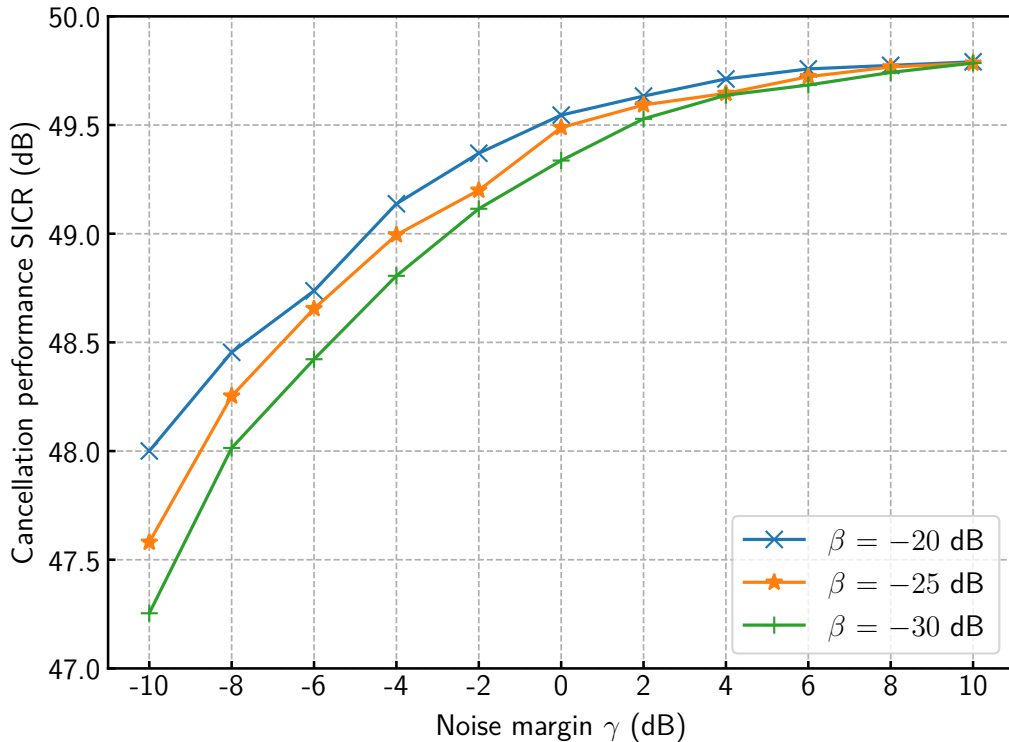


Figure 3.2: The median SICR of the proposed scheme at $-10 \text{ dB} \leq \gamma \leq 10 \text{ dB}$ with $\text{INR} = 50 \text{ dB}$. The RLS algorithm is used as the training algorithm. The smoothness factor of the LNA is $S_{\text{LNA}} = 3$.

set of basis functions for training $\mathcal{J}[k]$ becomes larger with increasing β as shown in (3.56)–(3.58). In the following simulations, we use $\beta = -20 \text{ dB}$ and $\gamma = 2 \text{ dB}$ because the proposed scheme with these parameters does not once achieve a SICR of less than 47 dB in all trials as we can see in Fig. 3.3.

In Fig. 3.5, the median cancellation performance of all trials on each canceller with the LS algorithm is shown at $N_{\text{tr}} = 60$ and $S_{\text{LNA}} = 3$. The time-domain linear canceller, which is implemented based on [1] without the conjugated term x^* , cannot reconstruct the nonlinear self-interference signal. Hence the cancellation performance of the linear canceller is saturated at about 22 dB. For a similar reason, the cancellation performance of the widely linear canceller [1], which can reconstruct both the linear term x and the conjugated term x^* only, is saturated at about 45 dB. In contrast, the nonlinear cancellers such as the augmented nonlinear canceller [13], the frequency-domain Hammerstein canceller [6], and the proposed scheme achieved an SICR of about 50 dB at INR of 50 dB. Hence, by the proposed

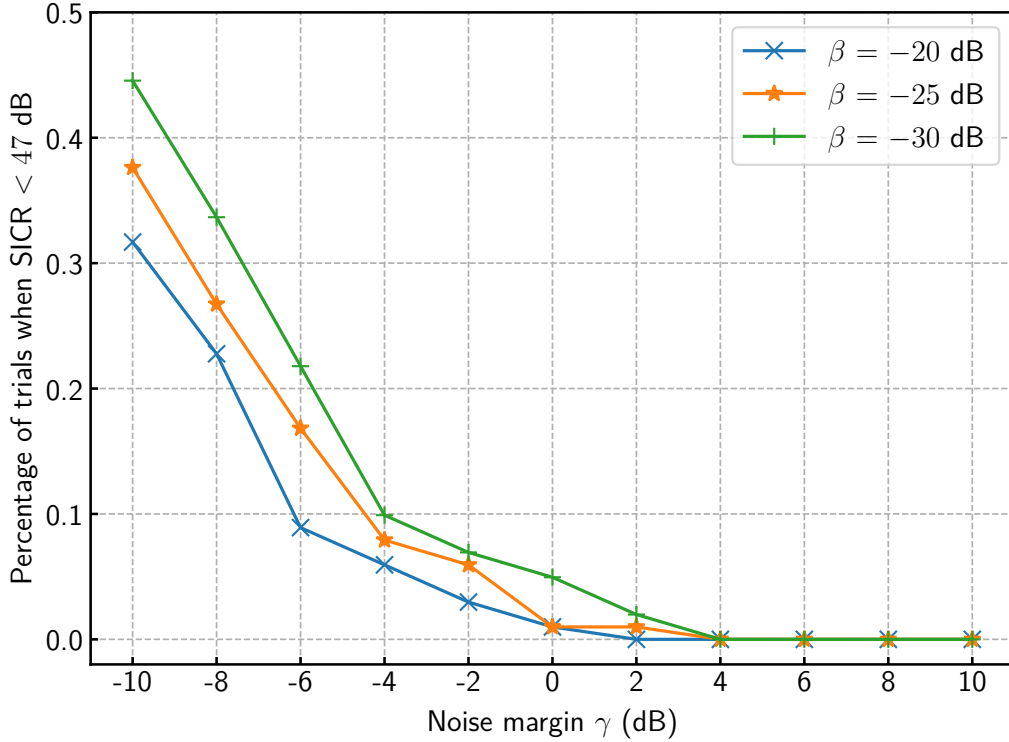


Figure 3.3: The percentage of trails where the SICR of the proposed scheme is lower than 47 dB in all trials at $-10 \text{ dB} \leq \gamma \leq 10 \text{ dB}$ with $\text{INR} = 50 \text{ dB}$. The RLS algorithm is used as the training algorithm. The smoothness factor of the LNA is $S_{\text{LNA}} = 3$.

basis function selection technique, the self-interference cancellation performance of the frequency-domain Hammerstein canceller hardly decreases.

In Fig. 3.6, the median cancellation performance of all trials on each canceller with the LS algorithm is shown at $N_{\text{tr}} = 60$ and $S_{\text{LNA}} = 1$. In this situation, we simulate the LNA as a highly nonlinear component like the PA of the transmitter. Even when $S_{\text{LNA}} = 1$, we can confirm that the proposed method achieves the same cancellation performance as a conventional time-domain canceller. Thus, cancellation performance is not degraded by the proposed selection technique even if nonlinearity of the LNA appears strongly. When $\text{INR} > 53 \text{ dB}$, the cancellation performance of all cancellers simulated in this chapter degrades because they cannot remove nonlinear signals generated by the LNA. The slope of the degradation is -2 [SICR dB / INR dB] because we can write the SICR with a strong nonlinear

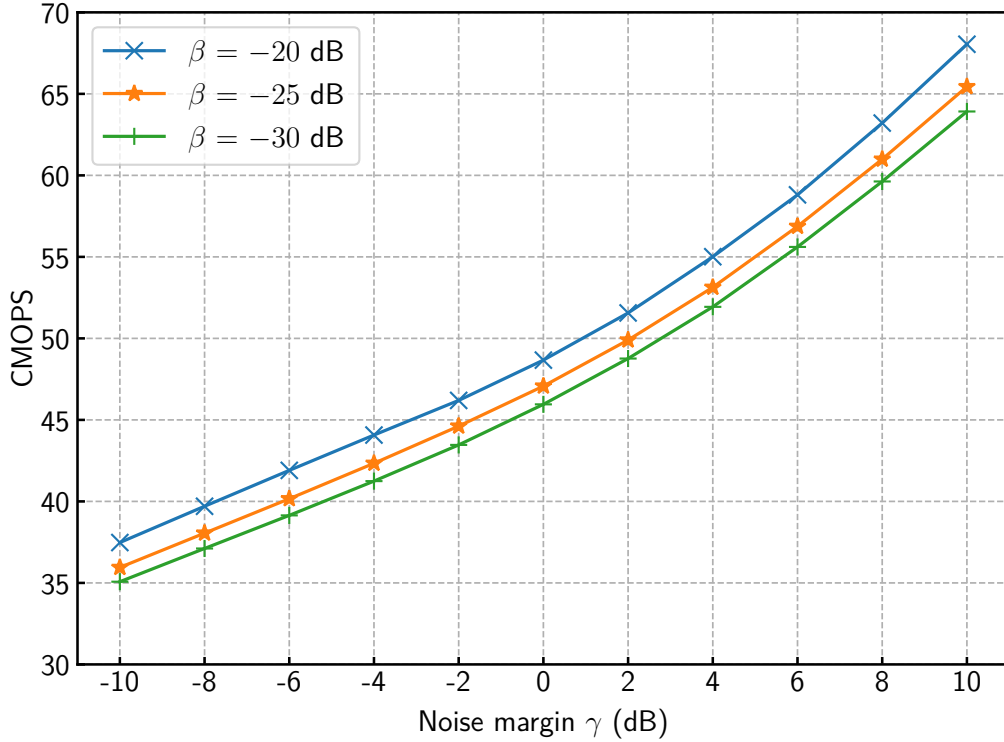


Figure 3.4: The computational cost of the proposed scheme at $-10 \text{ dB} \leq \gamma \leq 10 \text{ dB}$ with $\text{INR} = 50 \text{ dB}$. The RLS algorithm is used as the training algorithm. The smoothness factor of the LNA is $S_{\text{LNA}} = 3$.

signal $d_{\text{LNA}}[n]$ generated by the LNA as

$$\text{SICR} \approx \frac{\mathbb{E} [|y[n]|^2]}{\mathbb{E} [|z[n] + d_{\text{LNA}}[n]|^2]} = \mathcal{O} \left(\frac{I}{N + I^3} \right) = \mathcal{O} (I^{-2}), \quad (3.84)$$

where I is the power of self-interference signal. There are few papers which consider nonlinearities of the LNA such as [14, 15]. In Chapter 3 the author attacks the nonlinearity of the LNA.

In Fig. 3.7, the convergence performance of each canceller with the LS algorithm is shown at $\text{INR} = 50 \text{ dB}$. In Fig. 3.7, we can find that the proposed technique improves the initial convergence speed of the frequency-domain Hammerstein canceller, and it achieves better cancellation performance than the conventional method when the number of training symbols N_{tr} is less than eight. By removing the basis functions unnecessary for self-interference cancellation by the proposed

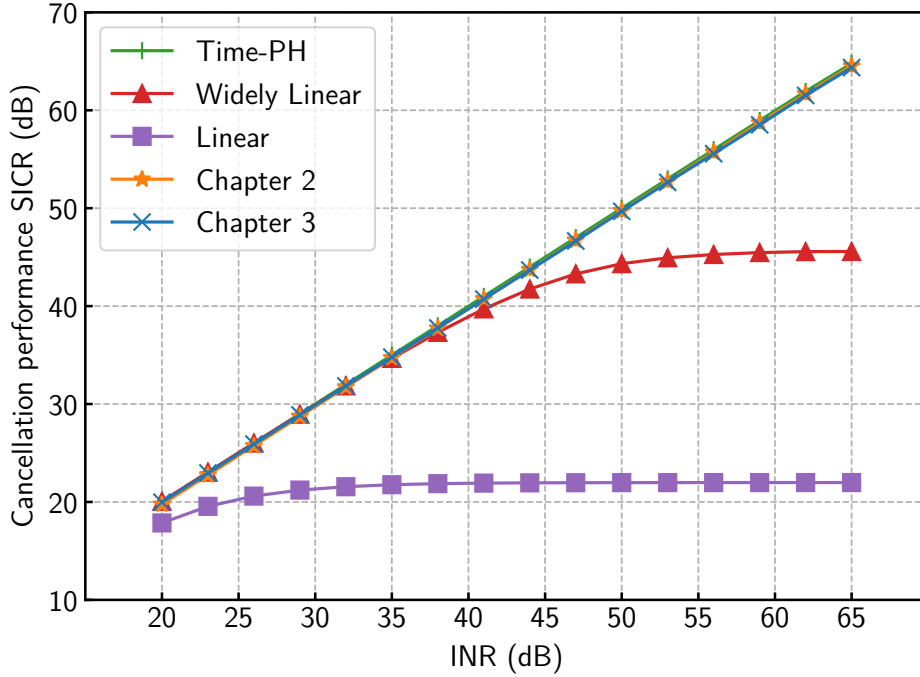


Figure 3.5: The median SICR value of each canceller with the LS algorithm at $N_{\text{tr}} = 60$. The smoothness factor of the LNA is $S_{\text{LNA}} = 3$. For the proposed scheme, $\beta = -20$ dB and $\gamma = 0$ dB.

technique, the number of parameters of the canceller decreases, and convergence performance is improved. In Fig. 3.8, the convergence performance of each canceller with RLS algorithm is shown at $\text{INR} = 50$ dB. In contrast with the case of the LS algorithm, the frequency-domain cancellers predominantly show better convergence performance than the time-domain nonlinear canceller. In the time domain, the input signal of the canceller is strongly colored, and convergence speed of an adaptive algorithm decreases with a colored input signal. However, the input signal of an adaptive algorithm of the frequency-domain Hammerstein canceller is almost white, and the convergence speed of them is faster than that seen in the time-domain case. In Fig. 3.9, the convergence performance of each canceller with the NLMS algorithm is shown at $\text{INR} = 50$ dB. As with the RLS algorithm, the frequency-domain cancellers show better convergence performance than the time-domain nonlinear canceller.

Fig. 3.10 shows the computational cost of the training stage at different INR, and Fig. 3.11 shows the selected percentage in all subcarriers for each basis function on

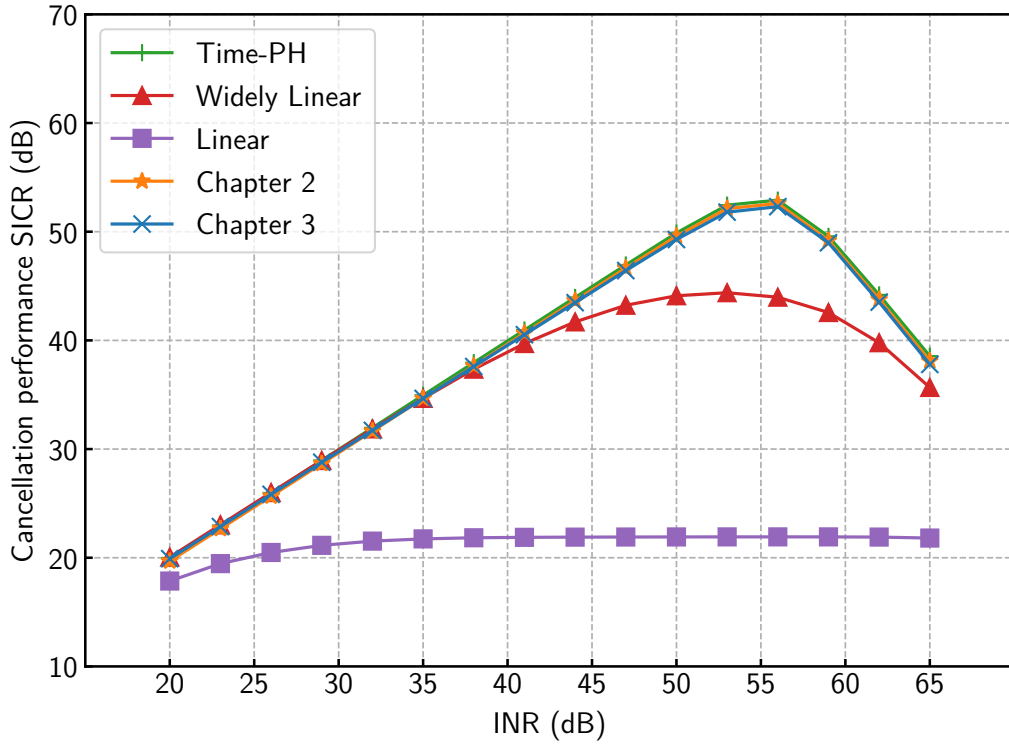


Figure 3.6: The median SICR value of each canceller with the LS algorithm at $N_{\text{tr}} = 60$. The smoothness factor of the LNA is $S_{\text{LNA}} = 1$. For the proposed scheme, $\beta = -20$ dB and $\gamma = 2$ dB.

Table 3.2: CMOPS of time-domain cancellers

Canceller	CMOPS
Linear with NLMS	128
Linear with RLS	1.66×10^4
Widely Linear with NLMS	256
Widely Linear with RLS	6.60×10^4
Parallel Hammerstein with NLMS	768
Parallel Hammerstein with RLS	5.90×10^5

the proposed selection technique. When the proposed selection technique is disabled, the CMOPS of the RLS case is about 147 at all INR. On the other hand, using the basis function selection, the necessary basis functions are selected according to the INR, which can be found in Fig. 3.11, and, as a result, computational cost is reduced. Since the computational complexity of the RLS algorithm increases with

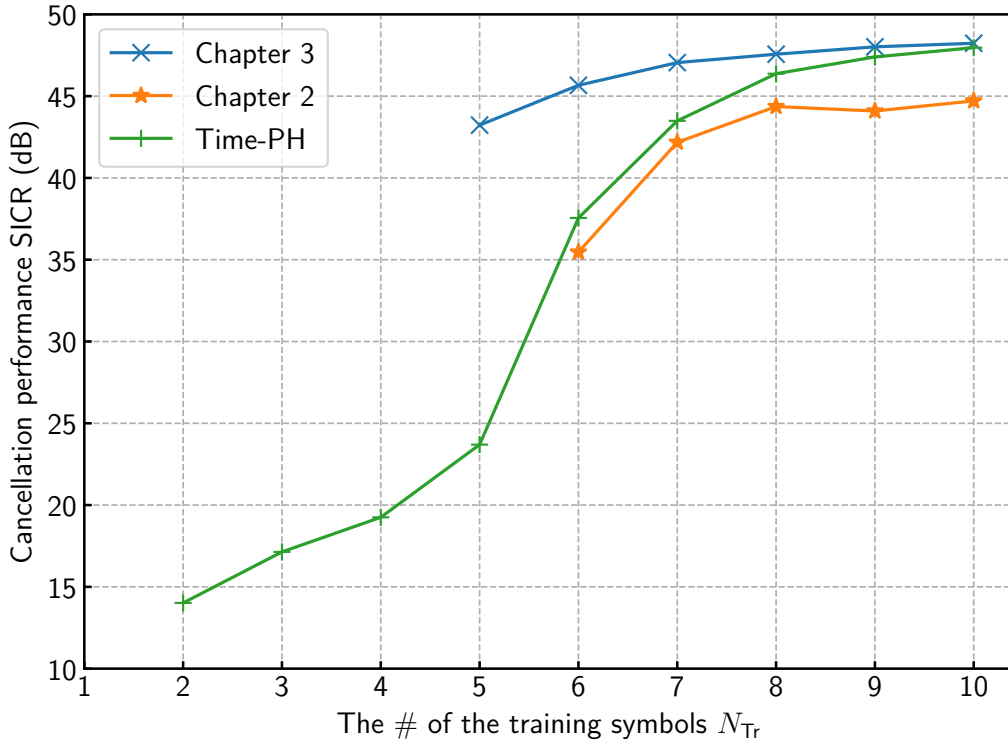


Figure 3.7: The convergence of each canceller with the LS algorithm at INR = 50 dB. SICR values are median values of all trials at each situation. The smoothness factor of the LNA is $S_{LNA} = 3$. For the proposed scheme, $\beta = -20$ dB and $\gamma = 2$ dB.

the square of the number of basis functions, it is susceptible to the effect of the selection technique, but the effect for the NLMS is small because the computational complexity of the NLMS algorithm increases linearly. When INR is 20 dB, the computational cost of the RLS case is less than 1/5 as compared with a case without the selection, and even when INR is 50 dB, it is less than half. When INR is greater than 50 dB, the difference of the CMOPS between $S_{LNA} = 1$ and $S_{LNA} = 3$ is gradually increased. The proposed technique assumes that the LNA is a linear component, and basis functions cannot be selected correctly when the nonlinearity of the LNA is greater than the noise. In Table 3.2, CMOPS values of time-domain cancellers are shown. Compared with the time-domain Hammerstein canceller optimized by the RLS algorithm, the proposed canceller achieves about 1.2×10^4 times lower computational cost on the training stage at INR = 50 dB. When the NLMS algorithm is used, the proposed canceller achieves about 45 times lower computational cost than the time-domain Hammerstein canceller at

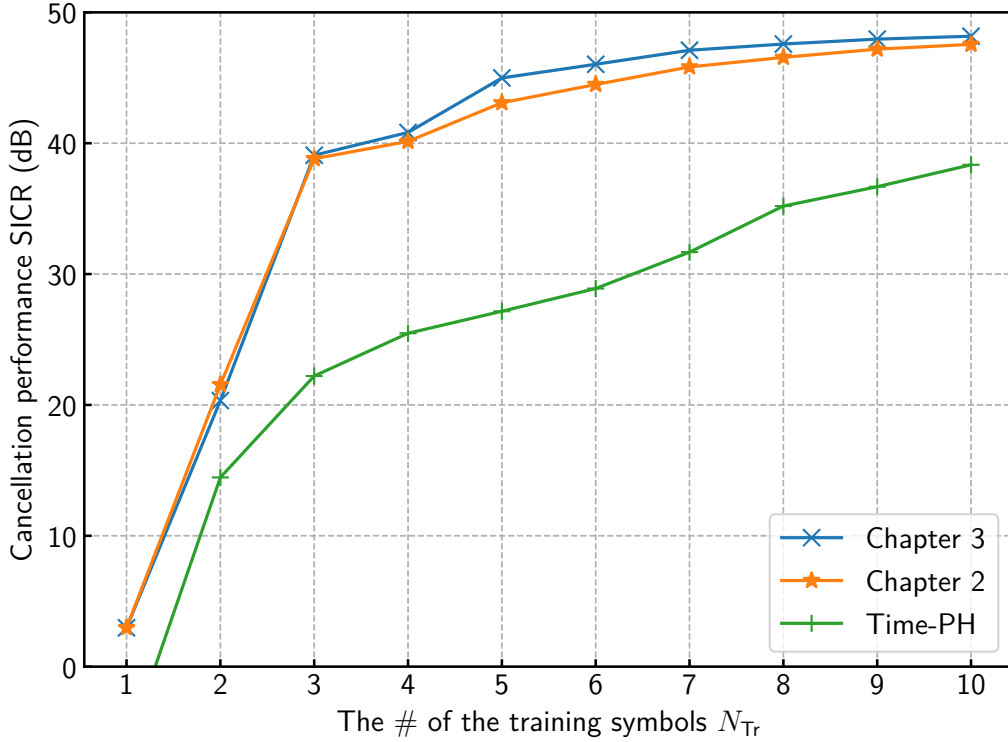


Figure 3.8: The convergence of each canceller with RLS algorithm at INR = 50 dB. SICR values are median values of all trials at each situation. The smoothness factor of the LNA is $S_{LNA} = 3$. For the proposed scheme, $\beta = -20$ dB and $\gamma = 2$ dB.

INR = 50 dB.

At the end of the simulation evaluation, we check how the self-interference cancellation performance of the proposed scheme is affected by fluctuations of the transmitter characteristics. Fig. 3.12 shows the percentage of trails in which the cancellation performance of the proposed scheme is lower than 47 dB in all trials at INR = 50 dB when log-normally distributed fluctuations are given to transmit power, IRR, IIP3 of the PA, and the gain of the PA independently. In other words, at the premeasurement stage we assign the values shown in Table 3.1 to each parameter, and at the training stage we assign log-normally distributed independent random variables to each parameter, respectively. It is found that the proposed scheme with $\gamma = 2$ dB is robust against fluctuations of 0.8 dB in variance. Generally, these parameters are dependent on temperature and supply voltage and vary by only about 1 dB at the maximum. Therefore, it can be seen that the proposed scheme is sufficiently effective against temporal characteristic fluctuations of equipment.

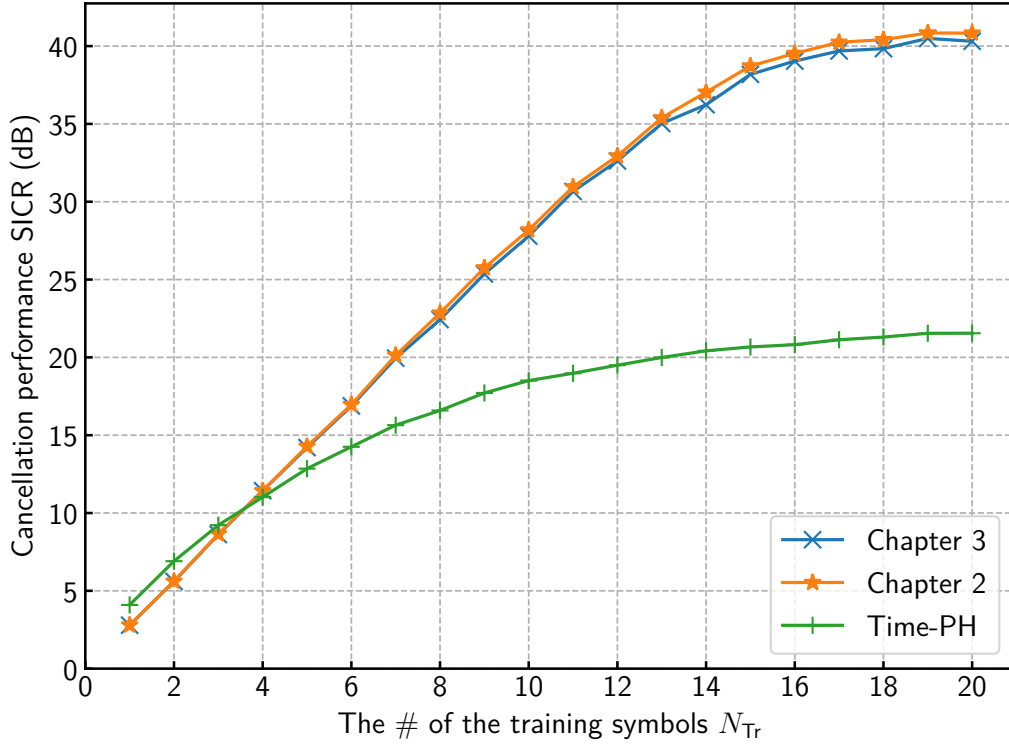


Figure 3.9: The convergence of each canceller with NLMS algorithm at INR = 50 dB. SICR values are median values of all trials at each situation. The smoothness factor of the LNA is $S_{LNA} = 3$. For the proposed scheme, $\beta = -20$ dB and $\gamma = 2$ dB.

3.5 Conclusion

In this chapter, the author has proposed a basis function selection technique of the frequency-domain Hammerstein self-interference canceller for in-band full-duplex communication systems. The estimation technique of the power spectral density of the received self interference is developed from the detailed nonlinear characteristics of a full-duplex terminal. The proposed selection technique reduces unnecessary basis functions for cancellation before the training stage according to the estimated self-interference power at each discrete frequency. Simulation results show that the proposed technique improves computational cost and convergence performance of the original frequency-domain Hammerstein canceller. It is shown that computational cost can be reduced to about one-fifth in the low self-interference situation by reducing the basis functions according to the estimated self-interference signal power. In addition, by the proposed basis function selection technique,

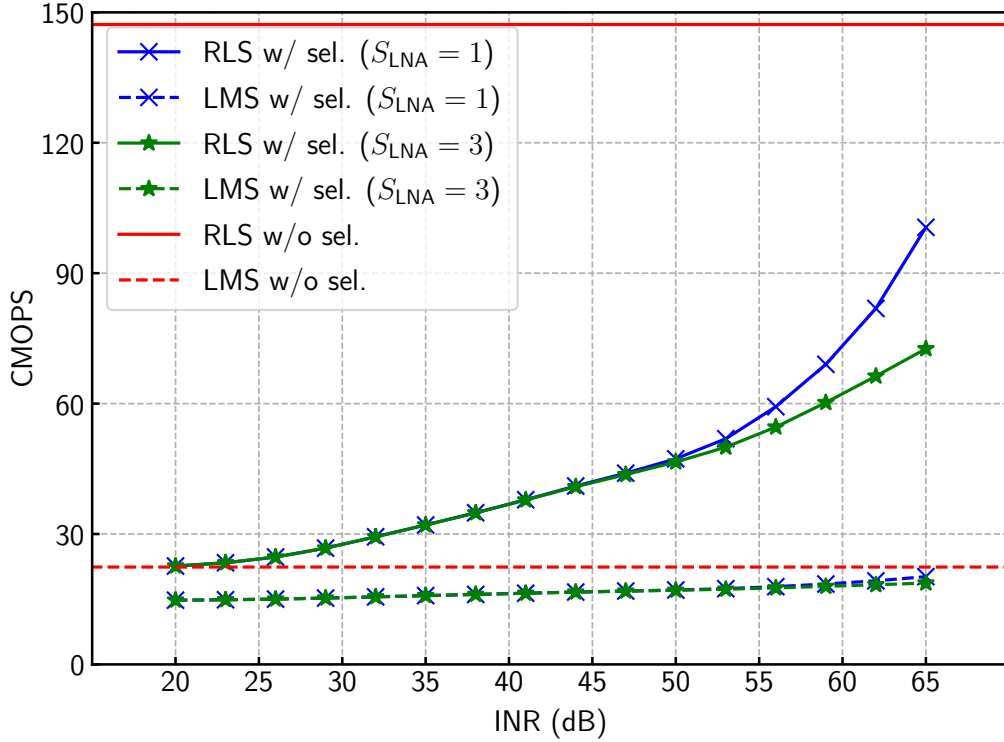


Figure 3.10: The computational cost at a training stage with $\beta = -20$ dB and $\gamma = 2$ dB.

self-interference cancellation performance of the frequency-domain Hammerstein canceller hardly decreases and achieves similar cancellation performance compared with the original.

Appendix 3.A Derivation of (3.52) and (3.53)

We can assume that $\Psi_{p_1, q_1, i}^{\text{swp}}[k]$ and $\Psi_{p_2, q_2, i}^{\text{swp}}[k]$ are independent when $(p_1, q_1) \neq (p_2, q_2)$, because they are sums of a large number of combinations of subcarriers as (3.19). When $\Psi_{p_1, q_1, i}^{\text{swp}}[k]$ and $\Psi_{p_2, q_2, i}^{\text{swp}}[k]$ are independent, $\mathbb{E}[|Y_{\text{VGA}}^{\text{swp}}[k]|^2]$ can be written as

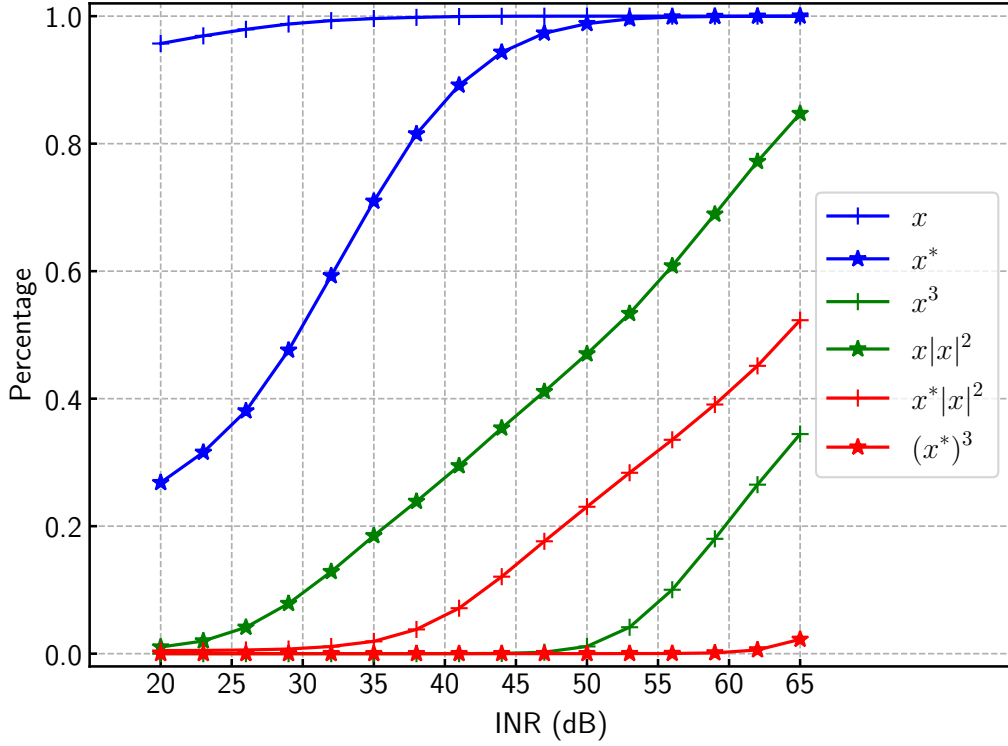


Figure 3.11: The selected percentage in all subcarriers for each basis function. In this figure, $\beta = -20$ dB, $\gamma = 2$ dB, and $S_{\text{LNA}} = 3$.

follows:

$$\begin{aligned}
 \mathbb{E} \left[|Y_{\text{VGA}}^{\text{SWP}}[k]|^2 \right] &= \sum_{p,q} \mathbb{E} \left[|a_{p+q} c_{p,q} H[k] \Psi_{p,q}^{\text{SWP}}[k]|^2 \right] \\
 &= \mathbb{E} \left[|a_1 H[k] \Psi_{1,0}^{\text{SWP}}[k]|^2 \right] \\
 &+ \underbrace{\sum_{(p,q) \neq (1,0)} \mathbb{E} \left[|a_{p+q} c_{p,q} H[k] \Psi_{p,q}^{\text{SWP}}[k]|^2 \right]}_{\geq 0},
 \end{aligned} \tag{3.85}$$

Thus, the following inequality is derived as:

$$\mathbb{E} \left[|a_1 H[k] \Psi_{1,0}^{\text{SWP}}[k]|^2 \right] \leq \mathbb{E} \left[|Y_{\text{VGA}}^{\text{SWP}}[k]|^2 \right]. \tag{3.86}$$

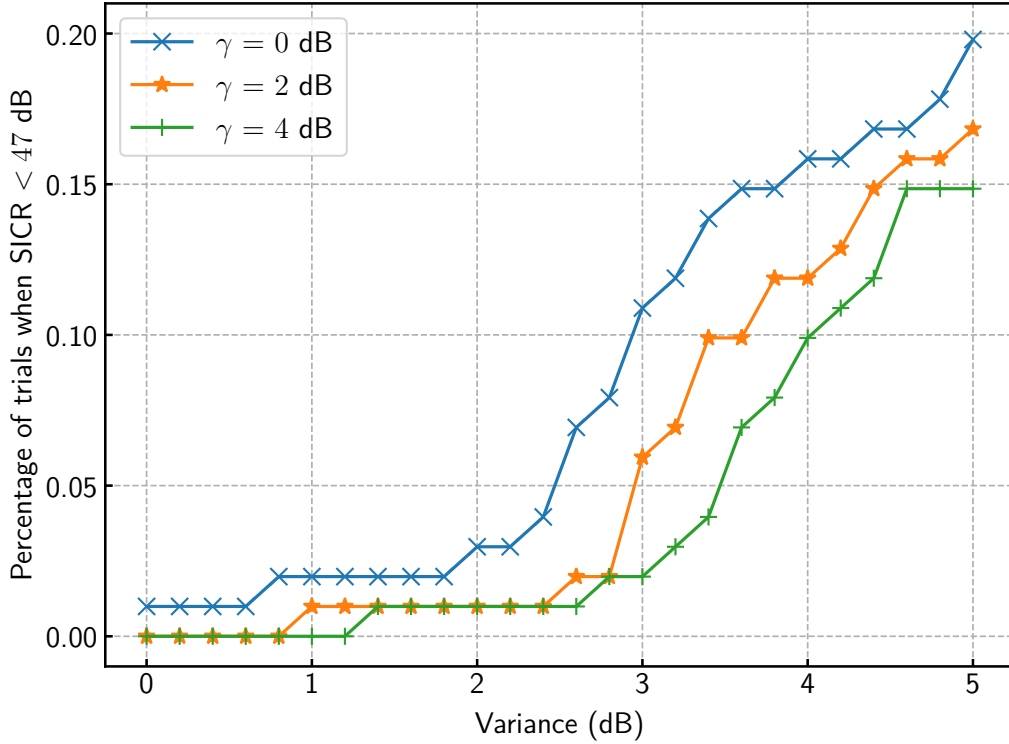


Figure 3.12: The percentage of trails where the SICR of the proposed scheme is lower than 47 dB in all trials when nonlinear parameters are varied on log-normal distribution. In this simulation, the LS algorithm is used as the training algorithm. INR, β , γ , and S_{LNA} are 50 dB, -20 dB, 2 dB, and 3 respectively.

Transforming (3.4) with respect to $Y_{VGA}^{swp}[k]$, (3.87) is derived.

$$Y_{VGA}^{swp}[k] = \frac{Y_i^{swp}[k] - b^{RX} (Y_i^{swp}[-k])^*}{1 - |b^{RX}|^2}. \quad (3.87)$$

Finally, we derive (3.52) and (3.53) from (3.86) by the triangle inequality.

References

- [1] D. Korpi, L. Anttila, V. Syrjälä, and M. Valkama, “Widely linear digital self-interference cancellation in direct-conversion full-duplex transceiver,” *IEEE J. Sel. Areas Commun.*, vol. 32, no. 9, pp. 1674–1687, Sept. 2014.
- [2] L. Anttila, D. Korpi, V. Syrjälä, and M. Valkama, “Cancellation of power amplifier induced nonlinear self-interference in full-duplex transceivers,” in *Proc. 47th Asilomar Conf. Signals, Syst., Comput.*, Nov. 2013.
- [3] E. Ahmed and A. M. Eltawil, “All-digital self-interference cancellation technique for full-duplex systems,” *IEEE Trans. Wireless Commun.*, vol. 14, no. 7, pp. 3519–3532, July 2015.
- [4] M. Valkama and M. Renfors, “Digital filter design for I/Q imbalance compensation,” in *Proc. 10th European Signal Process. Conf. (EUSIPCO)*, Sept. 2000, pp. 1–4.
- [5] M. Duarte, C. Dick, and A. Sabharwal, “Experiment-driven characterization of full-duplex wireless systems,” *IEEE Trans. Wireless Commun.*, vol. 11, no. 12, pp. 4296–4307, Dec. 2012.
- [6] K. Komatsu, Y. Miyaji, and H. Uehara, “Frequency-domain Hammerstein self-interference canceller for in-band full-duplex OFDM systems,” in *Proc. IEEE WCNC*, Mar. 2017.
- [7] W. H. Press, S. A. Teukolsky, W. T. Vetterling, and B. P. Flannery, *Numerical Recipes 3rd Edition: The Art of Scientific Computing*, 3rd ed. New York, USA: Cambridge University Press, 2007.
- [8] Maxim Integrated, “MAX2242: 2.4 GHz to 2.5 GHz linear power amplifier,” San Jose, CA, USA.

- [9] —, “MAX2692/MAX2695: WLAN/WiMAX low-noise amplifiers,” San Jose, CA, USA.
- [10] D. Korpi, T. Riihonen, V. Syrjälä, L. Anttila, M. Valkama, and R. Wichman, “Full-duplex transceiver system calculations: Analysis of ADC and linearity challenges,” *IEEE Trans. Wireless Commun.*, vol. 13, no. 7, pp. 3821–3836, July 2014.
- [11] C. Rapp, “Effects of HPA-nonlinearity on a 4-DPSK/OFDM-signal for a digital sound broadcasting system,” in *Proc. the Second European Conf. on Satellite Commun.*, Oct. 1991, pp. 179–184.
- [12] J. Joung, C. K. Ho, K. Adachi, and S. Sun, “A survey on power-amplifier-centric techniques for spectrum- and energy-efficient wireless communications,” *IEEE Commun. Surveys Tuts.*, vol. 17, no. 1, pp. 315–333, 2015.
- [13] D. Korpi, T. Huusari, Y.-S. Choi, L. Anttila, S. Talwar, and M. Valkama, “Digital self-interference cancellation under nonideal RF components: Advanced algorithms and measured performance,” in *Proc. IEEE SPAWC*, June 2015, pp. 286–290.
- [14] D. Korpi, S. Venkatasubramanian, T. Riihonen, L. Anttila, S. Otewa, C. Icheln, K. Haneda, S. Tretyakov, M. Valkama, and R. Wichman, “Advanced self-interference cancellation and multiantenna techniques for full-duplex radios,” in *Proc. 47th Asilomar Conf. Signals, Syst., Comput.*, Nov. 2013, pp. 3–8.
- [15] R. Li, A. Masmoudi, and T. Le-Ngoc, “Self-interference cancellation with nonlinearity and phase-noise suppression in full-duplex systems,” *IEEE Trans. Veh. Technol.*, vol. 67, no. 3, pp. 2118–2129, Mar. 2018.

Chapter 4

Iterative Nonlinear SI Canceller

This chapter presents an iterative estimation and cancellation technique for nonlinear in-band full-duplex transceivers with IQ imbalances and amplifier nonlinearities. The estimation process of the proposed scheme consists of three stages, namely, the channel response estimation, IQ imbalance estimation, and power amplifier and low-noise amplifier (LNA) nonlinearities estimation. For the estimation of the parameters and improvement of the accuracy, distortions are compensated by cancellation or inversion with the latest estimated parameters. On the one hand, the channel response is estimated on the time domain; on the other hand, the IQ imbalance and nonlinearities are estimated on the frequency domain for a more straightforward estimation and superior accuracy. In the cancellation process of the proposed scheme, the received signal is compensated with the estimated parameters of the LNA and receiver IQ imbalance before cancellation because the desired signal is received with a high-power self-interference and is distorted by the radio-frequency receiver impairments. Simulation results show that the proposed technique can achieve higher cancellation performance compared with the Hammerstein canceller when the LNA is saturated by the self-interference. Additionally, the performance of the proposed canceller converges much faster than that of the Hammerstein canceller.

4.1 Introduction

In general, inexpensive terminals suffer from nonlinearity problems more than expensive terminals. With powerful digital signal processing techniques, many digital cancellers have been developed to reduce effects of non-idealities, as shown in Table 4.1. The most problematic RF impairments are the IQ mixer imbalance and PA nonlinearity [1]. To deal with these impairments, Hammerstein cancellers [2–11] have been developed. This type of canceller estimates channel responses for all nonlinear basis functions by applying a least-squares estimation. A digital canceller with an auxiliary receiver [1, 12, 13], which is used to receive the output signal of the PA directly, can perfectly regenerate the nonlinear self-interference signal caused by the transmitter nonlinearities using lightweight digital signal processing. However, the nonlinearity due to the receiver LNA cannot be expressed by the Hammerstein model, and the Hammerstein canceller and the auxiliary receiver cannot cope with the nonlinear distortion of the LNA. In literature [14], a canceller that addresses the nonlinearity of both the PA and LNA has been developed. This canceller estimates the radio channel and the nonlinear characteristics alternately. However, IQ imbalance is not considered in this scheme. In other works [15–18], mitigation techniques of receiver nonlinearity were proposed for wideband receivers. These techniques do not employ self-interference cancellers and cannot deal with the nonlinear distortion of the transmitter. To use these techniques for self-interference cancellation, it is necessary to complement them with other cancellers that can mitigate the nonlinear distortion of the transmitter. The Volterra series-based cancellers [19–21] have the potential to mitigate the nonlinearities of the PA and LNA and the IQ imbalance. However, they need significantly higher computational power to estimate and regenerate the nonlinear self-interference signal than other practical cancellers. For example, the Hammerstein canceller and the canceller described in [21] need to estimate $12M = 576$ and $7M^3 + 3M^2 + 2M + 1 \approx 7.81 \times 10^5$ parameters for fifth-order nonlinearity cancellation, respectively, when the number of taps of the channel impulse response is $M = 48$. To the best of the author's knowledge, a digital self-interference canceller that addresses the nonlinearities of the PA and LNA, and the imbalance of IQ mixers with reasonable computational cost has not been developed yet. The development of such a canceller would enable the construction of inexpensive full-duplex terminals.

In small and inexpensive terminals, the performance of RF cancellers will be constrained in terms of size and cost. Therefore, the RF canceller cannot sufficiently

Table 4.1: Digital Cancellers and RF Impairments in the Literature

	Addressed RF Impairments			
	IQI	PA NL	LNA NL	Phase Noise
Linear [22]				
Widely Linear [23]	✓			
Hammerstein [2–11]	✓	✓		
Auxiliary Receiver [1, 12, 13]	✓	✓		
[14]		✓	✓	
[24]				✓
[25]		✓		✓
Volterra Series [19–21]	✓	✓	✓	
Proposed	✓	✓	✓	

remove the self-interference, and the nonlinearity of the LNA will be a problem to achieve in-band full-duplex communications. However, a practical digital self-interference canceller that takes into account the nonlinearities of both the LNA and PA and the mixer imbalance has not been developed yet. The contributions of this study are as follows:

- To develop a novel digital canceller, the author defines operators that characterize the nonlinearity of the self-interference signal. Even if the self-interference signal contains complex nonlinearities, the signal model with these operators tells us what operations are needed to estimate the parameters and eliminate self-interference.
- By referring to the nonlinear signal model with operators, the author introduces a novel estimation and cancellation scheme of the self-interference signal that can deal with the nonlinearity of the LNA. The estimation process of the proposed scheme is divided into three stages: IQ imbalance estimation, channel impulse response estimation, and PA and LNA nonlinearities estimation. These stages are executed iteratively in order, and the estimated parameters converge to better values. The proposed scheme can achieve high cancellation performance with much fewer learning symbols compared to Hammerstein cancellers because it estimates the simplest and smallest parameters that are sufficient to represent the nonlinear self-interference model.
- To achieve the best self-interference cancellation, the canceller should apply the inverse distortion of the receiver to the received signal. Conventional

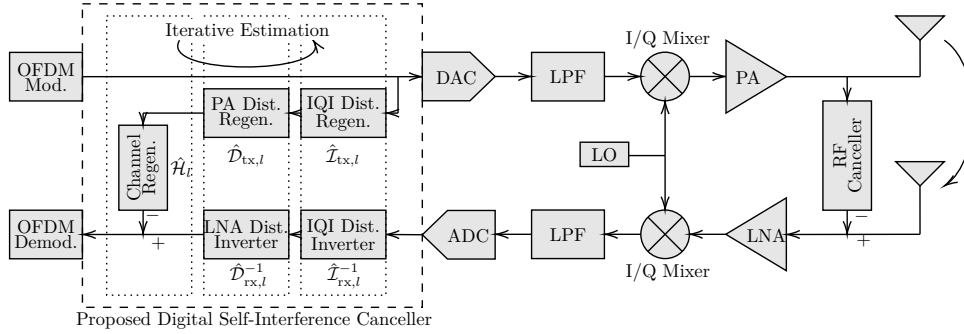


Figure 4.1: In-band full-duplex transceiver model with the proposed digital self-interference canceller

methods cannot generate the inverse characteristic of the receiver nonlinearity because they do not estimate the nonlinear characteristics of the transceiver and the characteristics of the channel separately. In contrast, the proposed method can generate the inverse characteristic of each distortion because the nonlinear distortion characteristics and channel impulse response are estimated separately. Thus, the proposed canceller applies a post-distortion to the received signal to compensate for the receiver RF impairments before self-interference cancellation. In addition, to avoid the synchronization problem of frequency-domain cancellers, these series of cancellations are processed in the time domain.

The rest of this chapter is organized as follows. In Section 4.2, a detailed model of the self-interference, which includes the nonlinearities of IQ mixers and amplifiers of the transceiver, and the mathematical operators that represent the input-output characteristic of each component are provided. The proposed estimation and cancellation scheme are presented in Section 4.3. In Section 4.4, the performance of the proposed scheme under different scenarios is analyzed with equivalent baseband signal simulations. Finally, this chapter is concluded in Section 4.5.

4.2 Self-Interference Signal Model

The signal model used in this study is the same as that reported in [9, 23]. In this section, the author describes the discrete-time and discrete-frequency baseband equivalent signal models corresponding to the input-output characteristics of each nonlinear RF components. The properties of each component are provided as

mathematical operators that only consist of sufficient parameters to represent their nonlinear properties. In Section 4.3, these operators are used to explain the proposed method. We assume that there is no signal other than the self-interference in the training period of the canceller. Hence, in this section, we focus on the self-interference signal only.

4.2.1 Transmit signal

The transmit OFDM signal with N_{sc} subcarriers is described as

$$x[n] = \sum_{\substack{k=-N_{sc}/2 \\ k \neq 0}}^{N_{sc}/2} X_i[k] e^{j2\pi k \Delta f n T_s}, \quad (4.1)$$

where $X_i[k]$ is the k th subcarrier at the i th OFDM symbol, and Δf and T_s are the frequency interval of each subcarrier and the sampling interval of the system, respectively. To estimate and remove the nonlinear self-interference signal, the bandwidth of the baseband signal processing, which is expressed as $1/T_s$, needs to be larger than $PN_{sc}\Delta f$, where P is the maximum nonlinear order of the canceller.

4.2.2 Imbalance of IQ mixers

The transmit signal $x[n]$ is upconverted from the baseband to the RF band on the IQ mixer of the transmitter. The IQ imbalance is one of the most significant distortions in direct-conversion transceivers, and it has been discussed extensively in the literature [23, 26, 27]. The frequency-independent imbalance model is described as

$$x_{IQ}[n] = c_{tx,1}x[n] + c_{tx,2}x^*[n] = c_{tx,1}\mathcal{I}_{tx}x[n], \quad (4.2)$$

where $c_{tx,1}$ and $c_{tx,2}$ are the coefficients of the input signal and conjugated signal, respectively. To simplify the explanation of the proposed scheme in Section 4.3, we define the operator \mathcal{I}_{tx} as follows:

$$\begin{aligned} \mathcal{I}_{tx}s[n] &= s[n] + \frac{c_{tx,2}}{c_{tx,1}}s^*[n] = s[n] + b_{tx}s^*[n], \\ \mathcal{I}_{tx}S_i[k] &= S_i[k] + \frac{c_{tx,2}}{c_{tx,1}}S_i^*[-k] = S_i[k] + b_{tx}S_i^*[-k], \end{aligned} \quad (4.3)$$

where $s[n]$ and $S_i[k]$ are baseband signals, and $b_{\text{tx}} = c_{\text{tx},2}/c_{\text{tx},1}$. In (4.3), the linear amplification factor is not included in the definition of the operator \mathcal{I}_{tx} because we want it to express the characteristics of IQ imbalance to a minimum form. The image rejection rate, which is an indicator of the IQ imbalance, is defined as

$$\text{IRR}_{\text{tx}} = \frac{|c_{\text{tx},1}|^2}{|c_{\text{tx},2}|^2} = |b_{\text{tx}}|^{-2}. \quad (4.4)$$

For the receiver IQ mixer, we also define $c_{\text{rx},1}$, $c_{\text{rx},2}$ and IRR_{rx} similarly to (4.2) and (4.4), respectively. Then, the operator \mathcal{I}_{rx} is defined as

$$\begin{aligned} \mathcal{I}_{\text{rx}}s[n] &= s[n] + \frac{c_{\text{rx},2}}{c_{\text{rx},1}^*}s^*[n] = s[n] + b_{\text{rx}}s^*[n], \\ \mathcal{I}_{\text{rx}}S_i[k] &= S_i[k] + \frac{c_{\text{rx},2}}{c_{\text{rx},1}^*}S_i^*[-k] = S_i[k] + b_{\text{rx}}S_i^*[-k], \end{aligned} \quad (4.5)$$

where $b_{\text{rx}} = c_{\text{rx},2}/c_{\text{rx},1}^*$. Thus, the received baseband signal can be expressed with the operator \mathcal{I}_{rx} as

$$y[n] = \mathcal{I}_{\text{rx}}(c_{\text{rx},1}y_{\text{LNA}}[n]), \quad (4.6)$$

where $y_{\text{LNA}}[n]$ is the output signal of the LNA.

4.2.3 Nonlinear distortions of amplifiers

The upconverted RF signal $x_{\text{IQ}}[n]$ is amplified by the variable gain amplifier and the PA to radiate from the antenna subsequently. Similar to the IQ imbalance, the self-interference signal is distorted by the nonlinearity of the amplifiers, and it is expressed as [28, page 69]

$$x_{\text{PA}}[n] = \sum_{p=1,3,\dots}^{\infty} a_{\text{tx},p}x_{\text{IQ}}[n]|x_{\text{IQ}}[n]|^{p-1}, \quad (4.7)$$

where $a_{\text{tx},p}$ is the gain of the p th nonlinear distortion of the PA, and $a_{\text{tx},1}$ is the linear gain of transmitter RF amplifiers. To simplify the explanation in Section 4.3, we define the operator \mathcal{D}_{tx} for any input signal $s[n]$ as

$$\mathcal{D}_{\text{tx}}s[n] = s[n] + \sum_{p=3,5,\dots}^{\infty} d_{\text{tx},p}s[n]|s[n]|^{p-1}, \quad (4.8)$$

where $d_{\text{tx},p} = |c_{\text{tx},1}|^{p-1} a_{\text{tx},p}/a_{\text{tx},1}$, and $d_{\text{tx},1}$ is equal to 1. Then, the transmit signal from the transmit antenna is expressed as

$$x_{\text{PA}}[n] = a_{\text{tx},1} c_{\text{tx},1} \mathcal{D}_{\text{tx}} \mathcal{I}_{\text{tx}} x[n]. \quad (4.9)$$

At the receiver, if the self-interference is strong enough to saturate the LNA, its nonlinear distortion will also occur from the LNA. The output signal of the LNA can be expressed as

$$y_{\text{LNA}}[n] = \sum_{p=1,3,\dots}^{\infty} a_{\text{rx},p} y_{\text{ASIC}}[n] |y_{\text{ASIC}}[n]|^{p-1}, \quad (4.10)$$

where $y_{\text{ASIC}}[n]$ is the signal after analog self-interference cancellation, and $a_{\text{rx},p}$ is the gain of the p th distortion signal of the LNA. Similar to the PA distortion operator of (4.9), we define the operator \mathcal{D}_{rx} as

$$\mathcal{D}_{\text{rx}} s[n] = s[n] + \sum_{p=3,5,\dots}^{\infty} d_{\text{rx},p} s[n] |s[n]|^{p-1}, \quad (4.11)$$

where

$$d_{\text{rx},p} = \frac{a_{\text{rx},p}}{a_{\text{rx},1} |c_{\text{rx},1} a_{\text{rx},1}|^{p-1}}. \quad (4.12)$$

Thus, the output signal of the received IQ mixer can be expressed as

$$y[n] = \mathcal{I}_{\text{rx}} \mathcal{D}_{\text{rx}} (c_{\text{rx},1} a_{\text{rx},1} y_{\text{ASIC}}[n]). \quad (4.13)$$

4.2.4 SI channel and RF cancellation

The TX and RX antennas are strongly coupled because terminals such as smartphones and IoT devices have limited size. Therefore, the self-interference channel can be modeled as a Rician fading channel with 20 dB or higher K factor [29]. Analog self-interference cancellation is used to reduce the received self-interference signal. Thus, the self-interference signal remaining after RF cancellation is expressed as

$$\begin{aligned} y_{\text{ASIC}}[n] &= (h_{\text{SI}}[m] - h_{\text{Cir}}[m]) * x_{\text{PA}}[n] \\ &= \sum_{m=0}^{M-1} (h_{\text{SI}}[m] - h_{\text{Cir}}[m]) x_{\text{PA}}[n - m], \end{aligned} \quad (4.14)$$

where $h_{\text{SI}}[m]$ is the wireless channel response, $h_{\text{Cir}}[m]$ is the RF canceller circuits response, and M is the number of taps of the wireless channel. To achieve high self-interference cancellation performance with an analog self-interference canceller, many variable attenuators and phase shifters are required, which increases the cost of the terminal. Thus, we assume that the RF canceller reduces only the direct wave of the self-interference, and the channel response $h_{\text{SI}}[m] - h_{\text{Cir}}[m]$ can be modeled as a Rayleigh fading channel.

Then, we define the operator \mathcal{H} as follows:

$$\begin{aligned}\mathcal{H}s[n] &= a_{\text{tx},1}a_{\text{rx},1}c_{\text{tx},1}c_{\text{rx},1}(h_{\text{SI}}[m] - h_{\text{Cir}}[m]) * s[n] \\ &= h[m] * s[n],\end{aligned}\tag{4.15}$$

$$\mathcal{H}S_i[k] = H[k]S_i[k]\tag{4.16}$$

where $h[m] = a_{\text{tx},1}a_{\text{rx},1}c_{\text{tx},1}c_{\text{rx},1}(h_{\text{SI}}[m] - h_{\text{Cir}}[m])$, and $H[k]$ is a frequency-domain representation of $h[m]$. To minimize the number of parameters for each operator, all amplification factors for linear SI components at the transmitter and receiver are aggregated into the operator \mathcal{H} . Then, the received SI signal $y[n]$ can be expressed simply as

$$y[n] = \mathcal{I}_{\text{rx}}\mathcal{D}_{\text{rx}}\mathcal{H}\mathcal{D}_{\text{tx}}\mathcal{I}_{\text{tx}}x[n],\tag{4.17}$$

Eq. (4.17) shows that the self-interference signal can be expressed concisely with operators and block diagrams as in Fig. 4.2. The operators \mathcal{I}_{tx} and \mathcal{I}_{rx} have only one parameter each, namely b_{tx} and b_{rx} , respectively. In addition, the operators \mathcal{D}_{tx} and \mathcal{D}_{rx} have $(P-1)/2$ parameters each if the nonlinear characteristic of an amplifier is approximated by a P -order polynomial. Thus, the total number of parameters of (4.17) is $P + M + 1$, where M is the number of taps of the channel impulse response $h[m]$.

4.3 Proposed Scheme

In this section, the author describes the proposed scheme, which consists of three estimation stages and a cancellation stage. The proposed scheme iteratively estimates the coefficients of IQ imbalance b_{tx} and b_{rx} , the impulse response of the SI channel $h[m]$, and the nonlinear gains of amplifiers $d_{\text{tx},p}$ and $d_{\text{rx},p}$. In this section, l denotes the iteration index of the estimation stage. On the l th iteration, the proposed method updates the estimated values to more accurate ones using the

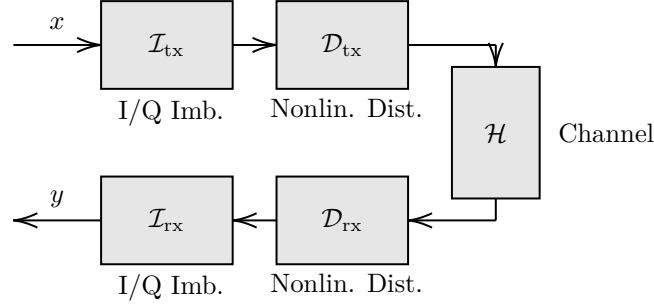


Figure 4.2: Block diagram and signal flow of the self-interference with each RF component and operator

values calculated at the $(l - 1)$ th iteration.

4.3.1 Definitions of operators

To explain the proposed scheme, we define the estimated value of each parameter on the l th iteration as $\hat{b}_{\diamond,l}$, $\hat{h}_l[m]$, and $\hat{d}_{\diamond,p,l}$, where $\diamond \in \{\text{tx}, \text{rx}\}$. The initial values of these parameters are defined as

$$\hat{b}_{\diamond,0} = 0, \quad (4.18)$$

$$\hat{d}_{\diamond,p,0} = \begin{cases} 1 & \text{for } p = 1, \\ 0 & \text{for } p > 1, \end{cases} \quad (4.19)$$

$$\hat{h}_0[m] = \text{NaN for all } m, \quad (4.20)$$

where NaN indicates that there is no initial value, and the proposed scheme does not need any initial values of $\hat{h}[m]$. Then, the estimated operators are defined using estimated parameters as

$$\hat{\mathcal{I}}_{\diamond,l}s[n] = s[n] + \hat{b}_{\diamond,l}s^*[n], \quad (4.21)$$

$$\hat{\mathcal{D}}_{\diamond,l}s[n] = s[n] + \sum_{p=3,5,\dots}^P \hat{d}_{\diamond,p,l}s[n] |s[n]|^{p-1}, \quad (4.22)$$

$$\hat{\mathcal{H}}_l s[n] = \sum_{m=0}^{M-1} \hat{h}_l[m]s[n-m], \quad (4.23)$$

$$\hat{\mathcal{H}}_l S_i[k] = \hat{H}_l[k]S_i[k], \quad (4.24)$$

where P is the maximum estimation order of the nonlinearities, and $\hat{H}_l[k]$ is the frequency-domain representation of $\hat{h}_l[m]$. The inverse operator of $\hat{\mathcal{I}}_{\diamond,l}$ can be

expressed as

$$\hat{\mathcal{I}}_{\diamond,l}^{-1} s[n] = \frac{s[n] - \hat{b}_{\diamond,l} s^*[n]}{1 - |\hat{b}_{\diamond,l}|^2}. \quad (4.25)$$

The inverse operator of $\hat{\mathcal{D}}_{\diamond,l}$ is defined by Newton's method with M_n times iterations, and it can be expressed as

$$\hat{\mathcal{D}}_{\diamond,l}^{-1} s[n] = D_{\diamond,l}^{-1}(|s[n]|) \frac{s[n]}{|s[n]|} \quad (4.26)$$

where

$$D_{\diamond,l}^{-1}(r_0) = r_{M_n} \frac{|u_{M_n}|}{u_{M_n}}, \quad (4.27)$$

$$r_{k+1} = r_k - \frac{(|u_k| - r_0) |u_k|}{\operatorname{Re}[u_k] \operatorname{Re}[v_k] + \operatorname{Im}[u_k] \operatorname{Im}[v_k]}, \quad (4.28)$$

$$u_k = \hat{\mathcal{D}}_{\diamond,l} r_k, \quad (4.29)$$

$$v_k = \sum_{p=1,3,\dots}^P \hat{d}_{\diamond,p,l} p r_k^{p-1}. \quad (4.30)$$

Detailed derivations of (4.26)–(4.30) are provided in Appendix A. We also define the operator \mathcal{F} , which denotes cyclic prefix (CP) removal and discrete Fourier transform for each OFDM symbol, and an operator \mathcal{F}^{-1} , which denotes the inverse discrete Fourier transform of each OFDM symbol.

4.3.2 IQ imbalance estimation

During the estimation of the IQ imbalance coefficients b_{tx} and b_{rx} , the other distortions, such as PA and LNA distortions, reduce the estimation accuracy. Thus, before estimating b_{tx} and b_{rx} at the l th iteration, we eliminate the distortion of the PA and LNA with the latest estimated values corresponding to the $(l-1)$ th iteration. In the proposed scheme, the transmitted and received signals for estimation are converted as follows:

$$x_l^{(1)}[n] = \hat{\mathcal{I}}_{\text{tx},l-1}^{-1} \hat{\mathcal{D}}_{\text{tx},l-1} \hat{\mathcal{I}}_{\text{tx},l-1} x[n], \quad (4.31)$$

$$y_l^{(1)}[n] = \hat{\mathcal{I}}_{\text{rx},l-1} \hat{\mathcal{D}}_{\text{rx},l-1}^{-1} \hat{\mathcal{I}}_{\text{rx},l-1}^{-1} y[n]. \quad (4.32)$$

If the latest estimated values converge to the true values sufficiently, the relation of $x_l^{(1)}[n]$ and $y_l^{(1)}[n]$ is expressed as

$$y_l^{(1)}[n] = \mathcal{I}_{\text{rx}} \mathcal{H} \mathcal{I}_{\text{tx}} x_l^{(1)}[n] + z_l^{(1)}[n], \quad (4.33)$$

where $z_l^{(1)}[n]$ is the error due to the estimation error of the latest estimated values. In (4.33), there is no distortion of the PA and LNA, and the error $z_l^{(1)}[n]$ can be decreased with each additional iteration. Thus, we can estimate the IQ imbalance coefficients b_{tx} and b_{rx} precisely from $x_l^{(1)}[n]$ and $y_l^{(1)}[n]$ when the latest estimated values have converged to the true values sufficiently. We use the frequency-domain representation of (4.31) and (4.32) to estimate the IQ imbalance coefficients. After CP removal and applying a discrete Fourier transform, we obtain the frequency representations $X_{i,l}^{(1)}[k]$ and $Y_{i,l}^{(1)}[k]$. The relation between these signal can be expressed as

$$\begin{aligned} Y_{i,l}^{(1)}[k] &= \underbrace{\{H[k] + b_{\text{rx}} b_{\text{tx}}^* H^*[-k]\}}_{H_{0,l}[k]} X_{i,l}^{(1)}[k] \\ &+ \underbrace{\{b_{\text{tx}} H[k] + b_{\text{rx}} H^*[-k]\}}_{H_{1,l}[k]} \left(X_{i,l}^{(1)}[-k] \right)^* + Z_{i,l}^{(1)}[k]. \end{aligned} \quad (4.34)$$

Then, the channel frequency responses $H_0[k]$ and $H_1[k]$ are estimated by the well-known least squares method with N_{tr} OFDM symbols at $-N_{\text{sc}} \leq k \leq N_{\text{sc}}$ and $k \neq 0$ as follows:

$$\begin{bmatrix} \hat{H}_{0,l}[k] \\ \hat{H}_{1,l}[k] \end{bmatrix} = \left\{ \left(\mathbf{X}_l^{(1)}[k] \right)^H \mathbf{X}_l^{(1)}[k] \right\}^{-1} \left(\mathbf{X}_l^{(1)}[k] \right)^H \mathbf{Y}_l^{(1)}[k] \quad (4.35)$$

where

$$\mathbf{X}_l^{(1)}[k] = \begin{bmatrix} X_{0,l}^{(1)}[k] & X_{1,l}^{(1)}[k] & \cdots & X_{N_{\text{tr}}-1,l}^{(1)}[k] \\ \left(X_{0,l}^{(1)}[-k] \right)^* & \left(X_{1,l}^{(1)}[-k] \right)^* & \cdots & \left(X_{N_{\text{tr}}-1,l}^{(1)}[-k] \right)^* \end{bmatrix}^T, \quad (4.36)$$

$$\mathbf{Y}_l^{(1)}[k] = \left[Y_{0,l}^{(1)}[k] Y_{1,l}^{(1)}[k] \cdots Y_{N_{\text{tr}}-1,l}^{(1)}[k] \right]^T. \quad (4.37)$$

The estimated channel response $\hat{H}_{0,l}[k]$ can be well approximated to the self-interference channel response $H[k]$ because the value $|b_{\text{rx}} b_{\text{tx}}^*| \ll 1$ [30, 31]. Therefore, $H_{1,l}[k]$ is expressed as

$$H_{1,l}[k] \approx b_{\text{tx}} \hat{H}_{0,l}[k] + b_{\text{rx}} \hat{H}_{0,l}^*[-k], \quad (4.38)$$

and then we get the estimated values of the IQ imbalance coefficients as

$$\begin{bmatrix} \hat{b}_{\text{tx},l} \\ \hat{b}_{\text{rx},l} \end{bmatrix} = (\mathbf{H}_{0,l}^H \mathbf{H}_{0,l})^{-1} \mathbf{H}_{0,l}^H \mathbf{H}_{1,l}, \quad (4.39)$$

where

$$\mathbf{H}_{0,l} = \begin{bmatrix} \hat{H}_{0,l}[N_{\text{sc}}] \cdots \hat{H}_{0,l}[1] \hat{H}_{0,l}[-1] \cdots \hat{H}_{0,l}[-N_{\text{sc}}] \\ \hat{H}_{0,l}^*[-N_{\text{sc}}] \cdots \hat{H}_{0,l}^*[-1] \hat{H}_{0,l}^*[1] \cdots \hat{H}_{0,l}^*[N_{\text{sc}}] \end{bmatrix}^T, \quad (4.40)$$

$$\mathbf{H}_{1,l} = [\hat{H}_{1,l}[N_{\text{sc}}] \cdots \hat{H}_{1,l}[1] \hat{H}_{1,l}[-1] \cdots \hat{H}_{1,l}[-N_{\text{sc}}]]^T. \quad (4.41)$$

4.3.3 Channel estimation

After the IQ imbalance coefficients estimation stage, the proposed canceller estimates the channel impulse response $h[m]$. During the estimation of the channel impulse response, the nonlinear distortions of the IQ imbalance, PA, and LNA reduce the estimation accuracy of the channel impulse response. Thus, before estimating $h[m]$ at the l th iteration, we eliminate the distortions with the latest estimated values. The transmitted and received signals for estimation are converted as follows:

$$x_l^{(2)}[n] = \hat{\mathcal{D}}_{\text{tx},l-1} \hat{\mathcal{I}}_{\text{tx},l} x[n], \quad (4.42)$$

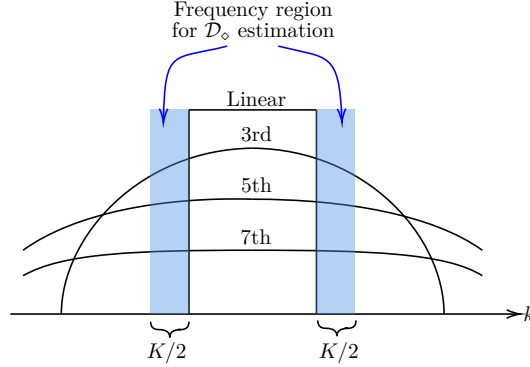
$$y_l^{(2)}[n] = \hat{\mathcal{D}}_{\text{rx},l-1}^{-1} \hat{\mathcal{I}}_{\text{rx},l}^{-1} y[n]. \quad (4.43)$$

If the latest estimated values converge to the true values sufficiently, the relation of $x_l^{(2)}[n]$ and $y_l^{(2)}[n]$ is expressed as

$$\begin{aligned} y_l^{(2)}[n] &= \mathcal{H} x_l^{(2)}[n] + z_l^{(2)}[n] \\ &= \sum_{m=0}^{M-1} h[m] x_l^{(2)}[n-m] + z_l^{(2)}[n], \end{aligned} \quad (4.44)$$

where $z_l^{(2)}[n]$ is the error caused by the estimation error of the latest estimated values. Then, the channel impulse response $h[m]$ is estimated by the well-known least-squares method with N_{tr} OFDM symbols as

$$\begin{bmatrix} \hat{h}_l[0] \\ \vdots \\ \hat{h}_l[M-1] \end{bmatrix} = \underbrace{\left\{ (\mathbf{X}_l^{(2)})^H \mathbf{X}_l^{(2)} \right\}^{-1}}_{\mathbf{T}_l^{-1}} (\mathbf{X}_l^{(2)})^H \mathbf{y}_l^{(2)} \quad (4.45)$$


 Figure 4.3: Frequency region to estimate $d_{\phi,p}$.

where $\mathbf{X}_l^{(2)}$ is the $(M + N_{\text{tr}}N_{\text{sym}} - 1) \times M$ matrix whose i th row and j th column element are

$$\mathbf{X}_l^{(2)}[i, j] = \begin{cases} 0 & \text{if } i - j < 0, \\ x_l^{(2)}[i - j] & \text{if } 0 \leq i - j < N_{\text{tr}}N_{\text{sym}}, \\ 0 & \text{if } N_{\text{tr}}N_{\text{sym}} \leq i - j, \end{cases} \quad (4.46)$$

and

$$\mathbf{y}_l^{(2)} = [y_l^{(2)}[0] y_l^{(2)}[1] \cdots y_l^{(2)}[M + N_{\text{tr}}N_{\text{sym}} - 2]], \quad (4.47)$$

and N_{sym} is the size of an OFDM symbol. In (4.45), \mathbf{T}_l is a Hermitian Toeplitz matrix [32], and fast algorithms to solve (4.45) with $\mathcal{O}(MN_{\text{tr}}N_{\text{sym}} + M^2)$ multiplications and additions exist [33].

4.3.4 Amplifier nonlinearity estimation

After the channel estimation stage, we estimate the nonlinear coefficients of the amplifiers. To estimate coefficients $d_{\text{tx},p}$ and $d_{\text{rx},p}$, we need to eliminate the effects of IQ imbalance to obtain a high accuracy result. After applying the operator $\mathcal{I}_{\text{rx}}^{-1}$ to both sides of (4.17) and some manipulations, we obtain the following equation:

$$\begin{aligned} \mathcal{I}_{\text{rx}}^{-1}y[n] &= \mathcal{H}\mathcal{I}_{\text{tx}}x[n] + \mathcal{H}(\mathcal{D}_{\text{tx}} - 1)\mathcal{I}_{\text{tx}}x[n] \\ &\quad + (\mathcal{D}_{\text{rx}} - 1)\mathcal{H}\mathcal{D}_{\text{tx}}\mathcal{I}_{\text{tx}}x[n]. \end{aligned} \quad (4.48)$$

In (4.48), $\mathcal{H}\mathcal{I}_{\text{tx}}x[n]$ denotes the linear component of the self-interference signal; $\mathcal{H}(\mathcal{D}_{\text{tx}} - 1)\mathcal{I}_{\text{tx}}x[n]$ is caused by the TX amplifier, and $(\mathcal{D}_{\text{rx}} - 1)\mathcal{H}\mathcal{D}_{\text{tx}}\mathcal{I}_{\text{tx}}x[n]$ is caused by the TX and RX amplifiers. When estimating the nonlinear distortion

coefficient, the signal of the linear component degrades the accuracy of the result. Thus, we need to eliminate the linear component from the received signal. In the discrete-frequency domain, when the frequency index k indicates the sidelobe of the OFDM signal, such as guard bands, the linear component of the self-interference signal is equal to zero. Therefore, when $|k| > N_{\text{sc}}/2$, we can write the following equation on the i th OFDM symbol:

$$Y_{i,l}^{(3)}[k] = \sum_{p=3,5,\dots}^P d_{\text{tx},p} \Psi_{\text{tx},p,i,l}^{(3)}[k] + \sum_{p=3,5,\dots}^P d_{\text{rx},p} \Psi_{\text{rx},p,i,l}^{(3)}[k] + Z_{i,l}^{(3)}[k], \quad (4.49)$$

where

$$Y_{i,l}^{(3)}[k] = \mathcal{F} \hat{\mathcal{L}}_{\text{rx},l}^{-1} y[n], \quad (4.50)$$

$$x_l^{(3)}[n] = \hat{\mathcal{L}}_{\text{tx},l} x[n], \quad (4.51)$$

$$u_l^{(3)}[n] = \mathcal{F}^{-1} \hat{\mathcal{H}}_l \mathcal{F} \hat{\mathcal{D}}_{\text{tx},l} x_l^{(3)}[n], \quad (4.52)$$

$$\Psi_{\text{tx},p,i,l}^{(3)}[k] = \hat{\mathcal{H}}_l \mathcal{F} \left(x_l^{(3)}[n] |x_l^{(3)}[n]|^{p-1} \right), \quad (4.53)$$

$$\Psi_{\text{rx},p,i,l}^{(3)}[k] = \mathcal{F} \left(u_l^{(3)}[n] |u_l^{(3)}[n]|^{p-1} \right), \quad (4.54)$$

and $Z_{i,l}^{(3)}[k]$ is the error caused by the estimation error of the latest estimated values. Thus, we can estimate the coefficients of the nonlinearities with K sidelobe subcarriers by

$$\hat{\mathbf{d}}_l = \left\{ \left(\Psi_l^{(3)} \right)^H \Psi_l^{(3)} \right\}^{-1} \left(\Psi_l^{(3)} \right)^H \mathbf{Y}_l^{(3)}, \quad (4.55)$$

where

$$\hat{\mathbf{d}}_l = [\hat{d}_{\text{tx},3,l} \cdots \hat{d}_{\text{tx},P,l} \hat{d}_{\text{rx},3,l} \cdots \hat{d}_{\text{rx},P,l}]^T, \quad (4.56)$$

$$\Psi_l^{(3)} = \left[(\Psi_{0,l}^{(3)})^T (\Psi_{1,l}^{(3)})^T \cdots (\Psi_{N_{\text{tr}}-1,l}^{(3)})^T \right]^T, \quad (4.57)$$

$$\Psi_{i,l}^{(3)} = \begin{bmatrix} \Psi_{\text{tx},3,i,l}^{(3)}[k_1] \cdots \Psi_{\text{tx},P,i,l}^{(3)}[k_1] & \Psi_{\text{rx},3,i,l}^{(3)}[k_1] \cdots \Psi_{\text{rx},P,i,l}^{(3)}[k_1] \\ \Psi_{\text{tx},3,i,l}^{(3)}[k_2] \cdots \Psi_{\text{tx},P,i,l}^{(3)}[k_2] & \Psi_{\text{rx},3,i,l}^{(3)}[k_2] \cdots \Psi_{\text{rx},P,i,l}^{(3)}[k_2] \\ \vdots & \ddots & \vdots & \ddots & \vdots \\ \Psi_{\text{tx},3,i,l}^{(3)}[k_K] \cdots \Psi_{\text{tx},P,i,l}^{(3)}[k_K] & \Psi_{\text{rx},3,i,l}^{(3)}[k_K] \cdots \Psi_{\text{rx},P,i,l}^{(3)}[k_K] \end{bmatrix}, \quad (4.58)$$

$$\mathbf{Y}_l^{(3)} = [\mathbf{Y}_{0,l}^{(3)} \mathbf{Y}_{1,l}^{(3)} \cdots \mathbf{Y}_{N_{\text{tr}}-1,l}^{(3)}]^T, \quad (4.59)$$

$$\mathbf{Y}_{i,l}^{(3)} = [Y_{i,l}^{(3)}[k_1] Y_{i,l}^{(3)}[k_2] \cdots Y_{i,l}^{(3)}[k_K]], \quad (4.60)$$

and k_1, k_2, \dots, k_K are selected from the discrete-frequency of sidelobe, as shown in Fig. 4.3.

4.3.5 Self-interference cancellation

After some iterations, the canceller cancels the self-interference from the received signal. The received signal, which includes the desired signal from another terminal, is also distorted by the RX amplifier and the IQ mixer imbalance. Thus, the best cancellation approach is nonlinear signal reconstruction and cancellation with post-distortion, which gives the received signal the inverse of the RX distortion. In the proposed scheme, we have the inverse operators $\hat{\mathcal{I}}_{\text{rx},L}^{-1}$ and $\hat{\mathcal{D}}_{\text{rx},L}^{-1}$, which can be used for the post-distortion. Therefore, the signal after cancellation is

$$y_{\text{DC}}[n] = \hat{\mathcal{D}}_{\text{rx},L}^{-1} \hat{\mathcal{I}}_{\text{rx},L}^{-1} y[n] - \hat{\mathcal{H}}_L \hat{\mathcal{D}}_{\text{tx},L} \hat{\mathcal{I}}_{\text{tx},L} x[n]. \quad (4.61)$$

4.3.6 Pseudo code and computational cost

Table 4.2 lists the computational cost of each operator. In addition, Table 4.3, Table 4.4, and Table 4.5 show the computation steps and computational costs of the estimation stages of IQ imbalance, channel, and nonlinearity, respectively. In these tables, N_{fft} is the number of samples of an OFDM symbol after CP removal, and “MULs/DIVs” and “ADDs/SUBs” denote “multiplications and divisions” and “additions and subtractions,” respectively. In the cancellation stage, the proposed scheme computes (4.61), and needs the following computational cost:

- # of MULs/DIVs per OFDM symbol is $N_{\text{sym}} \left(M + M_n (1.5P + 5.5) + \frac{1}{2}P + 6.5 \right)$.
- # of ADDs/SUBs per OFDM symbol is $N_{\text{sym}} \left(M + M_n (P + 2) + \frac{1}{2}P + 3.5 \right)$.
- # of \sqrt{x} per OFDM symbol is $N_{\text{sym}} (M_n + 2)$.

Table 4.2: Computational Cost of Primitive Operations with n -Length Signal

Operation	Defined by	MULs/DIVs	ADDs/SUBs	\sqrt{x}
$\hat{\mathcal{I}}_{\circ,l}s[i]$	(4.21)	n	n	0
$\hat{\mathcal{I}}_{\circ,l}^{-1}s[i]$	(4.25)	$3n$	$2n$	0
$\hat{\mathcal{H}}_l s[i]$	(4.23)	Mn	Mn	0
$\hat{\mathcal{H}}_l S[k]$	(4.24)	n	n	0
$\hat{\mathcal{D}}_{\circ,l}s[i]$ with Horner's algorithm	(4.22)	$\frac{1}{2}(P+1)n$	$\frac{1}{2}(P-1)n$	0
$\hat{\mathcal{D}}_{\circ,l}^{-1}s[i]$	(4.26)	$nM_n(P+2)$	$nM_n(1.5P+5.5)+2n$	$n(M_n+2)$
Solve triangular system [33, sec. 5.4]	–	$\frac{1}{2}n^2$	$\frac{1}{2}n^2$	0
Solve Toeplitz system	–	$3n^2$	$3n^2$	0
by Schur algorithm [33, sec. 5.4]	–	$\frac{1}{6}n^3 + \frac{1}{2}n^2 - \frac{5}{3}n + 1$	$\frac{1}{6}n^3 - \frac{1}{6}n$	n
Cholesky decomposition [34]	–	$\frac{1}{6}n^3 + \frac{3}{2}n^2 - \frac{5}{3}n + 1$	$\frac{1}{6}n^3 + n^2 - \frac{1}{6}n$	n
Solve Hermite system	–			
with Cholesky decomposition	–			

Table 4.3: Pseudo Code and Computational Cost of IQI Estimation Stage

Step	MULs/DIVs	ADDs/SUBs	\sqrt{x}
$x_l^{(1)}[n] \leftarrow (4.31)$	$N_{\text{sym}}N_{\text{tr}}\left(\frac{1}{2}P+4.5\right)$	$N_{\text{sym}}N_{\text{tr}}\left(\frac{1}{2}P+2.5\right)$	0
$y_l^{(1)}[n] \leftarrow (4.32)$	$N_{\text{sym}}N_{\text{tr}}\left(M_n(1.5P+5.5)+6\right)$	$N_{\text{sym}}N_{\text{tr}}\left(M_n(P+2)+3\right)$	$N_{\text{sym}}N_{\text{tr}}(M_n+2)$
Apply FFT to each symbol of $x_l^{(1)}[n]$	$\frac{1}{2}N_{\text{fft}}N_{\text{tr}}\log_2 N_{\text{fft}}$	$N_{\text{fft}}N_{\text{tr}}\log_2 N_{\text{fft}}$	0
Apply FFT to each symbol of $y_l^{(1)}[n]$	$\frac{1}{2}N_{\text{fft}}N_{\text{tr}}\log_2 N_{\text{fft}}$	$N_{\text{fft}}N_{\text{tr}}\log_2 N_{\text{fft}}$	0
Solve LS of (4.35) for all k	$N_{\text{sc}}(6N_{\text{tr}}+5)$	$N_{\text{sc}}(6N_{\text{tr}}+5)$	$2N_{\text{sc}}$
Solve LS of (4.39)	$6N_{\text{sc}}+5$	$6N_{\text{sc}}+5$	2

Table 4.4: Pseudo Code and Computational Cost of Channel Estimation Stage

Step	MULs/DIVs	ADDs/SUBs	\sqrt{x}
$x_l^{(2)}[n] \leftarrow (4.42)$	$N_{\text{sym}} N_{\text{tr}} \left(\frac{1}{2}P + 1.5 \right)$	$\frac{1}{2} N_{\text{sym}} N_{\text{tr}} (P + 1)$	0
$y_l^{(2)}[n] \leftarrow (4.43)$	$N_{\text{sym}} N_{\text{tr}} (M_n (1.5P + 5.5) + 5)$	$N_{\text{sym}} N_{\text{tr}} (M_n (P + 2) + 2)$	$N_{\text{sym}} N_{\text{tr}} (M_n + 2)$
Compute $\mathbf{T}_l = (\mathbf{X}_l^{(2)})^H \mathbf{X}_l^{(2)}$	$M \left(\frac{1}{2}M + N_{\text{sym}} N_{\text{tr}} - \frac{1}{2} \right)$	$M \left(\frac{1}{2}M + N_{\text{sym}} N_{\text{tr}} - \frac{1}{2} \right)$	0
Compute $\mathbf{u}_l = (\mathbf{X}_l^{(2)})^H \mathbf{y}_l^{(2)}$	$M (M + N_{\text{sym}} N_{\text{tr}} - 1)$	$M (M + N_{\text{sym}} N_{\text{tr}} - 1)$	0
Solve $\mathbf{T}_l \hat{\mathbf{h}}_l = \mathbf{u}_l$	$3M^2$	$3M^2$	0

Table 4.5: Pseudo Code and Computational Cost of Nonlinear Estimation Stage

Step	MULs/DIVs	ADDs/SUBs	\sqrt{x}
apply FFT to $\hat{h}_l[m]$	$\frac{1}{2} N_{\text{fft}} \log_2 N_{\text{fft}}$	$N_{\text{fft}} \log_2 N_{\text{fft}}$	0
$Y_{i,l}^{(3)}[k] \leftarrow (4.50)$	$N_{\text{tr}} \left(\frac{1}{2} N_{\text{fft}} \log_2 N_{\text{fft}} + 3N_{\text{sym}} \right)$	$N_{\text{tr}} (N_{\text{fft}} \log_2 N_{\text{fft}} + 2N_{\text{sym}})$	0
$x_l^{(3)}[n] \leftarrow (4.51)$	$N_{\text{fft}} N_{\text{tr}}$	$N_{\text{fft}} N_{\text{tr}}$	0
$u_l^{(3)}[n] \leftarrow (4.52)$	$N_{\text{fft}} N_{\text{tr}} \left(\frac{1}{2}P + \log_2 N_{\text{fft}} + 1.5 \right)$	$N_{\text{fft}} N_{\text{tr}} \left(\frac{1}{2}P + 2 \log_2 N_{\text{fft}} - \frac{1}{2} \right)$	0
$\Psi_{\text{rx},p,i,l}^{(3)}[k] \leftarrow (4.53)$	$\frac{1}{2} N_{\text{tr}} (N_{\text{fft}} (P + 1) + (K + \frac{1}{2} N_{\text{fft}} \log_2 N_{\text{fft}}) (P - 1))$	$\frac{1}{2} N_{\text{fft}} N_{\text{tr}} (P - 1) \log_2 N_{\text{fft}}$	0
$\Psi_{\text{rx},p,i,l}^{(3)}[k] \leftarrow (4.54)$	$N_{\text{fft}} N_{\text{tr}} \left(\frac{1}{2}P + \frac{1}{4} (P - 1) \log_2 N_{\text{fft}} + \frac{1}{2} \right)$	$\frac{1}{2} N_{\text{fft}} N_{\text{tr}} (P - 1) \log_2 N_{\text{fft}}$	0
Solve LS of (4.55)	$KN_{\text{tr}}P (P - 1) + \frac{P^3}{6} + P^2 - \frac{25P}{6} + 4$	$KN_{\text{tr}}P (P - 1) + \frac{P^3}{6} + \frac{P^2}{2} - \frac{5P}{3} + 1$	$P - 1$

4.4 Numerical Simulations

4.4.1 Simulation environment

We perform equivalent baseband simulations of the full-duplex transceiver to verify the proposed estimation and cancellation scheme. Table 4.6 and Table 4.7 list the parameters of the simulations. The baseband signal simulator is implemented with D programming language, and the details of the simulator are as follows.

In the simulations, the self-interference channel, which consists of the wireless multipath channel and the impulse response of the RF self-interference canceller, is modeled as a quasi-static Rayleigh fading channel with a constant impulse response on a simulation trial and has different impulse responses between different simulation trials. The power delay profile of the self-interference channel is modeled as an exponential decay profile with 40 dB decay at 48 delay samples, and each tap of the channel impulse response is independent and identically distributed on the complex normal distribution.

The most severe bottleneck for self-interference cancellation is the non-idealities of the IQ mixers, PA, and LNA. The simulation model of IQ mixers achieves IQ imbalance by adding an image signal, and its coefficients are predetermined based on the value of IRR. The nonlinearity of the PA and LNA is characterized by the Rapp model [35], which is often used to simulate the baseband behaviors of class AB solid-state amplifiers. The output baseband signal of a Rapp modeled amplifier is described as

$$v_{\text{out}} = \frac{Gv_{\text{in}}}{\left[1 + \left(\frac{|v_{\text{in}}|}{V_{\text{sat}}}\right)^{2s}\right]^{\frac{1}{2s}}}, \quad (4.62)$$

where v_{in} and v_{out} are the input and output signals of the amplifier, respectively; G , V_{sat} , and s are the gain, saturated input level, and smoothness factor of the Rapp model, respectively, and they characterize the nonlinearity of the amplifier.

To cancel nonlinearities up to seventh order, the maximum order of the nonlinear coefficients estimation, which is a parameter of the operator $\hat{\mathcal{D}}_{\circ,l}$ in (4.22), is $P = 7$ for the proposed canceller. Furthermore, the number of taps of channel estimation, which is a parameter of the operator $\hat{\mathcal{H}}_l$ in (4.23), is $M = 48$.

Following the standard convention, we define the self-interference cancellation

Table 4.6: OFDM Modulation Specifications

Parameter	Value
Modulation	OFDM
Constellation	16QAM
FFT size	64
Active subcarriers	52
Cyclic prefix size	16
Bandwidth	20 MHz

ratio (SICR), which indicates the performance of a digital canceller, as

$$\text{SICR} = \frac{\mathbb{E} [|y[n]|^2]}{\mathbb{E} [|y_{\text{DC}}[n]|^2]}. \quad (4.63)$$

In addition, we define the amount of attenuation of the antenna separation and the RF self-interference cancellation as

$$A_{\text{RF}} = \frac{\mathbb{E} [|x_{\text{PA}}[n]|^2]}{\mathbb{E} [|h_{\text{SI}}[m] * x_{\text{PA}}[n] - h_{\text{Cir}}[m] * x_{\text{PA}}[n]|^2]}. \quad (4.64)$$

Then, the self-interference to noise power ratio (INR) is defined as

$$\begin{aligned} \text{INR (dB)} = & \text{Transmission Power (dBm)} - \text{AWGN Power (dBm)} \\ & - \text{LNA Noise Figure (dB)} - A_{\text{RF}} \text{ (dB)}, \end{aligned} \quad (4.65)$$

which indicates the theoretical limit of the SICR when the LNA is not saturated.

Table 4.7: Simulation Specifications

Parameter	Value
Oversampling rate	8
Sampling rate	$20 \text{ MHz} \times 8 = 160 \text{ MHz}$
SI channel after RF-SIC	Rayleigh fading
SI channel length	48 samples
Channel profile	Exponential decay
IRR	25 dB
Transmission power	23 dBm
PA Gain	30 dB
PA input saturation level	$V_{\text{sat,PA}} = 0 \text{ dBm}$ (IBO = 7 dB @ Transmission power = 23 dBm)
PA smoothness factor	3
LNA noise figure	4 dB
LNA Gain	20 dB
LNA input saturation level	$V_{\text{sat,LNA}} = -6 \text{ dBm}$ (IIP3 is about 0.6 dBm)
LNA smoothness factor	1
# of ADC bits	14 bit
Order of canceller	$P = 7$
# of taps of canceller	$M = 48$
Trials	201

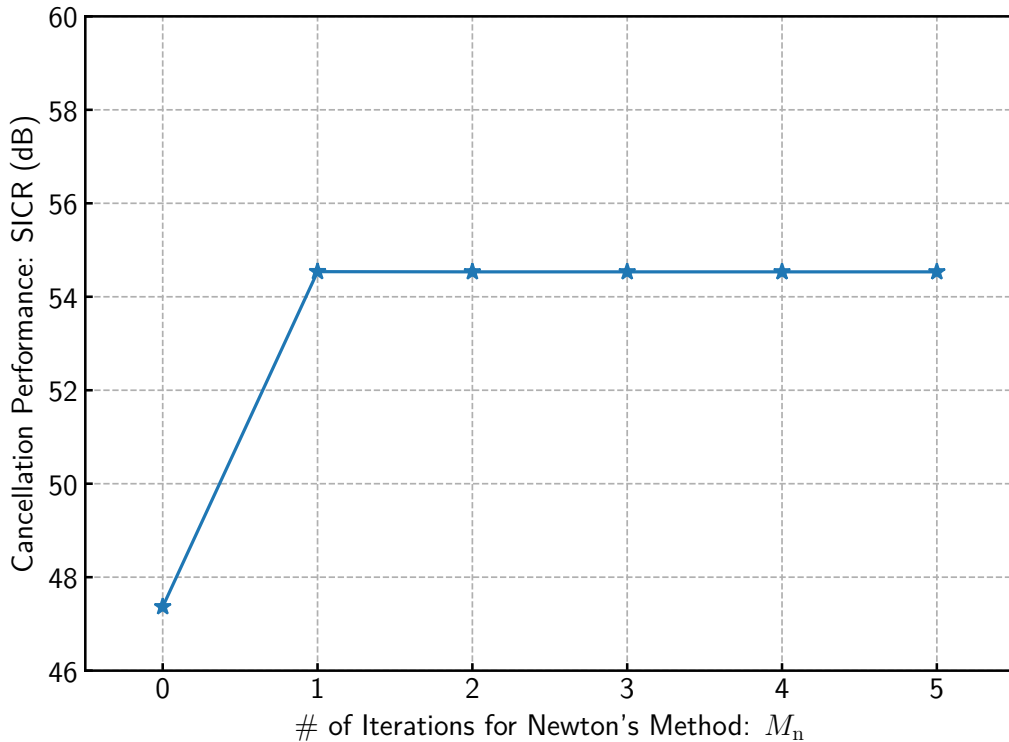


Figure 4.4: Performance of the proposed canceller with different numbers of iterations of Newton's method. The INR is 60 dB, and the proposed canceller estimates parameters in ten iterations. The canceller is trained with 20 OFDM symbols.

4.4.2 Results and discussions

Fig. 4.4 shows the performance of the proposed canceller with different numbers of iterations of Newton's method. In this result, the received signal saturates the LNA, and it is highly distorted. If the number of iterations is zero, Newton's method outputs the input signal without any changes. Thus, the estimated coefficients of the LNA nonlinearity are not used effectively for the next iteration, and the cancellation performance of the proposed scheme is degraded. When the number of the iteration is one, the cancellation performance is saturated at approximately 54 dB. Therefore, in the rest of this chapter, the number of Newton's method iterations is set as $M_n = 1$.

In Fig. 4.5, the performance of the proposed canceller is shown with different numbers of iterations of the estimation process in the same condition as that in

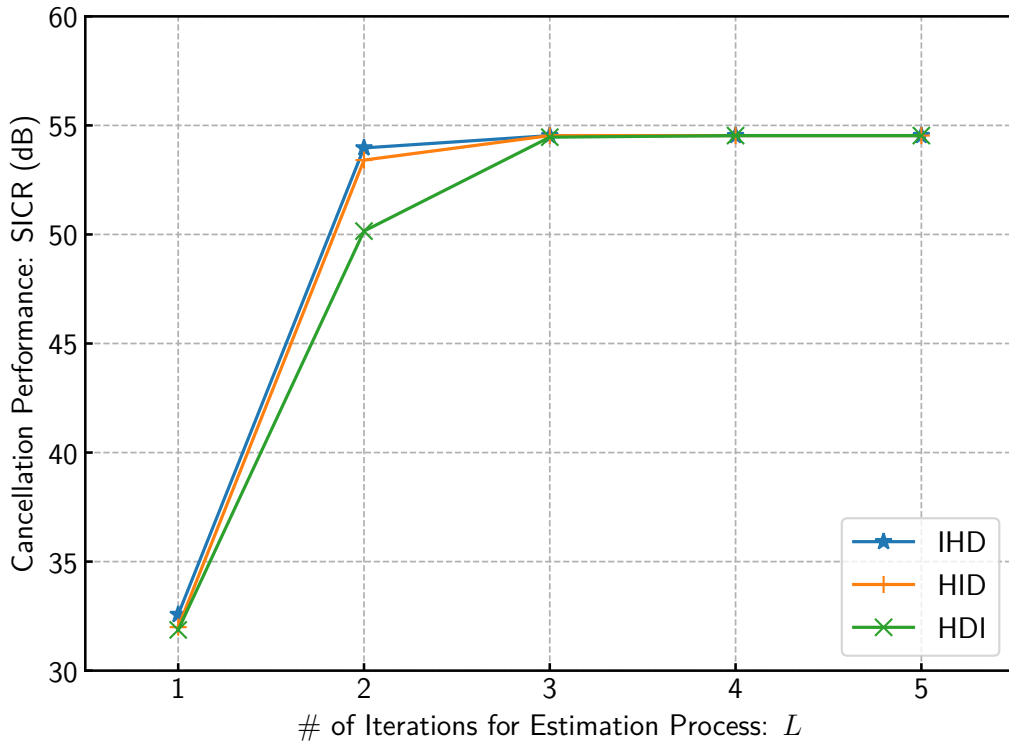


Figure 4.5: Performance of the proposed canceller with different numbers of iterative estimation and different orders of estimation. The INR is 60 dB, and the number of iterations of Newton’s method is one. The canceller is trained with 20 OFDM symbols.

Fig. 4.4. Labels, e.g. “IHD”, indicate the order of estimation stages, such as \mathcal{I}_\diamond , \mathcal{H} , and \mathcal{D}_\diamond , and “IHD” indicates the order described in Section 4.3. When the number of iterations is one, the proposed scheme does not use the first estimated parameters to improve the estimation quality. Thus, the cancellation performance with the single estimation iteration is approximately 22 dB lower than the saturated performance. If the number of iterations increases from one to two, the performance of the proposed scheme is significantly improved. Moreover, “IHD” achieves the best performance over the other orders. The reason is that the estimation stage of the imbalance coefficients does not depend on the estimated value of channel impulse response, and the number of these parameters is only two. In other words, the stage which is easiest to estimate is the estimation of the IQ imbalance coefficients. Therefore, we applied “IHD”-order and three-time iterations for the parameter estimation process because the proposed scheme can achieve sufficiently high cancellation performance

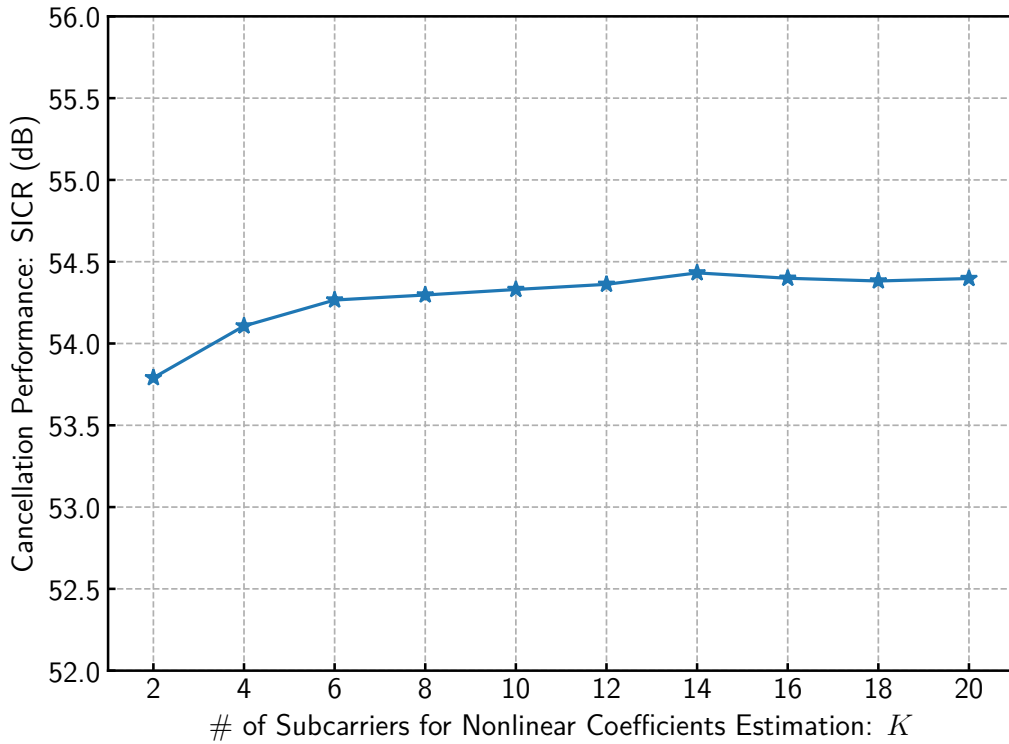


Figure 4.6: Performance of the proposed canceller with different numbers of subcarriers for estimation of nonlinear coefficients. The INR is 60 dB; the number of iterations of Newton’s method is one; the number of iterations of the estimation process is three. The canceller is trained with 20 OFDM symbols.

with these settings.

Fig. 4.6 shows the performance of the proposed canceller with different values of K , which is the number of sidelobe subcarriers for nonlinear coefficients estimations. The performance difference between $K = 2$ and $K = 20$ is less than 1 dB. Thus, there is no significant performance degradation, even if only a small number of sidelobe subcarriers can be used for estimation. Besides, the performance with $K = 8$ or more is almost the same as that with $K = 20$, and it is possible to estimate by using the guard band. Therefore, in the rest of this section, we use eight sidelobe subcarriers ($K = 8$) to estimate nonlinear coefficients.

In Fig. 4.7, we compare the performance of the proposed canceller (denoted as “It”) and a Hammerstein canceller with 20 basis functions (denoted as “Ha”) that can estimate and regenerate seventh-order PA nonlinearities and a 48-samples-delayed signal correctly. To make fair comparisons with the proposed

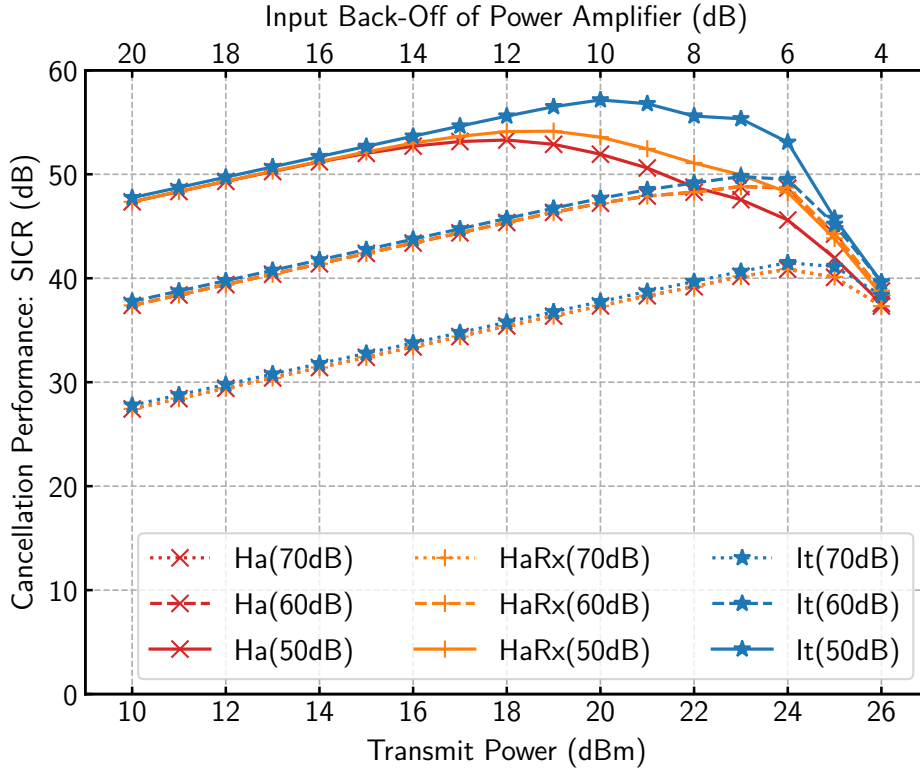


Figure 4.7: Performance of each canceller with 100 training symbols on different amounts of RF attenuation A_{RF} and different transmission powers. The numbers in parentheses in the legend denote the values of A_{RF} . In the proposed scheme, $M_n = 1$, $L = 3$, and $K = 8$.

canceller, the LS algorithm is used as the estimation algorithm for the Hammerstein canceller. For comparison with other methods that consider LNA nonlinearity, the author also shows the performance of a canceller (denoted as “HaRx”) based on the technique described in [15]. Because the RX nonlinearity mitigation technique presented in [15] is designed for wideband receivers, the HaRx canceller combines the technique described in [15] and the Hammerstein canceller. In Fig. 4.7, we give 100 training OFDM symbols to each canceller to compare their best performance. If the RF attenuation A_{RF} , which contains antenna separation and RF circuit cancellation, is larger than 60 dB, the performance of the three cancellers is almost the same. Additionally, if A_{RF} is 50 dB, the proposed canceller and the HaRx canceller achieve higher performance than the Hammerstein canceller when the transmission power is higher than 17 dBm. In this region, the received signal is larger than -33 dBm,

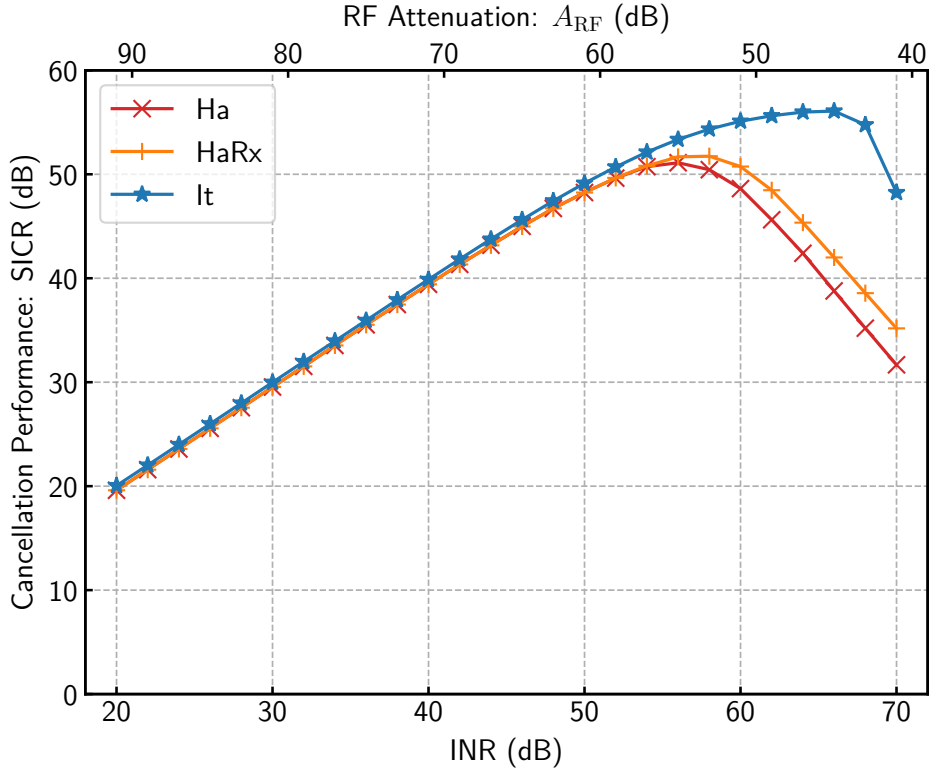


Figure 4.8: Performance of each canceller with 100 training symbols and different self-interference powers. In this result, $M_n = 1$, $L = 3$, and $K = 8$.

and the nonlinear distortion of the LNA becomes larger than the thermal noise level. The Hammerstein canceller cannot reduce the nonlinearity of the LNA, and its performance decreases significantly as the received power increases. In contrast, the HaRx canceller and the proposed canceller can mitigate the received self-interference signal distorted by the LNA. However, the HaRx canceller only improves the cancellation performance by a few dB because it is just a simple combination of the Hammerstein canceller and technique reported in [15], and each of its components operates independently. The proposed canceller achieves a better performance improvement than the HaRx canceller because parameters are estimated in cooperation with the three stages.

For a more detailed discussion, we compare the cancellers in Fig. 4.8, which shows the canceller performance when the INR is changed from 20 to 70 dB. Because the power of the received self-interference signal increases as the INR increases, the nonlinearity of the LNA increases as the INR increases. When the INR is larger

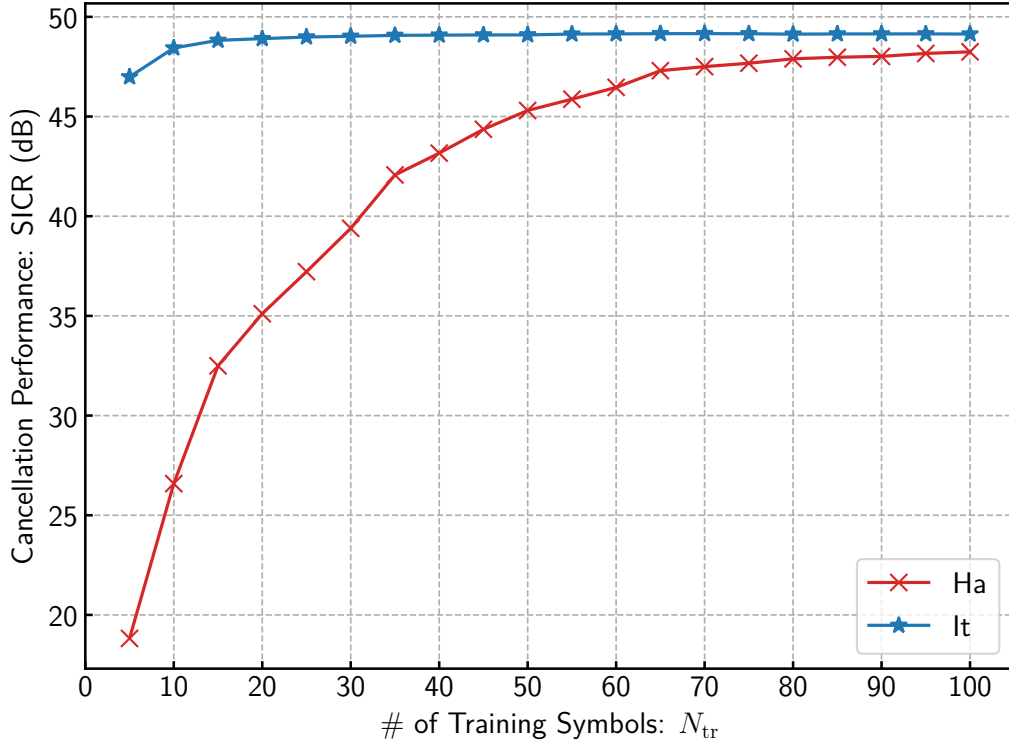


Figure 4.9: Convergence of each canceller at INR = 50 dB. In this result, $M_n = 1$, $L = 3$, and $K = 8$.

than approximately 52 dB, the performance of the Hammerstein canceller reaches 51 dB because it cannot regenerate the nonlinearity of the LNA. Fig. 4.8 shows that the proposed canceller achieves a performance up to 20 dB higher than that of the Hammerstein canceller, which indicates that the proposed canceller can apply the inverse of the LNA nonlinearity to the received signal and endure higher power of self-interference.

To discuss the convergence speed, we consider the results shown in Fig. 4.9 and 4.10. Fig. 4.9 shows the convergence performance of each canceller when the number of training symbols changes from 5 to 100. When a canceller is trained sufficiently, it achieves a cancellation performance close to 50 dB because the INR is 50 dB in these results. In these figures, we do not include the performance of the HaRx canceller because the power of the signal distorted by the LNA is lower than the thermal noise level in the situation, and the performance of the HaRx canceller is almost the same as that of the Hammerstein canceller. To achieve 45 dB cancellation, the Hammerstein canceller needs 50 OFDM symbols, while the

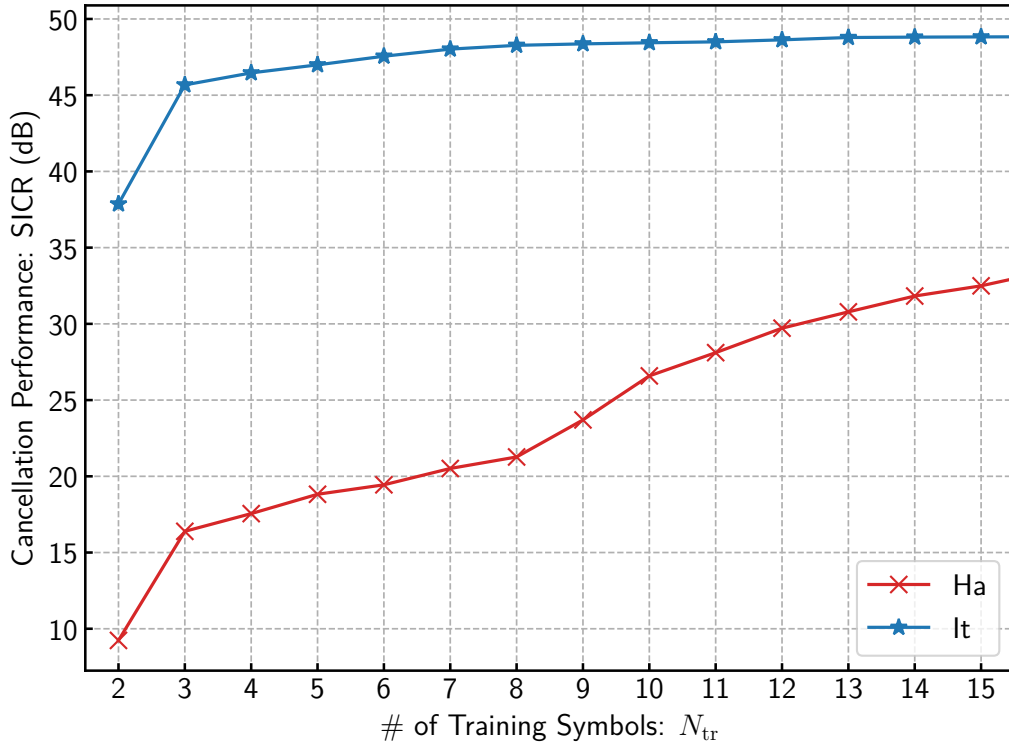


Figure 4.10: Short span convergence of each canceller at INR = 50 dB. In this result, $M_n = 1$, $L = 3$, and $K = 8$.

proposed canceller requires only five or fewer. From Fig. 4.10, we can confirm that the proposed canceller achieves around 47 dB cancellation with three training OFDM symbols and has a convergence speed more than 16 times higher than the Hammerstein canceller. Although the models of the two cancellers are different, the number of parameters is a rough measure of the convergence speed of both. The Hammerstein canceller has $20 \times 48 = 960$ coefficients. In contrast, the proposed canceller has $48 + 1 + 3 + 1 + 3 = 56$ coefficients, which are approximately 1/17 less than those of the Hammerstein canceller. From the comparison of the number of parameters, it can be shown that the proposed canceller has a faster convergence speed than the Hammerstein one.

4.4.3 Limitations of the proposed canceller

It is important to evaluate under what condition the proposed canceller performs worse than the Hammerstein canceller. Fig. 4.7 and Fig. 4.8 show comparisons

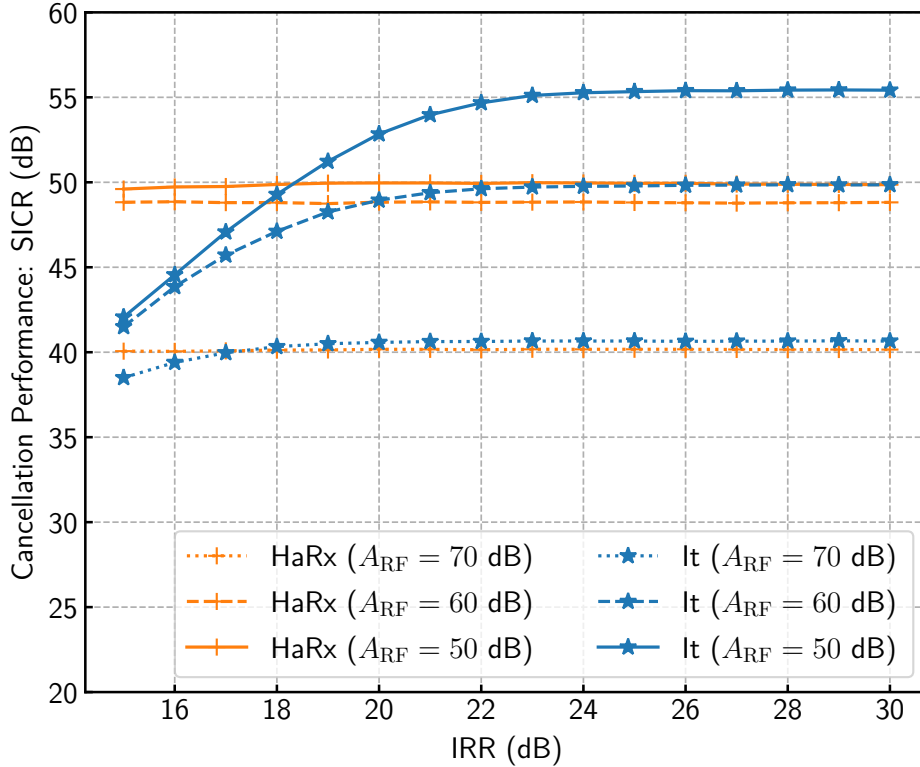


Figure 4.11: Performance of each canceller with 100 training symbols and different IRR values. In this result, $M_n = 1$, $L = 3$, and $K = 8$.

of the performance of the cancellers when the transmission power and the gain of the self-interference channel A_{RF} are changed, respectively. We confirm that the proposed canceller achieves the same or better performance than the Hammerstein canceller even if the nonlinearities of the PA and LNA are severe. We further discuss the limitation of the proposed canceller considering the performance of cancellers at various IRR values, as shown in Fig. 4.11. When the IQ imbalance is so strong that the IRR is less than 20 dB, the performance of the proposed canceller deteriorates significantly. When the IRR is very low, the assumption $|b_{rx}b_{tx}^*| \ll 1$, which is necessary to obtain (4.38) and derive the imbalance estimation stage, no longer holds. Thus, the proposed canceller cannot estimate the coefficients of the IQ imbalance well with severe IQ imbalance. The IRR of less than 20 dB is extremely severe case [30, 31], so that the degradation will hardly be a problem on actual terminals.

4.4.4 Computational cost

The computational cost is an important performance indicator of self-interference cancellers. The parameters, and their values, related to computational cost are listed in Table 4.8. The number of both multiplications and additions for training the Hammerstein canceller with 20 basis functions can be expressed as $20MN_{\text{tr}}N_{\text{sym}} \approx 3.07 \times 10^7$ when we perform the pseudo-inverse matrix of the LS algorithm a priori [3]. If the Hammerstein canceller is trained with a data signal instead of a training signal, substantial computational power is required due to the pseudo-inverse matrix. For training with the data signal, the least mean squares (LMS) algorithm is a practical solution. The number of both multiplications and additions of the LMS algorithm for the Hammerstein canceller with 20 basis functions is $40M$ per sample [9]. For training with 50 OFDM symbols, the LMS algorithm needs 6.14×10^7 multiplications and additions, which are more than those required by the LS algorithm with the pre-calculation technique. Moreover, the LMS algorithm is less convergent than the LS algorithm, so it needs a longer signal compared to the LS algorithm; more specifically, it requires more than 50 OFDM symbols and 6.14×10^7 multiplications and additions. The recursive-LS algorithm exhibits fast convergence like the LS algorithm, but its computational cost is not practical for the time-domain Hammerstein canceller [9].

We have discussed the computational cost of the proposed scheme in Section 4.3.6. According to the values in Table 4.8, the number of MULs/DIVs, ADDs/SUBs, and \sqrt{x} required for training the proposed canceller are approximately 1.23×10^6 , 1.28×10^6 , and 3.49×10^4 , respectively. Note that this cost is the same whether the used signal is a training signal or a data signal because we cannot implement any pre-calculation techniques for the proposed canceller. There is a multiplier-free algorithm to compute \sqrt{x} [36], which needs only 10 times addition for 14 bit fixed-point real value, which requires accuracy of 10^{-5} or less. Thus, the total cost to compute 3.49×10^4 times \sqrt{x} is sufficiently smaller than the total cost of 1.28×10^6 ADDs/SUBs. Therefore, the proposed canceller can complete training with less than one-tenth of the computational cost required to train the Hammerstein canceller.

For self-interference cancellation of an OFDM symbol, the proposed canceller needs about 4.73×10^4 MULs/DIVs, 4.10×10^4 ADDs/SUBs, and 1.92×10^3 square-roots. The computational cost of the Hammerstein canceller for cancellation of an OFDM symbol is $20MN_{\text{sym}} \approx 6.14 \times 10^5$ multiplications and additions. Thus, the

Table 4.8: Parameters, and Their Values, for Comparing Computational Costs

Parameter	Proposed	Hammerstein
N_{sym}	$(64 + 16) \times 8 = 640$	
N_{fft}	$64 \times 8 = 512$	
N_{sc}	52	
M	48	
P	7	
N_{tr}	3	50
M_{n}	1	–
K	8	–
L	3	–

proposed canceller can significantly reduce the computational cost of cancellation compared with the Hammerstein canceller.

4.5 Conclusion

The author has introduced operators that express characteristics of each RF component in a minimum form and have derived a nonlinear self-interference signal model. Then, the author has proposed a novel nonlinear self-interference canceller to effectively reduce the nonlinear self-interference caused by TX and RX IQ mixers, the PA, and the LNA. The estimation process of the proposed canceller consists of three stages, which estimate the characteristic of the corresponding operator of each RF component. Simulation results show that the proposed canceller can estimate and remove the received self-interference signal, which is distorted by the LNA. In addition, the proposed canceller achieves higher cancellation performance with fewer learning symbols and lower computational cost than the Hammerstein canceller.

Appendix 4.A Derivations of (4.26)–(4.30)

The relation of the input x and output y of an estimated nonlinear amplifier $\diamond \in \{\text{tx}, \text{rx}\}$ can be written as

$$\begin{aligned}
 y &= \hat{\mathcal{D}}_{\diamond, l} x = \sum_{p=1,3,\dots}^P \hat{d}_{\diamond, p, l} x |x|^{p-1} \\
 &= \hat{f}_{\diamond, l}(|x|) \frac{x}{|x|} \exp(j\hat{\phi}_{\diamond, l}(|x|)), \tag{4.66}
 \end{aligned}$$

where $\hat{f}_{\diamond,l}(|x|)$ and $\hat{\phi}_{\diamond,l}(|x|)$ are the amplitude-to-amplitude (AM/AM) modulation and amplitude-to-phase (AM/PM) modulation of the estimated amplifier, respectively. The amplitude of the output y can be written as

$$|y| = \hat{f}_{\diamond,l}(|x|) = \left| \sum_{p=1,3,\dots}^P \hat{d}_{\diamond,p,l} x |x|^{p-1} \right|. \quad (4.67)$$

Then, we can compute the amplitude of the input signal $|x|$ from the amplitude of the output signal $|y|$ by Newton's method as

$$r_{k+1} = r_k - \frac{|u_k| - |y|}{\hat{f}'_{\diamond,l}(r_k)}, \quad (4.68)$$

where

$$\hat{f}'_{\diamond,l}(r) = \frac{\operatorname{Re}[u_k] \operatorname{Re}[v_k] + \operatorname{Im}[u_k] \operatorname{Im}[v_k]}{|u_k|}, \quad (4.69)$$

$$u_k = \hat{\mathcal{D}}_{\diamond,l} r_k, \quad (4.70)$$

$$v_k = \frac{d}{dr} \left(\hat{\mathcal{D}}_{\diamond,l} r \right) \Big|_{r=r_k} = \sum_{p=1,3,\dots}^P \hat{d}_{\diamond,p,l} p r_k^{p-1}. \quad (4.71)$$

Then, (4.28) is derived from (4.68)–(4.71). Moreover, from (4.66), the phase of input signal can be written as

$$\frac{x}{|x|} = \frac{y}{\hat{f}_{\diamond,l}(|x|)} \exp(-j\phi_{\diamond,l}(|x|)) \approx \frac{y}{|y|} \frac{|u_{M_n}|}{u_{M_n}}. \quad (4.72)$$

The final approximation of (4.72) holds when $|x| \approx r_{M_n}$. Finally, (4.26) is derived from (4.28) and (4.72).

References

- [1] S. Li and R. D. Murch, “An investigation into baseband techniques for single-channel full-duplex wireless communication systems,” *IEEE Trans. Wireless Commun.*, vol. 13, no. 9, pp. 4794–4806, Sept. 2014.
- [2] D. Bharadia, E. McMillin, and S. Katti, “Full duplex radios,” in *Proc. ACM SIGCOMM'13*, 2013.
- [3] L. Anttila, D. Korpi, V. Syrjälä, and M. Valkama, “Cancellation of power amplifier induced nonlinear self-interference in full-duplex transceivers,” in *Proc. 47th Asilomar Conf. Signals, Syst., Comput.*, Nov. 2013.
- [4] L. Anttila, D. Korpi, E. Antonio-Rodriguez, R. Wichman, and M. Valkama, “Modeling and efficient cancellation of nonlinear self-interference in MIMO full-duplex transceivers,” in *Proc. IEEE GC Wkshps*, Dec. 2014, pp. 777–783.
- [5] M. Heino, D. Korpi, T. Huusari, E. Antonio-Rodriguez, S. Venkatasubramanian, T. Riihonen, L. Anttila, C. Icheln, K. Haneda, R. Wichman, and M. Valkama, “Recent advances in antenna design and interference cancellation algorithms for in-band full duplex relays,” *IEEE Commun. Mag.*, vol. 53, no. 5, pp. 91–101, May 2015.
- [6] D. Korpi, Y.-S. Choi, T. Huusari, L. Anttila, S. Talwar, and M. Valkama, “Adaptive nonlinear digital self-interference cancellation for mobile inband full-duplex radio: Algorithms and RF measurements,” in *Proc. IEEE GLOBECOM*, Dec. 2015.
- [7] D. Korpi, T. Huusari, Y.-S. Choi, L. Anttila, S. Talwar, and M. Valkama, “Digital self-interference cancellation under nonideal RF components: Advanced algorithms and measured performance,” in *Proc. IEEE SPAWC*, June 2015, pp. 286–290.

- [8] K. Komatsu, Y. Miyaji, and H. Uehara, “Frequency-domain Hammerstein self-interference canceller for in-band full-duplex OFDM systems,” in *Proc. IEEE WCNC*, Mar. 2017.
- [9] —, “Basis function selection of frequency-domain Hammerstein self-interference canceller for in-band full-duplex wireless communications,” *IEEE Trans. Wireless Commun.*, vol. 17, no. 6, pp. 3768–3780, June 2018.
- [10] L. Tian, S. Wang, Z. Cheng, and X. Bu, “All-digital self-interference cancellation in zero-IF full-duplex transceivers,” *China Communications*, vol. 13, no. 11, pp. 27–34, Nov. 2016.
- [11] P. P. Campo, D. Korpi, L. Anttila, and M. Valkama, “Nonlinear digital cancellation in full-duplex devices using spline-based hammerstein model,” in *Proc. IEEE GC Wkshps*, Dec. 2018.
- [12] E. Ahmed and A. M. Eltawil, “All-digital self-interference cancellation technique for full-duplex systems,” *IEEE Trans. Wireless Commun.*, vol. 14, no. 7, pp. 3519–3532, July 2015.
- [13] J. Li, H. Zhang, and M. Fan, “Digital self-interference cancellation based on independent component analysis for co-time co-frequency full-duplex communication systems,” *IEEE Access*, vol. 5, pp. 10 222–10 231, 2017.
- [14] E. Ahmed, A. M. Eltawil, and A. Sabharwal, “Self-interference cancellation with nonlinear distortion suppression for full-duplex systems,” in *Proc. 47th Asilomar Conf. Signals, Syst., Comput.*, Nov. 2013, pp. 1199–1203.
- [15] M. Grimm, M. Allen, J. Marttila, M. Valkama, and R. Thoma, “Joint mitigation of nonlinear RF and baseband distortions in wideband direct-conversion receivers,” *IEEE Trans. Microw. Theory Techn.*, vol. 62, no. 1, pp. 166–182, Jan. 2014.
- [16] M. Valkama, A. S. H. Ghadam, L. Anttila, and M. Renfors, “Advanced digital signal processing techniques for compensation of nonlinear distortion in wideband multicarrier radio receivers,” *IEEE Trans. Microw. Theory Techn.*, vol. 54, no. 6, pp. 2356–2366, June 2006.
- [17] E. A. Keehr and A. Hajimiri, “Equalization of third-order intermodulation products in wideband direct conversion receivers,” *IEEE J. Solid-State Circuits*, vol. 43, no. 12, pp. 2853–2867, Dec. 2008.
- [18] Q. Zou, M. Mikhemar, and A. H. Sayed, “Digital compensation of cross-modulation distortion in software-defined radios,” *IEEE J. Sel. Topics Signal Process.*, vol. 3, no. 3, pp. 348–361, June 2009.

- [19] J. Liu, H. Quan, Z. Li, H. Sun, and D. Yuan, “Digital nonlinear self-interference cancellation based on LMS-Volterra algorithm,” in *Proc. 3rd Int. Conf. Inf. Sci. Control Eng. (ICISCE)*, July 2016, pp. 1298–1302.
- [20] D. Korpi, M. Turunen, L. Anttila, and M. Valkama, “Modeling and cancellation of self-interference in full-duplex radio transceivers: Volterra series-based approach,” in *Proc. IEEE ICC Wkshps*, May 2018.
- [21] M. A. Islam and B. Smida, “A comprehensive self-interference model for single-antenna full-duplex communication systems,” in *Proc. IEEE ICC*, May 2019.
- [22] M. Jain, J. I. Choi, T. Kim, D. Bharadia, S. Seth, K. Srinivasan, P. Levis, S. Katti, and P. Sinha, “Practical, real-time, full duplex wireless,” in *Proc. ACM MobiCom'11*, 2011.
- [23] D. Korpi, L. Anttila, V. Syrjälä, and M. Valkama, “Widely linear digital self-interference cancellation in direct-conversion full-duplex transceiver,” *IEEE J. Sel. Areas Commun.*, vol. 32, no. 9, pp. 1674–1687, Sept. 2014.
- [24] E. Ahmed, A. M. Eltawil, and A. Sabharwal, “Self-interference cancellation with phase noise induced ICI suppression for full-duplex systems,” in *Proc. IEEE GLOBECOM*, Dec. 2013, pp. 3384–3388.
- [25] R. Li, A. Masmoudi, and T. Le-Ngoc, “Self-interference cancellation with nonlinearity and phase-noise suppression in full-duplex systems,” *IEEE Trans. Veh. Technol.*, vol. 67, no. 3, pp. 2118–2129, Mar. 2018.
- [26] M. Valkama and M. Renfors, “Digital filter design for I/Q imbalance compensation,” in *Proc. 10th European Signal Process. Conf. (EUSIPCO)*, Sept. 2000, pp. 1–4.
- [27] M. Sakai, H. Lin, and K. Yamashita, “Self-interference cancellation in full-duplex wireless with IQ imbalance,” *Elsevier Phy. Commun.*, vol. 18, pp. 2–14, Mar. 2016.
- [28] S. Benedetto and E. Biglieri, *Principles of Digital Transmission: With Wireless Applications*. Norwell, MA, USA: Kluwer Academic Publishers, 1999.
- [29] M. Duarte, C. Dick, and A. Sabharwal, “Experiment-driven characterization of full-duplex wireless systems,” *IEEE Trans. Wireless Commun.*, vol. 11, no. 12, pp. 4296–4307, Dec. 2012.
- [30] M. Valkama, M. Renfors, and V. Koivunen, “Advanced methods for I/Q imbalance compensation in communication receivers,” *IEEE Trans. Signal Process.*, vol. 49, no. 10, pp. 2335–2344, 2001.

- [31] A. Tarighat and A. Sayed, “Joint compensation of transmitter and receiver impairments in OFDM systems,” *IEEE Trans. Wireless Commun.*, vol. 6, no. 1, pp. 240–247, Jan. 2007.
- [32] T. Bäckström, “Vandermonde factorization of Toeplitz matrices and applications in filtering and warping,” *IEEE Trans. Signal Process.*, vol. 61, no. 24, pp. 6257–6263, Dec. 2013.
- [33] G. Heinig and K. Rost, “Fast algorithms for Toeplitz and Hankel matrices,” *Linear Algebra and its Applications*, vol. 435, no. 1, pp. 1–59, 2011.
- [34] R. Hunger, “Floating point operations in matrix-vector calculus,” *Technische Universität München, Associate Institute for Signal Processing, Tech. Rep.*, 2007.
- [35] C. Rapp, “Effects of HPA-nonlinearity on a 4-DPSK/OFDM-signal for a digital sound broadcasting system,” in *Proc. the Second European Conf. on Satellite Commun.*, Oct. 1991, pp. 179–184.
- [36] F. Auger, Z. Lou, B. Feuvrie, and F. Li, “Multiplier-free divide, square root, and log algorithms [DSP tips and tricks],” *IEEE Signal Process. Mag.*, vol. 28, no. 4, pp. 122–126, July 2011.

Chapter 5

Theoretical Analysis of IBFD Radios

In-band full-duplex (IBFD) communication systems utilize self-interference cancellation to mitigate high-power self-interference caused by simultaneous transmission and reception at the same frequency in the digital baseband domain. Self-interference is distorted by transceiver nonlinearity. Thus, the IBFD literature includes reports of nonlinear self-interference cancellers developed to achieve better cancellation performance. However, there are no detailed theoretical studies analyzing the performance of nonlinear cancellers in IBFD systems. This work develops a theoretical analysis technique for IBFD systems using a nonlinear self-interference canceller. The nonlinear characteristics of the system are expanded by a generalized Fourier series using orthonormal Laguerre polynomials. Then, the canceller's performance and the system's symbol error rate (SER) are analyzed using the obtained Fourier coefficients. The analytical results are compared with simulation results, demonstrating good correlation in a wide range of situations, from extremely nonlinear cases to good linear cases. Additionally, results show that the SER of the IBFD system is reduced by moderately nonlinearizing rather than linearizing the amplifier.

5.1 Introduction

The parallel Hammerstein canceller is one of most well-studied nonlinear cancellers in the IBFD literature. This type of canceller was initially developed to deal

with amplifier nonlinearity [1, 2], but versions have subsequently been developed to deal with IQ imbalance [3–5] and crosstalk in multiple-input and multiple-output (MIMO) systems [6]. These papers [1–6] have analyzed the performance of such Hammerstein cancellers using computer simulation. However, the literature does not contain any detailed theoretical analyses, or comparisons between simulation and theoretical results.

5.1.1 IIP-based distortion analysis

In the conventional radio-frequency (RF) engineering literature, the distortion from an RF component is usually calculated from the input intercept point (IIP). The power of the n -th order distortion from an RF component can be estimated as

$$D_n = \frac{P_{\text{out}}}{(\text{IIP}_n/P_{\text{in}})^{n-1}}, \quad (5.1)$$

where P_{in} and P_{out} are the input and output power of the RF component, respectively, and IIP_n is the n -th order IIP of the component. Some papers [2, 3, 7] have calculated the power of distortions caused in a transceiver using the IIP-based method.

Although this method is suitable for simple estimations of distortion power, it cannot be used in applications that require detailed analysis. Figure 5.1 shows the power growth of linear and nonlinear components with a two-tone signal and orthogonal frequency-division multiplexing (OFDM) signal as the input to a Rapp model [8] with AM-AM characteristic of $|x|(1 + |x|^4)^{-\frac{1}{4}}$. IIP-based analysis assumes that distortion power increases monotonically as the power of the input signal increases. However, we can see that the power of the fifth-order distortion has a local minimum value in Fig. 5.1 even in the two-tone case. In addition, in the high input power region in Fig. 5.1, as input power increases, the slope of the increase in distortion power decreases due to saturation. In the low input power region in Fig. 5.1, we can see that the slope of the third-order distortion does not increase for the third power of the input power, but clearly increases for the fifth power. These behaviors are not represented in (5.1).

Additionally, the results of the two-tone test are not useful for analyzing OFDM systems because the probability distributions and peak-to-average-power ratio (PAPR) of these two signals are completely different. In Fig. 5.1, the third-order component of the OFDM signal is about 10 dB or larger than that of the

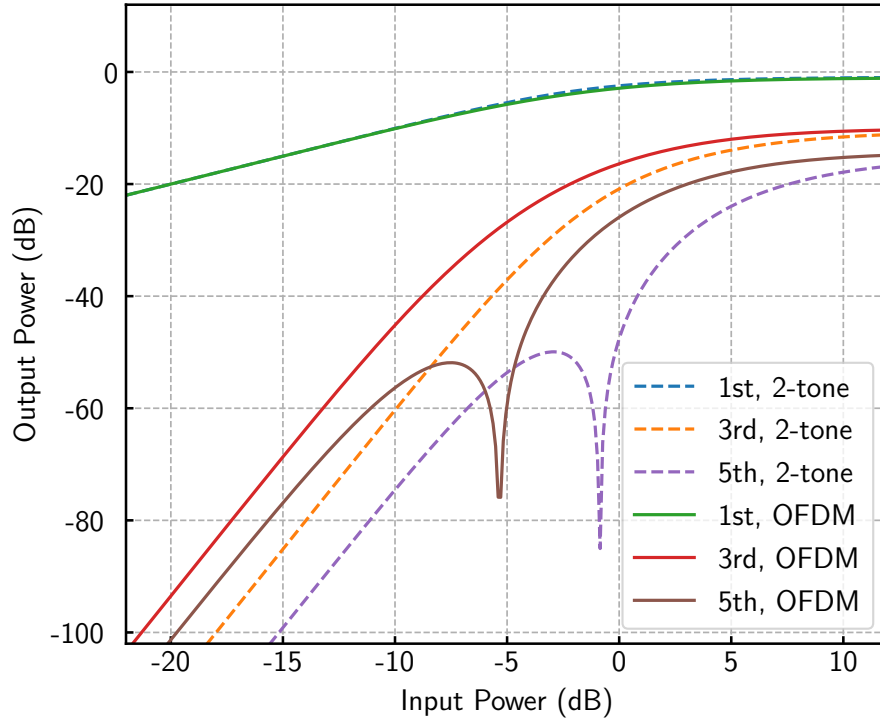


Figure 5.1: The linear and nonlinear component powers of two-tone and OFDM signals in the Rapp model. The smoothness factor of the Rapp model is $s = 2$, and the saturation level is $V_{\text{sat}} = 1$. In the two-tone case, each component power is computed by simulation. In the OFDM case, each component power is theoretically calculated as [9].

two-tone signal since the OFDM signal is more susceptible to nonlinear distortion due to its higher PAPR. As in the examples shown so far, the IIP-base analysis cannot be used for applications that require detailed analysis of current wireless systems.

5.1.2 Contributions

State-of-the-art studies of the theoretical analysis on in-band full-duplex radios [2, 3, 7] have calculated the power of distortions using IIP-based method. These studies are very useful and very important, e.g., for the design of full-duplex terminals and digital cancellers, as they allow easy estimation of distortion power using the IIP. However, as written in Section 5.1.1, IIP-based method is not an exact analysis

and involves rough approximations. Thus, these studies only analyze power level of distortions, and these techniques cannot calculate the performance of in-band full-duplex communications such as symbol error rate (SER) or bit error rate (BER). In this chapter, the author uses a generalized Fourier series expansion with orthonormal Laguerre polynomials to analyze the performance of in-band full-duplex radios with parallel Hammerstein cancellers. While amplifiers are modeled with a few parameters of IIP in the papers [2, 3, 7], they are modeled as arbitrary functions, which increases the degree of freedom of analysis. Arbitrary functions used here are mathematically infinite dimensional vectors, and the proposed method has infinite dimensional degrees of freedom for modeling of memoryless amplifiers. The core of our analysis is based on studies of OFDM systems in half-duplex communication [9–13]. The author extends them to include the analysis of nonlinear self-interference cancellers and in-band full-duplex systems that have nonlinear amplifiers in their transmitters and receivers. The proposed method can be used to analyze both the performance of parallel Hammerstein cancellers and the SER of in-band full-duplex systems. In addition, results of the proposed analysis and simulation show that both results match well each other.

5.1.3 Organization and notations

The rest of this chapter is organized as follows: In Section 5.2, the author provides a summary of papers [9–13] on nonlinear analysis, and present additional useful theorems for analysis of nonlinear cancellers. In Section 5.3, the author presents the detailed analysis method for nonlinear cancellers, which is the main contribution of this chapter. In Section 5.4, results obtained using this analysis approach are compared with results from equivalent baseband simulations, and discussed in detail. Finally, Section 5.5 concludes the paper.

In this chapter, the complex Gaussian distribution with mean μ and variance σ^2 is denoted $\mathcal{CN}(\mu, \sigma^2)$, and the exponential distribution with mean ρ^2 is denoted $\text{Exp}(\rho^2)$, i.e., $|x|^2 \sim \text{Exp}(\sigma^2)$ when $x \sim \mathcal{CN}(0, \sigma^2)$. The expected value of a random variable R is written as $\mathbb{E}[R] = \bar{R}$. The binary operator $*$ denotes convolution. For a matrix \mathbf{M} , the transpose of \mathbf{M} is denoted by \mathbf{M}^T , and the inverse of \mathbf{M} is denoted by \mathbf{M}^{-1} . \mathbf{I}_n denotes a $n \times n$ identity matrix, and $\mathbf{0}_{m \times n}$ denotes a $m \times n$ zero matrix. We write the Fourier transform for a signal $s(t)$ as $\mathcal{F}[s(t)]$. A tilde above a variable (e.g., \tilde{x}) indicates it to be a coefficient of a generalized Fourier series expansion with orthonormal Laguerre polynomials, as defined in Section 5.2.

Table 5.1: Variables used in this chapter

Variable	Defined by	Mean
$c_n(t)$	Fig. 5.4, Eq. (5.44)	Regenerated SI signal by the canceller on the terminal# n
$\tilde{c}_p(\tau), \tilde{C}_p(f)$	Eq. (5.27)	Response related to $\psi_p(x)$ of the canceller related on Fig. 5.3
$\dot{c}_p(\tau)$	Eq. (5.25)	Response related to $x x ^{p-1}$ of the canceller on Fig. 5.3
$d_\alpha(t)$	Eq. (5.15), Eq. (5.17)	Distorted output signal from $\alpha(x(t))$
$D_{ij}(f)$	Eq. (5.52)	PSD of the distorted signal from the terminal# i to the terminal# j
g_n	Fig. 5.4	Gain of the VGA of the terminal# n
$\tilde{h}_p(\tau), \tilde{H}_p(f)$	Eq. (5.21)	Response related to $\psi_p(x)$ of the SI model on Fig. 5.3
$\hat{h}_p(\tau)$	Eq. (5.31)	Response related to $x x ^{p-1}$ of the SI model on Fig. 5.3
$h_{ij}(\tau), H_{ij}(f)$	Eq. (5.33), Eq. (5.35)	Response from the terminal# i to the terminal# j on DSP
\bar{I}_{nn}	Eq. (5.47)	Mean power of the SI before digital cancellation on the terminal# n
\bar{I}_{nn}^R	Eq. (5.48)	Mean power of the residual SI after digital cancellation on the terminal# n
$I_{nn}^R(f)$	Eq. (5.53)	PSD of the residual SI after digital cancellation on the terminal# n
$\bar{I}_{nn}^R(f)$	Eq. (5.59)	Mean PSD of the residual SI after digital cancellation on the terminal# n
$l_{m,i}$	Eq. (5.4)	The i -th coefficient of the power series of $\psi_{2m+1}(x)$
$L_m^n(x)$	Eq. (5.3)	Generalized Laguerre polynomial
$\bar{N}_{NL,1}$	Eq. (5.39)	Mean power of $z_{NL,n}(t)$
\bar{N}_{thermal}	Eq. (5.49)	Power of the thermal noise
$\bar{N}_{\text{thermal}}(f)$	Eq. (5.49)	PSD of the thermal noise
$\bar{N}_{\text{tot},n}$	Eq. (5.49)	Mean power of the total noise $z_{\text{tot},n}(t)$ on the terminal# n
$\bar{N}_{\text{tot},n}(f)$	Eq. (5.54)	PSD of the total noise $z_{\text{tot},n}(t)$ on the terminal# n
P	Eq. (5.44)	Order of the nonlinear canceller
$R_{(\cdot)(\cdot)}$	–	Cross-correlation function or auto-correlation function
SER_n	Eq. (5.61)	Mean SER on the terminal# n
SICR_n	Eq. (5.46)	Performance of the SI canceller on the terminal# n
$\text{SIDNR}_n(f)$	Eq. (5.50)	SIDNR on the terminal# n
$U_{ij}(f)$	Eq. (5.51)	PSD of the useful signal from the terminal# i to the terminal# j
\bar{U}_{ij}	Eq. (5.60)	Mean PSD of the useful signal from the terminal# i to the terminal# j
$w_n(t)$	Fig. 5.4, Eq. (5.45)	Residual signal after SI cancellation on the terminal# n
$x_n(t)$	Fig. 5.4	Transmitted baseband signal from the terminal# n
$y_n(t)$	Fig. 5.4, Eq. (5.35)	Received baseband signal of the terminal# n
$z_n(t)$	Eq. (5.33)	Thermal noise on the terminal# n
$z_{NL,n}(t)$	Eq. (5.37)	Distorted signal from the LNA of the terminal# n
$z_{\text{tot},n}(t)$	Eq. (5.43)	Total noise: thermal noise plus distortion from the terminal# n 's LNA
$\alpha(x)$	Fig. 5.2	Nonlinear transfer function on Fig. 5.2
$\bar{\alpha}_p$	Eq. (5.9)	The p -th coefficient of the generalized Fourier series of $\alpha(x)$
$\alpha_n(x)$	Fig. 5.4	Transfer function of the PA on the terminal# n
$\bar{\alpha}_{n,p}$	Eq. (5.42)	The p -th coefficient of the generalized Fourier series of $\alpha_n(g_n x)$
$\beta_n(x)$	Fig. 5.4	Transfer function of the LNA on the terminal# n
$\beta_{n,1}$	Eq. (5.38)	Linear gain of the LNA of the terminal# n
$\lambda_{\text{sdr},n}(f)$	Eq. (5.56)	Inverse of SDR on the terminal# n
$\lambda_{\text{sinr},n}(f)$	Eq. (5.57)	Inverse of SINR on the terminal# n
ν_n^2	Eq. (5.40)	Transmission power from the terminal# n
ρ_p	Theorem 2	Gain of the response $H_p(f)$
ρ_{ij}	Eq. (5.36)	Channel gain of $h_{ij}(\tau)$
$\psi_p(x)$	Eq. (5.2)	Orthonormal polynomial for $\mathcal{CN}(0, 1)$
$ \Psi_p(f) ^2$	Eq. (5.12), Eq. (5.64)	PSD of $\psi_p(x(t))$

In contrast, a dot above a variable (e.g., \dot{a}) indicates it to be a coefficient of a power series expansion. The variables used in this chapter are listed in Table 5.1.

5.2 Theoretical Background and Theorems

In this section, the author describes a generalized Fourier series expansion and some related theorems that form the core of my theoretical analysis. In Section 5.2.1, the author provides a summary of papers [9–13] relevant to the analysis of the nonlinearities shown in Fig. 5.2. In Section 5.2.2, the author describes some useful

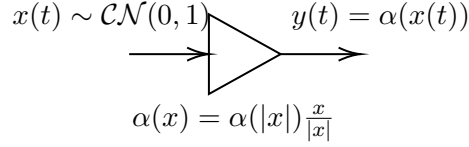


Figure 5.2: The signal model used in Section 5.2.1. The input signal has a complex Gaussian distribution with zero mean and unit variance. The nonlinear transfer function $\alpha(x)$ has AM-AM and AM-PM nonlinearities.

theorems for analyzing nonlinear self-interference cancellers using the signal model of Fig. 5.3.

5.2.1 Generalized Fourier series expansion with orthonormal Laguerre polynomials

We define orthonormal Laguerre polynomials as

$$\psi_{2m+1}(x) = \frac{(-1)^m}{\sqrt{m+1}} L_m^1(|x|^2)x = \sum_{i=0}^m l_{m,i} x|x|^{2i} \quad (5.2)$$

where $L_m^1(z)$ is a generalized Laguerre polynomial defined as

$$L_m^1(z) = \sum_{n=0}^m \frac{(-1)^n}{n!} \binom{m+1}{n+1} z^n, \quad (5.3)$$

and the coefficients $l_{m,i}$ can be expressed as

$$l_{m,i} = \frac{(-1)^{i+m}}{i! \sqrt{m+1}} \binom{m+1}{i+1}. \quad (5.4)$$

Equation (5.2) is orthonormal with the following inner product:

$$\begin{aligned} \langle \psi_p(x), \psi_q(x) \rangle &= \mathbb{E} [\psi_p(x) \psi_q^*(x)] \\ &= \frac{1}{\pi} \int_{\mathbb{C}} \psi_p(x) \psi_q^*(x) e^{-|x|^2} dx \\ &= \begin{cases} 1, & (p = q) \\ 0, & (p \neq q) \end{cases} \end{aligned} \quad (5.5)$$

where

$$\int_{\mathbb{C}} f(x) dx = \int_0^{2\pi} d\theta \int_0^{\infty} f(re^{j\theta}) r dr, \quad (5.6)$$

for an arbitrary function $f(x)$. Also, the cross-correlation of $\psi_p(x(t))$ has orthogonality as

$$R_{\psi_p \psi_q}(\tau) = \begin{cases} R_{xx}(\tau) |R_{xx}(\tau)|^{p-1}, & (p = q) \\ 0, & (p \neq q) \end{cases} \quad (5.7)$$

where $R_{xx}(\tau)$ is the cross-correlation function of $x(t)$ [11]. This means that the orthogonal polynomials of different orders are all uncorrelated. Then, for the signal model in Fig. 5.2, we define the generalized Fourier series expansion of nonlinear amplifier $\alpha(x)$ with orthonormal Laguerre polynomials as follows:

Definition 1 (generalized Fourier series expansion). *If an amplifier whose transfer function $\alpha(x) = \alpha(|x|) \frac{x}{|x|}$ has only AM-AM and AM-PM nonlinearity, and $\mathbb{E}[|\alpha(x)|^2] < \infty$ is satisfied by $x \sim \mathcal{CN}(0, 1)$, the transfer function can be expanded with the orthonormal Laguerre polynomials as*

$$\alpha(x) = \sum_{p=1,3,\dots}^{\infty} \tilde{\alpha}_p \psi_p(x), \quad (5.8)$$

where $\tilde{\alpha}_p$ is the p -th Fourier coefficient, given by

$$\begin{aligned} \tilde{\alpha}_p &= \frac{1}{\pi} \int_{\mathbb{C}} \alpha(x) \psi_p^*(x) e^{-|x|^2} dx \\ &= \int_0^{\infty} \alpha(r) \psi_p(r) \cdot 2r e^{-r^2} dr. \end{aligned} \quad (5.9)$$

The series expansion of (5.8) is referred to as the generalized Fourier series expansion with orthonormal Laguerre polynomials.

The generalized Fourier series expansion has suitable properties for analyzing nonlinear characteristics with a $\mathcal{CN}(0, 1)$ -distributed input signal. In [9, 11], the following theorem is introduced and proved.

Theorem 1. *For the signal model in Fig. 5.2, the autocorrelation function of the*

output signal $\alpha(x(t))$ is given by

$$R_{\alpha\alpha}(\tau) = \sum_{p=1,3,\dots}^{\infty} |\tilde{\alpha}_p|^2 R_{xx}(\tau) |R_{xx}(\tau)|^{p-1}, \quad (5.10)$$

where $R_{xx}(\tau)$ is the autocorrelation function of the input signal $x(t)$. Also, the power spectral density (PSD) of the output signal $\alpha(x(t))$ is given by

$$|A(f)|^2 = \sum_{p=1,3,\dots}^{\infty} |\tilde{\alpha}_p|^2 |\Psi_p(f)|^2, \quad (5.11)$$

where $|\Psi_p(f)|^2$ is defined as

$$\begin{aligned} |\Psi_{2m+1}(f)|^2 &= \mathcal{F} [R_{xx}(\tau) |R_{xx}(\tau)|^{2m}] \\ &= \underbrace{|X(f)|^2 * \dots * |X(f)|^2}_{(m+1)\text{-times convolution}} * \underbrace{|X(-f)|^2 * \dots * |X(-f)|^2}_{m\text{-times convolution}}, \end{aligned} \quad (5.12)$$

and $|X(f)|^2 = \mathcal{F} [R_{xx}(\tau)]$ is the PSD of $x(t)$.

Proof. See the proof in the paper [9, Eq. (9) and Appendix A with $2\sigma^2 = 1$] \square

We can then use **Theorem 1** to prove Parseval's theorem and Bussgang's theorem as follows:

Corollary 1 (Parseval's theorem). *In the signal model of Fig. 5.2, the expected output power of $\alpha(x)$ is given by*

$$\mathbb{E} [|\alpha(x)|^2] = \sum_{p=1,3,\dots}^{\infty} |\tilde{\alpha}_p|^2. \quad (5.13)$$

Proof. Substituting $\tau = 0$ in (5.10), we get the following equation:

$$\mathbb{E} [|\alpha(x(t))|^2] = \sum_{p=1,3,\dots}^{\infty} |\tilde{\alpha}_p|^2 \left(\mathbb{E} [|x(t)|^2] \right)^p. \quad (5.14)$$

Then, we obtain (5.13) since $\mathbb{E} [|x(t)|^2] = 1$. \square

Corollary 2 (Bussgang's theorem). *In the signal model of Fig. 5.2, we can express the output signal from a nonlinear transfer function $\alpha(x)$ with an input signal $x(t) \sim$*

$\mathcal{CN}(0, 1)$ as

$$\alpha(x(t)) = \tilde{\alpha}_1 x(t) + d_\alpha(t), \quad (5.15)$$

where $d_\alpha(t)$ is a distorted signal uncorrelated with $x(t)$. Also, the power of the output distorted signal $d_\alpha(t)$ can be written as

$$\mathbb{E} [|d_\alpha(t)|^2] = \sum_{p=3,5,\dots}^{\infty} |\tilde{\alpha}_p|^2 = \mathbb{E} [|\alpha(x(t))|^2] - |\tilde{\alpha}_1|^2. \quad (5.16)$$

Proof. By comparing (5.8) and (5.15), we can see that the distorted signal $d_\alpha(t)$ is described by

$$d_\alpha(t) = \sum_{p=3,5,\dots}^{\infty} \tilde{\alpha}_p \psi_p(x(t)). \quad (5.17)$$

Then, the cross-correlation of $x(t)$ and $d_\alpha(t)$ can be written as

$$R_{xd_\alpha}(\tau) = \sum_{p=3,5,\dots}^{\infty} \tilde{\alpha}_p R_{x\psi_p}(\tau), \quad (5.18)$$

where $R_{x\psi_p}(\tau)$ is the cross-correlation of $x(t)$ and $\psi_p(x(t))$. Since $\psi_1(x(t)) = x(t)$, Eq. (5.18) can be rewritten as

$$R_{xd_\alpha}(\tau) = \sum_{p=3,5,\dots}^{\infty} \tilde{\alpha}_p R_{\psi_1\psi_p}(\tau) = 0 \quad (5.19)$$

due to the orthogonality of (5.7). Thus, $d_\alpha(t)$ is uncorrelated with $x(t)$. In addition, from **Corollary 1**, the power of the distorted signal can be written as

$$\mathbb{E} [|d_\alpha(t)|^2] = \sum_{p=3,5,\dots}^{\infty} |\tilde{\alpha}_p|^2 = \left(\sum_{p=1,3,\dots}^{\infty} |\tilde{\alpha}_p|^2 \right) - |\tilde{\alpha}_1|^2 = \mathbb{E} [|\alpha(x(t))|^2] - |\tilde{\alpha}_1|^2. \quad (5.20)$$

□

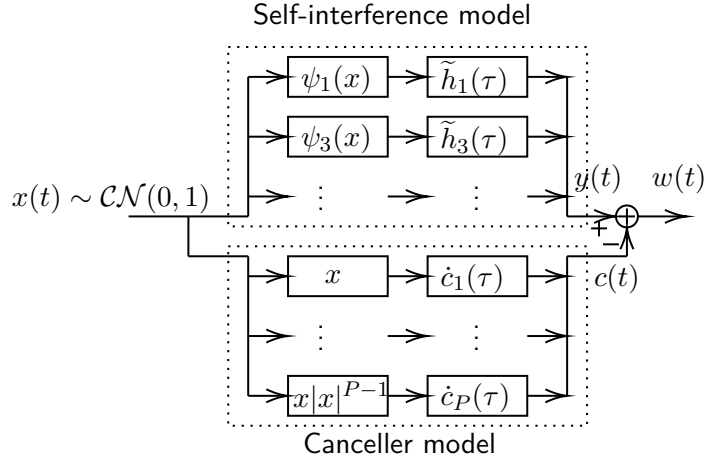


Figure 5.3: The signal model for Section 5.2.2. The self-interference model has infinite-order nonlinear components corresponding to the orthonormal polynomials $\psi_p(x)$. In contrast, the canceller can regenerate and cancel finite-order nonlinear components corresponding to the simple powers $x|x|^{p-1}$.

5.2.2 Theorems related to the parallel Hammerstein canceller

Theorem 1, **Corollary 1**, and **Corollary 2** are useful for evaluating the output signal of the nonlinear transmitter. However, these theorems are inadequate for analyzing the received self-interference since they do not consider a channel's impulse response. In Fig. 5.3, we assume that the input signal $x(t)$ is distributed on $\mathcal{CN}(0, 1)$. The following theorem can address the parallel Hammerstein model with orthonormal polynomials for Fig. 5.3.

Theorem 2. *For self-interference signal model of Fig. 5.3, it is assumed that the signal $y(t)$ can be expressed as*

$$y(t) = \sum_{p=1,3,\dots}^{\infty} \tilde{h}_p(\tau) * \psi_p(x(t)), \quad (5.21)$$

where $\tilde{h}_p(\tau)$ is an impulse response corresponding to the orthonormal Laguerre polynomials $\psi_p(x)$, and their frequency response is $\tilde{H}_p(f) = \mathcal{F}[\tilde{h}_p(\tau)]$. Then, the

following expressions hold:

$$|Y(f)|^2 = \sum_{p=1,3,\dots}^{\infty} \left| \widetilde{H}_p(f) \right|^2 \left| \Psi_p(f) \right|^2 \quad (5.22)$$

$$\mathbb{E} \left[|Y(f)|^2 \right] = \sum_{p=1,3,\dots}^{\infty} \rho_p^2 \left| \Psi_p(f) \right|^2, \quad (5.23)$$

$$\mathbb{E} \left[|y(t)|^2 \right] = \sum_{p=1,3,\dots}^{\infty} \rho_p^2, \quad (5.24)$$

where $Y(f) = \mathcal{F} [y(t)]$ is the frequency-domain representation of the output signal $y(t)$, and $\rho_p^2 = \mathbb{E} \left[\left| \widetilde{H}_p(f) \right|^2 \right]$.

Proof. See Appendix 5.A. □

To perform a theoretical analysis of nonlinear cancellers within a functional analysis framework, we must first define them in a manageable form. Thus, we define the parallel Hammerstein canceller as follows:

Definition 2 (parallel Hammerstein canceller). *For the signal model of Fig. 5.3, the output signal of the parallel Hammerstein canceller composed of up to P -order polynomials is defined as*

$$c(t) = \sum_{p=1,3,\dots}^P \dot{c}_p(\tau) * x(t) |x(t)|^{p-1}, \quad (5.25)$$

where $h_p(\tau)$ are impulse responses that minimize the following residual self-interference power:

$$\mathbb{E} \left[|y(t) - c(t)|^2 \right]. \quad (5.26)$$

Then, we can prove the existence of impulse responses $\tilde{c}_p(\tau)$ to satisfy (5.27) with some trivial manipulations.

$$c(t) = \sum_{p=1,3,\dots}^P \tilde{c}_p(\tau) * \psi_p(x(t)) \quad (5.27)$$

The impulse responses $\dot{c}_p(\tau)$ and $\tilde{c}_p(\tau)$ have the following relationships:

$$\underbrace{\begin{bmatrix} c_1(\tau) \\ c_3(\tau) \\ \vdots \\ c_P(\tau) \end{bmatrix}}_{\dot{\mathbf{c}}(\tau)} = \underbrace{\begin{bmatrix} l_{0,0} & l_{1,0} & l_{2,0} & \cdots & l_{m,0} \\ 0 & l_{1,1} & l_{2,1} & \cdots & l_{m,1} \\ 0 & 0 & l_{2,2} & \cdots & l_{m,2} \\ \vdots & \vdots & \ddots & \ddots & \vdots \\ 0 & 0 & 0 & \cdots & l_{m,m} \end{bmatrix}}_{\mathbf{L}_{m+1}} \underbrace{\begin{bmatrix} \tilde{c}_1(\tau) \\ \tilde{c}_3(\tau) \\ \vdots \\ \tilde{c}_P(\tau) \end{bmatrix}}_{\tilde{\mathbf{c}}(\tau)}$$

$$\Leftrightarrow \tilde{\mathbf{c}}(\tau) = \mathbf{L}_{m+1}^{-1} \dot{\mathbf{c}}(\tau), \quad (5.28)$$

where $m = (P-1)/2$. In other words, there is a method for completely transforming (5.25) and (5.27), and Eq. (5.27) also minimizes (5.26). Additionally, we can provide the following noteworthy theorem by taking advantage of the useful properties of (5.27) and orthonormal polynomials.

Theorem 3. *In the signal model of Fig. 5.3, the impulse responses $\tilde{c}_p(\tau)$ corresponding to the generalized Fourier expansion of the parallel Hammerstein canceller (5.27) are given by*

$$\tilde{c}_p(\tau) = \tilde{h}_p(\tau). \quad (5.29)$$

Proof. Equation (5.26) can be transformed into the following expression:

$$\begin{aligned} \mathbb{E} [|y(t) - c(t)|^2] &= \sum_{p=1,3,\dots}^P \int_{-\infty}^{\infty} \mathbb{E} \left[|\tilde{H}_p(f) - \tilde{C}_p(f)|^2 \right] |\Psi_p(f)|^2 df \\ &+ \sum_{p=P,P+2,\dots}^{\infty} \int_{-\infty}^{\infty} \mathbb{E} \left[|\tilde{H}_p(f)|^2 \right] |\Psi_p(f)|^2 df + \mathbb{E} [|z(t)|^2], \end{aligned} \quad (5.30)$$

where $\tilde{H}_p(f)$ and $\tilde{C}_p(f)$ are the frequency response of $\tilde{h}_p(\tau)$ and $\tilde{c}_p(\tau)$, respectively. When $\tilde{H}_p(f) = \tilde{C}_p(f)$ is satisfied, the above expression is minimized. Thus, (5.29) can be derived. \square

Theorem 3 states that if the received self-interference is approximated in the form of (5.21), we can analyze the theoretical characteristics of the parallel Hammerstein canceller. Additionally, we can analyze the characteristic of the residual self-interference signal, denoted $w(t) = y(t) - c(t)$. Although the author has described the time-domain Hammerstein canceller in **Theorem 3**, a

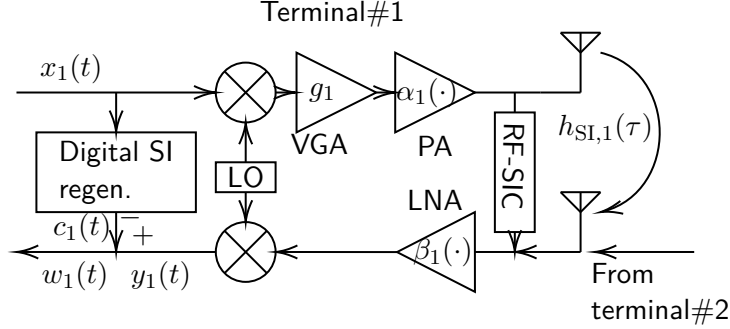


Figure 5.4: Analysis model of the full-duplex transceiver.

similar relationship, $\widetilde{H}_p(f) = \widetilde{C}_p(f)$, can be established for the frequency-domain Hammerstein canceller [5, 14] due to the one-to-one correspondence between the frequency response and the impulse response.

Note that even if the received signal is expanded to a Hammerstein model of $x|x|^{p-1}$ and impulse responses $\dot{h}_p(\tau)$ as

$$y(t) = \sum_{p=1,3,\dots}^{\infty} \dot{h}_p(\tau) * x(t)|x(t)|^{p-1} + z(t), \quad (5.31)$$

the p -th impulse response of the Hammerstein canceller $\dot{c}_p(\tau)$ is not represented by $\dot{h}_p(\tau)$, i.e.,

$$\dot{c}_p(\tau) \neq \dot{h}_p(\tau). \quad (5.32)$$

The author provides the proof for the above inequality in Appendix 5.B. In contrast, (5.29) is an identity, and it is always holds true for an arbitrary transfer function. Hence we use the generalized Fourier series expansion for the theoretical analysis of nonlinear self-interference cancellers. Of course, the model of (5.31) can be analyzed by transforming it into the model of (5.21) using the matrix \mathbf{L}_{m+1} . Equation (5.79) of Appendix 5.B is a formula of the transformation between the two models.

5.3 Theoretical Analysis of Nonlinear Self-Interference Canceller

In this section, the author describes a theoretical analysis technique for full-duplex transceivers and nonlinear self-interference cancellers. First, the author shows the

analytical model and apply equation deformations to make the analysis easier. Then, the author shows how the performance of the canceller and the symbol error rate can be analyzed.

5.3.1 Analytical model

In preparation for the analysis, the author describes the analytical model summarized in Fig. 5.4. Only one terminal is depicted, but the author assumes that there are two terminals, terminal#1 and terminal#2. The transmitted baseband signal is the OFDM signal with many subcarriers, and we can assume that its envelope amplitude and power have a Rayleigh distribution with $\sigma_x^2 = 0.5$ and an exponential distribution $\text{Exp}(1)$, respectively.

In the transmitter of terminal#1, the transmitted signal is distorted by the power amplifier (PA), and the signal received by the receiver antenna can be described as

$$y_{\text{ANT},1}(t) = h_{\text{SI},1}(\tau) * \alpha_1(g_1 x_1(t)) + h_{21}(\tau) * \alpha_2(g_2 x_2(t)) + z_1(t), \quad (5.33)$$

where $h_{\text{SI},1}(\tau)$ is the impulse response between the TX and RX antennas, $h_{21}(\tau)$ is the channel impulse response between terminal#1 and terminal#2, and $z_1(t)$ is the thermal noise. Also, $x_1(t)$ and $x_2(t)$ are the signal transmitted from terminal#1 and terminal#2, respectively. The nonlinear functions $\alpha_1(\cdot)$ and $\alpha_2(\cdot)$ are the AM-AM and AM-PM transfer functions of both terminals' PAs.

Generally, in full duplex, an RF canceller is used to prevent saturation of the receiver LNA or A/D converter. The residual self-interference, which is the input signal to the LNA, can be expressed as

$$y_{\text{RFSIC},1}(t) = (h_{\text{SI},1}(\tau) - h_{\text{Cir},1}(\tau)) * \alpha_1(g_1 x_1(t)) + h_{21}(\tau) * \alpha_2(g_2 x_2(t)) + z_1(t), \quad (5.34)$$

where $h_{\text{Cir},1}(\tau)$ is the impulse response of the RF canceller. Then, the nonlinear distorted signal from the LNA can be described as

$$y_1(t) = \beta_1 \left((h_{\text{SI},1}(\tau) - h_{\text{Cir},1}(\tau)) * \alpha_1(g_1 x_1(t)) + h_{21}(\tau) * \alpha_2(g_2 x_2(t)) + z_1(t) \right), \quad (5.35)$$

where $h_{11}(\tau) = h_{\text{SI},1}(\tau) - h_{\text{Cir},1}(\tau)$, and the nonlinear function $\beta_1(\cdot)$ is the AM-AM and AM-PM transfer function of the LNA. In this chapter, we assume that the self-interference channel after RF cancellation $h_{11}(\tau)$ and the channel between terminals

$h_{21}(\tau)$ are Rayleigh fading channels, and the mean power gain of $h_{11}(\tau)$ and $h_{21}(\tau)$ are ρ_{11} and ρ_{21} , respectively. In other words, ρ_{ij} can be written as

$$\rho_{ij}^2 = \mathbb{E} \left[|H_{ij}(f)|^2 \right], \quad (5.36)$$

where $H_{ij}(f)$ is the frequency response of $h_{ij}(\tau)$, and $H_{ij}(f)$ is distributed on $\mathcal{CN}(0, \rho_{ij}^2)$. To obtain the coefficients of the nonlinear canceller using **Theorem 3**, we need to transform (5.35) to the form of (5.21). Thus, we derive (5.37) from (5.35) using Bussgang's theorem.

$$y_1(t) = \tilde{\beta}_{1,1} h_{11}(\tau) * \alpha_1(g_1 x_1(t)) + \tilde{\beta}_{1,1} h_{21}(\tau) * \alpha_2(g_2 x_2(t)) + \tilde{\beta}_{1,1} z_1(t) + z_{\text{NL},1}(t), \quad (5.37)$$

where $\tilde{\beta}_{1,1}$ is the linear gain of the LNA, and $z_{\text{NL},1}(t)$ is the nonlinear distortion caused by the LNA. For simplicity, we make the following assumptions:

- If there is no self-interference signal, the LNA does not saturate and operates as a linear amplifier.
- The power of the self-interference is much larger than the received desired signal and noise.

From above assumptions, we can formulate the following equations:

$$\tilde{\beta}_{1,1} = \frac{1}{\rho_{11}\nu_1} \int_0^\infty \beta_1(\rho_{11}\nu_1 r) r \cdot 2re^{-r^2} dr, \quad (5.38)$$

$$\bar{N}_{\text{NL},1} = \mathbb{E} \left[|z_{\text{NL},1}(t)|^2 \right] = \int_0^\infty |\beta_1(\rho_{11}\nu_1 r)|^2 \cdot 2re^{-r^2} dr - \left| \tilde{\beta}_{1,1} \rho_{11} \nu_1 \right|^2, \quad (5.39)$$

where ρ_{11}^2 is the mean power gain of $h_{11}(\tau)$, $\bar{N}_{\text{NL},1}$ is the mean power of $z_{\text{NL},1}(t)$, and ν_1^2 is the mean transmission power of terminal#1, expressed as

$$\nu_1^2 = \int_0^\infty |\alpha_1(g_1 r)|^2 \cdot 2re^{-r^2} dr. \quad (5.40)$$

Applying the generalized Fourier series expansion with the orthonormal Laguerre polynomials to (5.37), we obtain

$$y_1(t) = \tilde{\beta}_{1,1} h_{11}(\tau) * \sum_{p=1,3,\dots}^{\infty} \tilde{\alpha}_{1,p} \psi_p(x_1(t)) + \tilde{\beta}_{1,1} h_{21}(\tau) * \sum_{p=1,3,\dots}^{\infty} \tilde{\alpha}_{2,p} \psi_p(x_2(t)) + z_{\text{tot},1}(t), \quad (5.41)$$

where

$$\tilde{\alpha}_{n,p} = \int_0^\infty \alpha_n(g_n r) \psi_p(r) \cdot 2r e^{-r^2} dr, \quad (5.42)$$

$$z_{\text{tot},1}(t) = \tilde{\beta}_{1,1} z_1(t) + z_{\text{NL},1}(t). \quad (5.43)$$

From **Theorem 3**, the regenerated self-interference signal of the nonlinear canceller composed of up to P -order polynomials can be written as

$$c_1(t) = \tilde{\beta}_{1,1} h_{11}(\tau) * \sum_{p=1,3,\dots}^P \tilde{\alpha}_{1,p} \psi_p(x_1(t)). \quad (5.44)$$

Thus, the residual signal after self-interference cancellation can be expressed as

$$\begin{aligned} w_1(t) = y_1(t) - c_1(t) = & \tilde{\beta}_{1,1} h_{11}(\tau) * \sum_{p=P+2,P+4,\dots}^{\infty} \tilde{\alpha}_{1,p} \psi_p(x_1(t)) \\ & + \tilde{\beta}_{1,1} h_{21}(\tau) * \sum_{p=1,3,\dots}^{\infty} \tilde{\alpha}_{2,p} \psi_p(x_2(t)) + z_{\text{tot},1}(t). \end{aligned} \quad (5.45)$$

5.3.2 Cancellation performance

The following self-interference cancellation ratio (SICR), which indicates the performance of a digital canceller, can be expressed as

$$\text{SICR}_1 = \frac{\bar{I}_{11} + \bar{N}_{\text{tot},1}}{\bar{I}_{11}^{\text{R}} + \bar{N}_{\text{tot},1}}, \quad (5.46)$$

where \bar{I}_{11} is the mean power of the self-interference before digital cancellation, and \bar{I}_{11}^{R} is the mean power of the residual self-interference after digital cancellation. From **Theorem 2**, \bar{I}_{11} and \bar{I}_{11}^{R} can be written as

$$\bar{I}_{11} = \mathbb{E} \left[\left| \tilde{\beta}_{1,1} h_{11}(\tau) * \alpha_1(g_1 x(t)) \right|^2 \right] = |\tilde{\beta}_{1,1}|^2 \rho_{11}^2 \nu_1^2. \quad (5.47)$$

$$\bar{I}_{11}^{\text{R}} = \mathbb{E} \left[\left| \tilde{\beta}_{1,1} h_{11}(\tau) * \sum_{p=P+2,P+4,\dots}^{\infty} \tilde{\alpha}_{1,p} \psi_p(x_1(t)) \right|^2 \right] = |\tilde{\beta}_{1,1}|^2 \rho_{11}^2 \left(\nu_1^2 - \sum_{p=1,3,\dots}^P |\tilde{\alpha}_{1,p}|^2 \right). \quad (5.48)$$

Also, the total noise power $\bar{Z}_{\text{tot},1}$, which is the power of $z_{\text{tot},1}(t)$, can be written as

$$\bar{N}_{\text{tot},1} = |\tilde{\beta}_{1,1}|^2 \bar{N}_{\text{thermal}} + \bar{N}_{\text{NL},1}, \quad (5.49)$$

where \bar{N}_{thermal} is the power of the thermal noise, and $\bar{N}_{\text{NL},1}$, which is defined in (5.39), is the power of the nonlinear distortion caused by the LNA.

5.3.3 Symbol error rate

To analyze the symbol error rate (SER), we need to derive statistical properties for the *signal to interference, distortion, and noise ratio (SIDNR)*. The SIDNR on terminal#1 is described by

$$\text{SIDNR}_1(f) = \frac{U_{21}(f)}{D_{21}(f) + I_{11}^{\text{R}}(f) + \bar{N}_{\text{tot},1}(f)}, \quad (5.50)$$

where $U_{21}(f)$ and $D_{21}(f)$ are the powers of the useful and distortion signals of the received desired signal, and $I_{11}^{\text{R}}(f)$ is the residual self-interference power after digital cancellation. $U_{21}(f)$, $D_{21}(f)$, and $I_{11}^{\text{R}}(f)$ can be written as

$$U_{21}(f) = |\tilde{\beta}_{1,1}|^2 |H_{21}(f)|^2 |\tilde{\alpha}_{2,1}|^2 |X(f)|^2, \quad (5.51)$$

$$D_{21}(f) = |\tilde{\beta}_{1,1}|^2 |H_{21}(f)|^2 \sum_{p=3,5,\dots}^{\infty} |\tilde{\alpha}_{2,p}|^2 |\Psi_p(f)|^2, \quad (5.52)$$

$$I_{11}^{\text{R}}(f) = |\tilde{\beta}_{1,1}|^2 |H_{11}(f)|^2 \sum_{p=P+2,P+4,\dots}^{\infty} |\tilde{\alpha}_{1,p}|^2 |\Psi_p(f)|^2. \quad (5.53)$$

The total noise contains the nonlinear distortion caused by the LNA, and its PSD $\bar{N}_{\text{tot},1}(f)$ is not flat in the band $-\frac{1}{2} < f < \frac{1}{2}$. In the proposed analysis, we approximate the PSD of the total noise as

$$\bar{N}_{\text{tot},1}(f) = |\tilde{\beta}_{1,1}|^2 \bar{N}_{\text{thermal}}(f) + \bar{N}_{\text{NL},1} |\Psi_3(f)|^2, \quad (5.54)$$

where $\bar{N}_{\text{thermal}}(f)$ is the PSD of the thermal noise. Thus, $\text{SIDNR}_1(f)$ can be expressed as

$$\text{SIDNR}_1(f) = \frac{1}{\lambda_{\text{sinr},1}(f) + \lambda_{\text{sdr},1}(f)}, \quad (5.55)$$

where

$$\lambda_{\text{sdr},1}(f) = \frac{D_{21}(f)}{U_{21}(f)} = \frac{1}{|\tilde{\alpha}_{2,1}|^2} \sum_{p=3,5,\dots}^{\infty} |\tilde{\alpha}_{2,p}|^2 |\Psi_p(f)|^2, \quad (5.56)$$

$$\lambda_{\text{sinr},1}(f) = \frac{I_{11}^{\text{R}}(f) + \bar{N}_{\text{tot},1}(f)}{U_{21}(f)}. \quad (5.57)$$

Since (5.56) does not depend on the channels' frequency responses, Eq. (5.56) is not a random variable and can have a fixed value. Thus, if the probability density function (PDF) of (5.57) is derived, we can formulate the PDF of the SIDNR and analyze the SER of the full-duplex system. From Appendix 5.C, the PDF of (5.57) can be written as

$$p_{\lambda_{\text{sinr},1}}(x; f) = \frac{\bar{N}_{\text{tot},1}(f)(x\bar{U}_{21} + \bar{I}_{11}^{\text{R}}(f)) + x\bar{U}_{21}\bar{I}_{11}^{\text{R}}(f)}{x(x\bar{U}_{21} + \bar{I}_{11}^{\text{R}}(f))^2} \exp\left(-\frac{\bar{N}_{\text{tot},1}(f)}{x\bar{U}_{21}}\right), \quad (5.58)$$

where

$$\bar{I}_{11}^{\text{R}}(f) = |\tilde{\beta}_{1,1}\rho_{11}|^2 \sum_{p=P+2,P+4,\dots}^{\infty} |\tilde{\alpha}_{1,p}|^2 |\Psi_p(f)|^2, \quad (5.59)$$

$$\bar{U}_{21} = |\tilde{\beta}_{1,1}\rho_{21}\tilde{\alpha}_{2,1}|^2. \quad (5.60)$$

Therefore, the average SER can be analyzed by averaging the random variable in the band $-\frac{1}{2} < f < \frac{1}{2}$ and can be expressed by the following integral:

$$\overline{\text{SER}}_1 = \int_{-1/2}^{1/2} \int_0^{\infty} P_s\left(\frac{1}{x + \lambda_{\text{sdr},1}(f)}\right) p_{\lambda_{\text{sinr},1}}(x; f) dx df, \quad (5.61)$$

where $P_s(\gamma)$ is the symbol error probability of the subcarrier modulation. If we use M -ary QAM for each subcarrier, $P_s(\gamma)$ can be written as [15]

$$P_s(\gamma) = 1 - \left[1 - \left(1 - \frac{1}{\sqrt{M}}\right) \operatorname{erfc}\left(\sqrt{\frac{3\gamma}{2(M-1)}}\right)\right]^2 \quad (5.62)$$

5.3.4 Analysis summary

In summary, we can analyze the performance of full-duplex communication using the following procedure:

1. Determine the following parameters:

- Nonlinear transfer function of amplifiers: $\alpha_1(x)$, $\alpha_2(x)$, $\beta_1(x)$, and $\beta_2(x)$
- The gain of the VGA g_n
- The input back-off:

$$\text{IBO}_n \text{ (dB)} = 20 \log_{10} \frac{A_{\text{sat},n}}{g_n G_n}, \quad (5.63)$$

where $A_{\text{sat},n}$ and G_n are the output saturation level and linear gain of $\alpha_n(x)$, respectively.

- Sum of propagation and RF cancellation (dB) = $-20 \log_{10} \rho_{nn}$
 - The propagation gain between terminals: ρ_{21} and ρ_{12}
 - Thermal noise level, including the noise figure of the LNA: \bar{N}_{thermal}
 - The nonlinear order of the canceller P
2. Compute the transmission power of the n -th terminal using (5.40).
 3. Compute the Fourier coefficients $\tilde{\alpha}_{n,p}$ of the n -th terminal's transmitter using (5.42).
 4. Compute the linear gain $\tilde{\beta}_{n,1}$ and nonlinear distortion power $\bar{N}_{\text{NL},n}$ of the n -th terminal's LNA with (5.38) and (5.39), respectively.
 5. Analyze the cancellation performance of a digital canceller SICR with (5.46)–(5.49).
 6. Analyze the SER with (5.54), (5.56), and (5.58)–(5.61), where the PSD of the orthonormal Laguerre polynomial can be written as [11]

$$|\Psi_p(f)|^2 = \sum_{k=0}^p \frac{(-1)^k}{(p-1)!} \binom{p}{k} \left(|f| - k + \frac{p}{2} \right)_+^{p-1}, \quad (5.64)$$

where

$$(u)_+^p = \begin{cases} u^p, & u > 0 \\ 0, & u \leq 0. \end{cases} \quad (5.65)$$

In the above procedure, we use numerical integration formulae because there some integrals cannot be evaluated with closed-form expressions.

Table 5.2: OFDM Modulation Specifications

Parameter	Value
Constellation	16QAM
FFT size	64
Active subcarriers	52
Cyclic prefix size	16
Bandwidth	20 MHz

Table 5.3: Simulation and Analysis Specifications

Parameter	Value
Oversampling rate	8
Sampling rate	20 MHz \times 8 = 160 MHz
SI channel after RF-SIC	Rayleigh fading
# of taps of SI channel	64 taps
Transmission power	23 dBm
PA Gain	30 dB
PA output saturation level	30 dBm
PA smoothness factor	3
LNA noise figure	4 dB
LNA Gain	20 dB
LNA output saturation level	14 dBm
LNA smoothness factor	3
# of taps of canceller	64 taps
# of training symbols of canceller	200 symbols
Trials	10001
# of transmission bits	10^5 bits on each trial

5.4 Examples and Verification

In this section, the author provides some results from the proposed analysis, and some simulation results for verifying the proposed analysis. Table 5.2 and Table 5.3 list the simulation parameters. In the simulations, the self-interference channel $h_{nn}(\tau)$, comprising the wireless channel and the RF self-interference canceller on the n -th terminal, was modeled as a quasi-static Rayleigh fading channel with a constant impulse response in a given simulation trial, with different impulse responses used in different simulation trials. We assumed there to be two full-duplex terminals, with identical nonlinear characteristics and parameters. Thus, in the simulation, the SICR_n and SER_n of the two terminals were identical. The nonlinearities of the

PAs and LNAs were implemented using the Rapp model [8], which is often used to simulate the baseband behaviors of class AB solid-state amplifiers. The AM-AM conversion of the Rapp model can be expressed as

$$\text{Rapp}(x; G, A_{\text{sat}}, s) = \frac{Gx}{\left(1 + \left(\frac{|Gx|}{A_{\text{sat}}}\right)^{2s}\right)^{\frac{1}{2s}}}, \quad (5.66)$$

where G is the linear gain of the amplifier, A_{sat} is the output saturation level, and s is the smoothness factor of the Rapp model. The larger the smoothness factor s , the stronger the linearity of the Rapp model. When the smoothness factor s is infinity, the Rapp model becomes an ideally predistorted amplifier, represented by the following AM-AM conversion:

$$\text{IdealPA}(x; G, A_{\text{sat}}) = \text{Rapp}(x; G, A_{\text{sat}}, \infty) = \begin{cases} Gx, & (|Gx| \leq A_{\text{sat}}), \\ A_{\text{sat}} \frac{x}{|x|}, & (|Gx| > A_{\text{sat}}). \end{cases} \quad (5.67)$$

We also implemented a time-domain parallel Hammerstein canceller [1, 2] in the simulator. We trained the canceller with the least squares algorithm with 200 OFDM symbols to achieve best performance. In this section, the author provides results from the Rapp model. For reference, in Appendix 5.D the author also provides results from the Saleh model [16], including both AM-AM and AM-PM nonlinearities.

5.4.1 Cancellation performance

Figure 5.5 shows the cancellation performance of the parallel Hammerstein canceller with different value of order P under various conditions of propagation and RF domain cancellation. We can confirm that the theoretical results and simulation results match well for nonlinear cancellers, demonstrating the accuracy of the proposed analysis method.

A more detailed discussion of Fig. 5.5 is as follows: The self-interference and noise ratio, INR, is defined as

$$\text{INR}_1 = \frac{\mathbb{E} \left[|h_{11}(\tau) * \alpha_1(g_1 x_1(t))|^2 \right]}{\mathbb{E} \left[|z_1(t)|^2 \right]} = \frac{\rho_{11}^2 \nu_1^2}{\overline{N}_{\text{thermal}}}, \quad (5.68)$$

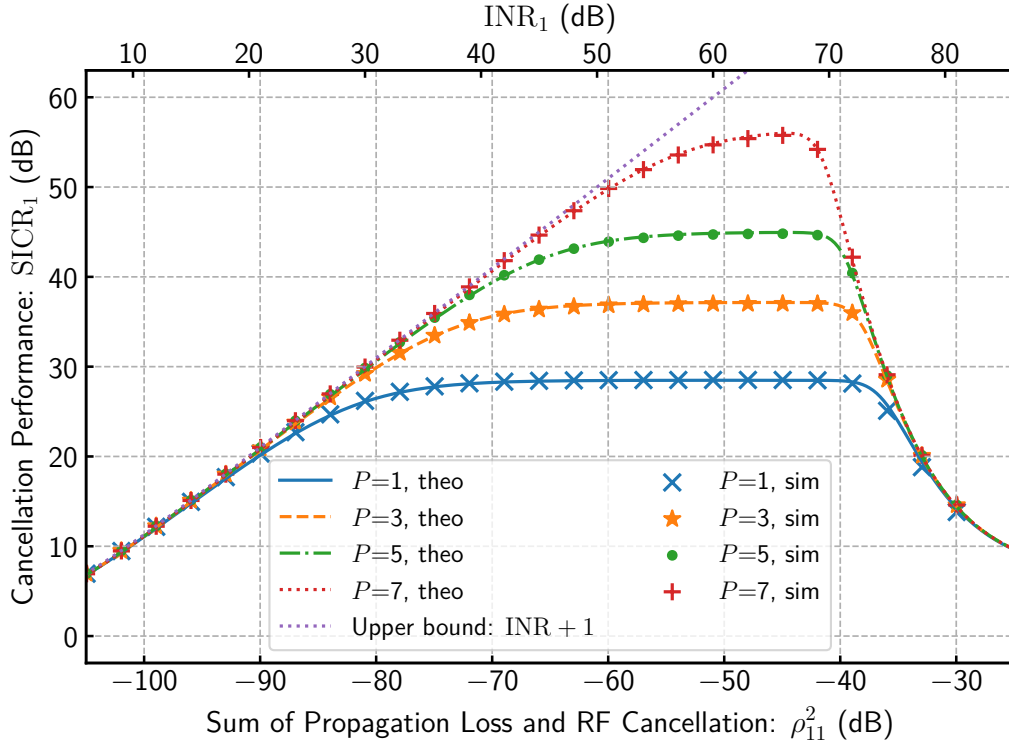


Figure 5.5: The performance of nonlinear self-interference cancellers with different values of received self-interference powers. The nonlinear amplifiers $\alpha_n(x)$ and $\beta_n(x)$ were modeled using the Rapp model.

where the numerator indicates the power of the self-interference on the first terminal. The upper bound of the cancellation performance SICR_1 can be expressed by using INR_1 as

$$\text{SICR}_1 \leq \frac{\bar{I}_{11} + \bar{N}_{\text{thermal}}}{\bar{N}_{\text{thermal}}} \leq \text{INR}_1 + 1. \quad (5.69)$$

Cancellers achieve the above upper bound when they have been trained with a sufficient number of OFDM symbols, and the LNA is not saturated by self-interference. In Fig. 5.5, we can see that the performance of the canceller with $P = 7$ reaches to the upper bound when $\rho_{11}^2 < -60$ dB. In contrast, when the order of the canceller P is less than seven, the performance cannot reach the upper bound when $\rho_{11}^2 < -60$ dB because the residual nonlinear self-interference distorted by the PA becomes larger than the thermal noise level. In Fig. 5.5, we can also see that the cancellation performance is significantly degraded by saturation of the LNA when

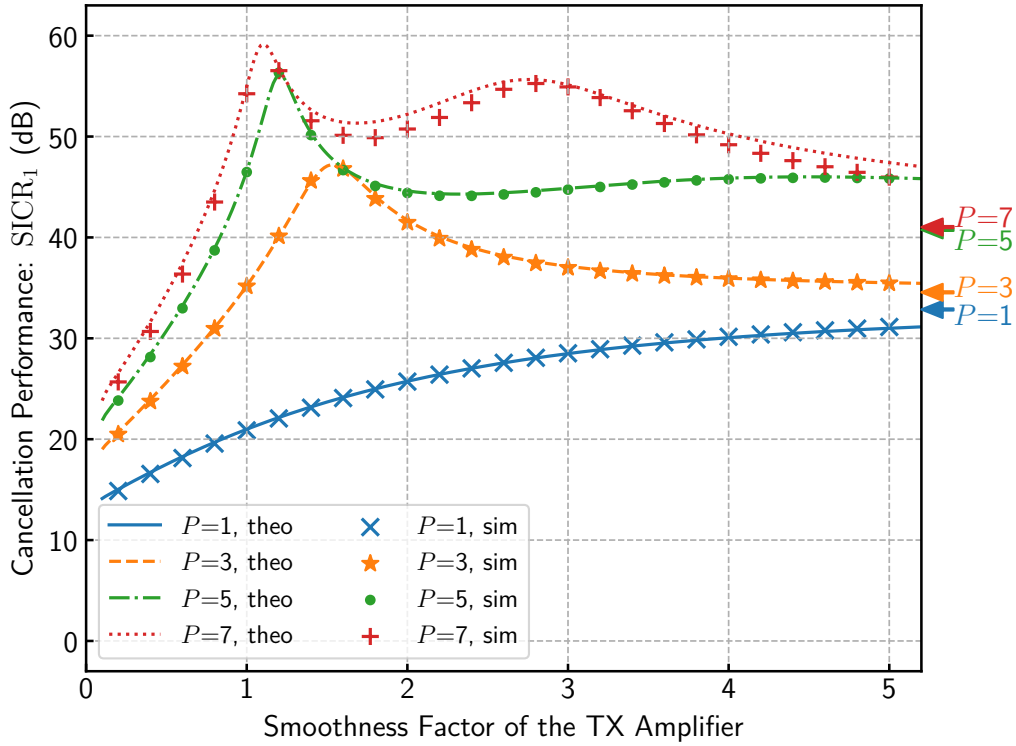


Figure 5.6: The performance of nonlinear self-interference cancellers with different values of smoothness factors for both terminals' PAs. The nonlinear amplifiers $\alpha_n(x)$ and $\beta_n(x)$ were modeled using the Rapp model. Arrows on the y-axis indicate the SICR_1 value of the infinite smoothness factor (ideally predistorted amplifier).

$\rho_{11}^2 > -55$ dB even if $P = 7$. The parallel Hammerstein canceller cannot estimate and regenerate the nonlinear self-interference caused by the LNA; to achieve higher performance, we need to consider the nonlinearity of the LNA [17–24].

Figure 5.6 shows the cancellation performance of the parallel Hammerstein canceller with various smoothness factors for both terminals' PAs. Firstly, we can confirm good correlation between the theoretical and simulation results. Furthermore, the linear canceller (i.e., $P = 1$) achieves the best cancellation performance when the PAs are ideally predistorted. The higher smoothness factor improves amplifier linearity. Thus, amplifier linearization is an effective technique for a full-duplex system with linear canceller. More interestingly, nonlinear cancellers such as $P = 3, 5, \text{ and } 7$ achieve maximum cancellation performance when the PAs show moderate nonlinearity. This means that the linearization degrades the cancellation performance of nonlinear cancellers. The author provides a detailed

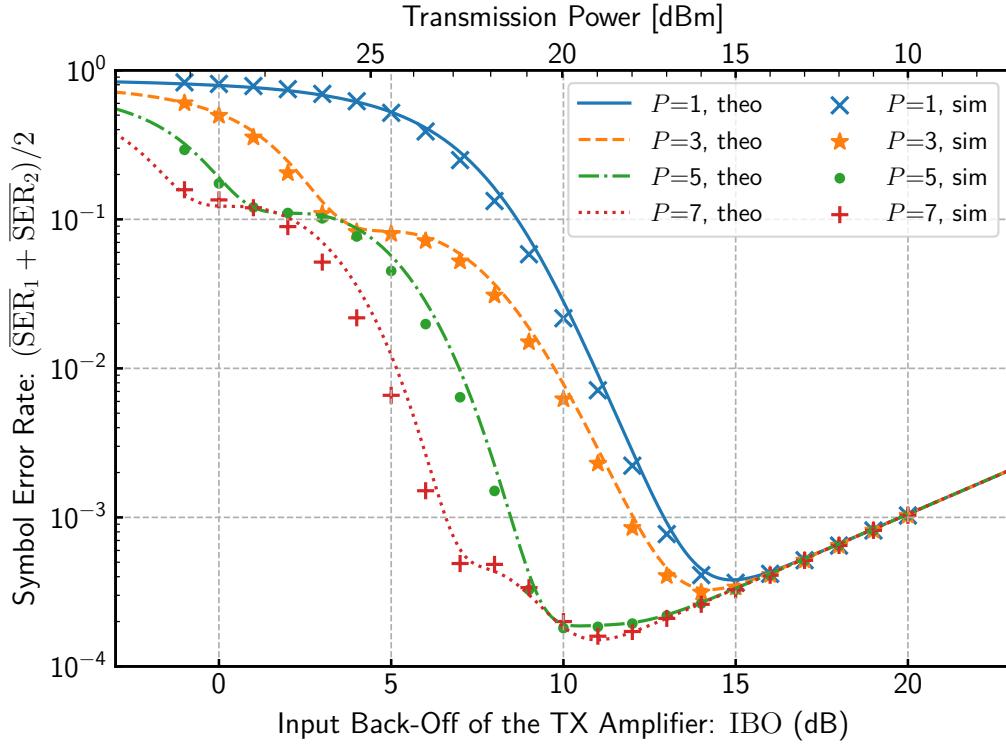


Figure 5.7: The average SER of the two full-duplex terminals with different values of input back-offs for both terminals' PAs. The nonlinear amplifiers $\alpha_n(x)$ and $\beta_n(x)$ were modeled using the Rapp model.

discussion of this phenomenon in Section 5.4.3.

5.4.2 Symbol error rate

Figure 5.7 shows the average SER of the full-duplex system under various back-offs for both terminals' PAs, i.e., under various transmit powers. Similar to the results of the cancellation performance shown in Fig. 5.5 and Fig. 5.6, the theoretical and simulation results match well in Fig. 5.7. When the input back-off is less than 10 dB, the SER degrades rapidly because the distortion introduced by the PAs increases. When the input back-off is greater than 15 dB, the SER also degrades slowly because the power of the desired signal decreases. Thus, there is an optimum back-off value, which depends on the nonlinear canceller's order P .

Figure 5.8 shows the average SER of the full-duplex system with various PA smoothness factors. Again, the theoretical and simulation results show good

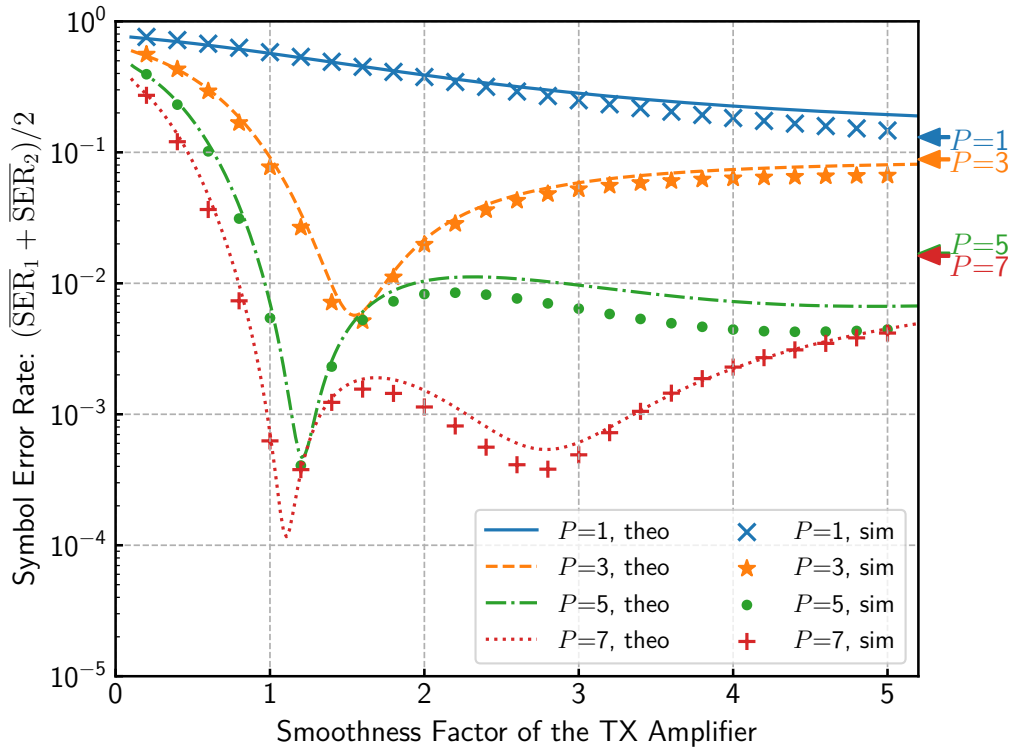


Figure 5.8: The average SER of the two full-duplex terminals with different values of smoothness factors for both terminals' PAs. The nonlinear amplifiers $\alpha_n(x)$ and $\beta_n(x)$ were modeled using the Rapp model. Arrows on the y-axis indicate results for the infinite smoothness factor (ideally predistorted amplifier).

correlation. The full-duplex system with a linear canceller such as $P = 1$ achieves the minimum SER when the PAs are ideally predistorted. In contrast, when we use nonlinear cancellers such as $P = 3, 5$, and 7 , the full-duplex system achieves the minimum SER for the smoothness factor $1 < s < 2$. As in Fig. 5.6, these results indicate that amplifier linearization is not the best approach for a full-duplex system with nonlinear cancellers. Although this result deviates from the common knowledge of half-duplex systems, it is confirmed by the theoretical analysis and simulation results shown in Fig. 5.8 for a full-duplex system with nonlinear self-interference canceller. These results are very interesting; in the following section we will clearly show why such results are obtained.

5.4.3 How can a nonlinear amplifier performance be better than the linearized amplifier?

From Fig. 5.6 and Fig. 5.8, we can confirm that the full-duplex terminal with a nonlinear canceller does not achieve the best performance using ideally linearized amplifiers for the transmitters. We can explain these results in terms of the residual self-interference power \bar{I}_{11}^R defined as (5.26) and rewritten as

$$\bar{I}_{11}^R = |\tilde{\beta}_{1,1}|^2 \rho_{11}^2 \left(|\tilde{\alpha}_{1,P+2}|^2 + |\tilde{\alpha}_{1,P+4}|^2 + \dots \right). \quad (5.70)$$

To achieve high cancellation performance and low SER, it is important to reduce the residual self-interference \bar{I}_{11}^R . For the linear canceller, $P = 1$, reducing the sum of all nonlinear distortions $|\tilde{\alpha}_{1,3}|^2 + |\tilde{\alpha}_{1,5}|^2 \dots$ leads to a reduction in \bar{I}_{11}^R . Thus, the linearization reducing the total distortion power is effective for the full-duplex system with a linear canceller. However, for nonlinear cancellers such as $P = 3, 5, 7, \dots$, reducing the sum of all nonlinear distortions $|\tilde{\alpha}_{1,3}|^2 + |\tilde{\alpha}_{1,5}|^2 \dots$ does not lead to a reduction in \bar{I}_{11}^R . This is because when the total power of distortions is reduced, the nonlinear component, with a higher order than P , does not necessarily become smaller. The third-order distortion has the greatest power among the nonlinear distortions. If the total distortion power can be reduced, the linearization will try to reduce the third-order distortion even if it increases the fifth- or seventh-order distortion power. Therefore, linearization does not reduce the residual self-interference when we use nonlinear cancellers. In summary, linearization is not the best approach for full-duplex systems with nonlinear cancellers. In addition, if we want to achieve higher performance in full-duplex communications, we should design predistorters such that the SER is small. The proposed analysis technique can be used to guide the design of such predistorters.

5.5 Conclusion

This chapter first presented some useful theorems for nonlinear self-interference cancellers and residual self-interference in full-duplex systems. Using these theorems, the author demonstrated that the performance of a full-duplex system with a nonlinear self-interference canceller can be expressed by coefficients of the general Fourier series expansion for nonlinear amplifiers. We compared results from the proposed analysis with simulation results in terms of self-interference cancellation

performance and SER, and confirmed that they match well. In addition, discussion of the results revealed that amplifier linearization is not the best approach in full-duplex systems with nonlinear cancellers. As a future challenge, we need to integrate the proposed analysis with the theoretical analysis of other nonidealities, such as IQ imbalance and phase noise, which have been analyzed in other literature.

Appendix 5.A Proof of Theorem 2

In this appendix, the author provides the proof of **Theorem 2**. The autocorrelation function of $y(t)$ is expressed as

$$R_{yy}(\tau) = \mathbb{E}_t [y(t)y^*(t + \tau)] = \sum_{p=1,3,\dots}^{\infty} \sum_{q=1,3,\dots}^{\infty} R_{yy}^{(p,q)}(\tau) \quad (5.71)$$

where $\mathbb{E}_t [\cdot]$ denotes the expected value for time t , and $R_{yy}^{(p,q)}(\tau)$ is defined as

$$\begin{aligned} R_{yy}^{(p,q)}(\tau) &= \mathbb{E}_t \left[\left(\int_0^{\infty} \tilde{h}_p(\tau_1) \psi_p(x(t - \tau_1)) d\tau_1 \right) \right. \\ &\quad \left. \times \left(\int_0^{\infty} \tilde{h}_q^*(\tau_2) \psi_q^*(x(t + \tau - \tau_2)) d\tau_2 \right) \right] \\ &= \int_0^{\infty} \int_0^{\infty} \tilde{h}_p(\tau_1) \tilde{h}_q^*(\tau_2) R_{\psi_p \psi_q}(\tau + \tau_1 - \tau_2) d\tau_1 d\tau_2, \end{aligned} \quad (5.72)$$

where $R_{\psi_p \psi_q}(\tau)$ is the cross-correlation function of $\psi_p(x(t))$ and $\psi_q(x(t))$. From (5.7), $R_{\psi_p \psi_q}(\tau) = 0$ when $p \neq q$. Thus, the frequency domain representation of $R_{yy}^{(p,q)}(\tau)$ can be expressed as

$$\mathcal{F} [R_{yy}^{(p,q)}(\tau)] = \begin{cases} |\tilde{H}_p(f)|^2 |\Psi_p(f)|^2, & (p = q) \\ 0, & (p \neq q) \end{cases} \quad (5.73)$$

where $\tilde{H}_p(f)$ is the frequency response of $\tilde{h}_p(\tau)$. Then, the PSD of $y(t)$ can be written as

$$|Y(f)|^2 = \sum_{p=1,3,\dots}^{\infty} |\tilde{H}_p(f)|^2 |\Psi_p(f)|^2. \quad (5.74)$$

By taking the expected values of both sides of the above equation, Eq. (5.23) can be derived. Also, the expected power of $y(t)$ can be expressed as

$$\begin{aligned}\mathbb{E} [|y(t)|^2] &= \int_{-\infty}^{\infty} \mathbb{E} [|Y(f)|^2] df = \sum_{p=1,3,\dots}^{\infty} \int_{-\infty}^{\infty} \rho_p^2 |\Psi_p(f)|^2 df \\ &= \sum_{p=1,3,\dots}^{\infty} \rho_p^2 \mathbb{E} [|\psi_p(x(t))|^2] = \sum_{p=1,3,\dots}^{\infty} \rho_p^2.\end{aligned}\quad (5.75)$$

Thus, Eq. (5.24) can be derived.

Appendix 5.B Condition of $\dot{c}_p(\tau) = \dot{h}_p(\tau)$

In this appendix, we prove the following theorem:

Theorem 4. *It is assumed that the received self-interference is expressed by a Q -order Hammerstein model as*

$$y(t) = \sum_{p=1,3,\dots}^Q \dot{h}_p(\tau) * x(t) |x(t)|^{p-1} + z(t), \quad (5.76)$$

where $\dot{h}_p(\tau)$ is an impulse response corresponding to $x(t) |x(t)|^{p-1}$, and $z(t)$ is a signal uncorrelated with the transmitted signal $x(t)$. Then, the impulse responses $\dot{c}_p(\tau)$ of the parallel Hammerstein canceller in (5.25) composed of up to P -order power series are given by the following identity

$$\dot{c}_p(\tau) = \dot{h}_p(\tau), \quad (5.77)$$

when $P \geq Q$. In contrast, when $P < Q$, $\dot{c}_p(\tau) \neq \dot{h}_p(\tau)$. In other words, we cannot theoretically analyze the residual nonlinear self-interference by using the non-orthogonal polynomial expansion.

Proof. The received signal $y(t)$ can be expressed as the following orthonormal Laguerre polynomial expansion:

$$y(t) = \sum_{p=1,3,\dots}^Q \tilde{h}_p(\tau) * \psi_p(x(t)) + z(t), \quad (5.78)$$

where $\tilde{h}_p(\tau)$ is an impulse response corresponding to $\psi_p(x(t))$. Similar to (5.28), we

can write the relationship between $\dot{h}_p(\tau)$ and $\tilde{h}_p(\tau)$ as

$$\tilde{\mathbf{h}}(\tau) = \mathbf{L}_{n+1}^{-1} \dot{\mathbf{h}}(\tau), \quad (5.79)$$

where $n = (Q - 1)/2$, and

$$\dot{\mathbf{h}}(\tau) = [\dot{h}_1(\tau) \ \dot{h}_3(\tau) \ \cdots \ \dot{h}_Q(\tau)]^T, \quad (5.80)$$

$$\tilde{\mathbf{h}}(\tau) = [\tilde{h}_1(\tau) \ \tilde{h}_3(\tau) \ \cdots \ \tilde{h}_Q(\tau)]^T. \quad (5.81)$$

From **Theorem 3**, when $P \geq Q$, $\tilde{\mathbf{c}}(\tau)$ is given by

$$\tilde{\mathbf{c}}(\tau) = \begin{bmatrix} \mathbf{I}_{n+1} \\ \mathbf{0}_{m-n \times n+1} \end{bmatrix} \tilde{\mathbf{h}}(\tau), \quad (5.82)$$

where $m = (P - 1)/2$. Using (5.28) and (5.79), $\dot{\mathbf{c}}(\tau)$ is given by

$$\dot{\mathbf{c}}(\tau) = \mathbf{L}_{m+1} \begin{bmatrix} \mathbf{I}_{n+1} \\ \mathbf{0}_{m-n \times n+1} \end{bmatrix} \mathbf{L}_{n+1}^{-1} \dot{\mathbf{h}}(\tau) = \begin{bmatrix} \dot{\mathbf{h}}(\tau) \\ \mathbf{0}_{m-n \times n+1} \end{bmatrix} \quad (5.83)$$

Thus, $\dot{c}_p(\tau) = \dot{h}_p(\tau)$ is derived: when the order of the self-interference model Q is less than the order of the canceller P (i.e., $P \geq Q$), all self-interference of (5.76) can be removed. However, the theoretical analysis of the case where all self-interference is removed is easy. Also, our main focus is the case where there is a residual nonlinear self-interference, i.e., $P < Q$. When $P < Q$, $\dot{c}_p(\tau)$ is given by

$$\begin{aligned} \dot{\mathbf{c}}(\tau) &= \mathbf{L}_{m+1} \begin{bmatrix} \mathbf{I}_{m+1} & \mathbf{0}_{m+1 \times n-m} \end{bmatrix} \mathbf{L}_{n+1}^{-1} \dot{\mathbf{h}}(\tau) \\ &= \begin{bmatrix} \dot{h}_1(\tau) \\ \dot{h}_3(\tau) \\ \vdots \\ \dot{h}_P(\tau) \end{bmatrix} + \begin{bmatrix} l'_{0,m+1} & l'_{0,m+2} & \cdots & l'_{0,n} \\ l'_{1,m+1} & l'_{1,m+2} & \cdots & l'_{1,n} \\ \vdots & \vdots & \ddots & \vdots \\ l'_{m,m+1} & l'_{m,m+2} & \cdots & l'_{m,n} \end{bmatrix} \begin{bmatrix} \dot{h}_{P+2}(\tau) \\ \dot{h}_{P+4}(\tau) \\ \vdots \\ \dot{h}_Q(\tau) \end{bmatrix} \end{aligned} \quad (5.84)$$

where $l'_{i,j} = (\mathbf{L}_{n+1}^{-1})_{i,j}$. Then, we derive $\dot{c}_p(\tau) \neq \dot{h}_p(\tau)$ when $P < Q$. The result shows that the analysis of residual self-interference is very difficult when using the non-orthogonal polynomial expansion. □

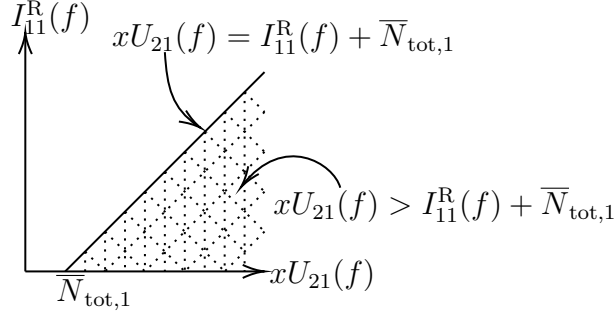


Figure 5.9: Domain of the two-dimensional integration in (5.89).

Appendix 5.C Probability Density Function of (5.57)

In this appendix, we derive the PDF of (5.57). We assume that $|H_{11}(f)|^2$ and $|H_{21}(f)|^2$ are have exponential distributions $\text{Exp}(\rho_{11}^2)$ and $\text{Exp}(\rho_{21}^2)$, respectively. Thus, $I_{11}^R(f)$ and $U_{21}(f)$ are distributed exponentially, and expected values for these random variables in $-\frac{1}{2} < f < \frac{1}{2}$ can be expressed as

$$\bar{I}_{11}^R(f) = \mathbb{E} [I_{11}^R(f)] = \left| \tilde{\beta}_{1,1} \rho_{11} \right|^2 \sum_{p=P+2, P+4, \dots}^{\infty} |\tilde{\alpha}_{1,p}|^2 |\Psi_p(f)|^2, \quad (5.85)$$

$$\bar{U}_{21} = \mathbb{E} [U_{21}(f)] = \left| \tilde{\beta}_{1,1} \rho_{21} \tilde{\alpha}_{2,1} \right|^2. \quad (5.86)$$

Thus, the probability distribution function of $I_{11}^R(f)$ and $U_{21}(f)$ can be described as

$$p_{I_{11}^R}(x; f) = \frac{1}{\bar{I}_{11}^R(f)} \exp\left(-\frac{x}{\bar{I}_{11}^R(f)}\right), \quad (5.87)$$

$$p_{U_{21}}(x) = \frac{1}{\bar{U}_{21}} \exp\left(-\frac{x}{\bar{U}_{21}}\right). \quad (5.88)$$

Then, the cumulative distribution function of (5.57) in $-\frac{1}{2} < f < \frac{1}{2}$ can be written as

$$\begin{aligned}
 \text{Prob} \{ \lambda_{\text{sinr},1}(f) < x \} &= \text{Prob} \{ I_{11}^{\text{R}}(f) + \bar{N}_{\text{tot},1} < xU_{21}(f) \} \\
 &= \int_{\bar{N}_{\text{tot},1}/x}^{\infty} \left(\int_0^{xU - \bar{N}_{\text{tot},1}} p_{I_{11}^{\text{R}}}(I; f) dI \right) p_{U_{21}}(U) dU \\
 &= \exp \left(-\frac{\bar{N}_{\text{tot},1}}{x\bar{U}_{21}} \right) \left\{ 1 - \frac{1}{\bar{U}_{21}} \left(\frac{x}{\bar{I}_{11}^{\text{R}}(f)} + \frac{1}{\bar{U}_{21}} \right)^{-1} \right\}, \tag{5.89}
 \end{aligned}$$

where $p_{I_{11}^{\text{R}}}(x; f)$ and $p_{U_{21}}(x)$ are PDFs of the exponential distributions of $I_{11}^{\text{R}}(f)$ and $U_{21}(f)$, respectively. In (5.89), the domain of the two-dimensional integration is as shown in Fig. 5.9. Thus, the PDF of (5.57) can be described as

$$\begin{aligned}
 p_{\lambda_{\text{sinr},1}}(x; f) &= \frac{d}{dx} \text{Prob} \{ \lambda_{\text{sinr},1}(f) < x \} \\
 &= \frac{\bar{N}_{\text{tot},1}(x\bar{U}_{21} + \bar{I}_{11}^{\text{R}}(f)) + x\bar{U}_{21}\bar{I}_{11}^{\text{R}}(f)}{x(x\bar{U}_{21} + \bar{I}_{11}^{\text{R}}(f))^2} \exp \left(-\frac{\bar{N}_{\text{tot},1}}{x\bar{U}_{21}} \right). \tag{5.90}
 \end{aligned}$$

Appendix 5.D Analysis Examples on Saleh Model

To prove that the proposed technique can analyze AM-PM characteristics as well as AM-AM characteristics, the author shows additional analysis results using the Saleh model [16]. The transfer function of the Saleh model can be expressed as

$$f(x) = \frac{A_1 x}{1 + B_1 |x|^2} \exp \left(j \frac{A_2 |x|^2}{1 + B_2 |x|^2} \right), \tag{5.91}$$

where A_1 , A_2 , B_1 , and B_2 are parameters that characterize the nonlinearity of the Saleh model. When the linear gain, output saturation level, and phase displacement at the saturation point are G , A_{sat} , and Φ_{sat} respectively, the parameters of the Saleh model can be expressed as

$$A_1 = G, \quad A_2 = \frac{2\Phi_{\text{sat}}G^2}{4A_{\text{sat}}^2}, \quad B_1 = B_2 = \frac{G^2}{4A_{\text{sat}}^2}. \tag{5.92}$$

In this chapter, we use $\Phi_{\text{sat}} = \pi/6$, and G and A_{sat} , as with the Rapp model. Figure 5.10 shows the average symbol error rate of the full-duplex system which

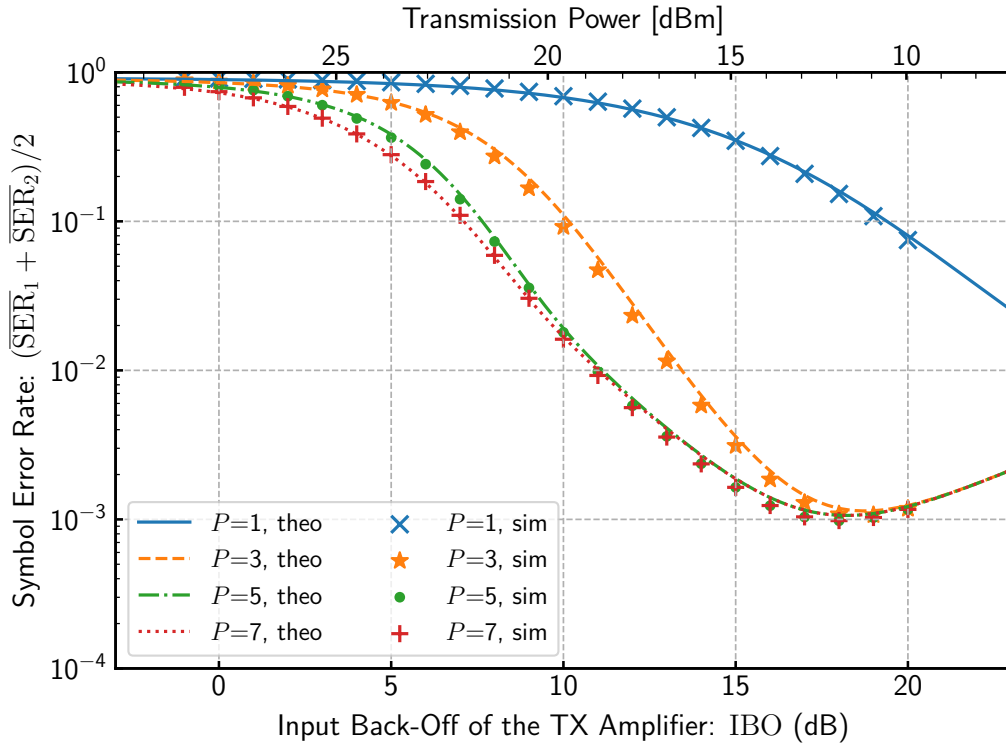


Figure 5.10: The average symbol error rate (SER) of the two full-duplex terminals with different values of input-back-offs of both terminals' PAs. The nonlinear amplifiers $\alpha_n(x)$ and $\beta_n(x)$ are modeled using the Saleh model.

has Saleh-modeled amplifiers with various back-offs. The simulation and analysis parameters of Fig. 5.10 are the same as those in Fig. 5.7 except for the nonlinear transfer function. As with the results of the Rapp model, which does not have an AM-PM characteristic, we can also confirm that the theoretical results and simulation results match well even if the transfer functions have an AM-PM characteristic.

References

- [1] D. Bharadia, E. McMillin, and S. Katti, “Full duplex radios,” in *Proc. ACM SIGCOMM'13*, 2013.
- [2] L. Anttila, D. Korpi, V. Syrjälä, and M. Valkama, “Cancellation of power amplifier induced nonlinear self-interference in full-duplex transceivers,” in *Proc. 47th Asilomar Conf. Signals, Syst., Comput.*, Nov. 2013.
- [3] D. Korpi, L. Anttila, V. Syrjälä, and M. Valkama, “Widely linear digital self-interference cancellation in direct-conversion full-duplex transceiver,” *IEEE J. Sel. Areas Commun.*, vol. 32, no. 9, pp. 1674–1687, Sept. 2014.
- [4] D. Korpi, T. Huusari, Y.-S. Choi, L. Anttila, S. Talwar, and M. Valkama, “Digital self-interference cancellation under nonideal RF components: Advanced algorithms and measured performance,” in *Proc. IEEE SPAWC*, June 2015, pp. 286–290.
- [5] K. Komatsu, Y. Miyaji, and H. Uehara, “Basis function selection of frequency-domain Hammerstein self-interference canceller for in-band full-duplex wireless communications,” *IEEE Trans. Wireless Commun.*, vol. 17, no. 6, pp. 3768–3780, June 2018.
- [6] D. Korpi, L. Anttila, and M. Valkama, “Nonlinear self-interference cancellation in MIMO full-duplex transceivers under crosstalk,” *EURASIP J. Wireless Commun. Netw.*, vol. 2017, Feb. 2017.
- [7] D. Korpi, T. Riihonen, V. Syrjälä, L. Anttila, M. Valkama, and R. Wichman, “Full-duplex transceiver system calculations: Analysis of ADC and linearity challenges,” *IEEE Trans. Wireless Commun.*, vol. 13, no. 7, pp. 3821–3836, July 2014.

- [8] C. Rapp, “Effects of HPA-nonlinearity on a 4-DPSK/OFDM-signal for a digital sound broadcasting system,” in *Proc. the Second European Conf. on Satellite Commun.*, Oct. 1991, pp. 179–184.
- [9] P. Banelli and S. Cacopardi, “Theoretical analysis and performance of OFDM signals in nonlinear AWGN channels,” *IEEE Trans. Commun.*, vol. 48, no. 3, pp. 430–441, Mar. 2000.
- [10] R. Raich and G. Zhou, “Theory and applications of orthogonal polynomials for Gaussian input,” in *Proc. IEEE Stat. Signal Process. Wrkshps*, 2003, pp. 106–109.
- [11] ———, “Orthogonal polynomials for complex Gaussian processes,” *IEEE Trans. Signal Process.*, vol. 52, no. 10, pp. 2788–2797, Oct. 2004.
- [12] P. Banelli, G. Baruffa, and S. Cacopardi, “Effects of HPA nonlinearity on frequency multiplexed OFDM signals,” *IEEE Trans. Broadcast.*, vol. 47, no. 2, pp. 123–136, June 2001.
- [13] P. Banelli, “Theoretical analysis and performance of OFDM signals in nonlinear fading channels,” *IEEE Trans. Wireless Commun.*, vol. 2, no. 2, pp. 284–293, Mar. 2003.
- [14] K. Komatsu, Y. Miyaji, and H. Uehara, “Frequency-domain Hammerstein self-interference canceller for in-band full-duplex OFDM systems,” in *Proc. IEEE WCNC*, Mar. 2017.
- [15] J. G. Proakis, *Digital communications*, 3rd ed., ser. electrical and computer engineering. McGraw-Hill, 1995.
- [16] A. A. M. Saleh, “Frequency-independent and frequency-dependent nonlinear models of TWT amplifiers,” *IEEE Trans. Commun.*, vol. 29, no. 11, pp. 1715–1720, 1981.
- [17] M. Grimm, M. Allen, J. Marttila, M. Valkama, and R. Thoma, “Joint mitigation of nonlinear RF and baseband distortions in wideband direct-conversion receivers,” *IEEE Trans. Microw. Theory Techn.*, vol. 62, no. 1, pp. 166–182, Jan. 2014.
- [18] M. Valkama, A. S. H. Ghadam, L. Anttila, and M. Renfors, “Advanced digital signal processing techniques for compensation of nonlinear distortion in wideband multicarrier radio receivers,” *IEEE Trans. Microw. Theory Techn.*, vol. 54, no. 6, pp. 2356–2366, June 2006.
- [19] E. A. Keehr and A. Hajimiri, “Equalization of third-order intermodulation products in wideband direct conversion receivers,” *IEEE J. Solid-State Circuits*, vol. 43, no. 12, pp. 2853–2867, Dec. 2008.

- [20] Q. Zou, M. Mikhemar, and A. H. Sayed, “Digital compensation of cross-modulation distortion in software-defined radios,” *IEEE J. Sel. Topics Signal Process.*, vol. 3, no. 3, pp. 348–361, June 2009.
- [21] J. Liu, H. Quan, Z. Li, H. Sun, and D. Yuan, “Digital nonlinear self-interference cancellation based on LMS-Volterra algorithm,” in *Proc. 3rd Int. Conf. Inf. Sci. Control Eng. (ICISCE)*, July 2016, pp. 1298–1302.
- [22] D. Korpi, M. Turunen, L. Anttila, and M. Valkama, “Modeling and cancellation of self-interference in full-duplex radio transceivers: Volterra series-based approach,” in *Proc. IEEE ICC Wkshps*, May 2018.
- [23] M. A. Islam and B. Smida, “A comprehensive self-interference model for single-antenna full-duplex communication systems,” in *Proc. IEEE ICC*, May 2019.
- [24] K. Komatsu, Y. Miyaji, and H. Uehara, “Iterative nonlinear self-interference cancellation for in-band full-duplex wireless communications under mixer imbalance and amplifier nonlinearity,” *IEEE Trans. Wireless Commun.*, vol. 19, no. 7, pp. 4424–4438, July 2020.

Chapter 6

Overall Conclusions

Nonlinear SI cancellers exhibit certain problems, such as a high computational cost, the requirement of large training data, and vulnerability to the nonlinearity of LNAs. Moreover, no theoretical studies have been conducted on the performance of IBFD radios with nonlinear cancellers. This thesis has presented studies on nonlinear SI cancellers for IBFD radios regarding these problems.

In Chapter 1, the background to this thesis was provided. Moreover, a detailed model of non-idealities in IBFD radios was presented. Thereafter, the time-domain parallel Hammerstein SI canceller, which is one of the most well-studied nonlinear cancellers, has been summarized.

In Chapter 2, a novel frequency-domain parallel Hammerstein SI canceller to reduce the computational cost while taking into account the nonlinearity of I/Q mixers and PAs was described. OFDM signals have discontinuities between symbols. Time-domain cancellers can estimate the effect of the discontinuities, but conventional frequency-domain cancellers cannot. To estimate the effect of the discontinuities, swapped OFDM symbols consisting of the first and second half of different symbols were introduced. The proposed scheme decreases the computational cost by estimating the characteristic of the SI channel in the frequency domain and by using the overlap-save method for regenerating SI signals. Moreover, the proposed scheme exhibits good compatibility with time-domain parameter estimation algorithms such as LS, RLS, and normalized LMS. The simulation results demonstrate that the proposed scheme can achieve as high cancellation performance

as the time-domain scheme and fast convergence with a low computational cost.

In Chapter 3, a basis function selection technique for the frequency-domain Hammerstein SI canceller, which was presented developed in Chapter 2, was proposed. This selection technique enables the computational cost of the canceller to be reduced further. The estimation technique of the PSD of the received SI is developed from the detailed nonlinear characteristics of a full-duplex terminal. The proposed selection technique reduces unnecessary basis functions for cancellation prior to the training stage according to the estimated SI power at each discrete frequency. The simulation results demonstrate that the proposed technique improves the computational cost and convergence performance of the original frequency-domain Hammerstein canceller. It is revealed that the computational cost can be reduced to approximately one-fifth in the low SI situation by reducing the basis functions according to the estimated SI signal power. Moreover, by using the proposed selection technique, the SI cancellation performance of the frequency-domain Hammerstein canceller hardly decreases and similar cancellation performance to that of the original is achieved.

The frequency-domain Hammerstein canceller presented in Chapters 2 and 3 achieves a much lower computational cost than that of time-domain Hammerstein cancellers. However, the frequency-domain Hammerstein canceller cannot remove distortions caused by the receiver LNA as effectively as time-domain Hammerstein cancellers. Both cancellers are based on the parallel Hammerstein model and the SI signal with the LNA cannot be described by the parallel Hammerstein model. Thus, in Chapter 4, operators were introduced that express the characteristics of each RF component in a minimum form, and a nonlinear SI signal model was derived instead of the parallel Hammerstein model. Thereafter, a novel nonlinear SI canceller was proposed to reduce the nonlinear SI caused by the transmitter and receiver and I/Q mixers, PA, and LNA effectively. The estimation process of the proposed canceller consists of three stages, which estimate the characteristics of the corresponding operator of each RF component. The simulation results demonstrate that the proposed canceller can estimate and remove the received SI signal that is distorted by the LNA. Moreover, the proposed canceller achieves higher cancellation performance with fewer learning symbols and a lower computational cost than the Hammerstein canceller.

Through the studies of Chapters 2 to 4, high-performance and low computational complexity nonlinear SI cancellers have been developed that can be integrated into

small and inexpensive terminals. In particular, the iterative canceller in Chapter 4 can achieve higher cancellation and training performance, while reducing the computational cost to a tenth of that of the least computationally expensive training method of conventional time-domain parallel Hammerstein cancellers. However, the general knowledge of nonlinear cancellers has not been expanded in these studies; for example, how to increase the cancellation performance of these cancellers further. Therefore, a detailed theoretical analysis on nonlinear cancellers is required to promote the research on more advanced IBFD systems. The envelope of an OFDM signal with a sufficiently large number of subcarriers can be assumed to follow a complex Gaussian distribution according to the central limit theorem. Chapter 5 focused on PA and LNA nonlinearities, and presented several useful theorems for nonlinear SI cancellers and residual SI in full-duplex systems based on the analysis of nonlinear half-duplex systems with a complex Gaussian signal. Using these theorems, it was demonstrated that the performance of a full-duplex system with a nonlinear SI canceller can be expressed by the coefficients of the general Fourier series expansion for nonlinear amplifiers. The results from the proposed scheme analysis have been compared with simulation results in terms of SI cancellation performance and SER, and it was confirmed that the results match well. Moreover, a discussion of the results revealed that amplifier linearization is not the best approach in full-duplex systems with nonlinear cancellers. That is, the further performance improvement of full-duplex radios requires the design of terminals combined with nonlinear SI cancellers and nonlinearizing predistorters.

As a future challenge, it is necessary to integrate the proposed analysis described in Chapter 5 with the theoretical analysis of other non-idealities, such as I/Q imbalance and phase noise, which have been analyzed in other works. Moreover, if we wish to achieve higher performance in full-duplex communications, predistorters should be designed such that the SER is small. Our proposed analysis technique can be used to guide the design of such predistorters. It is predicted that the development of such predistorters will require a precise estimation of the PA characteristics, and Appendix A, which presents a novel estimation method for the memoryless nonlinearity of an amplifier, will aid in this.

Appendix A

Weighted Least Squares with Orthonormal Polynomials and Numerical Integration for Estimation of Memoryless Nonlinearity

The nonlinearity of amplifiers is one of the major impairments in wireless communications. In this appendix, the author proposes a novel estimation method for the memoryless nonlinearity of amplifiers using weighted least squares and provide its theoretical error analysis on complex Gaussian signals. In the proposed method, the input signal and weight value are obtained via numerical integration formulas. Simulation results show that the proposed method can achieve a sufficiently low reconstruction error with 10 measurement samples on the estimation of the 13th-order nonlinearity. In addition, the simulation and theoretical results are consistent with each other.

A.1 Introduction

Wireless communication systems suffer from the nonlinearities of amplifiers or other radio-frequency (RF) circuits. Accordingly, the estimation and compensation of these nonlinearities are important research objectives. The memoryless nonlinearity of an amplifier needs to be estimated accurately to achieve better pre-distortion [1] or better self-interference cancellation [2]. In the simplest model of the nonlinearity

estimation problem, the relation between the input signal x_n and the output signal y_n can be written as

$$y_n = f(x_n) + z_n, \quad (\text{A.1})$$

where $f(x)$ is the nonlinear transfer function of the target amplifier and z_n is additive white Gaussian noise that is independent of x_n and distributed on $\mathcal{CN}(0, \sigma_z^2)$. In the model of (A.1), we focus on the accurate estimation of the transfer function of the amplifier with a small number of observation samples under the assumption that the output of the amplifier can be observed directly. The simplest solution of this problem is achieved using polynomial approximation and least squares estimation. Accordingly, the transfer function of the amplifier $f(x)$ is approximated to the following P -th order memoryless polynomial:

$$f(x) \approx a_1x + a_3x|x|^2 + \cdots + a_Px|x|^{P-1}, \quad (\text{A.2})$$

and the coefficients a_1, a_3, \cdots, a_P are estimated using the following least squares method with N measurement samples:

$$\hat{\mathbf{a}} = [\hat{a}_1 \ \hat{a}_3 \ \cdots \ \hat{a}_P]^T = (\mathbf{X}^H \mathbf{X})^{-1} \mathbf{X}^H \mathbf{y}, \quad (\text{A.3})$$

where $(\cdot)^T$ and $(\cdot)^H$ denote the transpose and Hermitian transpose of a matrix, respectively, \hat{a}_p represents the estimated coefficients, and

$$\mathbf{X} = \begin{bmatrix} x_1 & x_1|x_1|^2 & \cdots & x_1|x_1|^{P-1} \\ x_2 & x_2|x_2|^2 & \cdots & x_2|x_2|^{P-1} \\ \vdots & \vdots & \ddots & \vdots \\ x_N & x_N|x_N|^2 & \cdots & x_N|x_N|^{P-1} \end{bmatrix}, \quad (\text{A.4})$$

$$\mathbf{y} = [y_1 \ y_2 \ \cdots \ y_N]^T. \quad (\text{A.5})$$

However, this solution has severe numerical instability due to the large condition number of the Gram matrix $\mathbf{X}^H \mathbf{X}$ on high-order nonlinearity estimation [1, 3, 4]. Existing literature [1,3,4] provides an improved method for mitigating the instability, using orthonormal polynomials instead of $x|x|^{p-1}$. Because of their advantages of orthonormality and orthogonality, orthogonal polynomials have been applied to not only estimation problems but also the latest studies on nonlinearities in a wide

range of wireless communications such as the analysis of massive multiple-input multiple-output (MIMO) systems [5] and nonlinear equalizers [6].

In the improved version of the least squares estimation, the transfer function $f(x)$ is approximated to the following P -th order expansion:

$$f(x) \approx b_1\psi_1(x) + b_3\psi_3(x) + \dots + b_P\psi_P(x), \quad (\text{A.6})$$

where $\psi_p(x)$ is a p -th order orthonormal polynomial. For the expansion (A.6), among the various types of orthogonal polynomials, a polynomial that satisfies the following orthonormality is used, to achieve better stability:

$$\mathbb{E} [\psi_p(x)\psi_q^*(x)] = \int_{\mathbb{C}} \psi_p(x)\psi_q^*(x)p_x(x)dx = \delta_{pq}, \quad (\text{A.7})$$

where δ_{pq} is the Kronecker delta, $p_x(x)$ is the probability density function of x , and $\int_{\mathbb{C}} dx$ indicates integration on the complex plane. The orthonormal polynomial $\psi_p(x)$ depends on the distribution of the communication signal because the expectation of (A.7) depends on it. Most current communication systems use orthogonal frequency-division multiplexing (OFDM) as the modulation scheme. The OFDM signal is distributed on the complex Gaussian distribution due to a high number of subcarriers and the central limit theorem [3, 7]. When the complex Gaussian signal has a unit variance, i.e., unit power, the orthonormal polynomial $\psi_p(x)$, which satisfies the orthonormality of (A.7), can be written as

$$\psi_{2m+1}(x) = \frac{(-1)^m}{\sqrt{m+1}} L_m^1(|x|^2)x, \quad (\text{A.8})$$

where $L_m^1(z)$ is the following generalized Laguerre polynomial:

$$L_m^\alpha(z) = \sum_{n=0}^m \frac{(-1)^n}{n!} \binom{m+\alpha}{m-n} z^n. \quad (\text{A.9})$$

Therefore, the estimated coefficient vector of the orthonormal expansion (A.6) obtained using the improved least squares can be expressed as

$$\hat{\mathbf{b}} = [\hat{b}_1 \ \hat{b}_3 \ \dots \ \hat{b}_P]^T = (\mathbf{\Psi}^H \mathbf{\Psi})^{-1} \mathbf{\Psi}^H \mathbf{y}, \quad (\text{A.10})$$

where

$$\mathbf{\Psi} = \begin{bmatrix} \psi_1(x_1) & \psi_3(x_1) & \cdots & \psi_P(x_1) \\ \psi_1(x_2) & \psi_3(x_2) & \cdots & \psi_P(x_2) \\ \vdots & \vdots & \ddots & \vdots \\ \psi_1(x_N) & \psi_3(x_N) & \cdots & \psi_P(x_N) \end{bmatrix}. \quad (\text{A.11})$$

In (A.10), the (i, j) element of the Gram matrix $\mathbf{\Psi}^H \mathbf{\Psi}$ can be written as

$$\left(\mathbf{\Psi}^H \mathbf{\Psi}\right)_{i,j} = \sum_{n=1}^N \psi_{2i-1}^*(x_n) \psi_{2j-1}(x_n). \quad (\text{A.12})$$

When the number of measurements N is sufficiently large, the equation

$$\lim_{N \rightarrow \infty} \frac{1}{N} \left(\mathbf{\Psi}^H \mathbf{\Psi}\right)_{i,j} = \mathbb{E} \left[\psi_{2i-1}^*(x) \psi_{2j-1}(x) \right] = \delta_{ij} \quad (\text{A.13})$$

holds due to the orthonormality of $\psi_p(x)$ because $\frac{1}{N} \left(\mathbf{\Psi}^H \mathbf{\Psi}\right)_{i,j}$ is a sample average, and it converges to the expected value when $N \rightarrow \infty$. Thus, (A.13) indicates that, if a sufficiently large number of measurement samples is available, the condition number of the Gram matrix converges to 1.

However, the convergence speed of (A.13) is very low when the measurement signal x_n is randomly generated from a complex Gaussian distribution. The intuitive reason is that (A.12) is the Monte Carlo integration. It is known that the error of the Monte Carlo integration decreases as $1/\sqrt{N}$, and it is much slower than other numerical integration schemes. The same issue arises on $\mathbf{\Psi}^H \mathbf{y}$ of (A.10). The i -th element of $\mathbf{\Psi}^H \mathbf{y}$ is written as

$$\left(\mathbf{\Psi}^H \mathbf{y}\right)_i = \sum_{n=1}^N \psi_{2i-1}^*(x_n) y_n. \quad (\text{A.14})$$

When the number of measurements N is sufficiently large, the equation

$$\begin{aligned} \lim_{N \rightarrow \infty} \frac{1}{N} \left(\mathbf{\Psi}^H \mathbf{y}\right)_i &= \mathbb{E} \left[\psi_{2i-1}^*(x) f(x) \right] \\ &= \frac{1}{\pi} \int_{\mathbb{C}} f(x) \psi_{2i-1}^*(x) e^{-|x|^2} dx = b_{2i-1} \end{aligned} \quad (\text{A.15})$$

holds due to the orthonormality of $\psi_p(x)$. However, the convergence speed of (A.15) is very low due to the Monte Carlo integration.

To summarize, the conventional least squares method has the following problems:

- Large condition number: When the number of measurement signals is not sufficient, the condition number of the Gram matrix becomes a large value.
- Low convergence speed: When the number of measurement signals is not sufficient, the estimated value does not converge to a true value.

These problems are related to random sampling observation, and the authors of the paper [8] proposed a sample selection method based on the genetic algorithm to solve these problems on digital pre-distortion with non-orthogonal polynomials. In contrast, in this appendix, the author proposes a weighted least squares method with orthonormal polynomials and numerical integration. In the proposed method, the measurement input signal x_n and the weights of the least squares are easily obtained via numerical integration formulas.

The details of the proposed method are described in Section A.2. In Section A.3, the proposed scheme and the conventional least squares method are compared via numerical simulations. Section A.4 presents the conclusion of the letter.

A.2 Proposed Method

The proposed method uses the weighted least squares method. The measurement samples and weights are obtained using a numerical integration formula. In the proposed method, we approximate the transfer function to the orthonormal polynomial expansion of (A.6). Then, the vector of the estimated coefficients is expressed as

$$\hat{\mathbf{b}} = (\mathbf{\Psi}^H \mathbf{W} \mathbf{\Psi})^{-1} \mathbf{\Psi}^H \mathbf{W} \mathbf{y}, \quad (\text{A.16})$$

where $\mathbf{\Psi}$ and \mathbf{y} are the same as (A.11) and (A.5), respectively, and $\mathbf{W} = \text{diag}\{w_1, w_2, \dots, w_N\}$ is a diagonal weight matrix. The main difference between the conventional and proposed methods is that the measurement samples x_n and the weight w_n are obtained using a numerical integration formula that can calculate the following two integrals:

$$\mathbb{E} [\psi_{2i-1}^*(x) \psi_{2j-1}(x)] = \frac{1}{\pi} \int_{\mathbb{C}} \psi_{2i-1}^*(x) \psi_{2j-1}(x) e^{-|x|^2} dx, \quad (\text{A.17})$$

$$\mathbb{E} [f(x) \psi_{2i-1}^*(x)] = \frac{1}{\pi} \int_{\mathbb{C}} f(x) \psi_{2i-1}^*(x) e^{-|x|^2} dx, \quad (\text{A.18})$$

with a high accuracy even if the number of measurements N is very small. Generally, a numerical integration formula with N samples can be written as

$$\mathbb{E}[g(x)] \approx \sum_{n=1}^N g(x_n)w_n, \quad (\text{A.19})$$

where $g(x)$ is an arbitrary function, and x_n and w_n are the computing points and weights of the numerical integration, respectively. In the proposed method, we use the computing points as measurement samples, and the n -th element of the diagonal weight matrix \mathbf{W} is w_n . Then, we can expect that the following two equations:

$$\left(\Psi^H \mathbf{W} \Psi\right)_{i,j} = \sum_{n=1}^N \psi_{2i-1}^*(x_n) \psi_{2j-1}(x_n) w_n, \quad (\text{A.20})$$

$$\left(\Psi^H \mathbf{W} \mathbf{y}\right)_i = \sum_{n=1}^N y_n \psi_{2i-1}^*(x_n) w_n, \quad (\text{A.21})$$

rapidly converge to the expected values of (A.17) and (A.18), respectively, if the noise is ignored. Therefore, the Gram matrix $\Psi^H \mathbf{W} \Psi$ becomes the identity matrix, and the estimated vector $\hat{\mathbf{b}}$ stably converges to the true coefficient vector \mathbf{b} , even if the number of measurement samples is very small. In addition, if the Gram matrix is approximately the identity matrix, the estimate can be given as $\hat{\mathbf{b}} \approx \Psi^H \mathbf{W} \mathbf{y}$.

A.2.1 Example 1: Gauss–Laguerre quadrature

The integrations of (A.17) and (A.18) can be rewritten as

$$\begin{aligned} \mathbb{E}[g(x)] &= \frac{1}{\pi} \int_0^{2\pi} \int_0^\infty g(re^{j\theta}) e^{-r^2} r dr d\theta \\ &= \int_0^\infty g(r) \cdot 2r e^{-r^2} dr = \int_0^\infty g(\sqrt{t}) e^{-t} dt, \end{aligned} \quad (\text{A.22})$$

where $g(x) = \psi_{2i-1}(x) \psi_{2j-1}^*(x)$ for (A.17), and $g(x) = f(x) \psi_{2i-1}^*(x)$ for (A.18). The reason for the above transformation is that $g(x) = g(|x|)$ holds in both cases. The last term of (A.22) is a semi-infinite integral with an exponentially decaying weight function, and the Gauss–Laguerre quadrature is a good choice for integrating it with high accuracy. In the Gauss–Laguerre quadrature, the computing point t_n is the n -th root of the Laguerre polynomial $L_N(x) = L_N^0(x)$, and the weights are given

by [9, Eq. 25.4.45]

$$w'_n = \frac{x_n}{(N+1)^2 [L_{N+1}(x_n)]^2}. \quad (\text{A.23})$$

Then, the measurement samples and weights of the proposed method are $x_n = \sqrt{t_n}$ and $w_n = w'_n$, respectively. Moreover, the error of the Gauss–Laguerre quadrature is given by [9, Eq. 25.4.45]

$$R_N[g] = \frac{(N!)^2}{(2N)!} \left. \frac{d^{2N}}{dt^{2N}} g(\sqrt{t}) \right|_{t=\xi}. \quad (0 < \xi < \infty) \quad (\text{A.24})$$

Thus, the convergence speed of the Gauss–Laguerre quadrature is much higher than that of the Monte Carlo integration because $\frac{(N!)^2}{(2N)!} \ll 2^{-N}$.

In Section A.3, when the number of measurements is larger than 100, the 100 measurement samples and weights are repeated $N/100$ times to generate N measurement samples and weights because the Gauss–Laguerre quadrature has very high accuracy, even if $N = 20$. Thus, we use $x_n = \sqrt{t_{(n\%100)}}$ and $w_n = \frac{100}{N} w'_{(n\%100)}$ when $N > 100$, where the binary operator $\%$ indicates the remainder after division, and t_n and w_n are obtained from 100-points Gauss–Laguerre quadrature.

A.2.2 Example 2: Rectangular rule

Generally, the rectangular rule is not a highly accurate integration method, but it is practical for the proposed method. The middle term of (A.22) is an integration with a rapidly decreasing weight e^{-r^2} , and we can obtain sufficient accuracy even if the integration interval is only $[0, 5]$ instead of $[0, \infty)$. Then, the measurement samples and weights of the proposed method with the rectangular rule can be written as

$$x_n = \frac{5}{N}n, \quad w_n = \frac{10}{N}x_n e^{-x_n^2}. \quad (\text{A.25})$$

In (A.22), the integrand can be approximated to zero at both ends of the integration domain, i.e., $g(r) \cdot 2re^{-r^2} \approx 0$ at $r = 0$ and $r = 5$. Then, the rectangular rule for (A.22) is almost equal to the trapezoidal rule, and the error of the integration can be expressed as [9, Eq. 25.4.2]

$$R_N[g] \approx \frac{125}{12N^2} \left. \frac{d^2}{dr^2} [g(r) \cdot 2re^{-r^2}] \right|_{r=\xi}. \quad (0 < \xi < 5) \quad (\text{A.26})$$

Thus, the convergence speed of the rectangular rule is higher than that of the Monte Carlo integration because $R_N[g] \sim \mathcal{O}(N^{-2})$.

It can be observed from (A.25) that the measurement samples can be viewed as a ramp signal. This is an interesting aspect of the rectangular rule for the proposed method.

A.2.3 Theoretical error analysis

In this subsection, we analyze the following total reconstruction error:

$$E_{\text{tot}}^2 = \mathbb{E} \left[|f(x) - \hat{f}(x)|^2 \right], \quad (\text{A.27})$$

where $\hat{f}(x)$ is the reconstructed nonlinearity defined as

$$\hat{f}(x) = \hat{b}_1 \psi_1(x) + \hat{b}_3 \psi_3(x) + \cdots + \hat{b}_P \psi_P(x). \quad (\text{A.28})$$

Furthermore, the nonlinear function $f(x)$ can be expanded to an infinite series as

$$f(x) = b_1 \psi_1(x) + b_3 \psi_3(x) + \cdots = \sum_{p=1,3,\dots}^{\infty} b_p \psi_p(x). \quad (\text{A.29})$$

Thus, the total error can be rewritten as

$$\begin{aligned} E_{\text{tot}}^2 &= \mathbb{E} \left[\left| \sum_{p=1,3,\dots}^P (b_p - \hat{b}_p) \psi_p(x) + \sum_{p=P+2,P+4,\dots}^{\infty} b_p \psi_p(x) \right|^2 \right] \\ &\stackrel{(a)}{=} \underbrace{\sum_{p=1,3,\dots}^P \mathbb{E} \left[|b_p - \hat{b}_p|^2 \right]}_{\text{Estimation error: } E_{\text{est}}^2} + \underbrace{\sum_{p=P+2,P+4,\dots}^{\infty} |b_p|^2}_{\text{Approximation error: } E_{\text{app}}^2}. \end{aligned} \quad (\text{A.30})$$

The transform of $\stackrel{(a)}{=}$ is due to the orthonormality of (A.7). The proposed method has two errors: the estimation error E_{est}^2 and the approximation error E_{app}^2 . The approximation error is the error caused by approximating the series expansion of $f(x)$ in finite dimensions. The conventional method also has this error due to the approximation of (A.6). The approximation error can be written as [10, eq. (3.2.7),

section 3.2, p. 217]

$$E_{\text{app}}^2 = \mathbb{E} [|f(x)|^2] - \sum_{p=1,3,\dots}^P \left| \mathbb{E} [f(x)\psi_p^*(x)] \right|^2. \quad (\text{A.31})$$

In (A.31), the approximation error monotonically decreases as the order P increases. This error has the same value in both the proposed and conventional methods if the order P is the same.

In contrast, the estimation error E_{est}^2 leads to a performance variation between the proposed and conventional methods. When the Gram matrix converges to the identity matrix sufficiently, the estimated coefficient \hat{b}_p can be written as

$$\begin{aligned} \hat{b}_{2i-1} &= (\Psi^H \mathbf{W} \mathbf{y})_i \\ &= \sum_{n=1}^N f(x_n) \psi_{2i-1}^*(x_n) w_n + \sum_{n=1}^N z_n \psi_{2i-1}^*(x_n) w_n. \end{aligned} \quad (\text{A.32})$$

Thus, the estimation error E_{est}^2 can be rewritten as

$$\begin{aligned} E_{\text{est}}^2 &= \sum_{p=1,3,\dots}^P \left| \sum_{n=1}^N f(x_n) \psi_p^*(x_n) w_n - b_p \right|^2 \\ &\quad + \sum_{p=1,3,\dots}^P \mathbb{E} \left[\left| \sum_{n=1}^N z_n \psi_p^*(x_n) w_n \right|^2 \right]. \end{aligned} \quad (\text{A.33})$$

In the right-hand side of (A.33), the first term indicates the square of the quadrature error, and the second term indicates the error caused by the noise. The square of the quadrature error is $(R_N[f(r)\psi_p^*(r)])^2$, and the error rapidly decays at a rate of $\mathcal{O}(N^{-4})$, even for the rectangular rule. In addition, the noise error can be rewritten as

$$\sum_{p=1,3,\dots}^P \mathbb{E} \left[\left| \sum_{n=1}^N z_n \psi_{2i-1}^*(x_n) w_n \right|^2 \right] = \sigma_z^2 \sum_{p=1,3,\dots}^P \sum_{n=1}^N |\psi_p(x_n) w_n|^2. \quad (\text{A.34})$$

Equation (A.34) shows that the effect of noise depends on the values of the measurement samples and weights determined by the numerical integration method employed, and the sum of their squares is an indicator of the influence of noise. When the rectangular rule is used for the proposed method, the summation of the

right-hand side of (A.34) with a large N can be asymptotically expressed as

$$\sum_{n=1}^N |\psi_p(x_n)w_n|^2 \approx \frac{5}{N} \int_0^\infty \{\psi_p(x_n) \cdot 2re^{-r^2}\}^2 dr \sim \mathcal{O}(N^{-1}). \quad (\text{A.35})$$

The noise error decays at a rate of $\mathcal{O}(N^{-1})$, and the quadrature error is negligibly small compared with the noise error.

To summarize this section, we can estimate the error of the proposed method as

$$E_{\text{tot}}^2 \approx E_{\text{app}}^2 + \sigma_z^2 \sum_{p=1,3,\dots}^P \sum_{n=1}^N |\psi_p(x_n)w_n|^2. \quad (\text{A.36})$$

The first term is a constant for the number of measurements N , and the second term decays at a rate of $\mathcal{O}(N^{-1})$. Thus, the convergence rate of the proposed method is the same as that of the conventional Monte-Carlo-based least squares method whose rate of square error is $\mathcal{O}(N^{-1})$. This is because the conventional method is exactly same as the proposed method with randomly generated samples x_n and weights $w_n = 1/N$. However, the rate is a characteristic of $N \rightarrow \infty$, and we compare the characteristics of each method from a small to a large number N in numerical experiments in the following section.

A.3 Results of Numerical Experiments

In this section, we evaluate and compare the condition number and total reconstruction error, which is defined as (A.27), for the proposed and conventional methods using 10^4 times Monte Carlo simulation. In the simulation, we use the Rapp model [11] as an amplifier, and its transfer function can be written as

$$f(x) = \frac{x}{\left(1 + (|x|/B)^{2s}\right)^{\frac{1}{2s}}}, \quad (\text{A.37})$$

where B indicates the input back-off (IBO), and s is the smoothness factor. Furthermore, we use $B = \sqrt{10}$ (i.e., 10 dB IBO) and $s = 3$.

Figure A.1 shows the condition number of the Gram matrix of each method. As mentioned in the Introduction, the condition number of the conventional method is much larger than that of the proposed method because it is based on the Monte Carlo integration. The proposed method successfully reduces the condition number

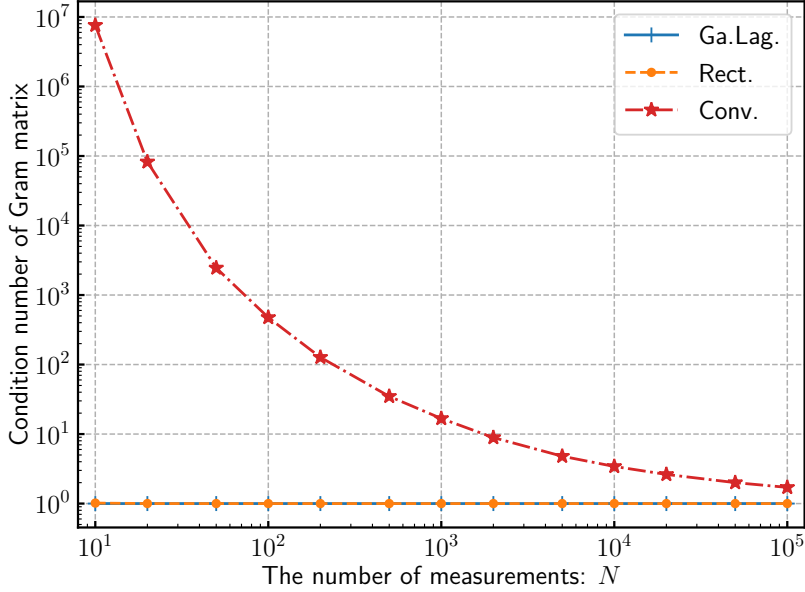


Figure A.1: Condition number of the Gram matrix of each method when $P = 7$. The value is averaged over 10^4 times independent Monte Carlo simulation.

because of its high accuracy of numerical integration. This indicates that the proposed method can achieve better stability than the conventional least squares method.

Figures A.2, A.3, A.4, and A.5 show the simulation results and theoretical results of the total reconstruction error for each method, with $P = 7$ and $P = 13$, from a very noisy case to an almost noise-free case for a wide range of applications such as pre-distortion, post-distortion, and self-interference cancellers. The error of the proposed method is much smaller than that of the conventional method, as the proposed method has good stability and better accuracy of integration. Surprisingly, even when only 10 measurements are used, the proposed method maintained the reconstruction error below the noise. In contrast, in Fig. A.2, the error of the conventional method is smaller than that of the proposed method when $N > 10^4$. Therefore, the conventional method is more effective than the proposed method when a sufficient number of samples are used under low signal-to-noise ratio (SNR). In addition, the theoretical and simulation results are consistent with each other in these figures. Thus, the analysis in this chapter is useful for the error estimation of the proposed method. Moreover, if the error is to be reduced further, a numerical integration method that reduces the value of (A.34) needs to be used.

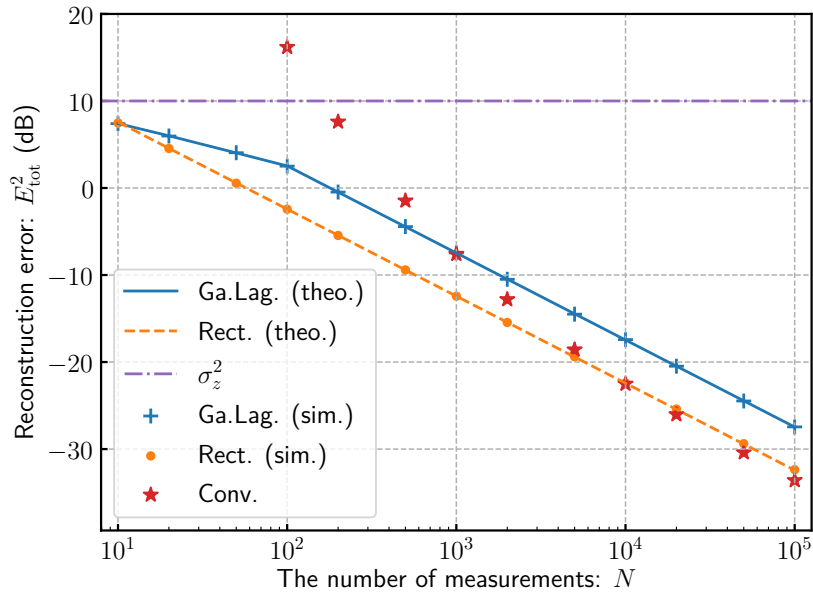


Figure A.2: Total reconstruction error E_{tot}^2 of each method with $P = 7$ and $\sigma_z^2 = 10^1$. The lines indicate theoretical results, and the markers indicate simulation results.

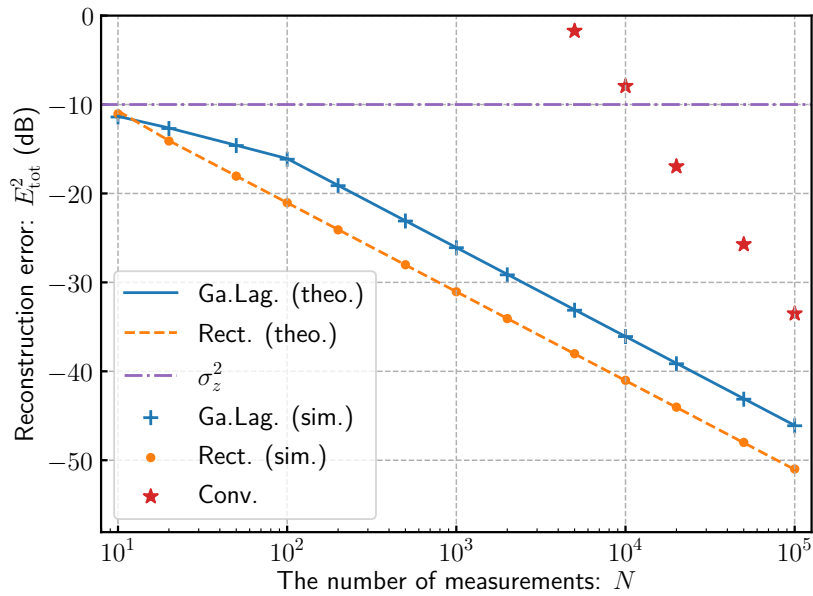


Figure A.3: Total reconstruction error E_{tot}^2 of each method with $P = 13$ and $\sigma_z^2 = 10^{-1}$. The lines indicate theoretical results, and the markers indicate simulation results.

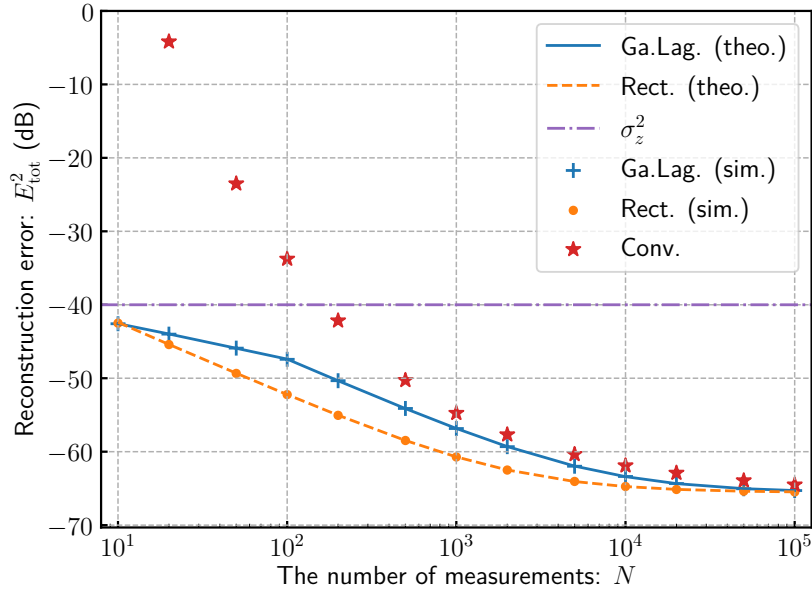


Figure A.4: Total reconstruction error E_{tot}^2 of each method with $P = 7$ and $\sigma_z^2 = 10^{-4}$. The lines indicate theoretical results, and the markers indicate simulation results.

A.4 Conclusion

In this appendix, the author proposed a novel estimation method for the memoryless nonlinearity of an amplifier. The method uses weighted least squares with orthonormal polynomials and numerical integration. The measurement signal and weights of the proposed method were designed based on the numerical integration method to converge the Gram matrix to the unit matrix with high accuracy, even with a small number of observations. Moreover, we derived the theoretical error of the proposed method. The simulation results showed that the proposed method dramatically improved the accuracy of the conventional least squares method and achieved sufficient accuracy with 10 measurement samples. The theoretical results and simulation results were consistent with each other.

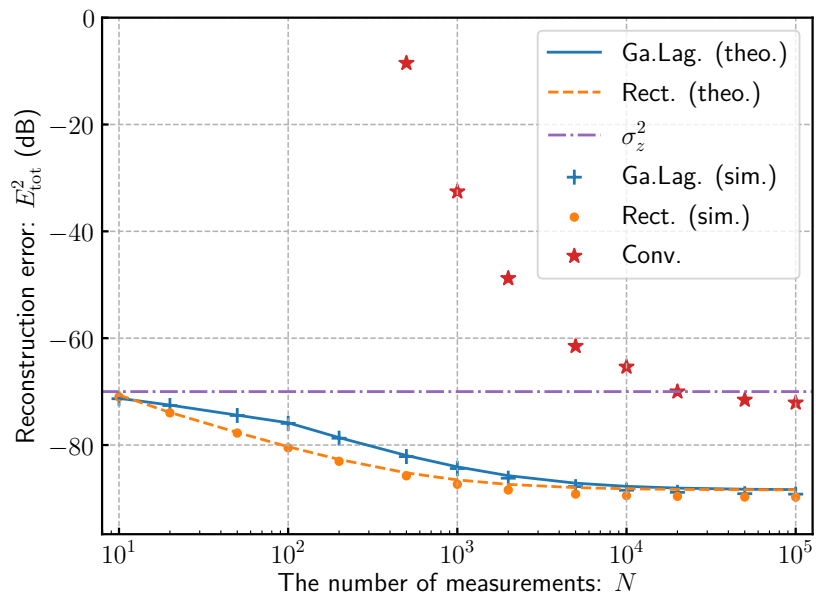


Figure A.5: Total reconstruction error E_{tot}^2 of each method with $P = 13$ and $\sigma_z^2 = 10^{-7}$. The lines indicate theoretical results, and the markers indicate simulation results.

References

- [1] H. Qian, S. Yao, H. Huang, and W. Feng, “A low-complexity digital predistortion algorithm for power amplifier linearization,” *IEEE Trans. Broadcast.*, vol. 60, no. 4, pp. 670–678, Dec. 2014.
- [2] K. Komatsu, Y. Miyaji, and H. Uehara, “Basis function selection of frequency-domain Hammerstein self-interference canceller for in-band full-duplex wireless communications,” *IEEE Trans. Wireless Commun.*, vol. 17, no. 6, pp. 3768–3780, June 2018.
- [3] R. Raich and G. Zhou, “Orthogonal polynomials for complex Gaussian processes,” *IEEE Trans. Signal Process.*, vol. 52, no. 10, pp. 2788–2797, Oct. 2004.
- [4] R. Dallinger, H. Ruotsalainen, R. Wichman, and M. Rupp, “Adaptive predistortion techniques based on orthogonal polynomials,” in *Proc. 44th Asilomar Conf. Signals, Syst., Comput.*, Nov. 2010, pp. 1945–1950.
- [5] S. Teodoro, A. Silva, R. Dinis, F. M. Barradas, P. M. Cabral, and A. Gameiro, “Theoretical analysis of nonlinear amplification effects in massive MIMO systems,” *IEEE Access*, vol. 7, pp. 172 277–172 289, 2019.
- [6] L. Shen, B. Henson, Y. Zakharov, and P. D. Mitchell, “Adaptive nonlinear equalizer for full-duplex underwater acoustic systems,” *IEEE Access*, vol. 8, pp. 108 169–108 178, 2020.
- [7] P. Banelli and S. Cacopardi, “Theoretical analysis and performance of OFDM signals in nonlinear AWGN channels,” *IEEE Trans. Commun.*, vol. 48, no. 3, pp. 430–441, Mar. 2000.

- [8] J. Kral, T. Gotthans, R. Marsalek, M. Harvanek, and M. Rupp, “On feedback sample selection methods allowing lightweight digital predistorter adaptation,” *IEEE Trans. Circuits Syst. I*, vol. 67, no. 6, pp. 1976–1988, 2020.
- [9] M. Abramowitz and I. A. Stegun, *Handbook of Mathematical Functions with Formulas, Graphs, and Mathematical Tables*. New York City: Dover, 1964.
- [10] W. Gautschi, *Orthogonal Polynomials: Computation and Approximation*, ser. Numerical mathematics and scientific computation. Oxford University Press, 2004.
- [11] C. Rapp, “Effects of HPA-nonlinearity on a 4-DPSK/OFDM-signal for a digital sound broadcasting system,” in *Proc. the Second European Conf. on Satellite Commun.*, Oct. 1991, pp. 179–184.

Appendix B

List of Related Publications by the Author

B.1 Journal Papers and Letters

1. K. Komatsu, Y. Miyaji, and H. Uehara, “Weighted least squares with orthonormal polynomials and numerical integration for estimation of memoryless nonlinearity,” *IEEE Wireless Communications Letters*, vol. 9, no. 12, pp. 2197–2201, Dec. 2020.
2. T. Fukui, K. Komatsu, Y. Miyaji, and H. Uehara, “Analog self-interference cancellation using auxiliary transmitter considering IQ imbalance and amplifier nonlinearity,” *IEEE Transactions on Wireless Communications*, vol. 19, no. 11, pp. 7439–7452, Nov. 2020.
3. K. Komatsu, Y. Miyaji, and H. Uehara, “Iterative nonlinear self-interference cancellation for in-band full-duplex wireless communications under mixer imbalance and amplifier nonlinearity,” *IEEE Transactions on Wireless Communications*, vol. 19, no. 7, pp. 4424–4438, July 2020.
4. K. Komatsu, Y. Miyaji, and H. Uehara, “Basis function selection of frequency-domain Hammerstein self-interference canceller for in-band full-duplex wireless communications,” *IEEE Transactions on Wireless Communications*, vol. 17, no. 6, pp. 3768–3780, June 2018.

B.2 Conference Papers

1. K. Komatsu, Y. Miyaji and H. Uehara, “Frequency-domain Hammerstein self-interference canceller for in-band full-duplex OFDM systems,” *IEEE Wireless Communications and Networking Conference (WCNC)*, San Francisco, CA, 2017.
2. K. Komatsu, Y. Miyaji and H. Uehara, “Low computational complexity training scheme for orthogonalized parallel Hammerstein self-interference canceller,” *Interdisciplinary Research And Global Outlook (IRAGO) Conference*, Tokyo, 2016.

B.3 Presentations in Japanese

1. 佐藤栄作, 小松和暉, 宮路祐一, 上原秀幸, “帯域内全二重無線のための非線形補償受信機を用いたビット誤り率の改善,” 電子情報通信学会総合大会, B-5-109, 2021年3月.
2. 岡野公太, 小松和暉, 宮路祐一, 上原秀幸, “コンパANDING法を用いた帯域内全二重におけるビット誤り率の理論解析,” 電子情報通信学会総合大会, B-5-108, 2021年3月.
3. 田齊広太郎, 小松和暉, 宮路祐一, 上原秀幸, “RadComにおけるRF不完全性を考慮した距離と速さの検知,” 電子情報通信学会ソサイエティ大会, B-5-69, 2020年9月.
4. 蛭川泰丞, 小松和暉, 宮路祐一, 上原秀幸, “ベースバンド無線における帯域内全二重のためのヒルベルト変換を組み合わせた自己干渉除去,” 電子情報通信学会総合大会, B-5-136, 2020年3月.
5. 石井建至, 小松和暉, 宮路祐一, 上原秀幸, “無線チャネルの変動に対処した自己干渉キャンセラの再学習,” 電子情報通信学会総合大会, B-5-135, 2020年3月.
6. 小松和暉, 宮路祐一, 上原秀幸, “非線形自己干渉キャンセラを用いる帯域内全二重のための送信機AM-AM特性の最適化,” 電子情報通信学会総合大会, B-5-134, 2020年3月.
7. 岡野公太, 小松和暉, 宮路祐一, 上原秀幸, “帯域内全二重におけるPAPR低減手法によるデジタル自己干渉除去の性能改善,” 電子情報通信学会総合大会, B-5-133, 2020年3月.
8. 田齊広太郎, 小松和暉, 宮路祐一, 上原秀幸, “Radar and Communi-

- cationにおけるRF不完全性の影響の評価,” 電子情報通信学会総合大会, B-5-131, 2020年3月.
9. Chua Teong Zhe, 小松和暉, 宮路祐一, 上原秀幸, “Improving In-Band Full-Duplex Capacity by Transmitter Nonlinearization using Digital Predistortion,” 電子情報通信学会技術研究報告, vol. 119, no. 448, RCS2019-338, pp. 99–104, 2020年3月.
 10. 石井建至, 小松和暉, 宮路祐一, 上原秀幸, “増幅器の利得変動に対処した自己干渉キャンセラの部分的再学習,” 電子情報通信学会技術研究報告, vol. 119, no. 296, RCS2019-215, pp. 73–78, 2019年11月.
 11. Teong Zhe Chua, 小松和暉, 宮路祐一, 上原秀幸, “帯域内全二重におけるRappモデルによる電力増幅器の非線形歪みと自己干渉除去の性能向上に関する検討,” 電子情報通信学会ソサイエティ大会, B-5-85, 2019年9月.
 12. 福井崇久, 小松和暉, 宮路祐一, 上原秀幸, “帯域内全二重におけるRappモデルによる電力増幅器の非線形歪みと自己干渉除去の性能向上に関する検討,” 電子情報通信学会ソサイエティ大会, B-5-84, 2019年9月.
 13. 小松和暉, 宮路祐一, 上原秀幸, “非線形自己干渉キャンセラのための二次元正規直交ラゲール多項式を用いた理論的性能解析,” 電子情報通信学会技術研究報告, vol. 119, no. 90, RCS2019-76, pp. 239–244, 2019年6月.
 14. 福井崇久, 小松和暉, 宮路祐一, 上原秀幸, “補助送信機による自己干渉除去のためのWidely Linearフィルタ設計における適応アルゴリズムの評価,” 電子情報通信学会技術研究報告, vol. 119, no. 31, RCS2019-31, pp. 47–52, 2019年5月.
 15. Chua Teong Zhe, 小松和暉, 宮路祐一, 上原秀幸, “USRPにおける帯域内全二重におけるデジタルプリディストーションを用いた自己干渉除去,” 電子情報通信学会総合大会, B-5-103, 2019年3月.
 16. 田齊広太郎, 小松和暉, 宮路祐一, 上原秀幸, “帯域内全二重における深層学習を用いた自己干渉除去,” 電子情報通信学会総合大会, B-5-102, 2019年3月.
 17. 小松和暉, 宮路祐一, 上原秀幸, “非線形自己干渉キャンセラのためのラゲール陪多項式を用いた理論的性能解析,” 電子情報通信学会技術研究報告, vol. 118, no. 311, RCS2018-194, pp. 97–102, 2018年11月.
 18. 福井崇久, 小松和暉, 宮路祐一, 上原秀幸, “I/Qインバランスと位相

- 雑音を考慮した補助送信機によるアナログ自己干渉除去の伝搬遅延の影響,” 電子情報通信学会技術研究報告, vol. 118, no. 311, RCS2018-193, pp. 91–96, 2018年11月.
19. 宮路祐一, 石井建至, 福井崇久, 小網 敦, 小松和暉, 上原秀幸, “[依頼講演]帯域内全二重通信のソフトウェア無線での評価,” 電子情報通信学会技術研究報告, vol. 118, no. 254, RCS2018-156, pp. 37–37, 2018年10月.
 20. 福井崇久, 小松和暉, 宮路祐一, 上原秀幸, “周波数選択性I/Qインバランスを考慮した補助送信機によるアナログ自己干渉除去,” 電子情報通信学会ソサイエティ大会, B-5-108, 2018年9月.
 21. 小網敦, 小松和暉, 宮路祐一, 上原秀幸, “全二重通信における干渉除去がビット誤り率に与える影響,” 電子情報通信学会ソサイエティ大会, B-5-107, 2018年9月.
 22. 小網敦, 小松和暉, 宮路祐一, 上原秀幸, “全二重通信における残留干渉を考慮したリンク品質の均一化,” 電気・電子・情報関連学会東海支部連合大会, C2-4, 2018年9月.
 23. 石井建至, 小松和暉, 宮路祐一, 上原秀幸, “USRPを用いた帯域内全二重通信端末の試作機,” 電子情報通信学会総合大会, B-5-96, 2018年3月.
 24. 福井崇久, 小松和暉, 宮路祐一, 上原秀幸, “帯域内全二重におけるアナログ自己干渉除去のための補助送信機のUSRPによる実装,” 電子情報通信学会総合大会, B-5-95, 2018年3月.
 25. 宮路祐一, 小松和暉, 上原秀幸, “[依頼講演]帯域内全二重の実現に向けた自己干渉除去技術,” 電子情報通信学会技術研究報告, vol. 117, no. 246, RCS2017-193, p. 141, 2017年10月.
 26. 小松和暉, 宮路祐一, 上原秀幸, “非線形歪みを考慮したデジタル自己干渉除去フィルタのための直列接続方式の提案,” 電子情報通信学会東海支部卒業研究発表会, A-3-2, 2016年.
 27. 小松和暉, 宮路祐一, 上原秀幸, “直列接続型ハマーシュタイン・デジタル自己干渉除去アルゴリズムの提案,” 電子情報通信学会技術研究報告, vol. 115, no. 369, RCS2015-247, pp. 25–30, 2015年12月.

B.4 Awards

1. Young Researcher Awards, IEEE Nagoya Section, Dec. 2020.

2. 日本学術振興会，特別研究員DC2，2019年4月～2021年3月
3. 出版助成，公益財団法人 中部電気利用基礎研究振興財団，2018年8月
4. 学生研究奨励賞，電子情報通信学会東海支部，2018年6月
5. 優秀学生表彰，豊橋技術科学大学，2018年3月
6. 平成29年度学生表彰（個人学術研究活動），豊橋技術科学大学，2018年3月
7. 平成29年度最優秀特別研究発表賞，豊橋技術科学大学 電気・電子情報工学専攻，2018年2月
8. 優秀発表賞，第19回東海三大学通信系研究室合同修士論文発表会，2018年2月
9. Conference Presentation Award, IEEE Nagoya Section, April 2017
10. IEEE Communications Society Young Professionals Best Paper Award, IEEE Communications Society, Mar. 2017
11. Student Travel Grants for IEEE Wireless Communications and Networking Conference (WCNC) 2017, IEEE Communications Society and National Science Foundation, Mar. 2017
12. 平成28年度学生表彰（団体学術研究活動），豊橋技術科学大学，2017年3月
13. 大学研究展示奨励賞，Microwave Workshops & Exhibition (MWE) 2016，2016年12月
14. TUT Excellent Student Award, IEEE Nagoya Section, April 2016
15. 2015年度優秀学生賞，豊橋技術科学大学，2016年4月
16. 2015年度支部長賞，電気学会東海支部，2016年3月
17. 平成27年度最優秀卒業研究発表賞，豊橋技術科学大学 電気・電子情報工学課程，2015年12月